UNIVERSITÄT BONN
Physikalisches Institut

Search for the Associated Production of Charginos and Neutralinos in Proton-Antiproton Collisions at $\sqrt{s} = 1.96$ TeV with the DØ Detector at the Tevatron

von

Olav Michael Kåre Mundal

Abstract:

A search for Supersymmetry is performed via the associated production of charginos and neutralinos in final states consisting of three charged leptons and missing transverse energy using data collected with the DØ detector at a center-of-mass energy of 1.96 TeV at the Fermilab Tevatron Collider. The data sample corresponds to an integrated luminosity of ~ 2.3 fb^{-1}. This final state is considered one of the most promising channels in the search for supersymmetric particles because of its low Standard Model background. A dedicated event selection is developed and events with two muons plus an additional isolated track or events with two electrons plus an additional isolated track are analyzed. The requirement of an isolated track replaces the third charged lepton in the event. After all selection cuts are applied, in total 7 events are selected in the data with an expected number of background events of 5.24 ± 0.40 (stat)± 0.30 (syst). Due to the good agreement of events observed in data with the expectation of the Standard Model backgrounds, no evidence for Supersymmetry is found. The present analyses are considered in combination with three other decay channels and limits on the production cross section times leptonic branching fraction are set. The results are interpreted in a constrained scenario and exclusion regions are derived as a function of m_0 and $m_{1/2}$.

Post address:
Nußallee 12
D-53115 Bonn
Germany

BONN-IR-2009-03
Bonn University
March 2009

UNIVERSITÄT BONN
Physikalisches Institut

Search for the Associated Production of Charginos and Neutralinos in Proton-Antiproton Collisions at $\sqrt{s} = 1.96$ TeV with the DØ Detector at the Tevatron

Dissertation

zur

Erlangung des Doktorgrades (Dr. rer. nat.)

der

Mathematisch-Naturwissenschaftlichen Fakultät

der

Rheinischen Friedrich-Wilhelms-Universität Bonn

vorgelegt von

Olav Michael Kåre Mundal

aus

Oslo, Norwegen

Bonn 2008

Dieser Forschungsbericht wurde als Doktorarbeit von der mathematisch-naturwissenschaftlichen Fakultät der Universität Bonn angenommen.

Ersheinungsjarh: 2009

Diese Dissertation ist auf dem Hochschulschriftenserver der ULB Bonn unter http://hss.ulb.uni-bonn.de/diss_online elektronisch publiziert.

Angenommen:	Oktober 2008
Referent:	Prof. Dr. V. Büscher
Korreferent:	Prof. Dr. K. Desch

Contents

1. Introduction

Particle Physics seeks to answer some of the most fundamental questions man can ask. What is matter made from? Which forces act between the constituents of matter? Is there a fundamental theory that can describe all fundamental processes at high energy scales?

There is a remarkable succesfull theory that tries to answer these questions, the Standard Model of Particle Physics. So far, all measurements are in good agreement with the predictions from the Standard Model. With the exceptions of neutrino masses, the studies of the smallest constituents of matter, quarks and leptons, and the forces that act between them, have not revealed any direct evidence for physics beyond the Standard Model. However, the Standard Model leaves several questions unanswered. For example, the origin of electroweak symmetry breaking is not known and the origin of dark matter which seems to provide the majority of mass in our universe, is not described by the Standard Model. In addition, gravity is not included in the SM. By most physicists, the Standard Model is considered an effective low energetic approximation of a more fundamental theory. Without any direct observations, we do not know what is beyond the Standard Model. But there are theories that attempt to go further and predict new physics at higher energies. Supersymmetry is such a theory. It relates the properties of the bosons to those of the fermions. Each Standard Model particle gets a supersymmetric partner with the same quantum numbers and just the spin differing by $\frac{1}{2}$. Since the predicted supersymmetric particles have not yet been discovered, Supersymmetry, if realized in Nature, must be a broken in a way that the masses of Standard Model particles and their superpartners differ. Low mass supersymmetric partners are expected to be produced at a detectable rate at present or future collider experiments.

Searches for supersymmetric particles have been performed by the four LEP experiments, and since no evidence for such particles were found, lower limits on their masses have been derived. The search for supersymmetry is also carried out at the Tevatron collider located at the Fermi National Accelerator Laboratory in Batavia, Illinois. Two dedicated detectors, CDF and DØ are located along the Tevatron to analyze proton-antiproton collisions at a center-of-mass energy of 1.96 TeV. A particular promising discovery channel for supersymmetry within the Tevatron energy range is the *trilepton channel*. In this channel, the lighter supersymmetric partners of the Higgs and gauge bosons, the charginos and neutralinos, decay into final states with leptons or hadrons and missing energy. Using the leptonic final states, the signal can be separated from the Standard Model background.

In the analyses performed in this thesis, it is assumed that supersymmetric particles decay into their Standard Model partners and the lightest supersymmetric particle, which is only weakly interacting and carries away energy and momentum is stable, leading to detector signatures with large missing energy. Within the present thesis, a search for supersymmetry is performed in final states consisting of two electrons and an isolated track, or two muons and an isolated track. The data was collected with the DØ detector from April 2002 to August 2007, corresponding to a

total integrated luminosity of 2.3 fb^{-1}.

This document is organized as follows: Chapter 2 will give an introduction to the Standard Model and Supersymmetry. Chapter 3 introduces the Tevatron Collider and the DØ experiment. Chapter 4 describes the phenomenology of proton-antiproton collisions and in Chapter 5, an overview of the reconstruction of the resulting objects of the proton-antiproton collisions is given. The dataset and Monte Carlo samples are listed in Chapter 6 and Chapter 7 gives a detailed description of the production and decay of SUSY particles and the relevant Standard Model Backgrounds. In Chapter 8, various corrections done to the Monte Carlo is described and in Chapter 9, the analyses presented in this document are described in detail. Chapter 10 provides the interpretation of the results before Chapter 11 concludes the document.

2. Theory

The Standard Model is the theory of particles and their interactions, but it is believed that the Standard Model is not a complete theory of nature. In the first part of this chapter the Standard Model (SM) [1] of particle physics will be introduced. The second part of the chapter discusses a possible extension of the Standard Model, called Supersymmetry (SUSY) [2]. Supersymmetry is the theoretical framework for the analyses presented in this thesis.

2.1. The Standard Model

The Standard Model of particle physics is a relativistic quantum field theory developed in the second half of the last century. In the Standard Model, every physical system is described by a Lagrangian $\mathcal{L}$ which is a function of the fields and their derivatives. The equations of motion are derived from the Lagrangian by minimizing the action $S = \int \mathcal{L}\ d^4x$. From Noether's theorem it follows that to every operation that leaves the Lagrangian invariant, there is a conserved current. It is also a fundamental requirement that the Lagrangian is invariant under gauge transformations. This means that the Lagrangian should be invariant under a set of transformations that do not change the physical content of the Lagrangian. The consequences of this important requirement will become clear later.

In the Standard Model, the fundamental particles are divided into two groups according to their spin s: fermions and bosons. Bosons have integer spin while fermions have half-integer spin. The fermions are again divided into leptons and quarks. The SM fermions are listed in Table 2.1 and the bosons are listed in Table 2.2. Leptons participate only in electroweak interactions, while quarks carry strong charge (color) and hence also participate in strong interactions. The entire collection of fermions is divided into three generations. The leptons are comprised of the electron (e), the electron neutrino (ν_e), the muon (μ), the muon neutrino (ν_μ) the tau (τ) and the tau neutrino, (ν_τ). The six quarks are called up (u), down (d), charm (c), strange (s), top (t) and bottom (b). For each particle there is a corresponding anti-particle with the same properties but opposite electrical charge. The quarks additionally come in three different colors, and yet another property of all particles is their chirality. This means that left-handed fermions come in a weak-isospin doublet, while right-handed particles are singlets. Within the SM, neutrinos are massless thus no right-handed neutrinos exist, in contradiction to the present experimental data [3].

The forces between particles are mediated by the force carriers, the gauge bosons. There are four known interactions: electromagnetic, weak, strong and gravitational forces. For gravity, no quantum field theory exists, thus gravity is not incorporated in the SM. This is a good approximation since gravity at scales that are presently achievable is very weak. The three others are described by local gauge symmetries and are based on symmetry under the non-Abelian gauge

Table 2.1.: Overview of the Standard Model fermions and their masses, [4]. Throughout this thesis, natural units are used. The fundamental constants $\hbar$ and c are set to 1, and all quantities (e.g. masses) have the dimension of a power of energy.

Leptons			Quarks		
Name	Symbol	Mass	Name	Symbol	Mass
electron neutrino	ν_e	< 3 eV	up	u	1.5 to 4 MeV
muon neutrino	ν_μ	< 0.2 MeV	down	d	4 to 8 MeV
tau neutrino	ν_τ	< 18.2 MeV	strange	s	80 to 130 MeV
electron	e	511.0 keV	charm	c	1.15 to 1.35 GeV
muon	μ	105.7 MeV	bottom	b	4.6 to 4.9 GeV
tau	τ	1.777 GeV	top	t	172.4 ± 1.2 GeV

group

$$SU(3)_C \times SU(2)_L \times U(1)_Y,$$

where C refers to the color of quarks, L to the third weak-isospin component of the left-handed particles and Y to the hypercharge. The subgroup $SU(2)_L \times U(1)_Y$ represents the unification of the electromagnetic and the weak interaction.

2.1.1. Electroweak Interaction

The electromagnetic and the weak interactions are combined into one theory called the electroweak theory. The gauge group is $SU(2)_L \times U(1)_Y$ and the generators of the group are the hypercharge Y and the weak isospin $\mathbf{T}$. The electroweak theory is a non-abelian local gauge theory. A non-abelian group is a group where the generators do not commute. This leads to interactions between the gauge bosons.

The Lagrangian is required to be locally invariant under $SU(2)_L \times U(1)_Y$ transformations and

Table 2.2.: Standard Model gauge bosons and their properties [4].

Name	Field	Interaction	Charge [e]	Mass [GeV]
Photon γ	A_μ	electromagnetic	$< 5 \times 10^{-30}$	$< 6 \times 10^{-26}$
Z Boson	Z_μ	electroweak	0	91.1876 ± 0.0021
W Bosons	$W_\mu^\pm$	weak	± 1	80.425 ± 0.038
Gluon g	G_μ^a	strong	0	0

this leads to the introduction of four gauge fields: one (B_μ) to compensate for the local phase transformation of the $U(1)_Y$ group and three more (W_μ^a, $a = 1, 2, 3$) related to the transformations of $\mathrm{SU}(2)_L$. The Lagrangian density has the form

$$\mathcal{L}_{EW} = \bar{\Psi}\gamma_\mu D^\mu \Psi - \frac{1}{4}[W_{\mu\nu}W^{\mu\nu} + B_{\mu\nu}B^{\mu\nu}] \tag{2.1}$$

where D^μ is the covariant derivative

$$D^\mu = i\partial^\mu - g\mathbf{T} \times \mathbf{W}^\mu + g^{'} Y B^\mu \tag{2.2}$$

where $\mathbf{T}$ is the weak isospin and the field strength tensors $\mathbf{W}_{\mu\nu}$ and $B_{\mu\nu}$ are defined as

$$\mathbf{W}_{\mu\nu} = \partial_\mu \mathbf{W}_\nu \partial_\nu \mathbf{W}_\mu - g\mathbf{W}_\mu \times \mathbf{W}_\nu, \tag{2.3}$$

and

$$B_{\mu\nu} = \partial_\mu B_\nu - \partial_\nu B_\mu. \tag{2.4}$$

The neutral component W_μ^3 mixes with B_μ to form the physical fields A_μ and Z_μ.

$$A_\mu = B_\mu \cos\theta_w + W_\mu^3 \sin\theta_w \tag{2.5}$$

$$Z_\mu = -B_\mu \sin\theta_w + W_\mu^3 \cos\theta_w. \tag{2.6}$$

A_μ is identified as the photon field and Z_μ is identified as the neutral Z boson field. θ_w is the weak mixing angle (or Weinberg angle). It is determined by the two coupling constants g and $g^{'}$:

$$\cos\theta_w = \frac{g}{\sqrt{g^2 + g^{'2}}}. \tag{2.7}$$

The remaining fields W_μ^1 and W_μ^2 mix to form the electrically charged gauge bosons

$$W_\mu^\pm = \frac{1}{2}(W_\mu^1 \mp W_\mu^2) \tag{2.8}$$

The photon and the Z boson couple to left-handed and right-handed particles, but the charged gauge bosons (W) only couple to left handed particles. The coupling constants g and $g^{'}$ from Equation 2.2 are related to the electric charge by

$$e = g^{'} \cos\theta_w = g \sin\theta_w \tag{2.9}$$

where e is the elementary charge. The coupling of the Z boson is given by

$$-i\frac{g}{\cos\theta_w}\gamma^\mu\frac{1}{2}(c_V^f - c_A^f\gamma^5) \tag{2.10}$$

where γ^μ and γ^5 are Dirac matrices and c_V^f and c_A^f denote the vector and axialvector couplings. They are given by

$$c_V^f = T_3^f - 2\sin^2\theta_w q_f \tag{2.11}$$

$$c_A^f = T_3^f$$

For the charged gauge bosons, the coupling is given by

$$-i\frac{g}{\sqrt{2}}\gamma^\mu\frac{1}{2}(1-\gamma^5)$$

The electroweak Lagrangian does not contain any mass terms for the fermion and gauge fields. The introduction of explicit mass terms in the Lagrangian destroys renormalizability and gauge invariance. Mass terms are introduced by the Higgs mechanism through spontaneous symmetry breaking. This will be discussed in Section 2.1.3.

2.1.2. Strong Interaction

Quantum Chromodynamics (QCD) [5] is the theory describing the strong interactions of quarks and gluons. It is based on the $SU(3)_C$ gauge group. QCD is a non-abelian gauge theory and the Lagrangian can be written

$$\mathcal{L}_{QCD} = \mathcal{L}_{quark} + \mathcal{L}_{int} + \mathcal{L}_{glue}. \tag{2.12}$$

$\mathcal{L}_{quark}$ describes the propagation of the free quarks and yields the Dirac equation for spin 1/2 particle for each quark with a given flavor and color. Since the Dirac equation is not invariant under local gauge transformations, gauge invariance is restored in the same way as it is restored in QED or in the electroweak theory by introducing a compensating spin-1 field that interacts with the quark fields. This results in a quark-gluon interaction term $\mathcal{L}_{int}$ which needs to be added to the QCD Lagrangian:

$$\mathcal{L}_{int}(x) = g_s \sum_{q=u,d,s,...} \bar{\psi}_{qi}(x)\frac{(\lambda^a)^i_k}{2}\gamma^\mu\psi_q^k(x)A_\mu^a(x). \tag{2.13}$$

A_μ^a (with $a = 1...8$) denotes the gluon fields, g_s is the dimensionless coupling and λ^a are the generators of the SU(3) group. The indices i and k denote the quark color. In contrast to

the electromagnetic interaction, where the photon field is electrically neutral, the gluon fields also carry color charge which leads to gluon self-interaction. The gluon self-interaction limits the range of the strong force. Because of the gluon self-coupling, the coupling strength increases with distance, and quarks and gluons can not be observed as free particles. This phenomenon is called confinement. Quarks can only be observed in bound states: mesons ($q\bar{q}$) and baryons (qqq). With decreasing distance, the coupling between the quarks goes to zero. This is known as asymptotic freedom. Since the quarks can be approximately treated as free particles, perturbation theory can be used in this case.

The last term $\mathcal{L}_{glue}$ describes the propagation of the gluon fields:

$$\mathcal{L}_{glue}(x) = -\frac{1}{4} G^a_{\mu\nu}(x) G^{a\mu\nu}(x) \tag{2.14}$$

where

$$G^a_{\mu\nu} = \partial_\mu A^a_\nu - \partial_\nu A^a_\mu + g_s f^{abc} A^b_\mu A^c_\nu. \tag{2.15}$$

$G^a_{\mu\nu}$ is the gluon field-strength tensor, the f_{abc} $(a, b, c = 1...8)$ are the structure constants of SU(3). Local gauge invariance of $\mathcal{L}_{glue}$ implies that gluons are massless. $G^a_{\mu\nu}$ is more complicated than its QED analog $B_{\mu\nu}$ since it allows three- and four-gluon vertices (gluon self-interactions).

The QCD Lagrangian at tree level is given by:

$$\mathcal{L}_{QCD} = \sum_{q=u,d,s,...} \bar{\psi}_q (i D_\mu \gamma^\mu - m_q) \psi_q - \frac{1}{4} G^{\mu\nu}_a G_{a\mu\nu} \tag{2.16}$$

using the covariant derivative

$$D_\mu = \partial_\mu - i g_s \frac{\lambda^a}{2} \cdot A^a_\mu. \tag{2.17}$$

2.1.3. Higgs Mechanism

According to the electroweak and strong interactions described in the previous sections, all particles are massless. This is in direct conflict with experiment, because only photons and gluons are massless. The explicit introduction of mass terms, however, would break the gauge symmetry and destroy renormalizability. A solution is provided by the Higgs mechanism and spontaneous symmetry breaking [6].

A complex two-component scalar field Φ is introduced:

$$\Phi(x) = \begin{pmatrix} \Phi^+ \\ \Phi^0 \end{pmatrix} = \begin{pmatrix} \Phi_1 + i\Phi_2 \\ \Phi_3 + i\Phi_4 \end{pmatrix}$$

The additional kinematic term and the potential in the Lagrangian are given by

$$\mathcal{L}_{Higgs} = (D_\mu \Phi)^\dagger (D^\mu \Phi) - V(\Phi) \tag{2.18}$$

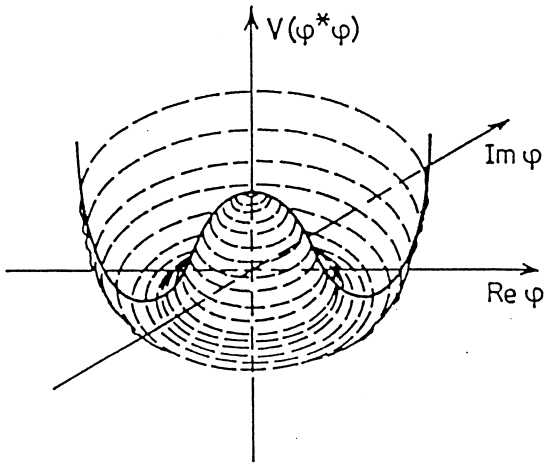

Figure 2.1.: The Higgs potential V for the case of a single complex scalar field ϕ.

where $V(\Phi)$, the Higgs potential, is given by

$$V(\Phi) = \mu^2 \Phi^\dagger \Phi + \lambda (\Phi^\dagger \Phi)^2$$

For $\mu^2 < 0$ and $\lambda > 0$, the Higgs potential has a nontrivial continuous minimum and a typical shape similar to a Mexican hat which is shown in Figure 2.1. The vacuum state corresponds to a certain choice within the minimum and the U(1) symmetry of the Higgs potential is not preserved for the chosen minimum. This is referred to as spontaneous symmetry breaking. The vacuum expectation value of the Higgs field is chosen to be:

$$\Phi(x) = \begin{pmatrix} 0 \\ v \end{pmatrix}$$

where v is defined by

$$\Phi^\dagger \Phi = \frac{1}{2}(\Phi_1^2 + \Phi_2^2 + \Phi_3^2 + \Phi_4^2) \equiv v^2. \tag{2.19}$$

The Φ^+ component of the Higgs field is zero to ensure the conservation of the electromagnetic charge.

The Higgs particle is interpreted as a space-time-dependent radial fluctuation $h(x)$ of the field Φ near the vacuum configuration:

$$\Phi = \frac{1}{\sqrt{2}} \begin{pmatrix} 0 \\ v + h(x) \end{pmatrix}. \tag{2.20}$$

The Lagrangian, expressed in terms of the vacuum expectation value v and the physical state h, effectively describes a scalar particle with a mass $m_h = \sqrt{2\lambda} v$:

$$\mathcal{L} = \frac{1}{2}\partial_\mu \partial^\mu h - \lambda v^2 h^2 - \lambda v h^3 - \frac{\lambda}{4} h^4. \tag{2.21}$$

The scalar particle described by the Lagrangian is referred to as the Standard Model Higgs boson. It is the only remaining neutral physical state after electroweak symmetry breaking, representing one of the four components introduced in Equation 2.19. The other three components manifest themselves as the longitudinally polarized components of the weak vector bosons. For the masses of the weak vector bosons follows:

$$\cos\theta_W = \frac{M_W}{M_Z}. \tag{2.22}$$

The Higgs boson is neutral and couples to fermions proportional to their masses and to massive gauge bosons. It is the only particle in the Standard Model that has not yet been discovered. A lower limit on the Standard Model Higgs boson mass has been set by the LEP experiments. Direct searches in electron- positron collisions up to a center-of-mass energy of $\sqrt{s} < 209$ GeV have excluded a Higgs boson mass of m_H =114.4 GeV and lower at 95% confidence level (CL) [7]. As illustrated in Figure 2.2, a combined fit of electroweak precision data from various measurements LEP, SLD and at DØ and CDF results in a preferred value for the Higgs boson mass at 84^{+36}_{-26} GeV, assuming the Standard Model to be the correct theory of Nature. Since the LEP experiments exclude the region $M_H < 114$ GeV, a light Higgs boson above the LEP limits is expected.

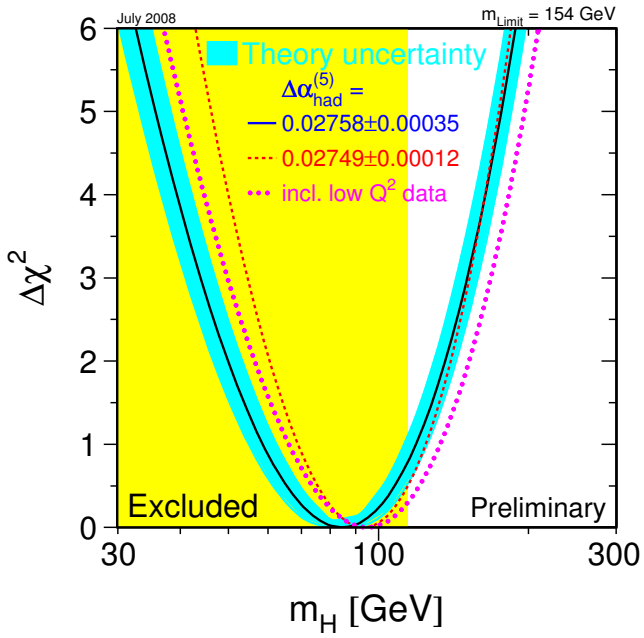

Figure 2.2.: $\Delta\chi^2$ curve derived from high-Q^2 precision electroweak measurements, performed at LEP and by SLD, CDF and DØ, as a function of the Higgs-boson mass, assuming the Standard Model to be the correct theory of nature. The preferred value for the Higgs mass, corresponding to the minimum of the curve, is at 84 GeV, with an experimental uncertainty of +34 and -26 GeV at 68% CL [7].

The Higgs boson couples to the heavies quark, the top quark, and the W boson. The mass of the W is sensitive to the mass of the top quark and the Higgs boson through higher order loop

corrections. The W mass corrections have a logarithmic depencence on the Higgs mass and a quadratic dependence on the top quark mass. This dependence can be used to set experimental constraints on the Higgs boson mass as shown in Figure 2.3. The Higgs boson mass is constant along the diagonal lines. The center of the solid ellipse indicates the direct measurements of m_{top} and m_w, and the ellipse marks the 68% confidence level. The solid curve shows the results of indirect measurements. Further reductions of the uncertainites on the top quark mass and the W boson mass will provide better constraints on the SM and better predictions of the Higgs boson mass.

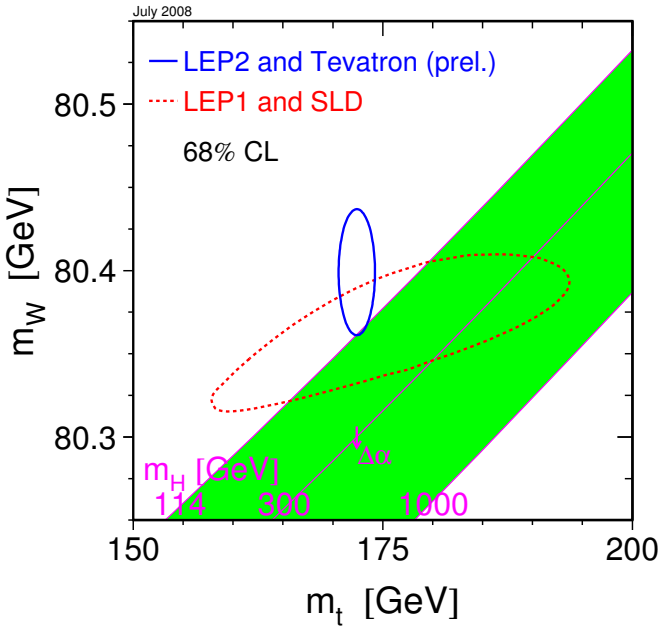

Figure 2.3.: Top quark mass versus W boson mass with lines of constant Higgs boson mass. The dashed ellipse shows the results of indirect measurements and the solid curve direct measurements [7].

2.1.4. Problems of the Standard Model

The Standard Model has been very successful in describing observed data in a large variety of experiments at energy scales up to the order of 100 GeV. Additonally, it has allowed for various predictions which could be confirmed by experiments and all predicted constituents except for the Higgs boson have been observed. Still, the Standard Model is regarded as an effective theory. It builds on many assumptions and leaves fundamental questions unanswered. There is for example no explanation for the existence of three generations of leptons and quarks, the value of the elementary charge or why leptons and quarks are fundamental particles. Below are listed further problems of the Standard Model.

- Gravity Problem

Gravity is the only remaining interaction that is not incorporated in the Standard Model. Due to its weakness at low energy scales, it is neglected in particle physics. However, gravity needs to be included at the latest at energies at the order of the Planck scale ($M_P = 1.2 \times 10^{19}$ GeV), at which quantum effects of gravity become strong. Gravity is described by the General Theory of Relativity which is not a quantum field theory and outside the framework of gauge theories, and adding gravity to the Standard Model destroys renormalizability. In addition, the gravitational force is difficult to derive from the principle of local gauge invariance [8].

- Fine Tuning Problem
  The Standard Model does not offer any explanation why the electroweak scale and the Planck scale differ by seventeen orders of magnitude. This is known as the mass hierarchy problem and is directly linked to the fine tuning problem [9]: Electroweak precision measurements indicate that the value of the Higgs boson mass is of the order of 100 GeV. Assuming that the Standard Model is valid up to a large energy scale, Λ, the squared Higgs boson mass receives quadratically divergent radiative corrections at the order of Λ^2. To solve the hierarchy problem, a fine tuning of the bare Higgs mass of the order of 10^{-34} is necessary, assuming $\Lambda^2 \sim m_p^2$, where m_p is the Planck mass. The corrections to the Higgs mass are shown in Figure 2.4.

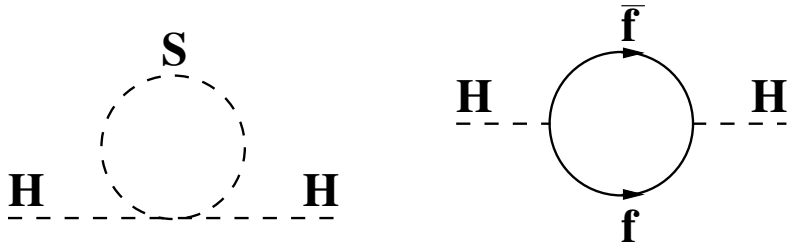

Figure 2.4.: Radiative corrections to the Higgs mass due to boson (left) and fermion (right) loops.

- Unification of Coupling Constants
  The three different coupling constants associated with the three different gauge groups are arbitrary in the SM. A more fundamental and predictive theory can be obtained by embedding the SM into a higher symmetry group, which is broken at low energy scales into the known SM symmetry groups. One of the implications of such a Grand Unified Theory (GUT) is the unification of the electroweak and strong couplings at the GUT scale. Extrapolating the current measurements of the couplings strengths towards higher energies hints at a unification of the coupling constants but the three do not meet in a single point.

- Cold Dark Matter (CDM)
  The Standard Model does not provide a candidate particle for cold dark matter. Only $\approx 4\%$ of the matter in the universe consists of baryonic matter, which belongs to the particle content of the SM, while $\approx 21\%$ is considered as CDM and is not part of the SM. The remaining fraction is mainly assigned to dark energy, corresponding to a cosmological constant, and can not be explained by the SM [10].

2.2. Supersymmetry

There are various extensions of the Standard Model. Supersymmetry (SUSY) [11] is one of the most popular models, providing possible solutions to problems such as the hierarchy problem, the unification of the coupling constants and the origin of cold dark matter (CDM). Figure 2.5 shows the scale dependence of the couplings in the Standard Model and in an MSSM scenario (discussed below). Supersymmetry is also necessary in String Theory [12].

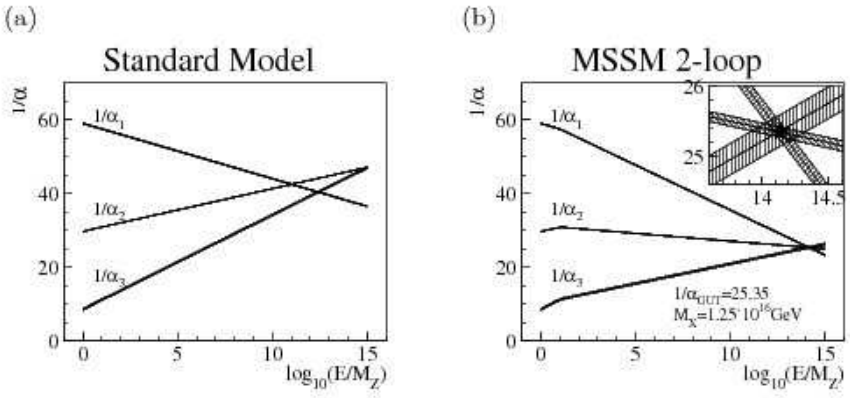

Figure 2.5.: Scale dependence of the couplings in (a) the SM and (b) in a SUSY scenario.

Supersymmetry postulates a symmetry between fermions and bosons. The operator Q changes the spin of a particle by half a unit: $Q\,|S\rangle \sim \left|S \pm \frac{1}{2}\right\rangle$, or

$$Q\,|Fermion\rangle \;\sim\; |Boson\rangle \tag{2.23}$$

$$Q\,|Boson\rangle \;\sim\; |Fermion\rangle\,. \tag{2.24}$$

Since Q only changes the spin, the mass of the supersymmetric particles should be equal to the mass of their standard model partner. Since no supersymmetric partners of the Standard Model particles have been observed yet, supersymmetry cannot be an exact symmetry and has to be broken. In turns, this means that the supersymmetric Lagrangian must contain terms that break the symmetry. It is not possible that the already known particles can be super-partners of each other, so supersymmetry requires a new partner for each Standard Model field.

The operator Q has to be an anti-commuting spinor operator because it carries half a unit of spin. In the framework of a relativistic field theory, the form of such an operator is restricted [11]. The commutation and anti commutation relations for Q are

$$\{Q_\alpha, Q_\beta\} = \{\bar{Q}\alpha, \bar{Q}\beta\} = 0 \tag{2.25}$$

$$\{Q_\alpha, P_\mu\} = \{\bar{Q}\alpha, P_\mu\} = 0 \tag{2.26}$$

$$\{Q_\alpha, \bar{Q}\beta\} = 2(\sigma^\mu_{\alpha\dot{\beta}})P_\mu. \tag{2.27}$$

The spinor indices α, β of Q ($\dot{\alpha}, \dot{\beta}$ of $\bar{Q}$) can have the values 1 and 2. P_μ is the translation operator and σ is defined by σ^μ=($\mathbf{1}, \sigma^i$), where σ^i denotes the Pauli matrices.

In the Standard Model, only one Higgs doublet is required, while in supersymmetry at least two Higgs doublets are required to give mass to both up and down quarks and to cancel gauge anomalies connected to the hypercharge Y.

2.2.1. R-Parity

R–parity is a multiplicative quantum number introduced in supersymmetry in order to forbid lepton and baryon number violating terms in the supersymmetric lagrangian. R-parity is defined as

$$R = (-1)^{3(B-L)+2S}, \tag{2.28}$$

where B is the baryon number, L is the lepton number and S is the spin of the particle. As a consequence, all SM particles have R– parity +1 while all SUSY particles have R–parity equal to -1. Conservation of R–parity implies that supersymmetric particles are produced in pairs. Another consequence is that there must a stable lightest supersymmetric particle (LSP). The LSP must carry zero electromagnetic and strong charge because of cosmological bounds on stable light charged or colored particles. It is only weakly interacting and therefore difficult to detect. This makes the LSP a very appealing candidate for Cold Dark Matter. R–parity violation is not ruled out experimentally, and searches are performed both assuming conservation of R–parity (RPC) and violation of R–parity (RPV). In the analyses presented in this thesis, R–parity conservation is assumed.

2.2.2. Minimal Supersymmetric Standard Model (MSSM)

The minimal supersymmetric Standard Model (MSSM) has the smallest possible field content necessary to give rise to all fields of the Standard Model with SUSY partners [13]. An overview of the SM fields and their SUSY partners is given in Table 2.3. The supersymmetric partners of quarks, leptons and neutrinos are called squarks, sleptons and sneutrinos. The index L or R denote that the corresponding Standard Model particle is either left-handed or right-handed. Since SUSY particles have spin 0, handedness does not apply to them. The Higgs bosons gain fermionic partners, called higgsinos, and also the gauge fields get fermionic partners. The supersymmetric partners of the gluons, $W^\pm$, Z and the γ are called gluinos, winos, zinos and photino. The common name for partners of the gauge fields is gauginos. Neutral higgsinos and gauginos mix to neutralino mass eigenstates and charged gauginos and higgsinos mix to chargino mass eigenstates because they have the same quantum numbers. The charginos are denoted $\tilde{\chi}_i^\pm$ (i=1,2) and the neutralinos $\tilde{\chi}_i^0$ (i =1,2,3,4). They are ordered by increasing mass.

2.2.3. MSSM Lagrangian

In supersymmetry, superfields are the generators of the supersymmetric multiplets. A superfield is a function of superspace. Superspace is an extension of ordinary space-time by the inclusion of additional fermionic coordinates. There are two different types of superfields in the MSSM:

- Chiral superfields $\mathbf{\Psi} = (\tilde{\psi}, \psi)$: chiral (or scalar) superfields represent the matter fields. They contain the fermions and Higgs bosons with their respective supersymmetric partners. A chiral superfield consists of a spin 0 field ψ and the corresponding spin half field $\tilde{\psi}$.
- Vector superfields $\hat{V} = (V, \tilde{V})$: vector superfields represent the vector gauge fields and their supersymmetric partners. A vector superfield contains the spin 1 gauge field V and the corresponding spin half gaugino field $\tilde{V}$.

The Lagrangian of the MSSM can be divided into three parts:

$$\mathcal{L}_{MSSM} = \mathcal{L}_{kin-gauge} + \mathcal{L}_{W} + \mathcal{L}_{soft}. \tag{2.29}$$

$\mathcal{L}_{kin-gauge}$ is constructed analogously to the Standard Model Lagrangian. It includes kinetic terms for scalar and fermion fields, gauge interactions and the self interaction of the gauge fields. $\mathcal{L}_{W}$ contains all additional terms that leave the Lagrangian invariant under gauge and supersymmetric transformations. It also contains the self interaction of the chiral superfields. $\mathcal{L}_{W}$ contains the superpotential W. The superpotential is a gauge- invariant function of the chiral superfields and can be split up in an R-parity conserving (RPC) and an R-parity violating (RPV) term:

$$W = W_{RPC} + W_{RPV} \tag{2.30}$$

The second term of this equation is set to zero assuming R-parity conservation. Since supersymmetry is a broken symmetry, the MSSM is only regarded as an effective low-energy theory. The

Table 2.3.: Overview of the SUSY particles in the MSSM.

R-parity: +1			R-parity: -1			
Spin	Name	Symbol	Spin	Name	Symbol	
$\frac{1}{2}$	quark	q	0	squark	$\tilde{q}_R$, $\tilde{q}_L$	
$\frac{1}{2}$	lepton	l	0	slepton	$\tilde{l}_R$, $\tilde{l}_L$	
$\frac{1}{2}$	neutrino	ν	0	sneutrino	$\tilde{\nu}$	
1	gluon	g	$\frac{1}{2}$	gluino	$\tilde{g}$	
1	photon	γ	$\frac{1}{2}$	photino	$\tilde{\gamma}$	
1	W, Z boson	$W^{\pm}$, Z	$\frac{1}{2}$	wino, zino	$\tilde{W}^{\pm}$, $\tilde{Z}$	$4 \times \tilde{\chi}^0$ and $2 \times \tilde{\chi}^{\pm}$
0	Higgs	$H^{\pm}$, H^0 h, A	$\frac{1}{2}$	Higgsino	$\tilde{H}_1^0$, $\tilde{H}_2^+$ $\tilde{H}_1^-$, $\tilde{H}_2^0$	

breaking of supersymmetry occurs at a high energy scale and is parametrized by soft-symmetry breaking mass terms. They are called soft mass terms because they are sufficiently small to not reintroduce the problem of quadratic divergencies. They are parametrized in the Lagrangian by terms in $\mathcal{L}_{soft}$:

$$\begin{aligned}\mathcal{L}_{soft} = & - \frac{1}{2}\sum_v M_v \tilde{V}_v \tilde{V}_v + \text{h.c.} \\ & - \sum_c \mathbf{m}_c^2 |\tilde{\psi}_c|^2 + \text{h.c.} \\ & - m_{12}^2 \left(\epsilon_{kl} H_1^k H_2^l + \text{h.c.}\right) \\ & - \epsilon_{kl}\left(\mathbf{a}_d H_1^k \tilde{q}_L^l \tilde{d}_R^* + \mathbf{a}_u H_2^k \tilde{q}_L^l \tilde{u}_R^* + \mathbf{a}_e H_1^k \tilde{l}_L^l \tilde{e}_R^*\right) + \text{h.c.}). \end{aligned} \tag{2.31}$$

SUSY-breaking terms are additional Majorana masses for gauginos (M_v), additional scalar masses ($\mathbf{m_c}$) and additional bi- and trilinear couplings of the scalars. The indices v and c correspond to the different vector and chiral superfields, respectively. The indices denote i, j the entries in the weak isospin doublet, and $\epsilon_{ij} = -\epsilon_{ji}$ and $\epsilon_{12} = 1$. $\tilde{q}_L$ and $\tilde{l}_L$ are the weak squark and slepton doublets, $\mathbf{a}_x$ are complex 3×3 matrices which parametrize the couplings between three scalars.

In its most general form, $\mathcal{L}_{soft}$ introduces more than 100 free parameters, but the number can be reduced making certain assumptions that will be discussed in the following.

2.2.4. Phenomenological Constraints

As described in the previous section, the introduction of SUSY breaking terms in the Lagrangian leads to a theory that contains more than 100 additional free parameters. The reduction of this number rests on a set of assumptions which are motivated by experimental evidence: supersymmetry should predict the measured amount of CP violation and the results concerning the Kaon mixing as well as the limits of flavor-changing neutral currents (FCNC) and on the electric dipole moments of the neutron and the electron. This is most easily achieved if the soft supersymmetry breaking parameters are real, the mass matrices are diagonal and the trilinear couplings are proportional to the Yukawa couplings.

2.3. Constrained MSSM

Despite its appealing characteristics, a feature of MSSM is the large number of unknown parameters. Simplifications are made by regarding the MSSM as a low-energy effective theory of a more fundamental theory at a large energy scale. This leads to simplifications of the soft supersymmetry breaking terms and the resulting model is called constrained MSSM (cMSSM). The number of free parameters is reduced from 124 to 23 (including the 18 Standard Model parameters). The cMSSM is based on the following assumptions at GUT scale:

- Gaugino mass unification: $M_i = m_{1/2},\ i = 1, 2, 3$

- Scalar mass unification: $\tilde{M}^2_{Q,u,d,L,e} = m_0^2$
- Common tri-linear coupling: $A_f = A_0,\ f = u, d, e$
- Ratio of the vacuum expectation values of the Higgs fields: $\tan\beta$
- Higgs mass parameter: μ.

2.4. Supersymmetry Breaking

The MSSM does not give an answer to the question of the origin of the supersymmetry breaking. The two most popular theories are gravity-mediated and gauge-mediated supersymmetry breaking. Common for all SUSY breaking theories is that SUSY is broken in a "hidden sector", which is distinct from the "visible sector" of the MSSM fields. SUSY breaking is transmitted from the hidden to the visible sector through messenger fields.

In gravity-mediated SUSY breaking models (SUGRA models) [14] it is assumed that the spontaneous local supersymmetry breaking takes place in a hidden sector at energy scale $\sqrt{F}$ giving rise to a gravitino of mass $m_{3/2} = \frac{F}{\sqrt{3}M_P}$. Gravitational interactions are responsible for transmitting the breaking to the visible sector because gravity couples to all massive fields in the hidden and in the visible sector. The resulting low energy theory consists of the unbroken MSSM together with all possible soft supersymmetry breaking terms. If the couplings of all gauginos and scalars to the hidden sector superfield are assumed to be equal at M_{GUT}, the model reduces to a minimal Supergravity (mSUGRA) model. In this model, the SUSY degrees of freedom are reduced to five parameters, commonly chosen as:

$$m_0,\ m_{1/2},\ A_0,\ \tan\beta \text{ and } sign(\mu). \tag{2.32}$$

The masses of all supersymmetric particles at the electroweak scale can be calculated from these parameters by using the renormalization group equations, RGE. Over most of the model space, the following relation holds:

$$2\ m_{\tilde{\chi}_1^0} \approx m_{\tilde{\chi}_2^0} \approx m_{\tilde{\chi}_1^\pm}. \tag{2.33}$$

Figure 2.6 [15] shows an example of the running of the masses with the energy Q from the GUT scale to the electroweak scale.

Another framework for supersymmetry breaking is gauge- mediated breaking, (GMSB) [16]. GMSB will not be discussed here, but it is mentioned that in this framework the LSP is the gravitino, with a mass in the eV–keV range.

The work presented in this thesis is performed within the framework of mSUGRA.

2.5. SUSY Mass Spectrum

As a consequence of supersymmetry breaking, sparticles acquire their masses in form of a combination from their coupling to the two Higgs fields and from direct mass terms. The particle fields

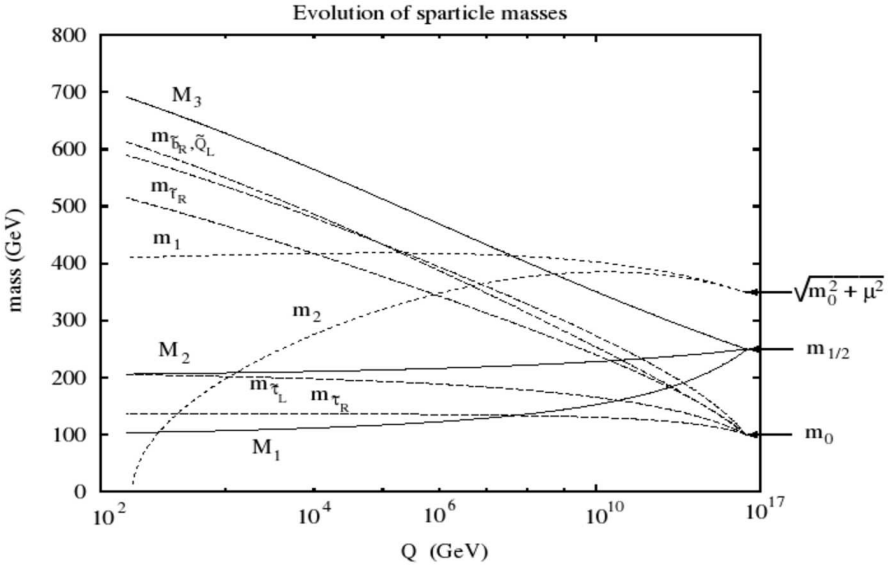

Figure 2.6.: An example of the running of the soft-supersymmetry breaking parameters with Q [15].

of the SUSY Lagrangian are gauge eigenstates and not mass eigenstates. The mass eigenstates are obtained by diagonalizing the mass– squared matrix. The sfermion mass matrices for the first generation are:

$$M^2_{\tilde{u},LR} = \begin{pmatrix} m_Q^2 + m_u^2 + (\frac{1}{2} - \frac{2}{3}s_W^2)Z_\beta^2 & m_u(A_u - \mu\cot\beta) \\ m_u(A_u - \mu\cot\beta) & m_U^2 + m_u^2 + \frac{2}{3}s_W^2 Z_\beta^2 \end{pmatrix}, \tag{2.34}$$

$$M^2_{\tilde{d},LR} = \begin{pmatrix} m_Q^2 + m_d^2 + (-\frac{1}{2} - \frac{1}{3}s_W^2)Z_\beta^2 & m_d(A_d - \mu\tan\beta) \\ m_d(A_d - \mu\tan\beta) & m_D^2 + m_d^2 - \frac{1}{3}s_W^2 Z_\beta^2 \end{pmatrix}, \tag{2.35}$$

$$M^2_{\tilde{e},LR} = \begin{pmatrix} m_L^2 + m_e^2 - (\frac{1}{2} - s_W^2)Z_\beta^2 & m_e(A_e - \mu\tan\beta) \\ m_e(A_e - \mu\tan\beta) & m_E^2 + m_e^2 - s_W^2 Z_\beta^2 \end{pmatrix}, \tag{2.36}$$

$$M^2_{\tilde{\nu}} = m_L^2 + \frac{1}{2}s_W^2 Z_\beta^2. \tag{2.37}$$

The abbreviations $s_W^2 \equiv \sin^2\theta_W$ and $Z_\beta^2 \equiv M_Z^2\cos 2\beta$ are used. The parameters m_L, m_E etc. are the explicit mass terms in the soft SUSY breaking Lagrangian $\mathcal{L}_{soft}$. The remaining terms are a consequence of the coupling to a Higgs field in $\mathcal{L}_{SUSY}$ or $\mathcal{L}_{soft}$. The off-diagonal elements of the matrices are proportional to the mass of the corresponding SM partner, and introduce a mixing between the two sfermion chirality states. For the first two generations, this effect can be ignored due to the small mass of the SM partner, however, for the third generation, the mixing can have a significant impact on the resulting mass terms.

The neutralino eigenstates, important for this thesis, are a mix of the neutral $\tilde{B}$ and $\tilde{W^3}$ gauginos. In the basis $(\tilde{B}, \tilde{W}^3, \tilde{H}_1^0, \tilde{H}_2^0)$, the mass matrix is given by:

$$M_{\chi^0} = \begin{pmatrix} M_1 & 0 & -c_\beta s_w M_Z & s_\beta s_w M_z \\ 0 & M_2 & c_\beta c_w M_Z & s_\beta c_w M_Z \\ -c_\beta s_w M_Z & +c_\beta c_w M_Z & 0 & -\mu \\ s_\beta s_w M_Z & -s_\beta c_W M_Z & -\mu & 0 \end{pmatrix}$$

The charged higgsinos and the charged gauginos mix to chargino mass eigenstates. The chargino mass matrix is in the basis ($\tilde{W}^+$, $\tilde{H}_2^+$, $\tilde{W}^-$, $\tilde{H}_1^-$) is given by:

$$M_{\tilde{\chi}^\pm} = \begin{pmatrix} 0 & X^T \\ X & 0 \end{pmatrix} \qquad \text{with } X = \begin{pmatrix} M_2 & \sqrt{2} s_\beta M_W \\ \sqrt{2} c_\beta M_W & \mu \end{pmatrix}. \tag{2.38}$$

The chargino masses follow by diagonalizing:

$$\begin{aligned} m^2_{\tilde{\chi}^\pm_{1,2}} &= \frac{1}{2}\Big[\, |M_2|^2 + |\mu|^2 + 2\, M_W^2 \\ &\mp \sqrt{(\, |M_2|^2 + |\mu|^2 + 2\, M_W^2\,)^2 - 4\,|\,\mu M_2 - M_W^2 \sin 2\beta|^2}\,\Big]. \end{aligned} \tag{2.39}$$

2.6. The Higgs Sector in the MSSM

The Higgs sector in the MSSM requires two Higgs doublets. This is necessary to generate the masses of the up- and down-type fermions within the MSSM and to avoid gauge anomalies. The first Higgs doublet carries hypercharge +1 and couples to up-type fermions, while the second Higgs doublet carries hypercharge -1 and couples to down-type fermions. Before symmetry breaking, the two complex Higgs doublets have 8 degrees of freedom. Three of these are absorbed to give mass to the W and Z bosons as in the SM, leaving 5 physical degrees of freedom. These are:

- two charged Higgs bosons: $H^\pm$,
- one CP-odd, neutral Higgs boson: A,
- two CP-even, neutral Higgs bosons: h, H (h is the lighter of the two).

Most of the experimental results are interpreted assuming CP conservation in the Higgs sector. In such scenarios the three neutral Higgs bosons are CP eigenstates. However, CP violation in the Higgs sector cannot be excluded a priori.

3. Production and Decay of SUSY Particles and Standard Model Background

The associated production of the lightest chargino $\tilde{\chi}_1^{\pm}$ and the next to lightest neutralino $\tilde{\chi}_2^0$ with subsequent decays into three charged leptons, neutrinos and LSPs, is one of the most promising channels in the search for supersymmetry at the Tevatron. The following chapter describes the production and decay channels of this process assuming R-parity conservation. Even though the Standard Model background is low, various Standard Model processes can give rise to a similar final state. The backgrounds can be divided into two categories: processes with three leptons and $\not\!\!E_T$ and events where leptons and/or $\not\!\!E_T$ is caused by mismeasurements. Both categories are discussed at the end of this chapter.

3.1. Production and Decay of SUSY Particles

At hadron colliders, SUSY particles can be produced by either strong or electroweak interactions. Colored particles (squarks, gluinos) are mainly produced in strong interactions, while electroweak interactions result in charginos, neutralinos and sleptons. The cross sections for the production of supersymmetric particles are comparable to the cross sections for the production of the respective Standard Model partners at same Q^2 since the couplings of SUSY particles are equal to the couplings of their Standard Model partners. Assuming R-parity conservation, supersymmetric particles are produced in pairs and the lightest supersymmetric particle is stable.

3.1.1. Production of Charginos and Neutralinos

Charginos and neutralinos are created when a quark and an antiquark interact weakly. The main production process is quark antiquark annihiliation with a W boson exchange in the s channel. The squark exchange in the t channel is expected to be suppressed because squark masses are typically heavy in GUT-constrained SUSY-models. In addition, the Tevatron experiments have excluded squark and gluino masses below 300-400 GeV [17, 18]. The relative contribution of the s- and t-channel amplitudes depend on the field content of the chargino and neutralino and on the squark masses. The gauge boson in the s-channel couples to the gaugino and higgsino components of the charginos and neutralinos. The squarks in the t-channel couple mainly to the gaugino components. Figure 3.1 shows the leading order diagrams for the production of chargino and neutralino pairs in quark-antiquark collisions.

At the Tevatron, the processes of interest are the pair production of the lightest chargino $(\tilde{\chi}_1^+, \tilde{\chi}_1^-)$, the associated production of chargino/neutralino $(\tilde{\chi}_1^{\pm}, \tilde{\chi}_2^0)$ and the pair production of the next-to-lightest neutralino, $(\tilde{\chi}_2^0, \tilde{\chi}_2^0)$. All other combinations are either very rare or impos-

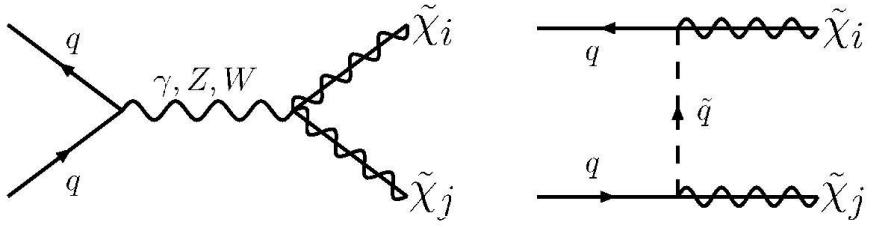

Figure 3.1.: Leading order diagrams for the production of chargino/neutralino pairs in quark-antiquark reactions.

sible to separate from the background. The NLO cross sections are shown in Figure 3.2 (left) as a function of the gaugino mass for these processes. The NLO production cross sections range from 0.1 to 1 pb. In the mass range beyond the lower bounds of LEP II, between 100 GeV and 150 GeV, the K–factor for chargino/neutralino production is in the range $1.23 < K_{NLO} < 1.26$. The K–factors as a function of chargino/neutralino mass are presented in Figure 3.2 (right) [19]. Of the processes discussed above, the $(\tilde{\chi}_2^0, \tilde{\chi}_2^0)$ production has the lowest cross section, and it is difficult to separate $(\tilde{\chi}_1^+, \tilde{\chi}_1^-)$ production from the background. The associated production of chargino and neutralino, $(\tilde{\chi}_1^\pm, \tilde{\chi}_2^0)$, has a reasonable high cross section and the tri-lepton final state is favourable, which will be discussed in the next sections.

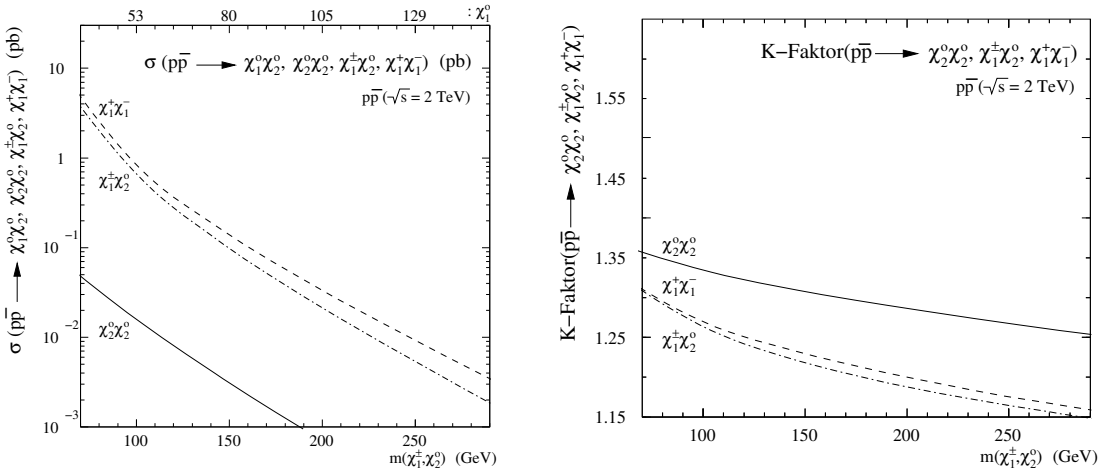

Figure 3.2.: NLO Cross section (left) and K–factors (right) for the associated production of charginos and neutralinos in $p\bar{p}$ collisions. The choice of parameters here are $m_0 = 100$ GeV, $A_0 = 300$ GeV, $\mu > 0$, tanβ=4 [19].

3.1.2. Decay of SUSY Particles

In R-parity conserving SUSY models, charginos and neutralinos decay directly or via cascades into the LSP and Standard Model particles. The decays are mediated by gauge bosons or sfermions. This will be discussed in detail in the following. The chargino can decay via a virtual W boson into two fermions and a lighter neutralino. If the mass difference between the chargino

and the neutralino is large enough, 2-body decay into a real W and a neutralino is dominant. If the sfermions are light enough, 3-body decays of the chargino mediated by a sfermion become important. The chargino then decays into a sfermion and the Standard Model weak isospin partner. Since the sfermion decays further into its fermion partner and a lighter neutralino, the final state is the same as expected from W boson mediated decays. If the sfermion mass is low enough, 2 body decays of the chargino into a real sfermion and a fermion become important. For the next to lightest neutralino, the 3-body decay via a virtual Z boson into a fermion pair and the lighter neutralino dominates in large regions of parameter space. 2-body decays into a lighter neutralino and a real Z are possible if the mass difference between the neutralinos is large enough. If the Z boson decays into charged leptons, the final state consists of the light neutralino and a charged lepton pair. If the sfermions are light enough, 3-body decays of the next to lightest neutralino is important and for sufficiently light sfermions, the 2-body decays of the neutralino is possible.

The production and decay modes for associated chargino and neutralino production are shown in Figure 3.3.

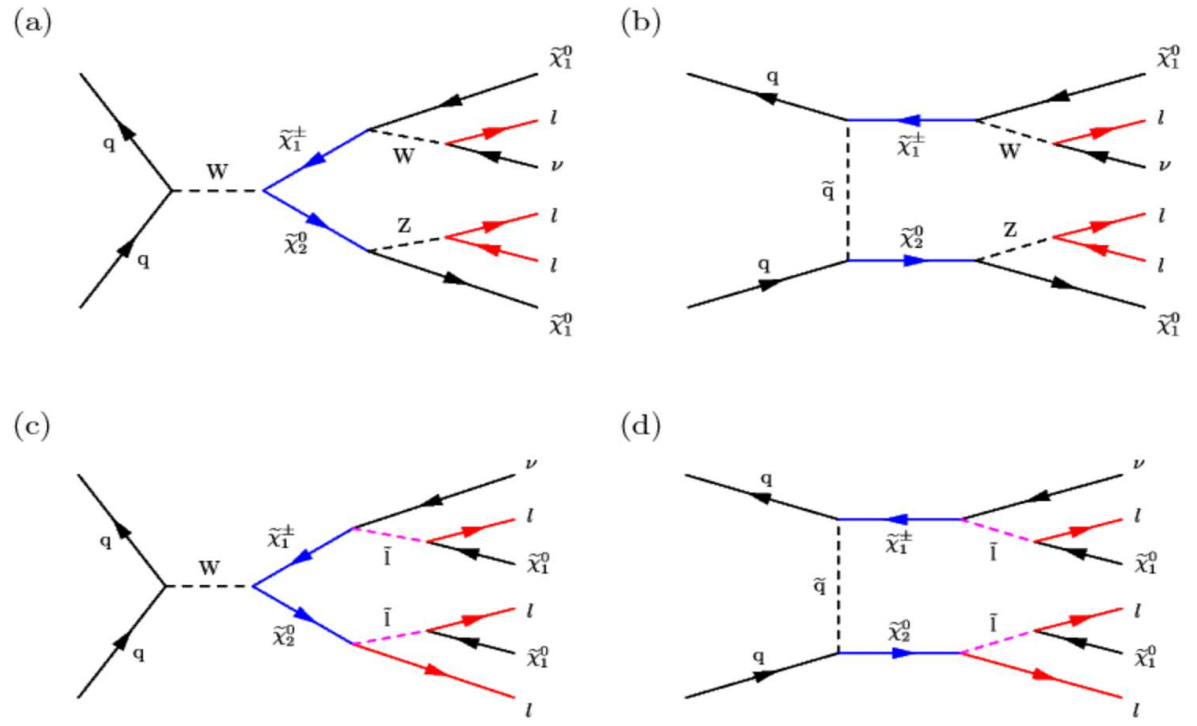

Figure 3.3.: Production and decay modes for associated chargino/neutralino production in trilepton final states. Figure (a) and (c) are s-channel, (b) and (d) are t-channel.

The branching ratios into the different fermions are determined by the field content of the gauginos, the sfermion masses and the sfermion chirality. If neutralino and chargino have a high wino field content, a coupling to the left handed fermions and their supersymmetry partners is favored. If neutralino and chargino have a high higgsino field content, decays into massive particles are preferred, and if the neutralinos and charginos have a high photino field content, they prefer a coupling to charged sfermions and fermions. The decay mediated by real sfermions

and gauge bosons are preferred if kinematically allowed.

Stau Mixing Effects

The leptonic final states are in general not equally composed of the three lepton generations due to a possible difference in the slepton masses. The large Standard Model tau mass can lead to different masses and field contents for the two stau particles in comparison to the other two slepton generations. This results in different branching ratios for final states with taus and final states with electrons or muons.

The off-diagonal elements in the stau mass matrix, which are proportional to the Standard Model tau mass and $A_\tau - \mu \tan\beta$ introduce a mixing between the two stau chirality states. As a result, the lightest stau can become significantly lighter than the lightest selectron or smuon and therefore increase the branching ratio into taus. In addition it acquires a left-handed component which couples to the $SU(2)_L$ gauginos. Assuming that A_τ and μ are of the order of the electroweak scale, the stau mixing is mostly a function of $\tan\beta$. This dependence is shown in Figure 3.4 [20] where the gaugino and slepton masses and $\sigma\times$ BR into three lepton final states is shown. From the dependence on $\tan\beta$ follows that final states with tau leptons dominate for large $\tan\beta$. The scan is performed for low values of m_0, leading to a low sfermion mass and 2-body decays of $\tilde{\chi}_2^0$ into a light slepton and its Standard Model partner.

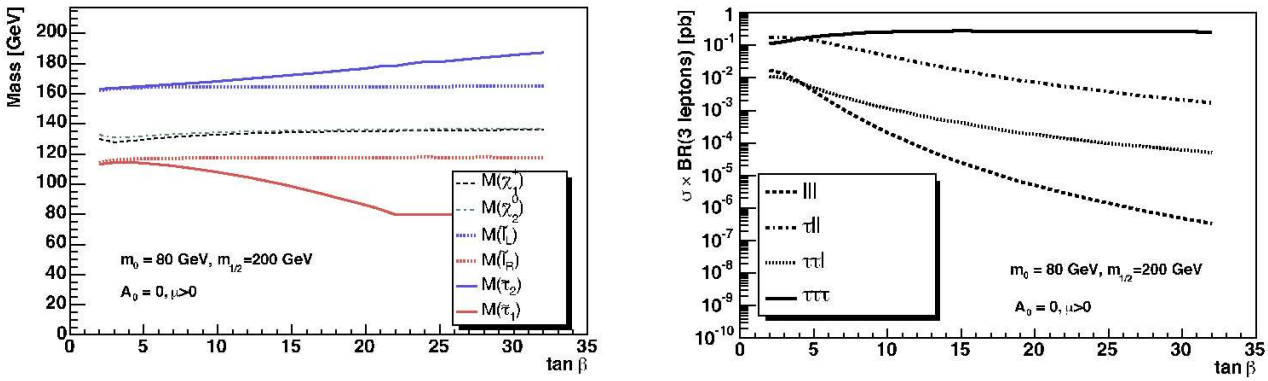

Figure 3.4.: Masses of SUSY particles (left) and cross section times branching fraction (right) for the associated production of the lightest chargino and the second lightest neutralino into various trilepton states as a function of $\tan\beta$ for $\mu > 0$, $m_{1/2} = 200$ GeV, $m_0 = 80$ GeV and $A_0 = 0$ [20].

3.1.3. Signal Topology

The available phase space for the three final state leptons depends strongly on the mass differences of the involved particles. Figure 3.5 (left) [21] indicates the regions of different decay modes of the lightest chargino and second lightest neutralino in the mSUGRA model in the $(m_0, m_{1/2})$ plane.

For larger values of $m_{\tilde{\chi}_1^\pm}$ and $m_{\tilde{\chi}_2^0}$, the decays into real W and Z are dominating. When $m_{\tilde{\chi}_1^\pm} < M_W + m_{\tilde{\chi}_1^0}$ and $m_{\tilde{\chi}_2^0} < M_Z + m_{\tilde{\chi}_1^0}$, the charginos and neutralinos decay via virtaul sleptons and gauge bosons if the sleptons are heavier that the next to lightest neutralino. The line $m_{\tilde{\chi}_2^0} \approx m_{\tilde{\ell}}$ separates the region of 2-body decays of the charginos and neutralinos via sleptons at small m_0 from the 3-body decay region at larger m_0. For the region of parameter space where $m_{\tilde{\nu}} < m_{\tilde{\chi}_2^0}$, the decay into real sneutrinos is possible. The chargino can then decay into a sneutrino and a lepton, and the neutralino can decay into a sneutrino and a neutrino, and no charged leptons are present in the final state. In the 2-body region of the considered mSUGRA scenario, the decay into staus of the lightest chargino is favored because of the high wino field content of the $\tilde{\chi}_1^\pm$ and leads to a helicity suppressed decay into selectrons and smuons.

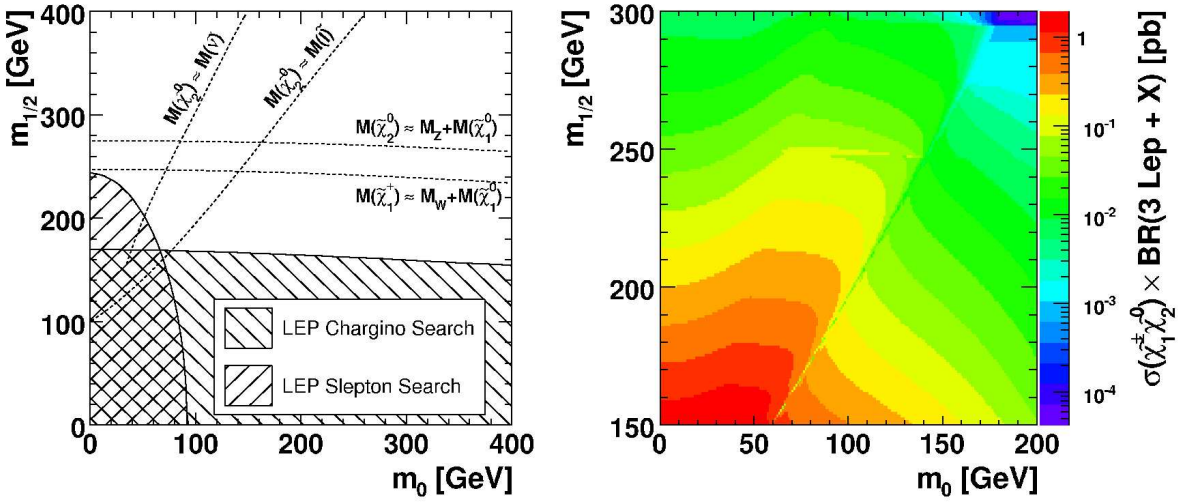

Figure 3.5.: Regions of changing kinematics in the decays of the lightest chargino and the second lightest neutralino in the mSUGRA model for tan β=3, $A_0 = 0$ and $\mu > 0$ (left). and the trilepton cross section times branching fraction into three leptons in the $(m_0, m_{1/2})$-plane for tan β=3, $A_0 = 0$ and $\mu > 0$) (right) [21].

Figure 3.5 (right) shows the trilepton cross section $\sigma \times \mathrm{BR}(3\ell)$in the $(m_0, m_{1/2})$ plane in the region where the sensitivity of the presented trilepton searches is expected. The shape of this region is determined by the decreasing production cross section $\sigma(\tilde{\chi}_1^\pm, \tilde{\chi}_2^0)$ with increasing gaugino masses towards larger $m_{1/2}$, and the changing branching ratio into three leptons. The cross sections and SUSY spectra are determined as explained in 7.2.2. The kinematics of the cascade decays of chargino and neutralino result from the mass differences of the particles involved.

Figure 3.6 (upper left) shows the branching fraction of the lightest chargino into stau as a function of mass difference of slepton (right handed selectron) and next to lightest neutralino in the 2-body region, where the mass difference is negative, $m_{\tilde{\chi}_2^0} > m_{\tilde{\ell}}$. From the plot it can be seen that this decay is dominating until the decay into real sneutrinos open up. The branching fraction of the lightest chargino into sneutrinos is in Figure 3.6 (upper right). Figure 3.6 bottom shows the branching fraction of the lightest chargino into leptons as a function of mass difference between slepton and next to lightest neutralino. The plot includes both decays via virtual sleptons and virtual W bosons. The leptonic branching fraction increases when the mass difference between the slepton and next to lightest neutralino decreases because the slepton gets

lighter.

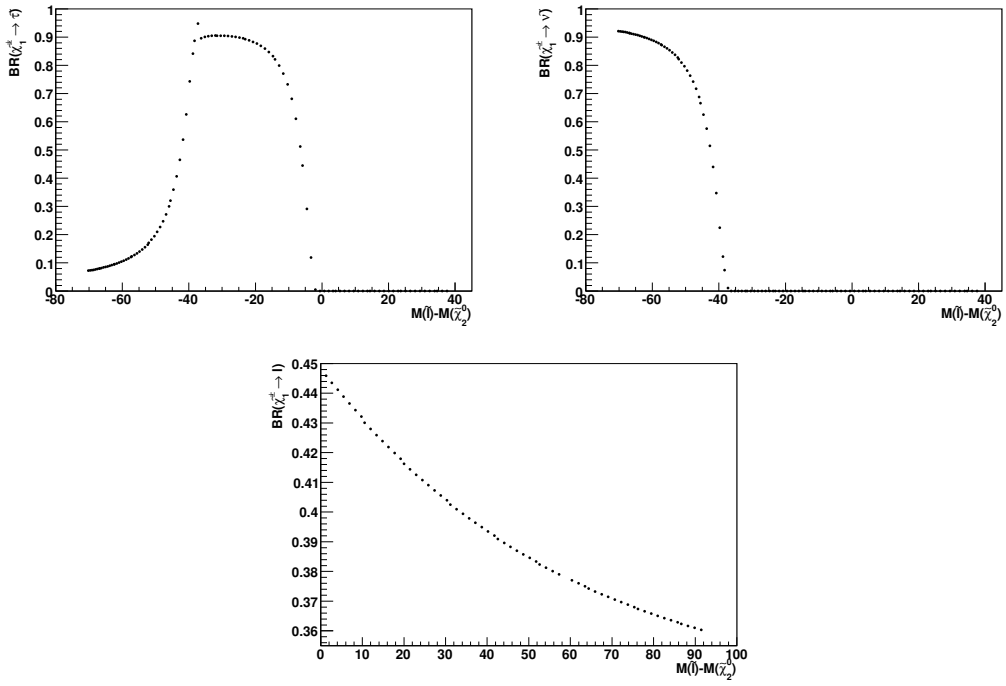

Figure 3.6.: Branching fraction of the lightest chargino into staus in the 2-body region (upper left), branching fraction of the lightest chargino into sneutrinos in the 2-body region (upper right) and branching fraction of the lightest chargino into leptons in the 3-body region (bottom). All plots are shown as a function of mass difference between slepton and next to lightest neutralino.

In the 3-body region, the kinematics is predominantly determined by the mass of the lightest chargino. This is shown in Figure 3.7 where the p_T distribution of the leading, next to leading and third lepton in chargino decays with increasing chargino mass are shown. Table 3.1 lists the chargino mass, the neutralino mass, slepton masses and cross section times branching fraction for these points. In the transition region between 2- and 3-body decay, the available phase space for the lepton from the decay of the neutralino is reduced. The resulting softness of the lepton momentum reduces the reconstruction efficiency and the sensitivity of the trilepton analyses. This behaviour is demonstrated in Figure 3.8, and Table 3.2 lists the particle masses, the mass difference and cross section times branching fraction for these points.

Table 3.1.: Parameters and masses for the SUSY points shown in Figure 3.7. All points have $A_0 = 0$, $\tan\beta$=3 and $\mu > 0$. All masses are given in GeV while the $\sigma \times \mathrm{BR}(3\ell)$ is given in pb.

m_0	$m_{1/2}$	$m_{\tilde{\chi}_1^\pm}$	$m_{\tilde{\chi}_2^0}$	$m_{\tilde{\ell}_\mathrm{R}}$	$m_{\tilde{\tau}1}$	$\sigma \times \mathrm{BR}(3\ell)$
150	150	88.8	93.0	164.8	163.8	0.1898
150	180	115.5	117.7	169.0	168.0	0.0746
150	200	133.4	134.4	172.2	171.2	0.0432
150	250	176.7	176.4	181.2	180.3	0.0114

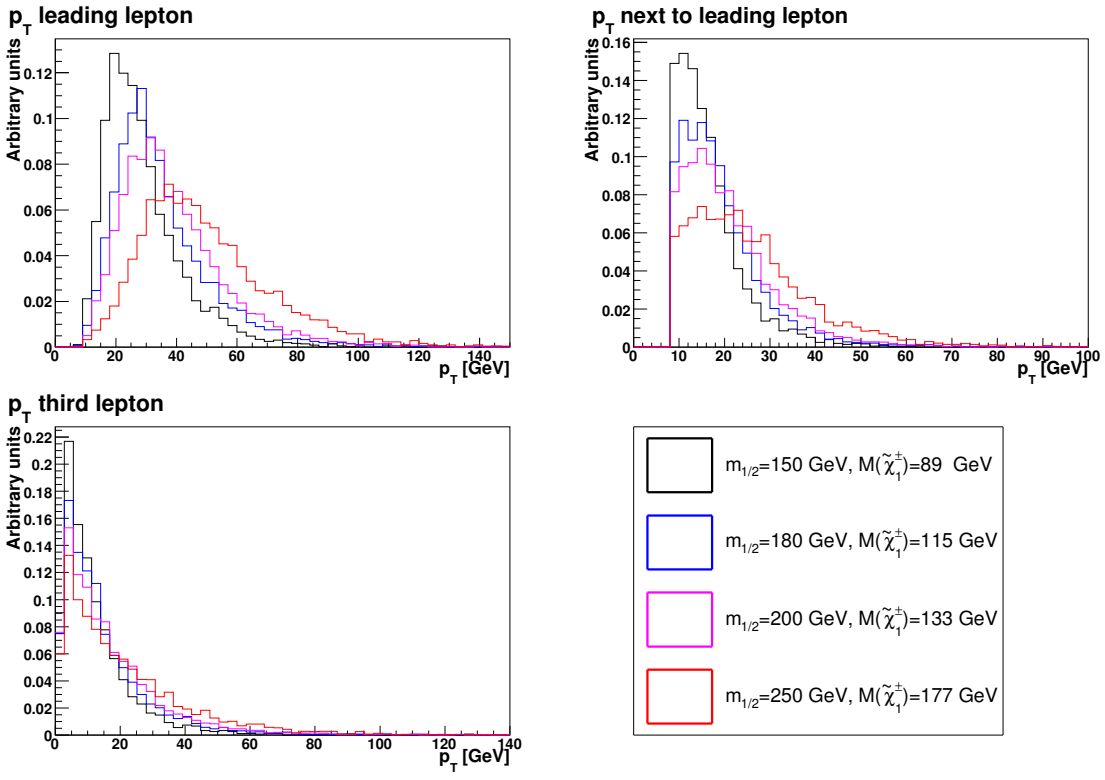

Figure 3.7.: p_T of leading and next to leading lepton (above) and third lepton (below) for leptons in chargino decays with increasing chargino mass. The spectra get harder with increasing chargino mass.

Table 3.2.: Parameters and particle masses for the SUSY points shown in Figure 3.8. All points have $A_0 = 0$, tan β=3 and $\mu > 0$. All masses are given in GeV while the $\sigma \times \mathrm{BR}(3\ell)$ is given in pb. $\Delta m \equiv m_{\tilde{\ell}} - m_{\tilde{\chi}_2^0}$

m_0	$m_{1/2}$	$m_{\tilde{\chi}_1^\pm}$	$m_{\tilde{\chi}_2^0}$	$m_{\tilde{\ell}_\mathrm{R}}$	$m_{\tilde{\tau}1}$	Δm	$\sigma \times \mathrm{BR}(3\ell)$
70	189	121.6	123.7	107.3	105.9	7.8	0.1898
82	179	112.8	115.5	113.1	111.9	-2.4	0.0746
90	172	106.7	109.8	117.6	116.3	-16.4	0.0432

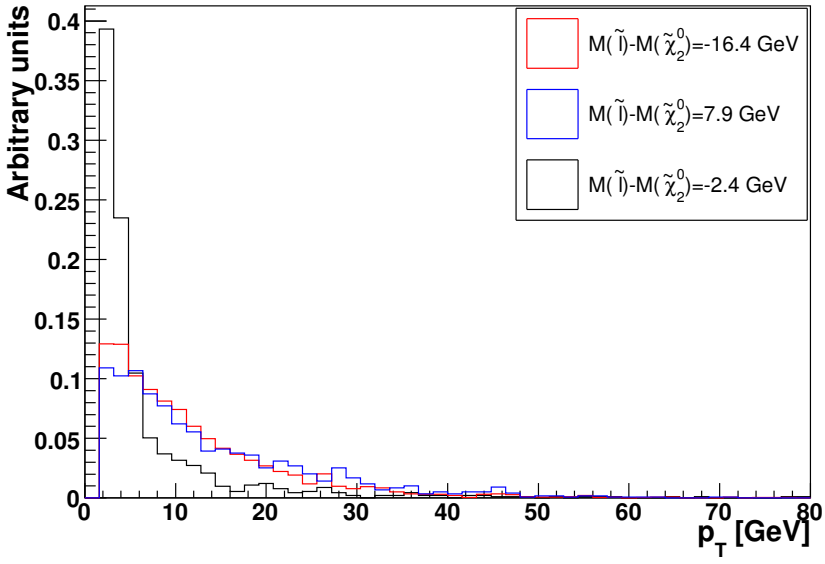

Figure 3.8.: p_T of third track for three different choices of mass difference between $\tilde{\chi}_2^0$ and $\tilde{\ell}$. For the point with small mass difference, the p_T spectrum of the track is clearly softer than for the two others.

3.1.4. Analysis Strategy

Two analyses are presented in this thesis. One searches for the associated production of the lightest chargino and the second lightest neutralino in final states with two electrons, a third lepton and missing transverse energy ($ee\ell$) and the other searches for the associated production in final states with two muons, a third lepton and missing transverse energy ($\mu\mu\ell$). The final state with three charged leptons is appealing because of its low Standard Model background, which makes it the most promising channel for searches for charginos and neutralinos at the Tevatron.

The results of the analysis are combined with results of searches for SUSY in the $e\mu\ell$ final state and the final state with one muon, one hadronically decaying τ and a third lepton ($\mu\tau_h\ell$),

see Section 10.2.2. Analyses with tau leptons in the final states, are important because, as discussed in Section 3.1.2, in parameter regions with large values of tan β, decays into tau leptons dominate.

3.2. Standard Model Background

Most Standard Model processes can be effectively suppressed by requiring three charged leptons and missing transverse energy. The Standard Model process that produces a signature closest to this SUSY signature, is WZ production with subsequent decay into leptons. However, a variety of processes can produce a similar signature if a lepton is faked by for example a jet or the missing transverse energy is mismeasured. An overview of the different background processes is given below. The cross sections multiplied with the branching fraction into three leptons $\sigma \times BR(3\ell)$ are presented in Table 3.3. In this table is also stated whether real leptons are expected for different background processes and if real $\not\!\!E_T$ is expected. Feynman diagrams of different background processes are presented in Figures 3.9, 3.13, 3.15 and 3.17. For all background processes various kinematic distributions are shown. These kinematic variables are p_T of the three charged leptons, invariant mass of the two leading leptons, $\not\!\!E_T$ and $\Delta\phi$ between the two leading leptons. For comparison, these distributions are also shown for two selected chargino masses. The distributions for point $m_0 = 150$, $m_{1/2} = 150$ and $m_0 = 150$, $m_{1/2} = 250$ are shown in Figure 3.20 and in Figure 3.21, respectively. The chargino mass can be found in Table 3.1.

Table 3.3.: Standard Model backgrounds for the SUSY trilepton selections. The cross sections times branching fraction into three charged leptons, are listed in the column $\sigma \times Br(3\ell)$ and are given in units of pb. The column true "$\not\!\!E_T$" indicates if the final state is chararcterized by true $\not\!\!E_T$ or if the missing transverse energy is due to mismeasurements of the momentum balance in the event. The column "remarks" summarizes how the background process fakes the trilepton signature.

Process	$\sigma \times Br(3\ell)[pb]$	leptons	true $\not\!\!E_T$	remarks
$W \to \ell\nu$ (+γ/jet)	2583	1	yes	γ/jets fake 2nd and 3rd lepton
$Z \to \ell\ell$ (+γ/jet)	241.6	2	no	γ/jets fake 3rd lepton, mismeasured $\not\!\!E_T$
WZ	3.68	3	yes	most signal like standard model process
WW	12.0	2	yes	γ/jets fake 3rd lepton
ZZ	1.42	2-4	no/yes	misidentified leptons/mismeasured $\not\!\!E_T$
$t\bar{t}$	7.91	2	yes	jet fakes 3rd lepton
$q\bar{q}$	7×10^{10}	0	no	jet fakes leptons, mismeasured $\not\!\!E_T$

- Di-boson: WZ, WW, ZZ
  The most important irreducible background consists of the associated production of a W and a Z boson with subsequent leptonic decays of both gauge bosons. The resulting final state is identical to the trilepton final state, with the missing transverse energy stemming from the $W \to \ell\nu$ decay. The invariant mass of two opposite-sign leptons of the same flavor is expected to be in the range of the Z mass. The Feynman diagrams are presented in Figure 3.9 (a) and (c). Various kinematic distributions are shown in Figure 3.10.

The production of two W bosons can lead to final states with two leptons of opposite sign and real missing transverse energy. The Feynman diagrams are shown in Figure 3.9 (b) and (d). A jet or a photon from $WW + jet$ or $WW + \gamma$ can be misreconstructed as a third lepton. In this case, the p_T distribution is expected to be softer than in the case for WZ since the isolated track is a fake. This can be seen by comparing the p_T distribution of the third track in Figure 3.10 (top right) and Figure 3.11 (top right).

Another background source is ZZ production shown in 3.9 (e). If both Z bosons decay into charged leptons, the final state consists of at least three leptons that are expected to be isolated. If the energy is mismeasured or a muon is outside the acceptance, the event will be selected. If one of the Z bosons decays into electrons or muons and the other into two neutrinos or two tau leptons, real missing transverse energy comes from the neutrinos in the final state. In this case, the third track comes from a jet or a photon or a tau. For ZZ background, the $\not\!\!E_T$ distribution is harder compared to $Z \to \ell\ell$. The track p_T distribution is softer compared to WZ but harder compared to $Z \to \ell\ell$. The kinematic distributions are shown in Figure 3.12.

- $W \to \ell\nu$:
  Another large background source due to its large cross section is the $W(+\gamma/jet) \to \ell\nu + jet$ process. A jet or a converted photon can be misidentified as the second lepton and the third lepton is also a fake. The $\not\!\!E_T$ in the event is real and caused by the neutrino. In Figure 3.13, the leading order Feynman graphs for $W + (\gamma/jet)$ are shown. In Figure 3.14 the kinematic distributions are presented. Since the next to leading lepton and the third track are fakes, the p_T distributions are exponentially falling.

- $Z/\gamma^* \to \ell\ell$:
  This background creates two opposite sign leptons in the final state. Significant missing transverse energy can arise from mismeasurement of the energies of leptons and jets in the event. The event is selected if an additonal jet or photon is misreconstructed as a third lepton. Figure 3.15 presents leading order graphs for Z/γ^* production, and Figure 3.16 shows various kinematic distributions for $Z/\gamma^* \to ee$ background for the mass range 60–130 GeV.

- $Z/\gamma^* \to \tau\tau$:
  This background creates two opposite sign leptons in the final state and the $\not\!\!E_T$ spectrum is expected to be harder than the $\not\!\!E_T$ for $Z \to \ell\ell$ because of the neutrinos in the event. The event is selected if an additonal jet or photon is misreconstructed as a third lepton.

- QCD jet production:
  The QCD jet production is the background process with the largest cross section. No isolated leptons are produced in this process. Jets can be misidentified as isolated electrons and muons in b-jets can be misreconstructed as isolated. Mismeasurements of the jet energy can lead to artificial missing transverse energy. In Figure 3.19 the most important kinematic variables are presented.

- $t\bar{t}$:
  The production of a $t\bar{t}$ pair with subsequent decay of the W bosons into leptons gives two leptons, two hard b jets and missing transverse energy in the final state. The event is selected if a jet is faking the third lepton. The Feynman graphs are shown in Figure 3.17.

Since the third track is faked by high momentum b-jets, the p_T distribution of the track is expected to be harder than for other background processes where the track is faked by a jet. This is shown in Figure 3.18 together with other kinematic distributions.

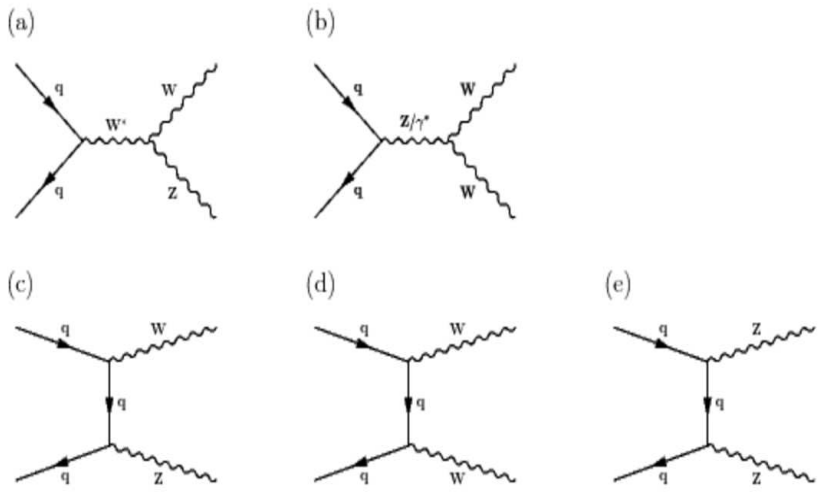

Figure 3.9.: Leading order graphs for diboson production at the Tevatron.

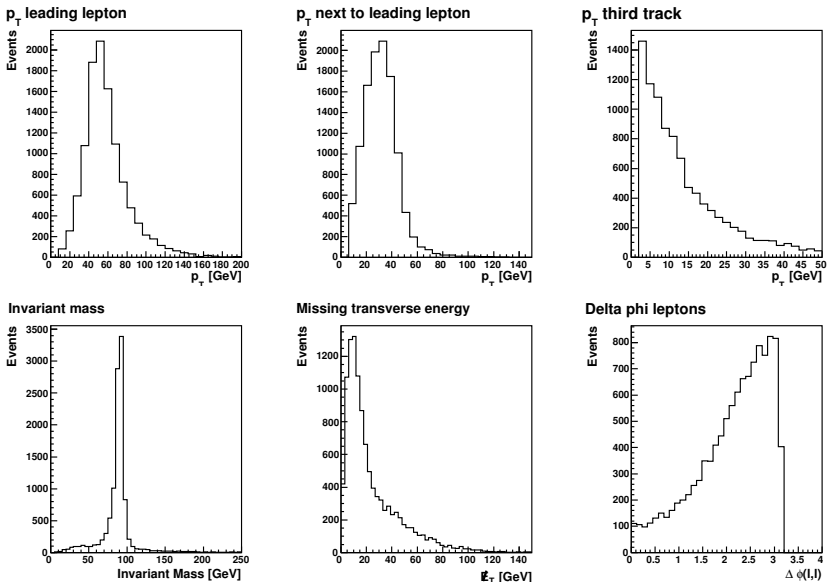

Figure 3.10.: Various kinematic distributions for the WZ background. From upper left: p_T of leading lepton, p_T of next to leading lepton, p_T of the third track, invariant mass of the two leading leptons in the event, missing transverse energy ($\not\!\!E_T$) and $\Delta\phi$ between the two leading leptons.

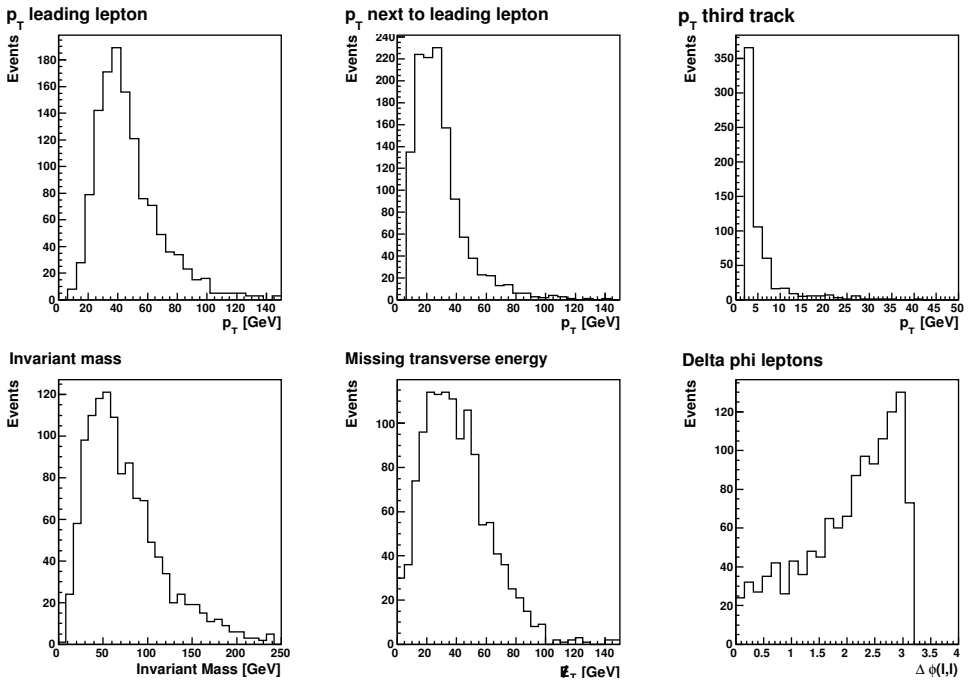

Figure 3.11.: Kinematic distributions for the WW background. The p_T spectrum of the third track is exponentially falling since the track is caused by a fake and is significantly softer than the p_T distribution of the third track for WZ that can be seen in Figure 3.10.

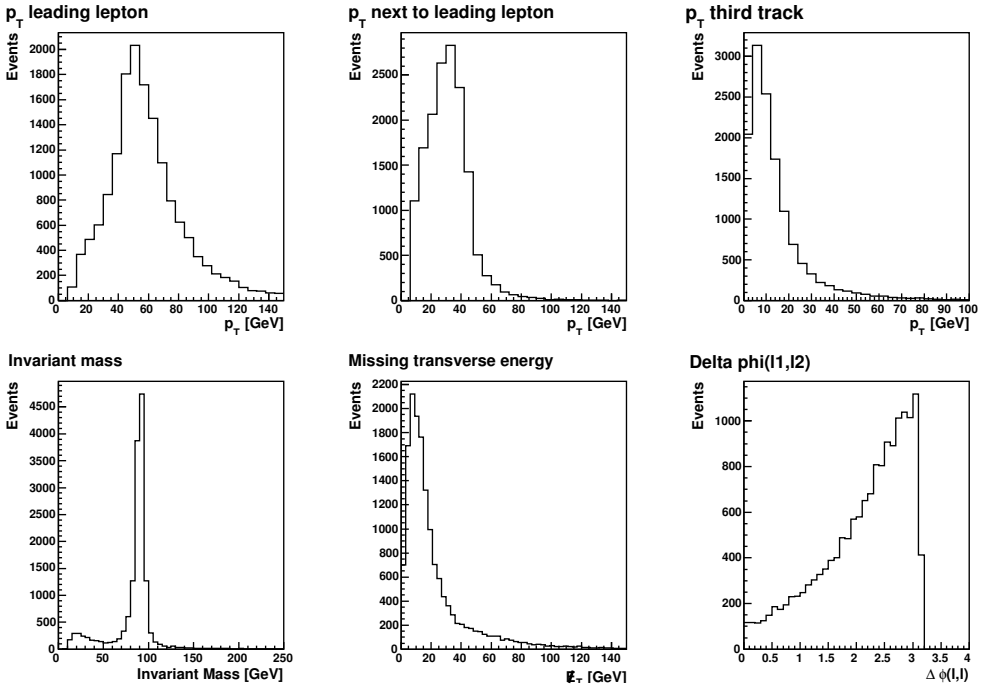

Figure 3.12.: Kinematic distributions as for the ZZ background. The leading and next-to-leading leptons are real, but the track can come from a real lepton, or it could be a fake.

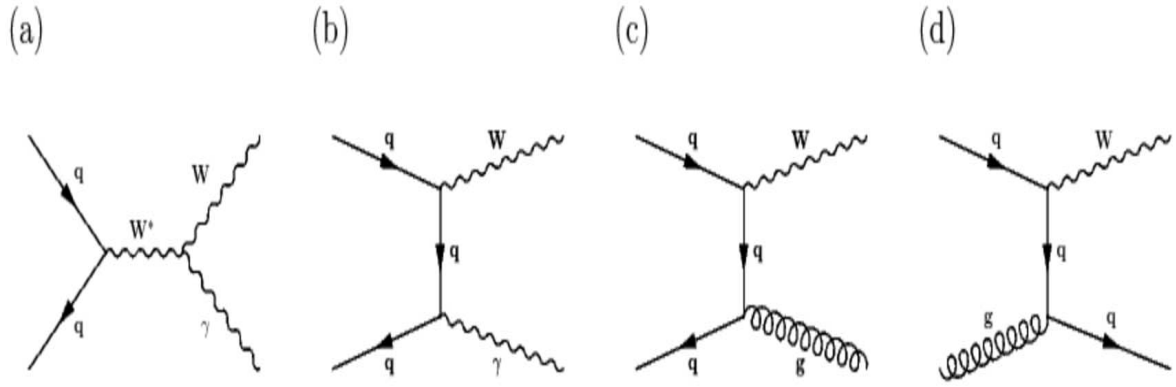

Figure 3.13.: Some leading-order diagrams for W($+\gamma/jet$) production at the Tevatron.

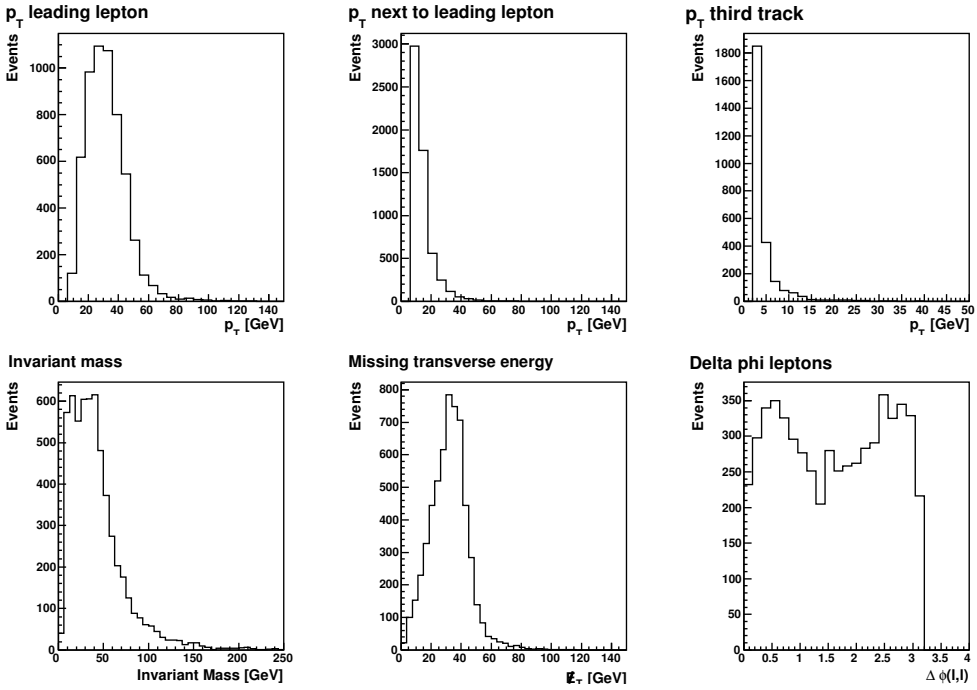

Figure 3.14.: Kinematic distributions for $W \to \ell\nu$ decays. Both the second lepton and the track are from fakes, hence the soft spectra. The $\not\!\!E_T$ is real, and is considerably harder than for example the $\not\!\!E_T$ spectrum from ZZ.

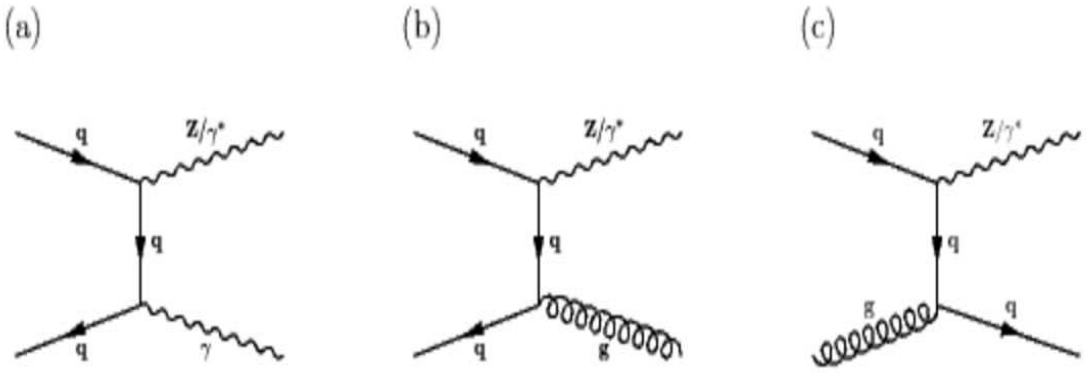

Figure 3.15.: A selectio of leading order diagrams for $Z + \gamma$/jet production at the Tevatron.

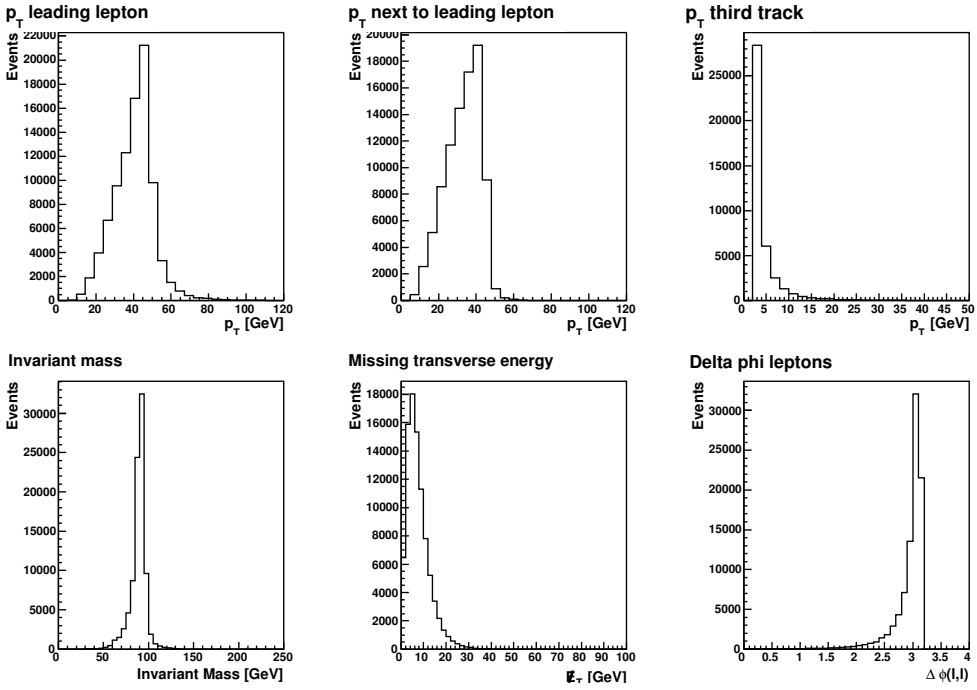

Figure 3.16.: Kinematic distributions for resonant $Z \to ee$ decays. Both the leading and next to leading lepton are real but the third lepton (track) is a fake and has a very soft spectrum. In $Z \to ee$ decays, there is no real $\not\!\!E_T$ and the $\not\!\!E_T$ spectrum is considerably softer compared to processes with real $\not\!\!E_T$, for example $W \to \ell\nu$.

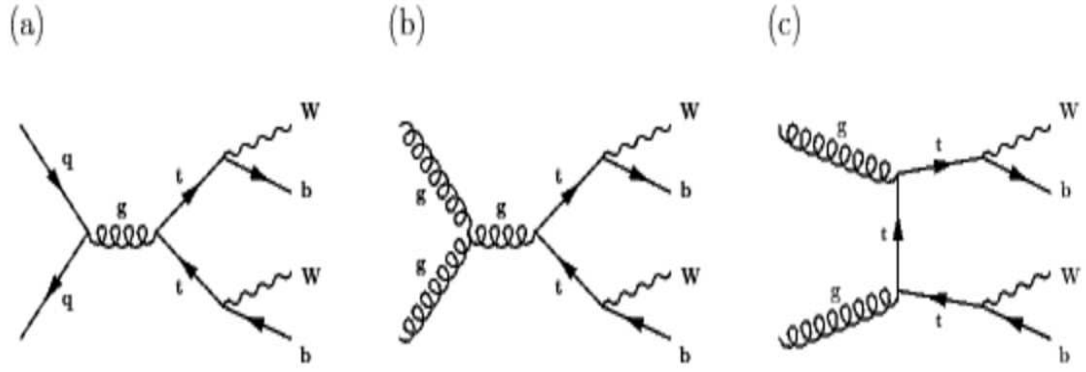

Figure 3.17.: Leading order diagrams for $t\bar{t}$ production at the Tevatron.

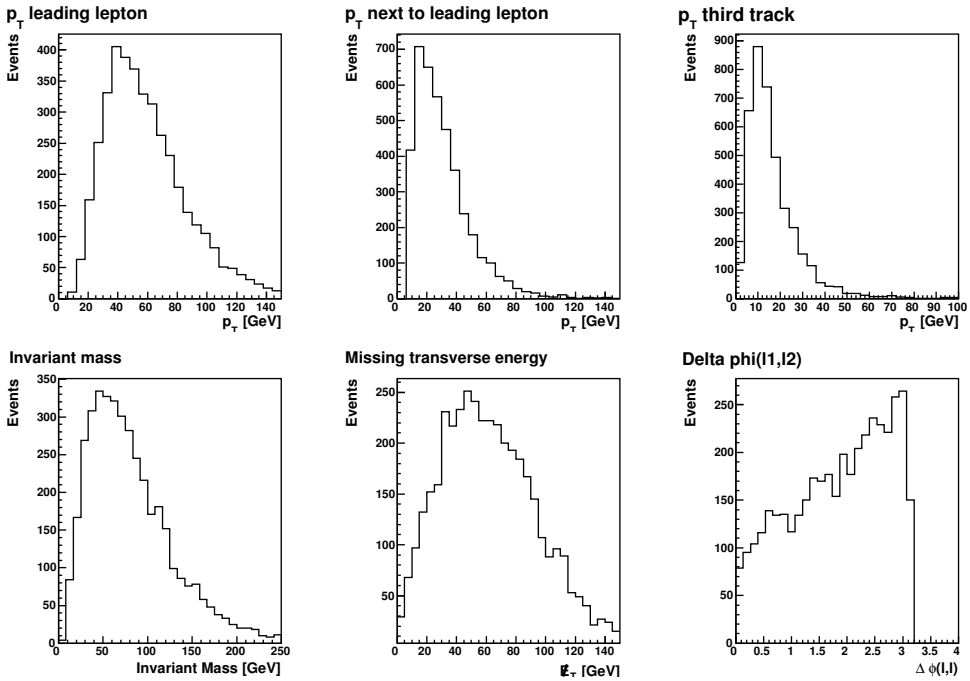

Figure 3.18.: The same kinematic distributions for $t\bar{t} \rightarrow ee$ events. Even though the third track is a fake, the p_T spectrum is relatively hard since it is faked by high-momentum jets. There is real $\not\!\!E_T$ in the events which is obvious from the $\not\!\!E_T$ distribution.

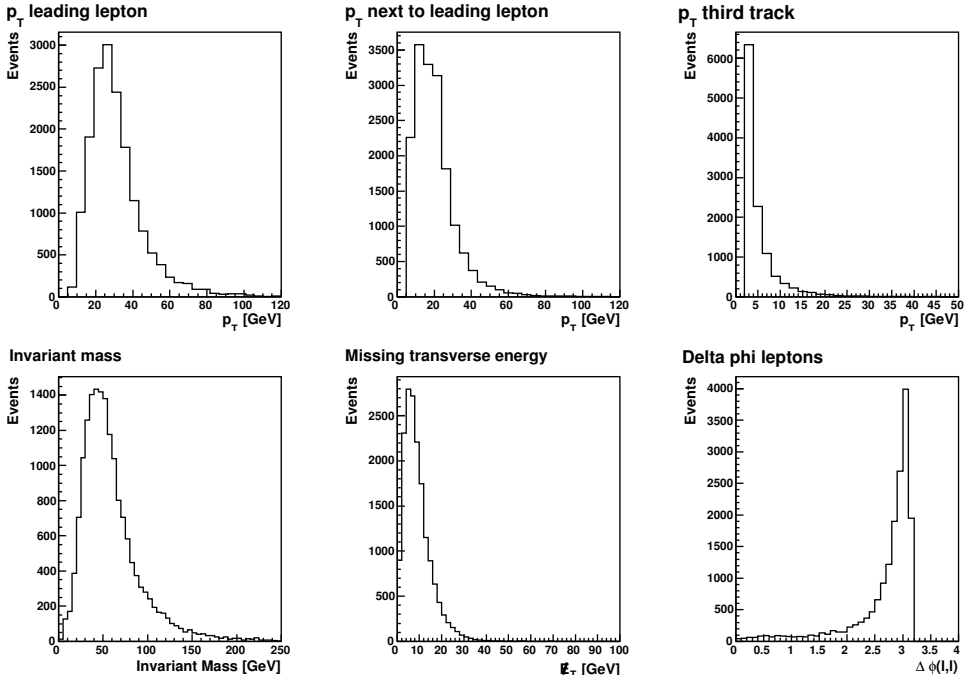

Figure 3.19.: Kinematic distributions of QCD multijet background. No real leptons or real $\not\!\!E_T$ is present in the final state. Nevertheless, because of mismeasurements of lepton and jet energies, $\not\!\!E_T$ can artificially be created and QCD events can pass the selection.

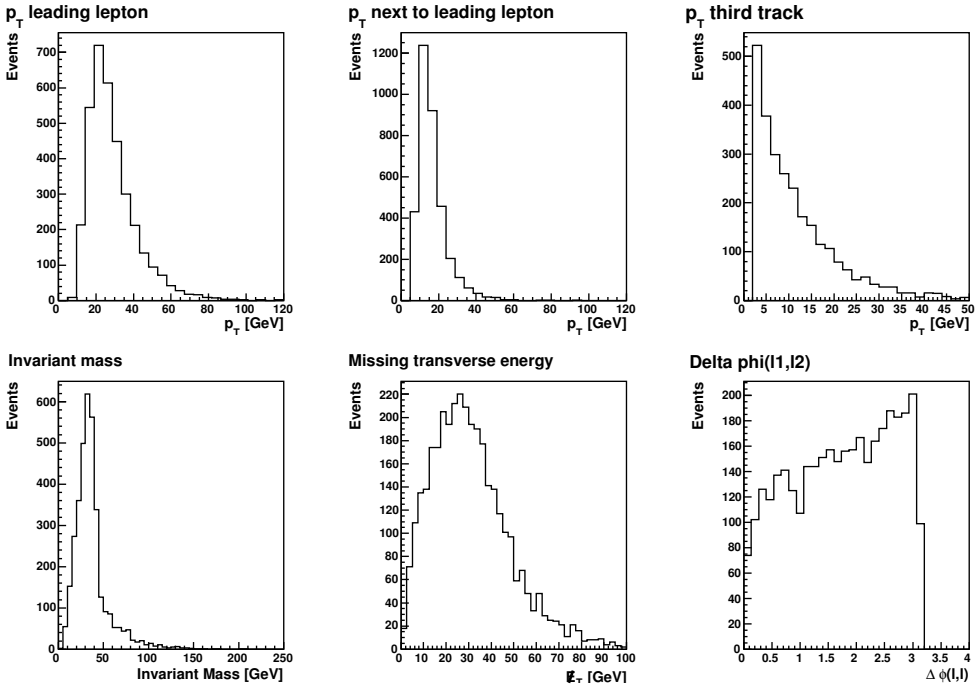

Figure 3.20.: Kinematical distributions for susypoint $m_0 = 150$ GeV, $m_{1/2} = 150$ GeV. The other susy parameters are listed in Table 3.1.

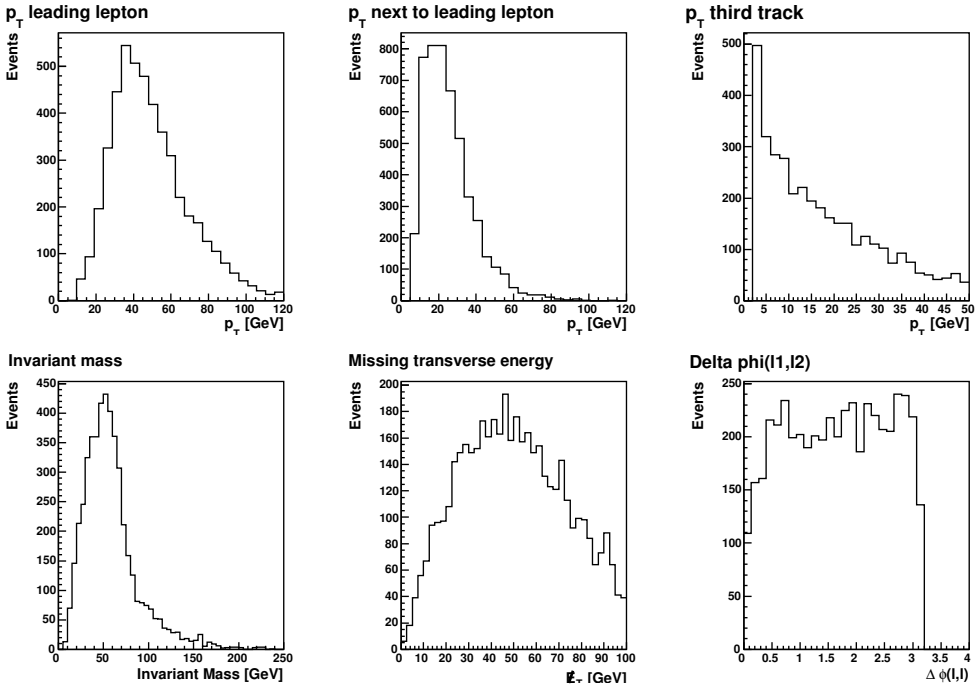

Figure 3.21.: Kinematical distributions for susypoint $m_0 = 150$ GeV, $m_{1/2} = 250$ GeV. The other susy parameters are listed in Table 3.2.

3.3. Search for Supersymmetry

Despite extensive efforts to find supersymmetric particles, no such particles have been found yet. This section will focus on the efforts that have been made to discover Supersymmetry. First direct searches from LEP and Tevatron will be discussed followed by a more brief discussion of indirect searches and cosmological results.

3.3.1. Direct SUSY Searches

Direct searches for supersymmetric particles have been carried out at LEP and the Tevatron and the results have set stringent limits on the SUSY parameter space.

Results from LEP

The search for charginos by the four collaborations at LEP II (ALEPH, DELPHI, L3 and OPAL) was performed in final states with jets, leptons and jets, and purely leptonic final states [22]. In Figure 3.22 (top) [22] the lower limits on the slepton masses are shown in the $(m_{\tilde{\ell}_R}, m_{\tilde{\chi}_1^0})$-plane. The lower mass limit for the selectrons is 99.9 GeV [23]. Figure 3.22 (bottom) shows the mass limit as a function of sneutrino mass. For $m_{\tilde{\nu}} > 300$ GeV, the lower mass limit is $m_{\chi_1^\pm} > 103.5$ GeV at 95% CL.

In Figure 3.23 (left), the exclusion region in the $(m_0, m_{1/2})$ for tanβ=10, A$_0$=0 and $\mu > 0$ is presented [24]. For small m_0, slepton searches allow exclusion of $m_{1/2}$ values below 240 GeV. Results from Higgs boson searches allow to exclude $m_{1/2}$ values less than 270 GeV.

Also lower limits of the LSP mass were derived at LEP II [25]. The results were interpreted in an mSUGRA scenario. The limit on $m_{1/2}$ can be translated into limits on the mass of the LSP. Figure 3.23 (right) shows the LSP mass limit for $\mu > 0$ and $\mu < 0$ as a function of $\tan\beta$ for any A_0 and different top masses. Neutralino masses below 50 GeV can be excluded.

Tevatron Trilepton Search in Run I and Run II

During Run I of the Tevatron, searches for the associated production of lightest chargino and next-to-lightest neutralino were performed at DØ [26] and CDF [27]. The results were not compatible with the results from LEP, and will therefore not be discussed here.

The search for the associated production of charginos and neutralinos continued in Run II of the Tevatron [28]. The analyses presented in this thesis, are a continuation of a result based on an integrated luminosity of $\sim$300 pb^{-1}. The expected and observed limits published in [28] are presented in Figure 3.24. The limits are compared to the predictions of different benchmark scenarios. These benchmark scenarios are:

- Models where the sleptons are mass degenerate with the second neutralino and the latter decays dominantly via sfermion- mediated 3-body diagrams, such that the leptonic

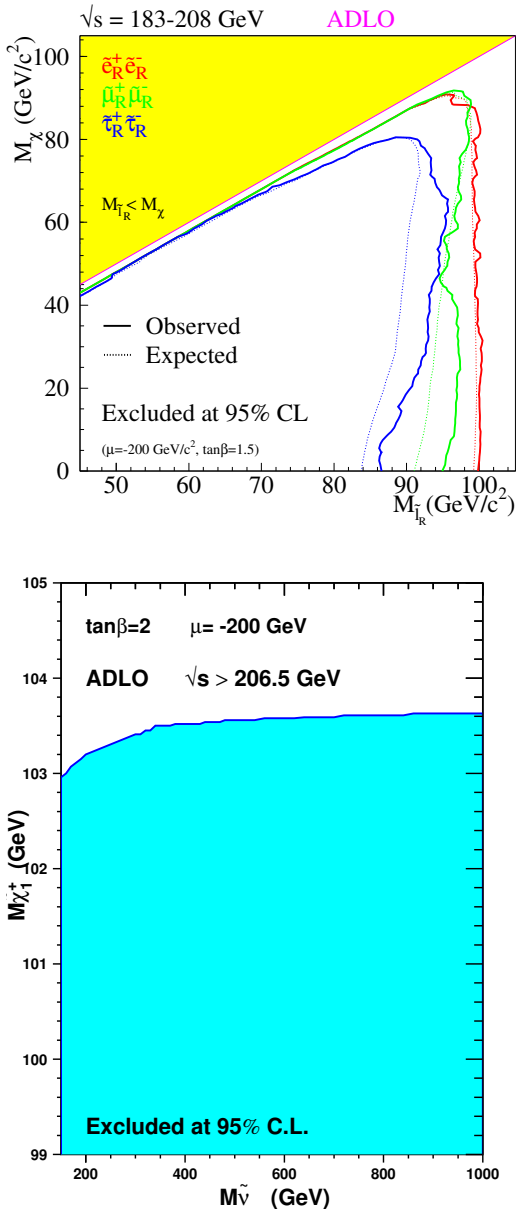

Figure 3.22.: Combined exclusion from the LEP experiments on the charged slepton masses as a function of $m_{\tilde{\chi}^0_1}$ mass (top) [23] and upper limit on the mass of the lightest chargino as a function of sneutrino mass (bottom) [22].

branching ratio for 3-body topologies is maximally enhanced (3ℓ-max scenario). When calculating the cross section unification of squark and slepton masses is assumed.

- If the unification of slepton and squark masses is dropped and the squarks are assumed to be very heavy (∼1 TeV), one arrives at the heavy-squark scenario. Since the squarks are heavy, the destructive interference from the t-channel contribution is suppressed and the cross section is maximally enhanced.

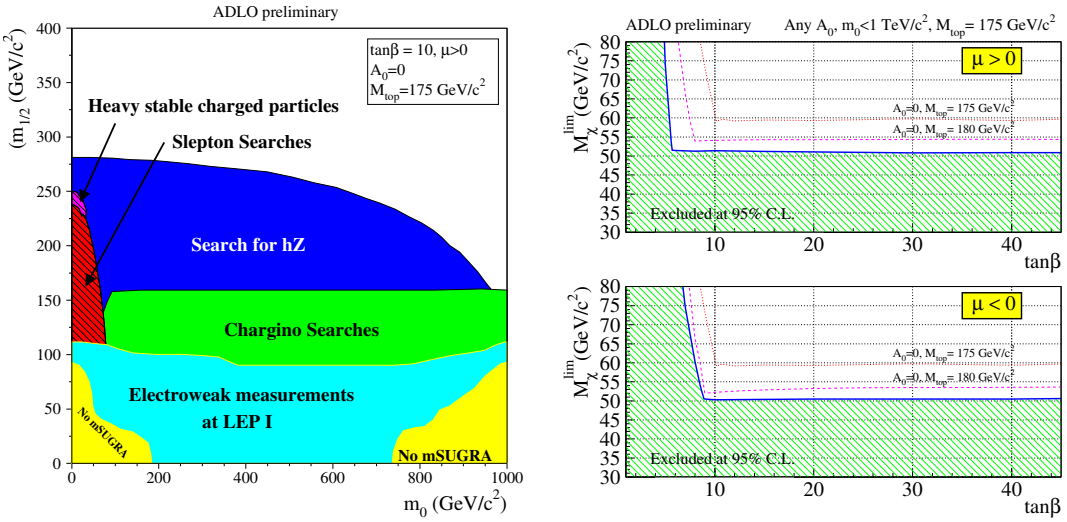

Figure 3.23.: Excluded region at 95% CL in the $m_0, m_{\frac{1}{2}}$ plane for $\tan\beta$=10, $\mu > 0$, $A_0 = 0$, and M_{top} =175 GeV (left) [24] and lower limit on LSP mass as function of $\tan\beta$ (right) for $\mu > 0$ (upper) and $\mu < 0$ (lower) [25].

- Raising m_0 to the TeV scale assuming scalar mass unification leads to the large-m_0 scenario characterized by large slepton and squark masses. Charginos and neutralinos decay via gauge boson mediated 3-body decays. For large slepton masses the impact of $\tilde{\tau}$ mixing on the branching ratios is negligible, since the slepton mass difference is small compared to the slepton mass.

In the 3ℓ-max scenario, a lower limit on the mass of the lightest chargino of 117 GeV is derived.

3.3.2. Indirect SUSY Searches

If SUSY exists, it is expected to influence the effective values of Standard Model parameters via radiative corrections. Hence the precise measurement of these values constrains the allowed SUSY parameter space. Electroweak precision variables and B-physics observables can be combined in a χ^2 to estimate favored values of SUSY parameters [29]. The observables that were included in the χ^2 constructed in [29] are the mass of the W boson, M_W, the effective leptonic weak mixing angle, $\sin^2\theta_{\text{eff}}$, the anomalous magnetic moment of the muon, $(g-2)_\mu$, the mass of the lightest CP-even Higgs boson, M_h, the branching ratio BR$(b \to s\gamma)$ and the branching ratio BR$(B_s \to \mu\mu)$. Assuming the six observables to be uncorrelated, a χ^2 has been defined

$$\chi^2 = \sum_{n=1}^{4} \left(\frac{R_n^{exp} - R_n^{theo}}{\sigma_n} \right)^2 + \chi^2_{M_h} + \chi^2_{B_s} \tag{3.1}$$

where R_n^{exp} is the experimental central value of the nth observable, R_n^{theo} is the corresponding MSSM prediction and σ_n denotes the error, taking into account both theoretical and statistical errors (see [29] for details). $\chi^2_{M_h}$ and $\chi^2_{B_s}$ are the contribution to the χ^2 from the experimental

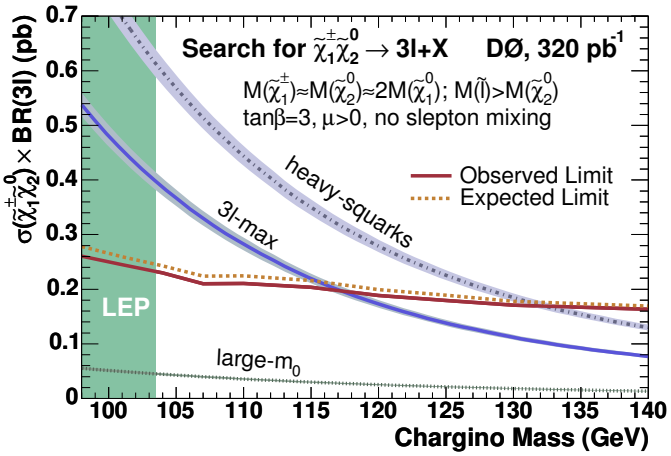

Figure 3.24.: The expected and observed limit as a function of $\tilde{\chi}_1^{\pm}$mass in the first Run II DØ tri-lepton analysis [28]. Comparing the limits to the prediction from different benchmark scenarious allows for setting limits on the mass of the lightest chargino, assuming the mass relation $m_{\tilde{\chi}_1^{\pm}}\approx m_{\tilde{\chi}_2^0}\approx 2m_{\tilde{\chi}_1^0}$ and tanβ=3 and $\mu > 0$.

limits on the lightest CP-even MSSM Higgs boson and BR($B_s \rightarrow \mu\mu$), respectively.

Figure 3.25 shows the $\Delta\chi^2$=1,4,9 (indicated $\Delta_1, \Delta_4, \Delta_9$) using the observables listed above. Relatively low values ($\sim$ 500 GeV) are favored for $m_{1/2}$. For m_0, smaller values are preferred considering the Δ_1, but going to Δ_4, hardly any bound can be obtained.

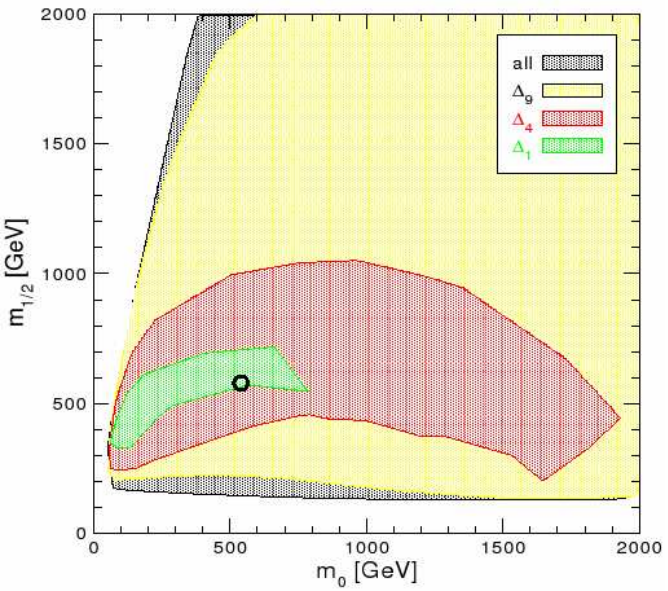

Figure 3.25.: The $\Delta_{1,4,9}$ regions in the $(m_0, m_{1/2})$ plane in the constrained MSSM scenario and $\mu > 0$. The best-fit point is marked with a circle and the Δ_1 region is mediumd shaded (green) [29].

Since the LSP is a good candidate for cold dark matter (CDM), measurements of cold dark matter densities, Ω_{CDM}, are interpreted as measurements of SUSY parameters. Measurements of Ω_{CDM} are done by The Wilkinson Microwave Anisotropy Probe (WMAP) [30]. A study was performed in [31] regarding the impact of the density of cold dark matter, and it was found that apart from expanding the range of m_0, removing the Ω_{CDM} constraint has small effect on the preferred regions of the CMSSM parameter space in the $(m_0, m_{1/2})$, (tan β, $m_{1/2}$) and (tan β, m_0) planes, as shown in Figure 3.26.

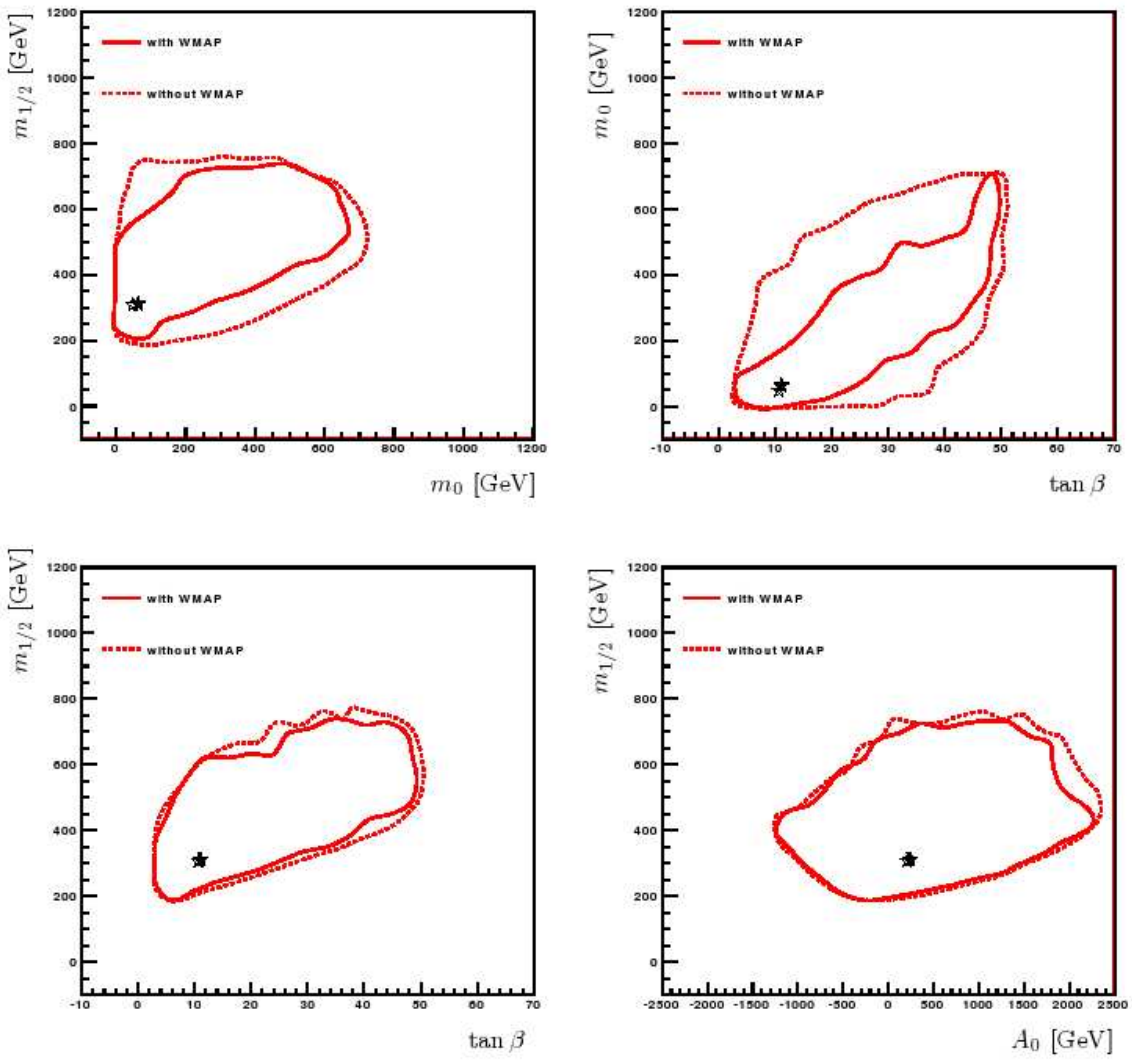

Figure 3.26.: 95% CL allowed regioins in the MSSM parameter space [31] in the $(m_0, m_{1/2})$ plane (upper left), in the (tan β,m_0) plane (upper right), in the (tan β,$m_{1/2}$) plane (lower left), and in the (A_0,$m_{1/2}$) plane (lower right). Solid lides indicate inclusion of the WMAP constraint and dotted lines include exclusion of the WMAP constraint. The best-fit points are marked with a filled (open) star for including (excluding) WMAP data.

4. Experimental Setup

The data used in this thesis was collected by the DØ detector [32] at the Tevatron [33] located at Fermi National Accelerator Laboratory (FNAL) [34] near Chicago. At the Tevatron, protons and antiprotons are collided at a center-of-mass energy of $\sqrt{s} = 1.96$ TeV. Tevatron is currently the highest-energy collider in the world, before the start of the Large Hadron Collider (LHC) [35] at CERN [36]. Two multi-purpose experiments, CDF [37] and DØ are located along the Tevatron ring.

The first data taking period (Run I) started in 1992 and continued until 1996. During Run I, the top quark was discovered [38, 39] and each experiment collected an integrated luminosity of $\int \mathcal{L}dt = 120$ pb^{-1} at a the centre-of-mass energy of 1.8 TeV. The second data taking period (Run II) started in 2001 after a downtime where both experiments as well as the accelerator were extensively upgraded. Throughout this thesis, Run IIa will refer to the data taking period between April 2002 and Februay 2006. Between February and June 2006, there was a shutdown where the DØ detector and the accelerator were further upgraded. The upgrade of the DØ detector and trigger system will be discussed in Section 4.3.1 and 4.3.6. In summer 2006 the period referred to as Run IIb started. By the end of Run II, an integrated luminosity of 6-7 fb^{-1} is expected for each experiment.

4.1. Coordinate System

Spherical coordinates are used to describe the position of the particles: r, ϕ (azimuthal angle) and θ (polar angle). The coordinate system is centered at the center of the detector. The z direction is defined to be along the beamline in the proton direction. The x-axis is pointing to the center of the ring and the y-axis is pointing upward. It is customary to use the quantity pseudo-rapidity, η, instead of the polar angle θ. The pseudo-rapidity is defined as

$$\eta = -\ln(\tan\frac{\theta}{2}) \tag{4.1}$$

In the relativistic limit the pseudo-rapidity is approximately equal to the true rapitidy, y, defined as

$$y = \frac{1}{2}\ln\frac{(E+p_z)}{(E-p_z)} \tag{4.2}$$

Assuming equal beam energy and particle types of the colliding particles, the number of particles in a collision is roughly constant as a function of η. The η of a particle can be given with respect to the center of the detector, $\eta_{detector}$, or with respect to the vertex where the interaction took

place, $\eta_{physics}$.

The separation of two objects is given by ΔR:

$$\Delta R = \sqrt{(\Delta\phi)^2 + (\Delta\eta)^2}. \tag{4.3}$$

4.2. Accelerator

The Tevatron is the last stage of an accelerator chain that consists of consecutive accelerators of increasing energies. Figure 4.1 shows a schematic view of the accelerator chain. It starts with a Cockroft-Walton accelerator where the protons are accelerated to 750 keV and turned into negative hydrogen ions, H^-. The energy is increased to 400 MeV by the LINAC linear accelerator and after this step, the negative ions pass through a carbon foil to strip off the electrons. The protons are then accelerated up to 8 GeV by the Booster synchroton and transferred to the Main Injector synchroton ring where they are accelerated up to 150 GeV and arranged into a bunch structure transferred to the Tevatron. The antiprotons are produced by directing 120 GeV proton bunches from the Main Injector at a nickel/copper target and only 15 antiprotons are produced per one million protons. The target is followed by a lithium lens to focus the secondary particles, and then a dipole magnet to select 8 GeV antiprotons from the beam. These are sent to the Debuncher, a triangular 8 GeV synchrotron to reduce the momentum spread and to cool them. From there, the antiprotons are stacked in the Accumulator, another 8 GeV synchrotron.

In the final stage, protons and antiprotons are arranged into 3 super bunches each composed of 12 smaller bunches. The time between each super bunch is 2.6 μs and 396 ns between each small bunch. This results in 36 bunches of protons and 36 bunches of antiprotons travelling the beam line in opposite directions. Each proton bunch consists of $\approx 3 \times 10^{11}$ protons and each antiproton bunch consists of $\approx 3 \times 10^{10}$ antiprotons. One bunch is approximately 60 cm long. The interaction region at DØ is spread out according to a Gaussian distribution with a standard deviation of ≈ 25 cm.

Current instantaneous luminosities are over $2 \times 10^{32} \mathrm{cm}^{-2}\mathrm{s}^{-1}$ and this number has been steadily increasing during RunII. Figure 4.2 shows the initial peak luminosity and integrated luminosity delivered by the Tevatron Collider during RunII. The limiting factor to the luminosity of the Tevatron has been the number of antiprotons available. Therefore, a more recent addition has been the Recycler which is an 8 GeV storage ring with permanent magnets which shares the tunnel with the Main Injector. As the Accumulator fills up, stacking efficiency decreases. The antiprotons are then transferred to the Recycler so that the stacking efficiency in the Accumulator increases again. Electron cooling was also implemented during the upgrade in 2006 to further improve the antiproton beam and increase the luminosity.

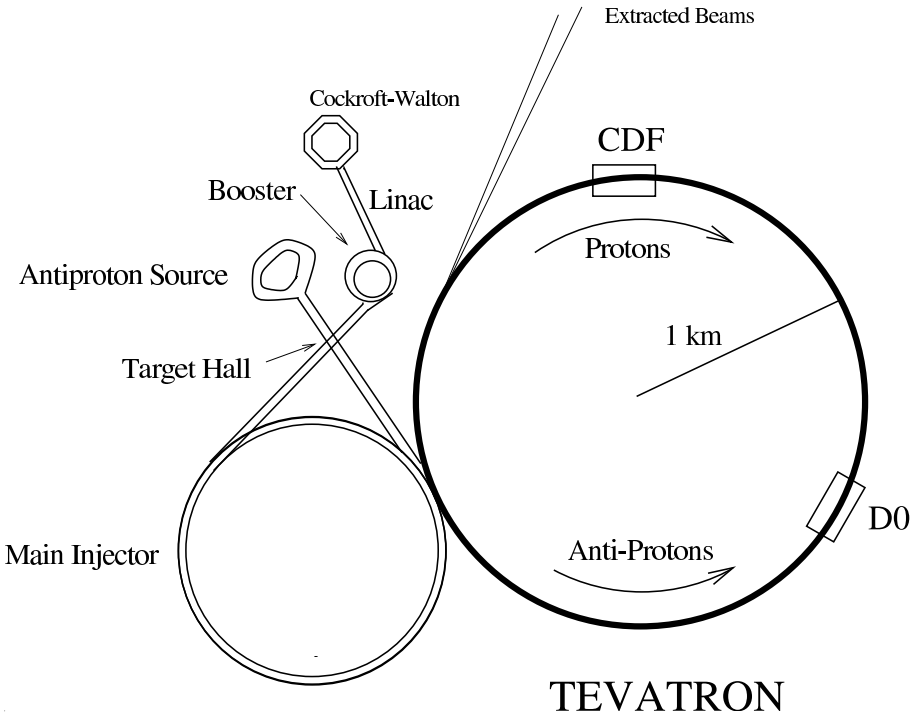

Figure 4.1.: The accelerator chain at Fermilab.

4.3. DØ Detector

The DØ detector [40, 41] is a general purpose detector which consists of several subdetectors arranged cylindrically around the interaction point. The innermost layer is the silicon microstrip vertex detector (SMT). Then, moving outward, we find the central fiber tracker (CFT). The SMT and the CFT are immersed in the field of a superconducting solenoid magnet. Outside of the solenoid is the liquid-argon sampling calorimeter followed by three layers of muon chambers with a toroid magnet between layer one and two. Figure 4.3 shows a side view of the RunII DØ detector. The detector is approximately 20 m long and 13 m high.

4.3.1. Tracking System

The purpose of the tracking system is to measure the trajectories of the charged particles produced in a collision and to determine the primary interaction vertex. A charged particle with transverse momentum p_T will travel on a helix with radius

$$r[\mathrm{m}] = \frac{p_T[\mathrm{GeV}]}{0.3 \cdot B[\mathrm{T}]}, \tag{4.4}$$

where p_T is the transverse momentum of the particle and B is the magnetic field strength. The DØ tracking system consists of two trackers. Closest to the beamline is the silicon microstrip

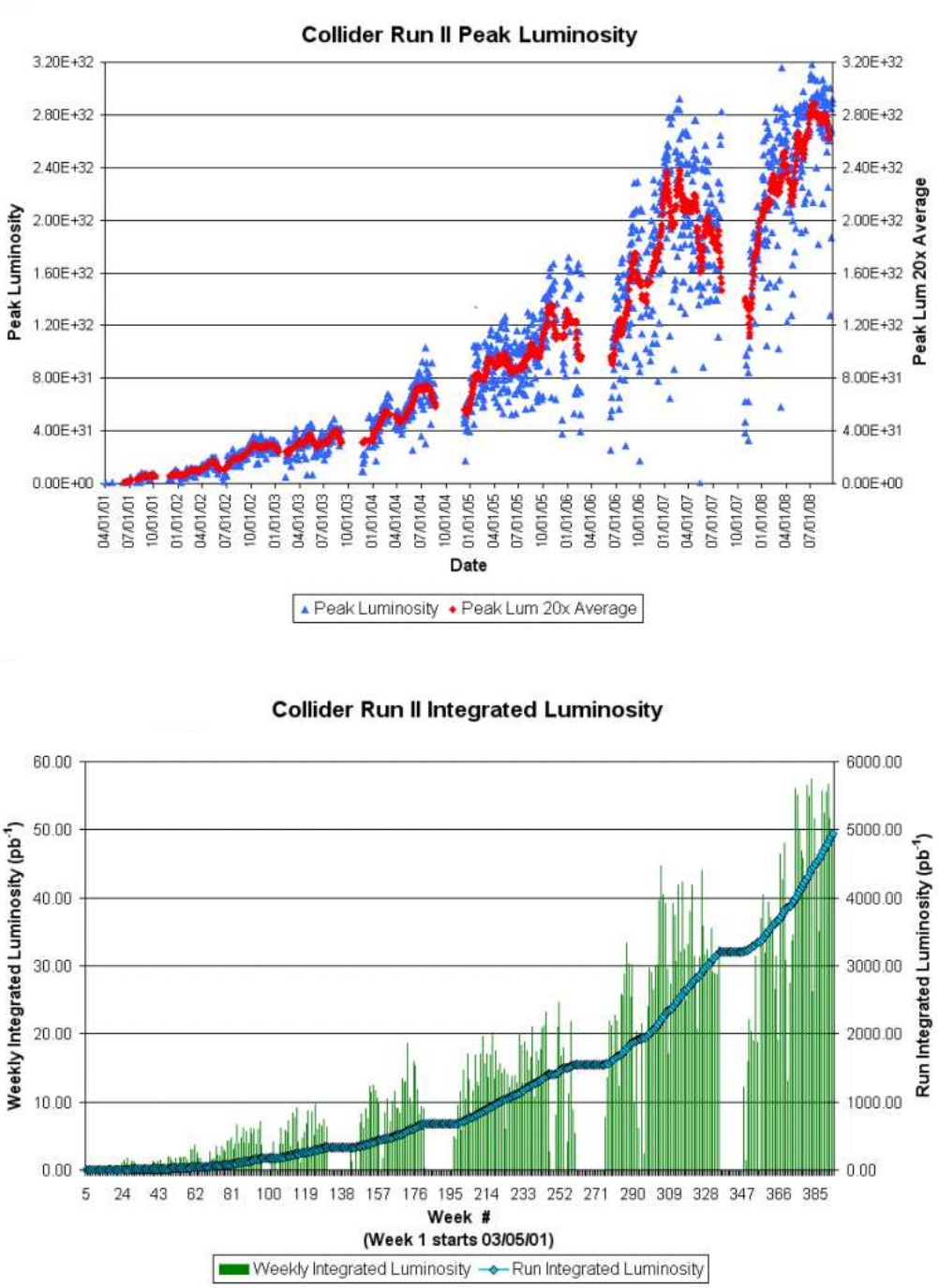

Figure 4.2.: Initial peak luminosity (upper) and integrated luminosity delivered by the Tevatron Collider (lower) [33].

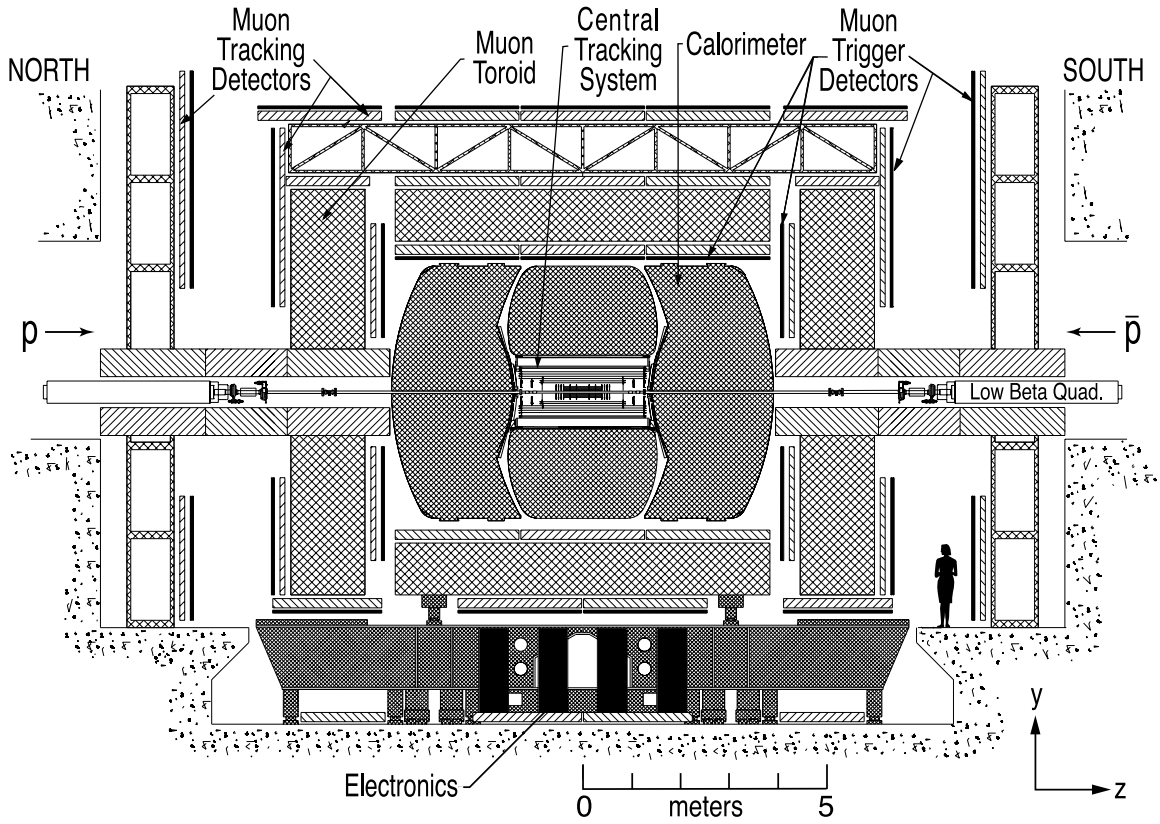

Figure 4.3.: Side view of the DØ detector [41].

tracker and outside of it resides the central fiber tracker. Outside the tracker systems is a 2 T strong superconducting solenoidal magnet. The tracking system can locate interaction vertices with a resolution of about 35 μm along the beamline and achieve an impact parameter resolution of better than 15 μm in $r - \phi$ for charged particles with a tranvserse momentum $p_T > 10$ GeV at $|\eta_{det}| = 0$. The relative transverse momentum resolution of the tracking detector is shown in Figure 4.4.

Silicon Microstrip Tracker

The silicon microstrip tracker (SMT) is the innermost tracking detector starting at a radius of 1.6 cm. It provides tracking and vertexing over the full η range and covers the whole interaction region ($\sigma \approx 25$ cm). It is also important that the SMT tracker is capable of reconstructing secondary vertices of hadrons from bottom-quark decays, in order to identify jets orginating from bottom quarks, as well as to distinguish them from jets that come from the fragmentation of light quarks or gluons. In the central region ($|z| < 35$ cm), the detector consists of six barrel modules. Each barrel is capped with a disk of twelve double-sided wedge detectors (F-disks) at large values of $|z|$. Each barrel module consists of four silicon readout layers. Layer 1 and 2 are equipped with 12 double-sided silicon readout modules (ladders) and layer 3 and 4 have 24 modules. Two large diameter disks (H-disks) provide tracking in the far forward regions at high $|\eta|$.

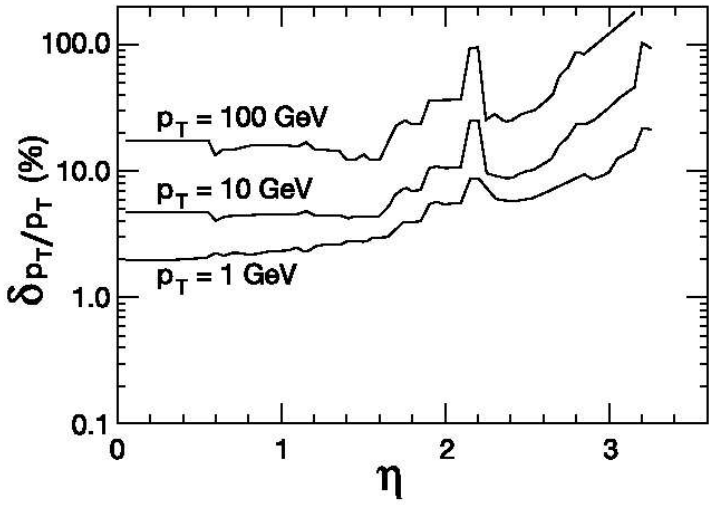

Figure 4.4.: Relative transverse momentum resolution of the central tracking system as a function of pseudorapidity for tracks with p_T=1, 10 and 100 GeV [41].

The barrel detectors primarily measure the $r\phi$ coordinate, while the disk detectors measure $r-z$ and $r-\phi$. Vertices for high-η particles are therefore reconstructed in three dimensions by the disks while vertices of particles with smaller $|\eta|$ are measured both in the barrels and the central fiber tracker. Figure 4.5 shows a three dimensional picture of the SMT tracker.

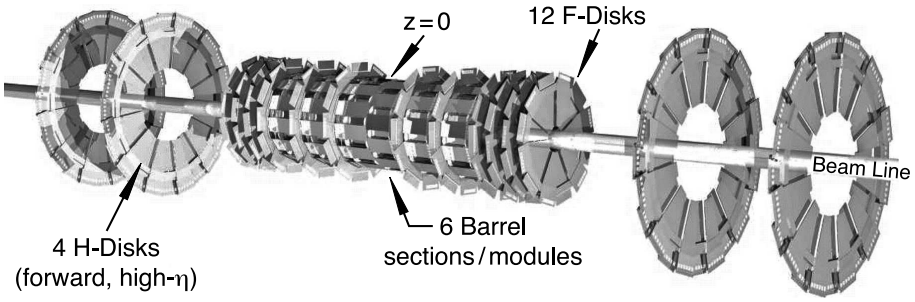

Figure 4.5.: 3-D view of the Silicon Microstrip Tracker.

The SMT was upgraded between RunIIa and RunIIb [42] to compensate for the radiation damage of the existing SMT. An additional layer of silicon was added to the detector. This layer is called Layer 0 because it was installed inside the existing SMT layers. The radius from the beampipe to Layer 0 is 1.6 cm and the radius to Layer 1 is 2.7 cm. There are various benefits from installing such a layer closer to the beampipe. Layer 0 improves tracking and b-tagging, important for $H \rightarrow b\bar{b}$ searches. It also provides an additional hit for pattern recognition and improves impact parameter resolution. Figure 4.6 shows the improvement in momentum resolution by adding Layer 0.

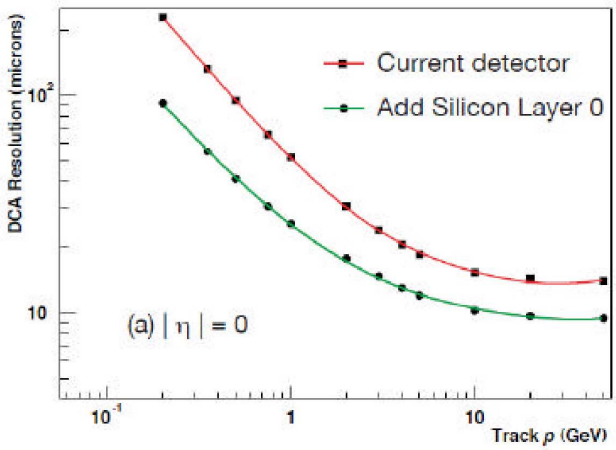

Figure 4.6.: The impact parameter resolution as a function of track momentum at $\eta = 0$. The plot shows the improvement of adding another layer to the SMT [42].

Central Fiber Tracker

The central fiber tracker (CFT) is located outside the SMT with a coverage of $|\eta_{det}| < 1.6$. It consists of scintillating fibers mounted on eight concentric support cylinders. The inner radius of the CFT is 20 cm and it extends out to 52 cm. The diameter of the scintillating fibers is 835 μm and the length is either 1.66 m (two innermost cylinders) or 2.52 m (outer six layers). The scintillation light is carried out by clear fiber waveguides to visible light photon counters (VLPCs) for read out.
The CFT has a total of 76800 readout channels and the signal are used to form a fast hardware trigger based on the number of track candidates above a specific p_T treshold.

Solenoid Magnet

The solenoid magnet is located outside the CFT. The radius is 60 cm and the length is 2.7 m and it provides a uniform magnetic field of 2 T inside the tracking volume. The magnet consists of two concentric coils of superconducting Cu:NbTi cable and is operated with a 4.7 kA current at a temperature of 10 K. The thickness of the superconducting solenoid coil plus cryostat wall is about 1 electromagnetic interaction length (X_0) at $\eta_{det} = 0$.

4.3.2. Preshower Detectors

The purpose of the preshower detectors is to enhance spatial matching resolution between tracks and electromagnetic showers. The detectors can also adjust the electromagnetic energy for energy losses in the solenoid and upstream material. Because of fast energy and position measurements the preshower information is also used in the trigger system.

The coverage of the central preshower detector (CPS) is $|\eta_{det}| < 1.3$ and it is located between the solenoid and the calorimeter. The forward preshower detectors (FPS) cover $1.5 < |\eta_{det}| < 2.5$. The central preshower detector consists of three cylindrical layers of scintillator strips, one with axial orientation and the others with stereo angles of -24^0 and +24^0, and a lead radiator of approximately one radiation length between the solenoid and the scintillators in the region $|\eta| < 1.3$ in order to induce electromagnetic showering. The material of the CPS, the coil and the cryostats corresponds to approximately two radiation lengths.

The FPS consists of four layers of scintillator: two layers at angle of 22.5^o relative to each other, then a $2X_0$ radiator made of lead and stainless steal, followed by two more layers of scintillator.

4.3.3. The Calorimeter System

The DØ calorimeter system consists of three liquid argon calorimeters. The purpose of the calorimeter is to identify and measure the energy of jets, electrons and photons. The full coverage in ϕ allows to establish the transverse energy balance in the event.

Photons and electrons start electromagnetic cascades in the inner layers of the calorimeter. Hadron jets start hadronic showers which deposit their energy in the electromagnetic and hadronic parts of the calorimeter.

The Liquid-Argon calorimeters

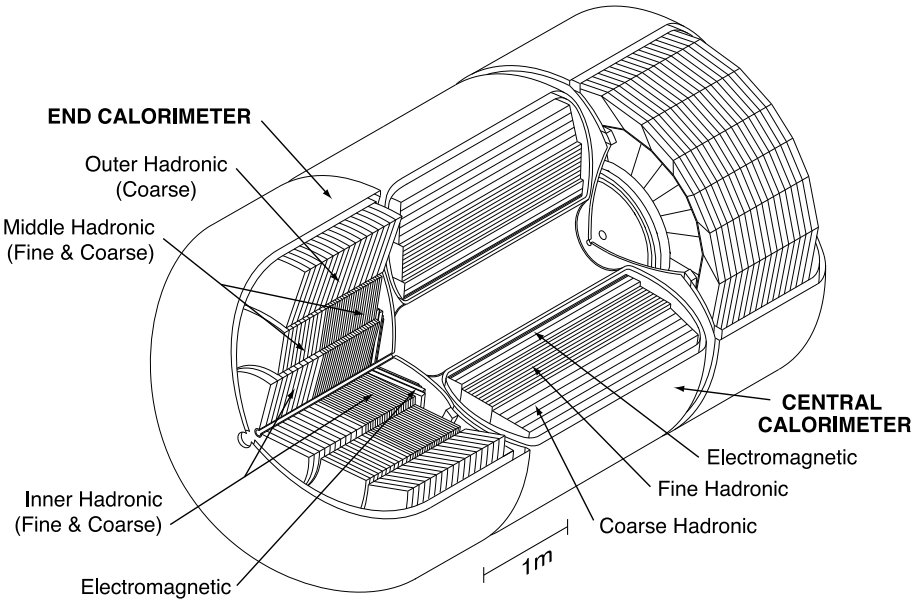

Figure 4.7.: Isometric view of the calorimeter.

The calorimeter is divided into three sections: the electromagnetic section (EM) closest to the interaction region, followed by the fine (FH) and coarse (CH) hadronic sections. The calorimeter

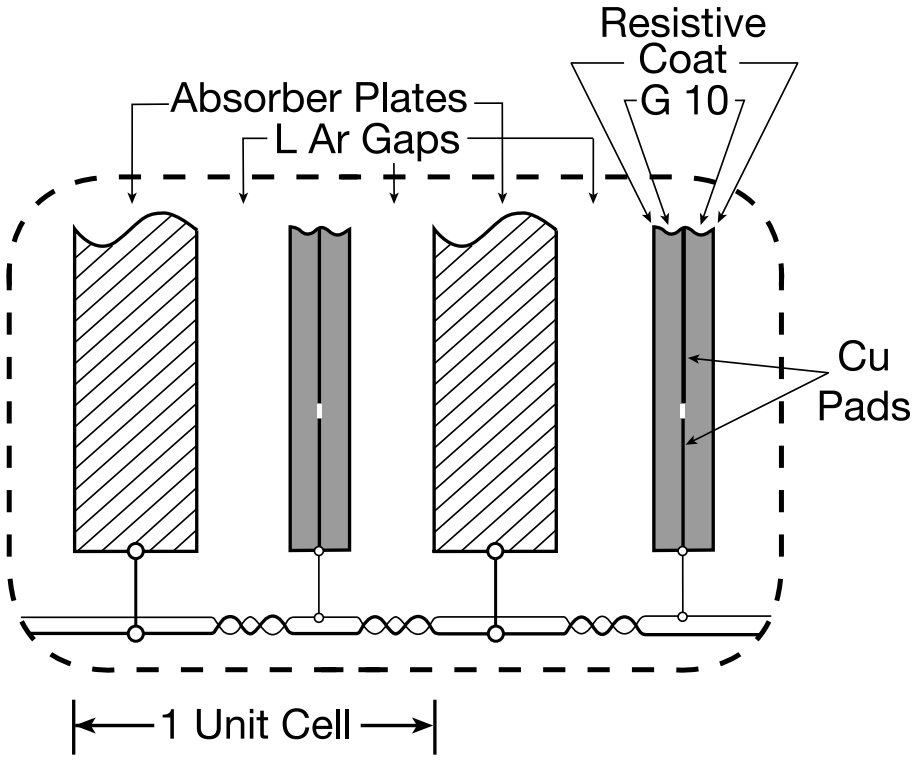

Figure 4.8.: Unit cell in the liquid-argon calorimeter.

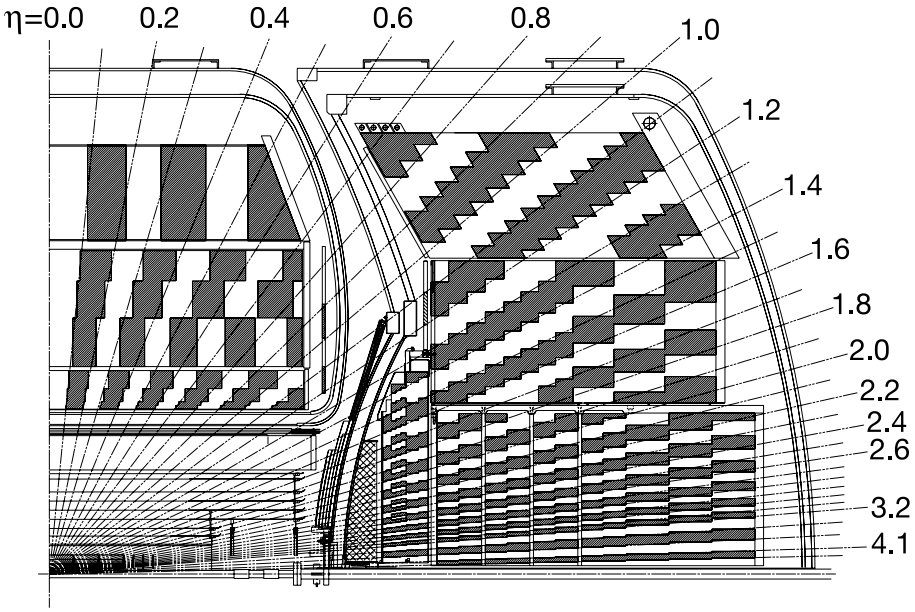

Figure 4.9.: Sections of a quarter of the calorimeter.

is shown in Figure 4.7. The coverage of the central calorimeter (CC) is $|\eta_{det}| < 1.1$ while the two end cap calorimeters ECN (north) and ECS (south) extend the coverage up to $|\eta_{det}| < 4.2$. Each part consists of an electromagnetic part closest to the beamline followed by fine and coarse hadronic sections. In all the calorimeters, liquid argon is used as the active medium and the temperature is kept at 80 K by a cryostat.

The smallest unit of each DØ calorimeter are cells. A cell consists of layers of absorber material within the active medium (liquid argon). In the electromagnetic section, nearly depleted uranium plates with thickness of 3 mm (CC) and 4 mm (EC) are used. The fine hadronic section is equipped with 6 mm uranium-niobium alloy, whereas 46.4 mm thick copper plates are used in the central coarse hadronic calorimeter. In the endcap part of the coarse hadronic calorimeter, stainless steel plates are used.

Figure 4.8 shows a typical calorimeter cell. The electromagnetic showers develop in the compact material of the absorber plates. The charged particles in the shower ionize the liquid argon in the gaps between the plates. The amount of ionization is proportional to the energy of the shower and is collected on copper electrodes which are set on positive high voltage relative to the grounded absorber plates. The typical drift time for electrons across the gap is 450 ns.

Figure 4.9 shows schematically the transverse and longitudinal pattern of readout cells. The centers of the cells are arranged on rays projecting from the center of the interaction region but with the cell boundaries and the absorber plates aligned with the cryostat borders. The cell boundaries lead to small non-sensitive regions in each layer. These regions are referred to as $\phi-$cracks. The dimension of a cell is typically 0.1 in η and in ϕ except in layer 3. The size increases for $\eta > 3.2$ to avoid very small absolute cell sizes.

The EM part of the central calorimeter has four cylindrical floors (EM1-4). At $\eta_{det} = 0$ this corresponds to 2+2+7+10 radiation lengths. The granularity of the cells of the third electromagnetic layer (EM3) is doubled in both η and ϕ because this is where the maximal energy deposition of the electromagnetic shower is expected.

The energy in the calorimeter is measured by integrating the charge produced in the liquid argon because the signal is proportional to the deposited energy, E. The count follows Poisson statistics and the relative resolution of the energy measurement goes as

$$\frac{\Delta E}{E} \sim \frac{\Delta n}{n} = \frac{1}{\sqrt{n}} \sim \frac{1}{\sqrt{E}}. \tag{4.5}$$

When contributions from calibration C, sampling fluctuations S, and noise N, are taken into account, Equation 4.5 modifies to

$$\left(\frac{\Delta E}{E}\right)^2 = C^2 + \frac{S^2}{E} + \frac{N^2}{E^2}. \tag{4.6}$$

The terms C, S and N can be briefly described as follows:

- Calibration term: $\Delta E/E \propto C$
  This term takes uncertainties from calibration, non-uniformities and non-linearities of the calorimeter devices into account. The resolution at high energies is limited by this contribution.
- Sampling term: $\Delta E/E \propto 1/\sqrt{E}$
  This term describes fluctuations in the energy deposition because the basic phenomena in showers are statistical processes. The accuracy of a calorimeter is intrinsically limited, but improves with energy.
- Noise term: $\Delta E/E \propto 1/E$
  The last term does not depend on energy and is due to instrumental efffects, like uranium noise or pedestal subtraction. This term dominates at low energies.

The values of C, S and N are measured in data and are listed in Table 4.1. Table 4.2 gives the energy resolution for electrons, photons and jets in the central calorimeter.

Table 4.1.: Energy resolution parameters (see Eq. 4.6) for the central calorimeter measured from data [43, 44].

Particle	C	S	N
e/γ	0.041	0.15 $\sqrt{GeV}$	0.29 GeV
jet	0.036	1.05 $\sqrt{GeV}$	2.13 GeV

Table 4.2.: Energy resolution in the central calorimeter for electrons, photons and jets with energies $E = 50$ GeV and $E = 100$ GeV [43, 44].

Particle	ΔE [GeV] ($E = 50$ GeV)	ΔE [GeV] ($E = 100$ GeV)
e/γ	2.3 (4.6%)	4.3 (4.3%)
jet	7.9 (16%)	11 (11%)

Intercryostat Region

As can be seen in Figure 4.9, there is a gap between the central and forward cryostat. This gap is used for the supply lines and cabling of the tracking system. The energy resolution in this region is degraded due to the substantial amount of unsampled material that the trajectories pass through before hitting the actual calorimeter structures. In order to add sampling to those trajectories, the massless gaps (MG) have been added within the cryostats, and the intercryostat detector (ICD) has been added between the cryostats. The massless gaps are standard calorimeter cells in front of the first layer of uranium in both the CC and the EC. The ICD covers $1.1 < |\eta| < 1.4$ and is a series of scintillating tiles. The tiles are divided into subtiles of $\Delta\eta \times \Delta\phi \approx 0.1 \times 0.1$ to match the calorimeter. The subtiles are read out and the signal sent to photo-multiplier tubes where the signal is shaped and made to be compatible to the standard calorimeter signals.

4.3.4. Muon System

In contrast to other charged particles, muons pass through the calorimeter leaving a MIP (minimum ionizing particle) signal and are detected in the muon system that surrounds the calorimeter. Hence, a muon leaves both hits in the tracking system and in the muon system. The muon system identifies muons, triggers on them and measures their momenta and charge from the curvature of their trajectories in the field of the toroid magnets.

The muon spectrometer is the outermost part of the DØ detector. It consists of 3 layers (from innermost to outmost: A, B and C) with an iron toroid magnet between layer A and B. The toroid surrounds the calorimeter at a radial distance of 3.18 m $< r <$ 4.27 m in the central parts and 4.54 m $< r <$ 6.10 m in the forward region. The toroid sets up an internal magnetic field of 1.8 T to allow for momentum measurements in the muon system.

The muon system consists of two parts. The central part (wide angle muon system, WAMUS) covers the range $|\eta| < 1$. The forward angle muon system (FAMUS) extends the coverage up to $|\eta| < 2$. Each part is composed of scintillators for fast triggering and timing measurements and of proportional drift tubes (PDTs) or mini drift tubes (MDTs) for precise position measurements.

The muon detectors can be seen in Figures 4.10 and 4.11.

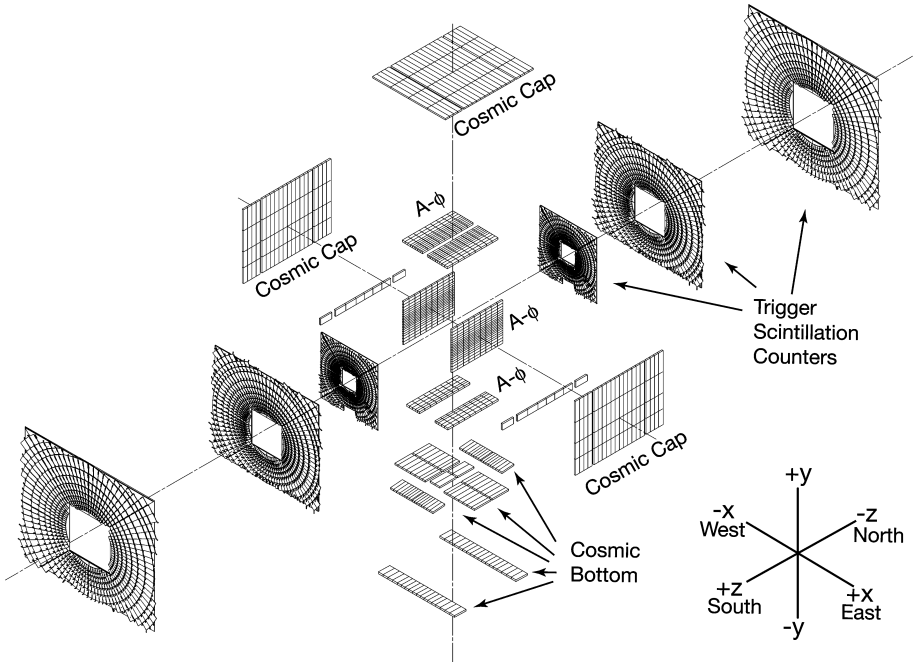

Figure 4.10.: The muon scintillation detectors.

Central Muon Detector

In the central muon system, proportional drift tubes (PDT) are used. The PDTs are typically 2.8×5.6 m^2 in cross section. A single drift cell is 10.1×5.5 cm^2. The gas mixture used in

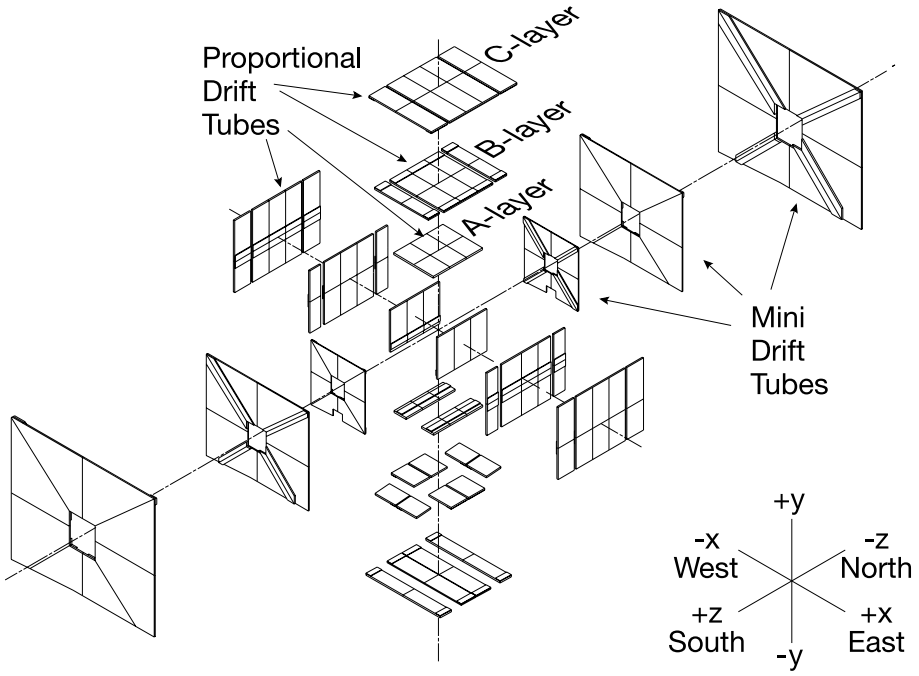

Figure 4.11.: The muon drift chambers.

the PDTs consists of 84% argon, 8% methane and 8% CF_4. This allows for a drift velocity of ≈ 10 cm/μs and a maximum drift time of about 500 ns. Each drift tube has an anode wire at the center, parallel to the field lines of the torodial magnet. To provide hit information along the wire, cathode pads are located above and below the wire. At the bottom of the detector ($4.25 < \phi < 5.15$), the muon system is only partially instrumented to give space to the support structure of the detector. The scintillation counters on the A layer PDTs are called $A\phi$ scintillation counters. Cosmic caps are mounted on the outside of layer C, except in the bottom region where they are partially mounted on layer B.

Forward Muon Detector

In the forward region, mini drift tubes (MDT) are used. The MDTs have short electron drift time, high segmentation and radiation hardness. Each MDT consists of eight cells, each with a cross section of 9.4×9.4 mm^2. The gas mixture is 90% CF_4 and 10% CH_4. The tubes are mounted along the magnetic field lines and contain a gold plated, grounded wolfram anode wire. The trigger scintillation counters in the forward system cover all three layers and are arranged in an $r - \phi$ geometry. As in the central system, the scintillation counters are used for triggering, whereas the MDTs are used for both triggering and coordinate measurements.

4.3.5. The Luminosity Monitor

The luminosity monitor (LM) measures the rate of inelastic $p\bar{p}$ in order to determine the Tevatron luminosity at the DØ interaction region [41, 45]. It also measures beam halo rates, makes a

fast measurement of the z position of the interaction vertex and identifies beam crossings with multiple $p\bar{p}$ interactions.

The LM detector consists of two arrays of 24 plastic scintillation counters that are read out with photomultipliers (PMT). Figure 4.12 shows a schematic view of one array of the LM. The arrays are located at $z = \pm 140$ cm, in front of the end calorimeter. The counters are 15 cm long and the η-range is $2.7 < |\eta_{det}| < 4.4$.

The instantaneous luminosity $\mathcal{L}$ is determined by measuring the rate of inelastic $p\bar{p}$ collisions with the LM detector:

$$\mathcal{L} = \frac{1}{\epsilon \times A \times \sigma_{p\bar{p}}} \frac{dN}{dt}(p\bar{p}), \tag{4.7}$$

where A is the acceptance and ϵ is the efficiency of the LM detector, and $\sigma_{p\bar{p}}$ is the inelastic cross section. To distinguish $p\bar{p}$ interactions from background from beam halo, precise time-of-flight measurements are made. Beam halo particles traveling along the beamline will have $z \approx \pm 140$ cm and can be cut out by requiring $|z| <$100 cm. The z coordinate of the vertex is estimated from the difference in time-of-flight for the two LM detectors.

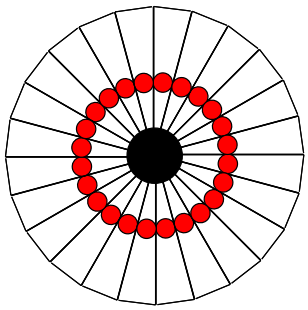

Figure 4.12.: Schematic view of the luminosity monitors. The filled circles are the PMTs.

The fundamental unit of time when measuring the luminosity is a luminosity block. Each block has its own luminosity block number (LBN). The LBN is increased at least every 60 seconds, which is sufficiently small for the instantaneous luminosity to be constant within one LBN.

4.3.6. Trigger and Data Acquisition

Most $p\bar{p}$ reactions are soft collisions of minor interest and a sophisticated trigger system is necessary to reduce the data flow and to select the interesting physics events. The rates need to be reduced from approximately 2 MHz to a recordable rate of 50-100 Hz. The trigger system is built up of three levels. Each level reduces the number of events and also examines the events in greater detail and with more complexity. A schematic view of the DØ trigger and data acquisition system is shown in Figure 4.13 and a more detailed disussion of the trigger framework is given in [41].

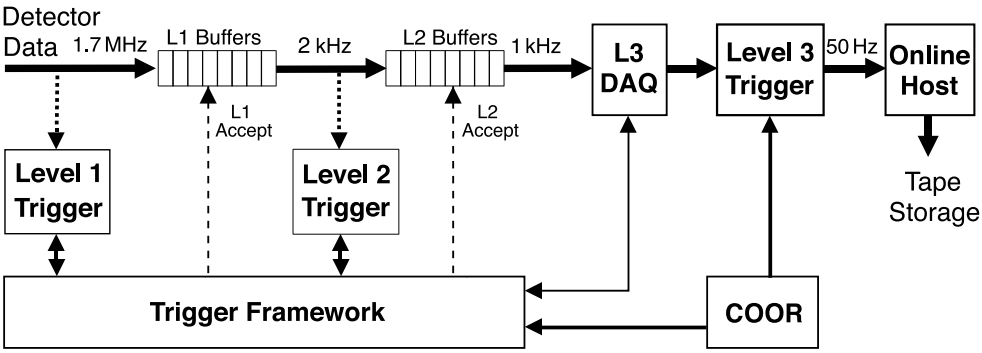

Figure 4.13.: The DØ trigger and data acquisition system. The rates are typical for RunIIa.

Level 1

The Level-1 (L1) trigger decision is based on hardware and provides nearly dead-time free trigger decisions within 3.5μs. The resulting reduction of the rate is from 1.7 MHz to 1.6 kHz in RunIIa and to 1.8 kHz in RunIIb. The following detector systems are used as input to the L1 trigger: calorimeter system (L1CAL), central/forward preshower detectors and central fiber tracker (central track trigger, L1CTT), muon system (L1MUO) and the forward proton detector (L1FPD). The L1CAL, L1CTT and L1MUO systems are the most important ones for analyses presented in this thesis and will be briefly described.

The L1CAL receives fast analog signals from the calorimeter system. The trigger objects are the summed transverse energy depositions within the electromagnetic or all layers of $\Delta\eta \times \Delta\phi = 0.2 \times 0.2$ calorimeter towers. In RunIIb, sliding window algorithms are used to maximize the transverse energy seen in the window (see below). In total there are 1280 electromagnetic and 1280 hadronic trigger towers: 40 slices in η covering $|\eta|$ <4 and 32 slices in ϕ covering the full azimuth. Jets are identified by using the total transverse energy, while electromagnetic objects are identified by using the EM layers only.

The L1CTT system provides fast trigger decisions for charged particles with $p_T > 1.5$ GeV. The decision is made by reconstructing tracks in the CFT. The fiber hits of the CFT are compared to approximately 20,000 predefined track equations using combinatorial logic in field programmable gate arrays (FPGA). It also stores sorted lists of tracks which are used as seeds by other trigger systems like L1MUO.

The L1MUO system uses hits from the wire chambers, muon scintillation counters and tracks from the L1CTT to make its decision. L1MUO uses FPGAs to perform combinatorial logic on approximately 60,000 muon channel and up to 480 tracks from the L1CTT per bunch crossing.

Level 2

The Level-2 (L2) trigger has two stages. The first stage consists of preprocessors for each detector subsystem working in parallel, the second stage is a global processor (L2Global) for

integration of the data. In the preprocessor stage, the information from the subsystems is collected separately to form objects such as tracks or energy clusters. The subsystems included are calorimeters, preshower detectors, CFT, SMT and muon system. All the information is combined at the global-processor stage to form physical objects such as electron candidates. Based on this information the trigger decision is made. L2 has a dead time of 5% at the highest data rates, requires less than 100μs for a decision, and reduces the data rate to 800Hz.

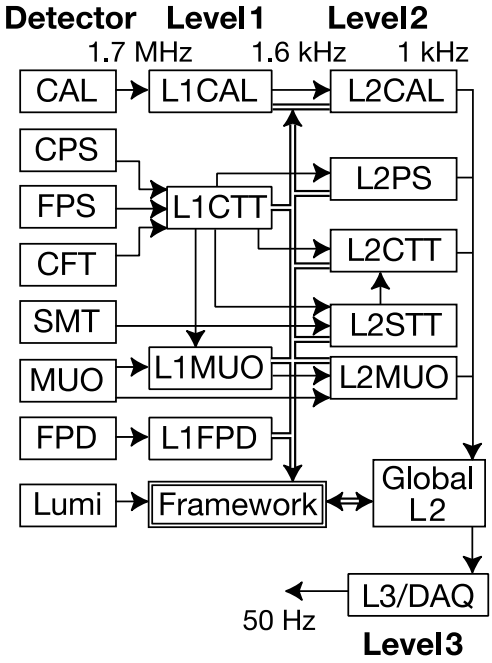

Figure 4.14.: Schematic view of the three levels of the DØ trigger system.

Level 3

At Level 3 (L3) a simplified reconstruction of the entire event is made on farm nodes. This reduces the data rate to the desired 100 Hz in RunIIb, which can be written to tape for offline analysis. The average event size is $\approx$ 250 kBytes.

The L3 tracking is based on CFT and SMT information. A global (SMT plus CFT) high-momentum-track finder starts from axial CFT tracks and propagates back to the SMT using a linear fit in $r-\phi$. Also the primary vertex is determined using CFT tracks. The L3 muon tools allow to identify muon tracks in three dimensions. A track match tool extrapolates the muon track to the central tracker allowing for an efficient matching between objects in both subdetectors. The L3 jet tools implement a simple cone algorithm, which relies on the high-precision calorimeter readout and primary vertex position. The L3 electron tools are based on a simple ΔR <0.25 jet cone, with additional requirements on the minimum electromagnetic fraction and the transverse shower shape.

Data Acquisition System

The data acquisition system consists of the L3DAQ and the online host system. L3DAQ transports detector component data stored in the readout crates to the processing nodes of the L3 trigger filtering farm. The online host system receives event data from the L3 farm nodes and distributes that data to logging and monitoring. The final repository for the raw event data is tape, maintained in a robotic tape system.

RunIIb Trigger Upgrade

The increase in instantaneous luminosity in RunIIb required a set of upgrades of the DØ trigger system [46]. The following trigger subsystems were upgraded:

- L1 calorimeter trigger (L1CAL),
- L1 central track trigger (L1CTT),
- new L1 system to match energy clusters in the calorimeter with tracks (Cal-TRK),
- L2 processors,
- L2 silicon track trigger (STT).

The L1 calorimeter trigger upgrade and the new Cal-TRK system will be briefly described below.

For the L1 calorimeter trigger, two major improvements took place. The first one was to introduce digital filters on the signals from the trigger towers to improve rejection of pileup effects and reduce the probability of triggering on the incorrect beamcrossing. The second improvement was to introduce sliding window algorithms of the trigger towers. Instead of single 0.2×0.2 trigger towers, sliding window algorithms aims to find the optimum region of the calorimeter for inclusion of energy from jets or EM objects by moving a window grid across the calorimeter η, ϕ space to maximize the transverse energy seen in each window. In addition, isolation requirements can be imposed on the calorimeter clusters.

To exploit matches in the azimuthal position of tracks from the L1CTT trigger with the position of EM and jet objects from the L1CAL trigger, the L1 Cal-TRK system was developed to reduce the L1 trigger rates of the EM and track triggers. Large rejection is also possible by matching the track triggers with calorimeter towers of modest energy. This is important in triggering on hadronic τ decays such as in $H \to \tau\tau$.

5. Phenomenology of $p\bar{p}$ Collisions

In the following chapter, a brief overview of the terminology common to hadron collider physics will be given. Also the event generation and detector simulation chain will be presented.

5.1. General Aspects

Protons and antiprotons are made of gluons and quarks (so called partons) and hence belong to the group of particles called hadrons. Hadrons consist of valence quarks, which determine the quantum numbers of the hadron, and sea quarks and gluons which do not contribute to their quantum numbers.

A high energetic collision between a proton and an antiproton is actually an interaction of the partons. The majority of the $p\bar{p}$ interactions are large-distance, or soft, collisions where the momentum transfer is small. Collisions with large momentum transfer are called hard scattering and these collisions result in particles with large transverse momentum (see below).

The longitudinal parton momentum inside an accelerated proton is not known while the transverse momentum should be close to zero. Partons that do not take part in the hard scattering, carry a significant amount of the energy of the hadrons and their interaction form the underlying event. As a consequence, the final state objects after a collision are characterized not by the momentum $\vec{p}$, but the projection of the momentum onto the transeverse plane, p_T, the transverse momentum.

The total number N of events of a certain process which are recorded, is given by the formula

$$N = \sigma L \epsilon \tag{5.1}$$

where σ is the cross section of the process, L is the integrated luminosity ($L = \int \mathcal{L} dt$) and ϵ is the efficiency to record this process.

The effective center of mass energy is also smaller than the center of mass energy of the machine ($\sqrt{s} = 1.96$ TeV) since the colliding particles are composite objects. The effective center of mass energy, $\sqrt{\hat{s}}$, is given by

$$\sqrt{\hat{s}} = \sqrt{x_1 x_2 s} \tag{5.2}$$

where x_1 and x_2 are the fractions of the proton/antiproton momentum carried by the two colliding partons.

In addition, the following processes are important:

- Initial State Raditation (ISR): This term describes the emission of for example a gluon or a photon from the incoming partons. ISR leads to corrections to the cross section and to the event topology.
- Final State Radiation (FSR): This term refers to the emission of a gluon or a photon from the outgoing partons. It leads to the same kind of corrections as ISR.
- Beam remnants: Only a part of the momentum of the colliding proton or antiproton is carried by the parton that participates in the hard scattering. The remaining momentum is carried by the beam remnant, which is not color neutral and can affect the event topology.
- Minimum bias events: A bunch crossing results in multiple soft inelastic interactions. This type of events is called minimum bias events. Its rate depend strongly on the instantaneous luminosity and the cross section for these kind of events is several orders of magnitude larger than the cross sections of interest, as can be seen in Figure 5.2. In the RunIIa data used in this thesis, the average number of minimum bias events was approximately two. Since the upgrade between RunIIa and RunIIb resulted in higher instantaneous luminosity, the average number of minimum bias events is higher in RunIIb (approximately 2.5).
- Pile-up: If detector components are not fast enough to resolve individual interactions, the current bunch crossing is overlaid by signals from the previous bunch crossing. For example, the calorimeter readout electronics is affected by pile-up since the shaping time is longer than the bunch spacing time.

The term underlying event means all procsses that take place in addition to the hard scattering. It refers to minimum bias events, beam remnants and possible interactions of the beam remnants [47].

5.1.1. Cross Section

Figure 5.1 shows a Feynman graph of one of the most important backgrounds in the analyses discussed in this thesis: the leading order contribution of the Drell-Yan production of leptons in a $p\bar{p}$ collider. The hard scattering process consists of the annihilation of a quark and an antiquark into a lepton pair $q\bar{q} \to \ell\ell$. The remaining hadron remnants fragment into hadrons.

The leading order cross section for this process is given by:

$$\frac{d\sigma}{dQ^2} = \sum_{q,\bar{q}} \int dx_1 \int dx_2 [f_q(x_1, Q^2) f_{\bar{q}}(x_2, Q^2) + f_{\bar{q}}(x_1, Q^2) f_q(x_2, Q^2)] \frac{d\hat{\sigma}}{dQ^2} \tag{5.3}$$

where $\hat{\sigma}$ is the cross section for the process $q\bar{q} \to \ell\ell$, Q^2 is the 4-momentum exchanged in the interaction and f_q and $f_{\bar{q}}$ are the parton distribution functions (PDFs(5.1.2)) for the quark and

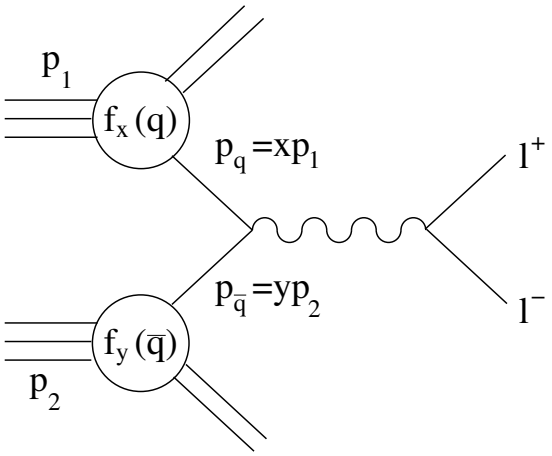

Figure 5.1.: Schematic view of a proton anti-proton interaction $p\bar{p} \rightarrow \ell\ell$X.

the antiquark.

Figure 5.2 shows the cross sections for selected processes at the Tevatron. The total inelastic cross section is approximately 70 mb which is three orders of magnitude larger than the dijet cross sections. The dijet cross section is in turn at least four orders of magnitude larger than the cross section of the physic processes of interest. A typical cross section for the production of SUSY particles is eight orders of magnitude lower than the dijet cross section.

5.1.2. Factorization and Parton Distribution Functions

Cross sections for processes involving strong interactions can be factorized into a short distance (hard) part and a long distance (soft) part. The hard part is calculable with perturbative QCD while the soft part is not. However, while the hard part depends on the particular process, the soft part is universal and measurable. Parton distribution functions (see next paragraph) describe the perturbative component in the initial state of the hadronic interactions, while the soft component in the formation of hadronic final states is described by fragmentation functions. A factorization scale μ_f is introduced which characterizes the boundary between the two energy regimes and is usually chosen at the order of the scale, Q, of the hard interaction.

The PDFs, $f_i(x, Q^2)$, parametrize the momentum fraction of the partons in the protons and need to be known in order to correctly simulate the interaction between the partons. The quantity $f_i(x, Q^2)$ is the probability that a parton of type i carries a momentum fraction between x and $x + dx$ of the momentum of the hadron, and it depends on the 4-momentum exchanged in the interaction Q^2.

Fig 5.3 shows a parameterization of the PDFs of valence quarks, gluons and sea quarks that the CTEQ [48] group provides. The plot is made for a typical Q^2 region for the processes of interest at the Tevatron. The charged partons carry approximately half of the total proton momentum while the other half of the momentum is carried by the large number of gluons. Sea quarks typically carry only a small momentum fraction.

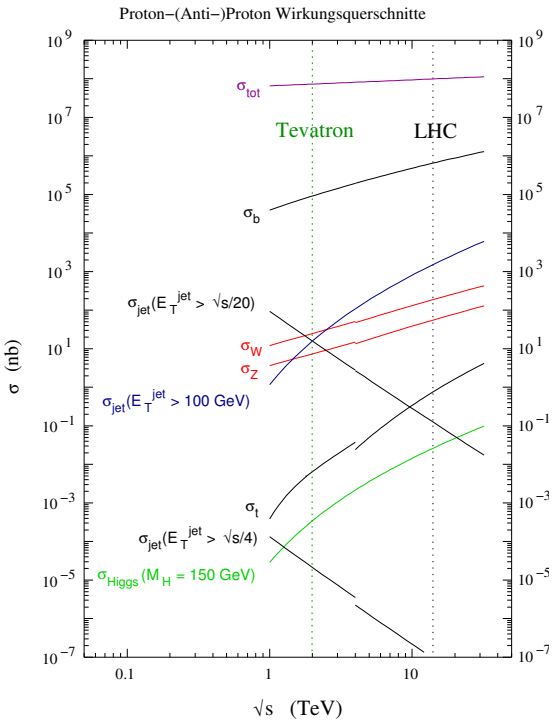

Figure 5.2.: Cross section for certain processes for proton-(anti)proton collisions as a function of center of mass energy.

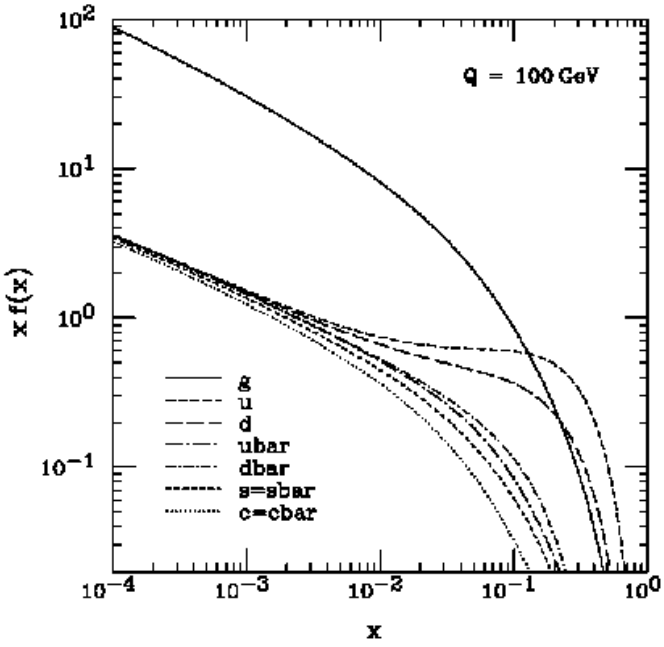

Figure 5.3.: Parton distribution function of the proton as calculated for $Q^2 = 10^4$ using CTEQ6 provided by the CTEQ group [48].

5.1.3. K–factors

In the previous section, only the leading order cross section was discussed. Next-to-leading order (NLO) contributions lead to corrections to this cross section. The higher order contributions consist of virtual corrections and emission of real particles. In a full NLO calculation, the singularities from virtual corrections and the soft and collinear singularities of the real emission cancel by negative interference such that the cross section receives a finite correction. This applies to all orders of perturbation theory. Figure 5.4(a) shows the Feynman diagram for the leading order process $\gamma \rightarrow q\bar{q}$, while (b) and (c) show the real NLO contributions to this process. The interference of processes (d)-(f) with the leading order process also give contributions of order α_s.

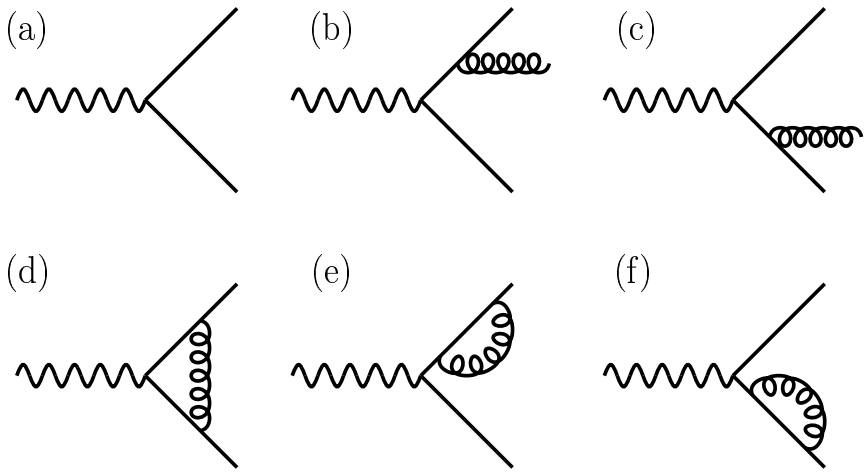

Figure 5.4.: : (a) Feynman diagram of leading order contribution to $\gamma \rightarrow q\bar{q}$. The diagrams (b) and (c) give contributions of the order α_s. This is also the case with the interference of terms (d)-(f) with (a).

NLO cross section have been calculated for most of the processes at hadron colliders. Next-to-next-to leading order (NNLO) calculations, however, have only been calculated for a smaller number of processes.Higher order corrections change the total cross section, and also change the kinematic and angular distributions in the final state. The effects are, however, often small compared to the accuracy of the experiments and it is sufficient to correct the total cross section with a factor and simulate the kinematic and angular distributions of the process at LO and use approximations for higher order effects on the topology. The correction to the LO cross section is called K–factor:

$$K_{NLO} = \frac{\sigma_{NLO}}{\sigma_{LO}}. \tag{5.4}$$

5.2. Event Simulation

Monte Carlo (MC) generators are necessary in order to study the complex processes of proton collisions. It is difficult to make a direct comparison of the theoretical predictions and the experimental results. A detailed and precise event simulation is necessary to address this problem.

The procedure starts with generating the 4-vectors of the final products expected from the interaction of interest, using Monte Carlo techniques to select the relevant variables according to the predicted probability distributions. The next step is to process the generated event through a detector simulation. The output of the detector simulation is called MC events in the following.

5.2.1. Event Generation

Most of the signal and background events that are used in the analyses described in this thesis are generated using the PYTHIA [49] event generator. PYTHIA is a multi-purpose high-energy particle collision simulator that can simulate e^+e^-, pp, $p\bar{p}$ and ep collisions. All Standard Model processes resulting from these collisions can be simulated, and also processes from new physics can be generated. For most of the processes LO matrix elements are used. The leading order calculations of the hard subprocess are supplemented by parton showering. In addition, PYTHIA performs the hadronization of colored partons into colorless hadrons. Both the modeling of initial/final state radiation and the fragmentation/hadronization processes will be discussed in the next sections.

For $W + \gamma$/jet background, the MC generator ALPGEN [50] is used. ALPGEN calculates the full matrix element at leading order but the parton showering and fragmentation is done by PYTHIA. This will be discussed in more detail in 7.2.1.

5.2.2. Modeling of ISR and FSR

ISR and FSR was introduced at the beginning of this chapter. ISR and FSR are taken into account by PYTHIA using the parton shower method. This method approximates the effects from ISR and FSR in a probabilistic approach by an evolution in a series of branchings of a mother parton into two daughter partons. The momentum fractions of the two daughter partons are z and $1-z$. The branching is described by the Altarelli-Parisi splitting functions, $P(z)$ [51]. Starting from the energy scale of the hard interaction Q^2_{max}, the evolution of the branchings is either performed forward (for FSR) or backwards (for ISR). The shower evolution is cut off at some lower scale $Q_0 \approx 1$ GeV. The parton shower method describes well the raditation of collinear and soft partons, but has limited predictive power for the emission of hard and wide angel partons.

As stated in 5.2.1, ALPGEN calculates the matrix element at leading order, but uses PYTHIA for the parton showering and fragmentation. Since extra jets in an event can be calculated explicitly by Feynman diagrams or created by the parton shower, double counting of jets can occur in determining the $X + n$ jets cross section, wher X is an arbitrary final state and n

denotes the inclusive jet multiplicity. ALPGEN uses the so-called MLM-matching to address this problem. Samples for each exclusive parton multiplicity are generated separately. The parton shower is then simulated, and jets are matched to initial partons. If the parton multiplicity does not match the jet multiplicity, the event will be rejected.

5.2.3. Fragmentation

As stated before perturbative QCD is only valid at short distances, while the perturbation theory breaks down at long distances. In the confinement regime, the colored partons are transformed into colorless hadrons. This process is called fragmentation or hadronization.

The fragmentation of partons into hadrons cannot be calculated and is described in analogy to the description of the partonic structure of the proton: fragmentation functions give the probability that a quark produces a hadron with a fraction of the quark energy. These fragmentation functions have been measured at LEP. The most successful theoretical approach in describing fragmentation is the string fragmentation [52]. In this model the confinement is represented by a string with a certain energy density between the partons that are moving apart. Quark antiquark pairs are created along the string in such a way that the string breaks up into hadrons. The resulting products are stable and instable hadrons. The decay of instable hadrons is simulated using decay matrix elements or results of measurements. PYTHIA uses the Lund string fragmentation model [53] implemented in the program JETSET.

5.2.4. Detector Simulation

The particles produced by the MC generator are passed through the detector simulation handled by the programs DØGSTAR [54] and DØSIM [55] in the DØ software versions p18 and p21.

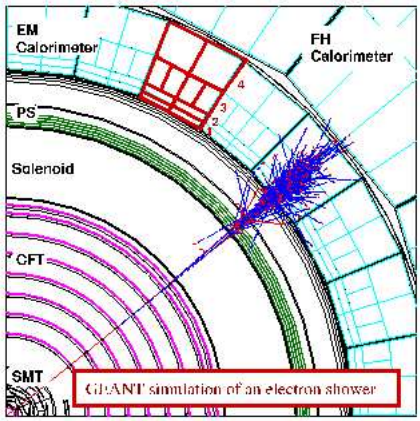

Figure 5.5.: GEANT simulation of an electron in the DØ detector.

The DØGSTAR program runs GEANT [56], a software tool that simulates the interaction of particles with the detector material. It also models the decay of long-lived particles in the detector.

This stage is the most timeconsuming part of the simulation, since the software has to model the particle interactions in great detail, including the ionization in the silicon detector and in the scintillating fibers, the development of electromagnetic and hadronic showers, interactions with the material of the superconducting coil and the border of the cryostats. Figure 5.5 shows the simulation of an electron shower in the DØ detector. The DØGSTAR package also simulates the response of the readout electronics.

The DØSIM software performs the remaining steps that are necessary in order to bring the simulation data to the same level of detail as the data. DØSIM modifies the simulated events to account for various detector related effects such as detector inefficiencies, noise from the detector and electronics, analog signal shaping and digitization of the data. Zero Bias events taken from data are overlaid the Monte Carlo to simulate the effect of multiple interactions, noise and pile-up [57]. Adding zero bias events from data improves the agreement between data and Monte Carlo, as compared to a pure Monte Carlo simulation of multiple interactions. The ouput of DØSIM is in the same format as the data recorded by the data acquisition system.

The output of the detector simulation is reconstructed with the reconstruction software DØRECO [58]. The same reconstruction software is used for the reconstruction of data and MC events. DØRECO provides offline reconstruction of all physics objects used for analysis. Two types of output format are provided, data summary tier (DST) and thumbnail (TMB). The DST contains all event information required to perform any analysis while in the TMB format some information is dropped and the remaining part is compressed. The size of an event in the DST format is $\approx$ 150 kBytes per event and $\approx$ 20 kBytes per event in TMB. The TMB format is also converted into ROOT format [59] ($\approx$ 35 kBytes per event) and in the same step more information is dropped.

6. Physics Objects

In total, the collected data consists of about one million channels of output. To identify objects and to reconstruct events, one relies on a collection of algorithms. The task of these algorithms is to translate the stream of readout signals from the detector (the raw data) into basic physics objects and to provide an accurate estimate of the kinematics of the interaction.

The analyses presented in this thesis use the properties of electrons, muons, tracks, jets and missing transverse energy. The following chapter will focus on the reconstruction and identification of these objects.

6.1. Tracks

A track is identified through energy deposition (hits) in the tracker system, SMT and CFT (see section 4.3.1). Charged particles passing through the tracking system in the magnetic field leave dot-like hits on their curved path through the various layers. Both detectors can be used for tracking $|\eta_{det}| < 1.6$, while only the SMT can be used up to $|\eta_{det}| < 3.0$. Track reconstruction relies on two different algorithms: the Alternate Algorithm (AA) and the Histogram Track Finder (HTF). The result of these two algorithms are combined in the end.

The AA [74] starts from any combination of three hits in the SMT barrels or disks. The algorithm extrapolates the sequence of hits moving outwards to the next SMT or CFT layer. If a hit is found within the search window, a χ^2 test is performed and the found hit is associated with the track candidate if the χ^2 is below a predefined cut. A miss is recorded when no hit is found in the layer. The construction of track candidates ends when the last CFT layer is reached or when three misses are recorded.

The HTF [75] method relies on a histogramming method. The trajectory of a charged particle moving perpendicular to a homogeneous magnetic field can be characterized by the radius of curvature ρ, the distance of closest approach (DCA) with respect to (0,0) d_0, and the direction of the track at the point of closest approach to (0,0) ϕ. For track candidates with small impact parameters, every pair of hits in x and y that belongs to the same track corresponds to a single point in the ρ - ϕ plane. Filling each pair of this into the 2-dimensional ρ - ϕ histogram, a peak in the histogram would correspond to a track candidate.

The final list of tracks is then obtained by merging the output of both algorithms and removing duplicates. The final track list is sorted by the number of hits, fewest misses and lowest χ^2 values.

The transverse momentum of a track is calculated from the curvature of the trajectory in the magnetic field. The track momentum resolution gets worse with increasing momentum $\frac{\sigma_{p_T}}{p_T} \propto p_T$

while the energy resolution of the calorimeter improves with increasing energy $\frac{\sigma_{E_T}}{E_T}$. Hence, the calorimeter gives a more accurate measurement of the electron kinematics for the electrons in the interesting p_T range. In addition, the p_T measurement from electron tracks suffers from bremsstrahlung due to the small mass of the electron. This effect can be neglected for heavier charged particles.

6.2. Electrons

The electron identification is based on electromagnetic showers in the calorimeter and information from the tracking system [60]. The longitudinal shower profile of a shower in the calorimeter is sampled in the four electromagnetic layers EM1–EM4, and in addition the first fine hadronic layer is used to sample the tail of the shower. The shower maximum is expected in EM3 which is why this layer has a higher granularity.

The electron reconstruction software uses cell towers in the first five calorimeter layers in a ΔR <0.4 cone to form the initial calorimeter clusters. This is done by a simple cone algorithm. The algorithm defines a list of towers, ordered in E_T. The $\Delta R = \sqrt{(\Delta\phi)^2 + (\Delta\eta)^2}$ distance between unassigned towers and the seed is calculated and the unsassigned tower is added to the seed if the distance is smaller than a specified cone size. If the unassigned tower cannot be matched to the seed, it is added to the list of seed towers. After all entries in the list of seed towers are processed, the list of seeds contains the found clusters.

The energy resolution is better in the calorimeter, but angles are determined in the tracker system if the energy deposition can be matched to a track. The main background sources are neutral pions, η mesons, photons, charged pions and unusual fluctuations in the development of jets. If a track-match is required, mainly background from neutral pions, which decay into photons, which in turn decay to e^+e^- pairs, or are accompanied by a charged particle that fakes a track constitute the most important background. Also η particles which decay either to neutral pions or photons are part of the background.

To reduce background from jets, further requirements are placed on the clusters. These requirements make use of the fact that jets are broader than clusters from electrons and that jets deposit a large fraction of the energy in the hadronic part of the calorimeter. The electromagnetic clusters are assigned an ID of 10 if they have $E_T > 1.5$ GeV and the electromagnetic fraction is above 0.9. If the cluster has a track loosely matched to it, the cluster gets an ID of $\pm$ 11. Furthermore, the isolation of the cluster is required to be less than 0.2. The isolation variable is defined as

$$f_{iso} = \frac{E_{tot}(\Delta R < 0.4) - E_{EM}(\Delta R < 0.2)}{E_{EM}(\Delta R < 0.2)} < 0.2. \tag{6.1}$$

where $E_{tot}(\Delta R < 0.4)$ and $E_{EM}(\Delta R < 0.2)$ denote the total energy and electromagnetic energy within a cone of radius 0.4 and 0.2, respectively Electromagnetic clusters that fulfill these requirements are called EM candidates. The energy of the EM candidate corresponds to the sum of the energy deposition in all five layers.

Requiring a track match with the cluster is a good discriminant against photons. There are two different ways to define a track match. The first one is called spatial track match, while the second one is called track match with E/p. The two approaches are described in the following.

Spatial Track Match

To find candidate tracks, the track algorithm (see section 6.1) searches in a window $\Delta R = \sqrt{(\Delta\phi)^2 + (\Delta\eta)^2} < 0.1$ around the calorimeter cluster center. The ϕ and η coordinates of the candidate tracks are extrapolated into the calorimeter performing this match. The spatial track match uses the difference of the z position and the azimuthal angle ϕ of track and cluster axis to calculate a χ^2:

$$\chi^2_{spatial} = \left(\frac{\Delta\phi}{\sigma_\phi}\right)^2 + \left(\frac{\Delta z}{\sigma_z}\right)^2. \tag{6.2}$$

The σ_z and σ_φ are the root mean squares of the experimental distributions of the quantities. To define the quality of the track match the probability for a track to have a certain χ^2, $P(\chi^2)$, is used. The track with highest χ^2 probability is selected as the electron track.

Track Match with E/p

Track match with E/p uses the same approach as spatial track match. Again, the algorithm searches for candidate tracks in a cone with $\Delta R = \sqrt{(\Delta\phi)^2 + (\Delta\eta)^2} < 0.1$ around the center of the calorimeter cluster. Since the track momentum is expected to match the measurement of the transverse energy in the calorimeter, the χ^2 has an additional term:

$$\chi^2_{trackmatch} = \left(\frac{\Delta\phi}{\sigma_\phi}\right)^2 + \left(\frac{\Delta z}{\sigma_z}\right)^2 + \left(\frac{E_T/p_T - 1}{\sigma_{E_T/p_T}}\right)^2, \tag{6.3}$$

The extra term uses the ratio of the track momentum p_T and transverse energy of the calorimeter cluster E_T. The drawback of using this track match is the worse momentum resolution of the tracking system for large p_T and in the forward direction, and bremsstrahlung which results in long tails in the E_T/p_T distribution.

6.2.1. HMatrix

An important calorimeter variable for electron identification is the HMatrix ($HMx7$) [62]. The purpose of the HMatrix is to determine if the shower in the calorimeter is consistent with a shower from an electron or is more consistent with shower from a jet. This is done using a covariance matrix. Given N EM candidates, the covariance matrix is defined as

$$M_{ij} = 1/N \sum_{n=1}^{N} (x_i^n - \bar{x}_i)(x_j^n - \bar{x}_j) \; i,j = 1,..,7 \tag{6.4}$$

where x_i^n is the value of the variable i for particle n and $\bar{x}_i^n$ is the mean. The inverse of the covariance matrix, is called the HMatrix. The χ^2 is calculated comparing the variables measured in data with the mean values derived from Monte Carlo electrons:

$$HMx7\ \chi^2 = \sum_{ij}^{7} (x_i^{data} - \bar{x}_i^{MC}) M_{ij}^{-1} (x_j^{data} - \bar{x}_j^{MC}). \tag{6.5}$$

The seven input variables to the HMatrix

- energy fractions in the four EM layers
- logarithm of the total energy
- vertex position
- transverse shower width in ϕ direction in the third EM layer.

6.2.2. Electron Likelihood

An electron likelihood is constructed to reject jets that fake electrons and electrons that are the result of a conversion [61]. The electron likelihood combines several quantities measured in the calorimeter and in the tracker and is defined as follows:

$$L = \frac{P_{sig(x)}}{P_{sig}(x) + P_{bkg}(x)} \tag{6.6}$$

where $P_{sig}(x) = \Pi_i P_{sig,i}(x_i)$ and $P_{bkg}(x) = \Pi_i P_{bkg,i}(x_i)$, that is, the probability for signal and background are the product of the probabilities for the individual quantities that enter the likelihood. The input variables for the likelihood calculation are:

- EM fraction of the electron candidate:
  Neutral pions are produced in association with other charged hadrons. Hence the electromagnetic fraction of the calorimeter cluster is lower because of significant hadronic energy from the surrounding hadrons.
- shower shape $HMx7\ \chi^2$:
  The HMatrix uses the distinct shower profile of an electron/photon to distinguish them from jets (see discussion above).
- number of tracks in a 0.05 cone around the electron candidate track (including the candidate):
  This variable is meant to supress fake electrons from photon conversions where at least one additional track is expected close to the electron.
- the χ^2 probability of the spatial match of the electron track:
  Neutral pions have to overlap a track from charged hadrons in order to fake an electron, hence their track matching can be poor.

- the p_T sum of all tracks in a 0.4 cone excluding the electron track:
  When a π^0 is produced in association with charged hadrons, additional tracks that are present around are likely to have larger p_T. For isolated electrons, no other tracks are expected, and the p_T sum of the tracks is small.

- the distance of closest approach (DCA):
  DCA measures the shortest distance of a track to the line parallel to the z-axis which passes through the primary vertex

- E_T/p_T:
  The calorimeter quantities of photon conversions are nearly identical to that of an electron, though they might be slightly wider than an electron shower. However, photon conversions are marked by the presence of a second track close to the electron track and larger values of E_T/p_T.

In Figures 6.1 and 6.2 some of the input distributions to the likelihood are shown. In these plots black is signal and red is background. The signal sample is a $Z \rightarrow ee$ sample and the background sample is a dijet sample where one jet fakes an electron. In the signal sample, two electrons with p_T >15 GeV are required and the invariant mass, $M(e,e)$, is required to be between 80 GeV and 100 GeV. In the background sample, exactly one electron with p_T >15 GeV is required. In addition, at between one and five jets required and the leading jet must fulfill p_T >25 GeV. In Figure 6.3 the likelihood distributions for signal and background are presented in linear and in logarithmic scale.

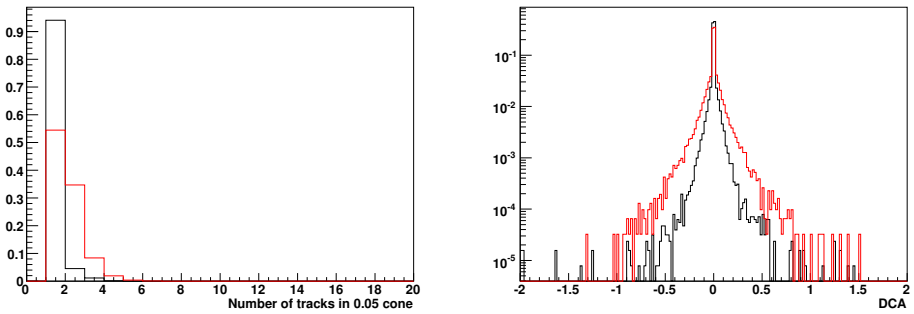

Figure 6.1.: Two of the input variables to the likelihood. Left is number of tracks in a 0.05 cone and right is distance of closest approach. Black histogram is signal, red histogram is background. All histograms are normalized to unit area.

EM candidates with a likelihood value that exceeds 0.2 are called loose electrons. If the likelihood exceeds 0.8, the electrons are refered to as tight electrons. Figure 6.4 shows the reconstruction efficiency as a funtion of p_T and η_{det} as measured in $Z \rightarrow ee$ events in data and Monte Carlo [63]. A study of the jet to electron fake rate was done in [64]. The jet to electron fake rate was determined defining a di-jet ($p_T > 15$ GeV) sample. The efficiency was obtained by determining how often a jet fakes an electron with likelihood > 0.2 and $p_T > 15$ GeV. The fakerate as a function of electron p_T and electron η_{det} are shown in Figure 6.5. It should be noted that in [64] the fake rate was determined including electrons from the ICD region ($1.1 < |\eta_{det}| < 1.4$) with degrated electron identification, while this is not the case for Figure 6.4.

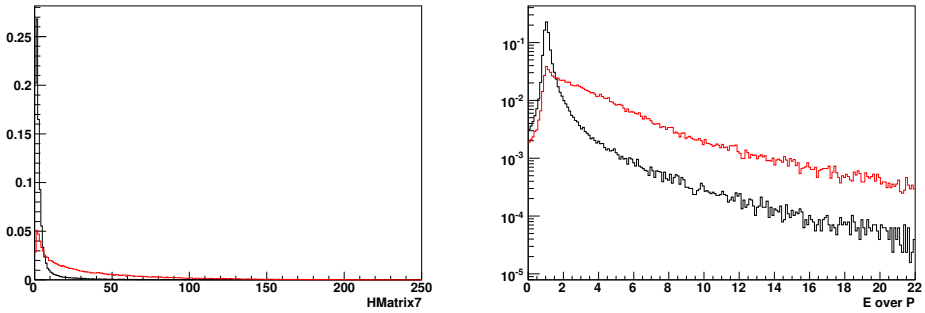

Figure 6.2.: Two of the input variables to the likelihood. Left is HMatrix and right is E_T/p_T. Black histogram is signal, red histogram is background. All histograms are normalized to unit area.

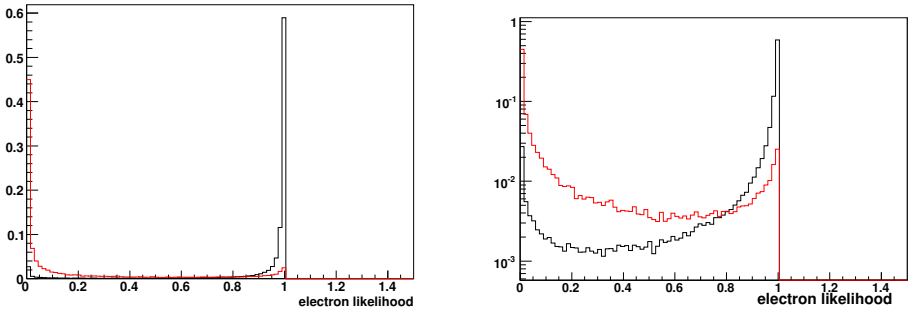

Figure 6.3.: Left is shown the electron likelihood for signal (black) and background (red). Both histograms are normalized to unit area. Right is the same in logarithmic scale on the y-axis.

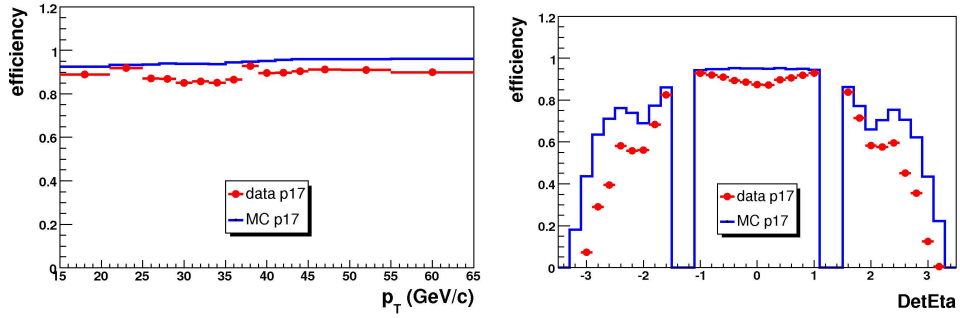

Figure 6.4.: Reconstruction efficiency in data and Monte Carlo as a function of p_T (left) and η_{det} (right) as measured in $Z \rightarrow ee$ events [63].

6.3. Muons

Muons are reconstructed using information from the muon system and the inner tracking system [65]. In order to determine the quality of a muon, three types of requirement are defined:

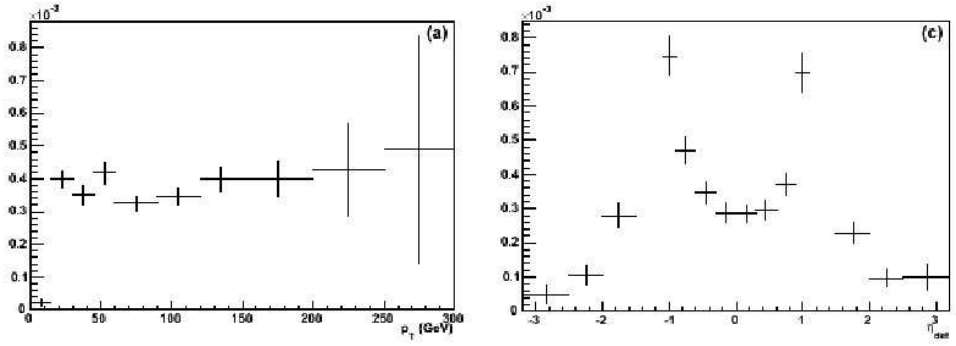

Figure 6.5.: Jet to electron fake rate as a function of p_T (left) and η_{det} (right). The jet and electron are required to have p_T >15 GeV and the electron to have a likelihood value greater than 0.2. From [64].

muon type, muon isolation and muon track match.

Muon candidates start from local muon tracks, which are formed using hits in the muon system layers. Based on hits in the muon systems, local muons are defined. The number of hits in the different layers determines the muon type.

The local muon is then matched to a track from the inner tracking system, taking into account the magnetic fields of the solenoid and the toroid. If there is a match, the muon candidate is classified as central track-matched muon. The momentum resolution of the tracking system is better than the resolution obtained in the muon system, so the former is used to determine the muon p_T. In addition, the calorimeter can be used to confirm the presence of a muon, since a muon deposits a relatively small amount of energy in the calorimeter.

The parameter nseg determines the type of muon. A positive value of nseg indicates that the local muon was matched to a track in the central tracking system. If the local muon could not be matched to a central track, it gets a negative nseg value. The absolute value |nseg|=1, 2 or 3 indicates that the local muon is made up of A-layer only hits, B or C-layer only hits (outside the toroid), or A- and B- and C-layers hits.

The quality criteria used for the muons considered in the $\mu\mu\ell$ analysis are the following:

- The muon candidate is required to be of type |nseg|=3, which means it has to have hits in all three layers of the muon system, the inner A layer and the outer B and C layers beyond the toroid.
- "Loose" muon quality, meaning:
  - at least two wire hits in the A layer
  - at least one scintillator hit in the A layer
  - at least two wire hits in the combined BC layers
  - at least one scintillator hit in the combined BC layers (except for central muons with < 4 BC wire hits).

- Timing information from the scintillator hits is used to reject background from cosmic rays. Muons from the collision traverse the muon system shortly after the time of the interaction, and the cosmic veto cut requires scintillator times t_A <10 ns and t_{BC} <10 ns following the central trigger.

Muons from heavy flavor decays ($B \rightarrow \mu$) tend to be inside a jet. To suppress this kind of background, the muons are required to be isolated. The isolation variables are either defined in terms of the track near the muon track or calorimeter energy surrounding the muon momentum vector. Muons are minimum ionizing particles in the calorimeter, therefore the energy deposited in the calorimeter cells by muons should be small. The isolation variables are defined as follows:

- TrackHalo = $|\Sigma^{tracks} p_T|$ in ΔR(track,muon track)<0.5 cone
- CalorimeterHalo = $|\Sigma^{cells} E_T|$ in 0.1 < ΔR(cal-cells,muon cal track)<0.4

If the TrackHalo is below 4 (1.5) GeV and CalorimeterHalo is below 4 (1.5) GeV the muon isolation is loose (tight).

6.4. Jet Reconstruction

Jets are identified in the calorimeter and cell towers are used as seeds [66, 67, 68]. Jets are showers of hadrons originating from quarks and gluons from the hard scatter. The jet algorithm uses the simple cone algorithm to build preclusters which serve as seeds for the Run II Cone Algorithm. This algorithm follows three steps: clustering, addition of midpoints and merging/splitting. An ideal jet algorithm should be infrared safe and collinear safe. Infrared safe means that it should work when the emission involves a soft gluon and collinear safe means that it should not be sensitive to situations where the parton energy is split across several cells by collinear radiation.

6.4.1. Jet Energy Scale

Figure 6.6 sketches the evolution of a typical parton from the hard scatter into a jet in the calorimeter. The measured jet energy is not equal to the sum of the particle energies nor to the energy of the parton. This is due to dead material, noise, non-linearities and showering effects in the calorimeter. The Jet Energy Scale (JES) attempts to correct the measured energy back to the particle jet level before any interaction in the detector [69, 70]. This does not, however, correct for hard gluon radiation, which can redirect energy at large angles relative to the original parton. The corrected jet energy is given by:

$$E_{jet}^{corr} = \frac{E_{jet}^{obs} - O}{F_\eta \cdot R \cdot S}, \tag{6.7}$$

where E_{jet}^{obs} is the uncorrected jet energy observed in the calorimeter, O an offset to the energy, F_η the relative response as a function of η_{det}, R the energy-dependent correction for absolute response, and S a correction for shower development. The main contribution to the JES corrections comes from the calorimeter response. Figures 6.7 and 6.8 show the jet energy correction for data and Monte Carlo, respectively.

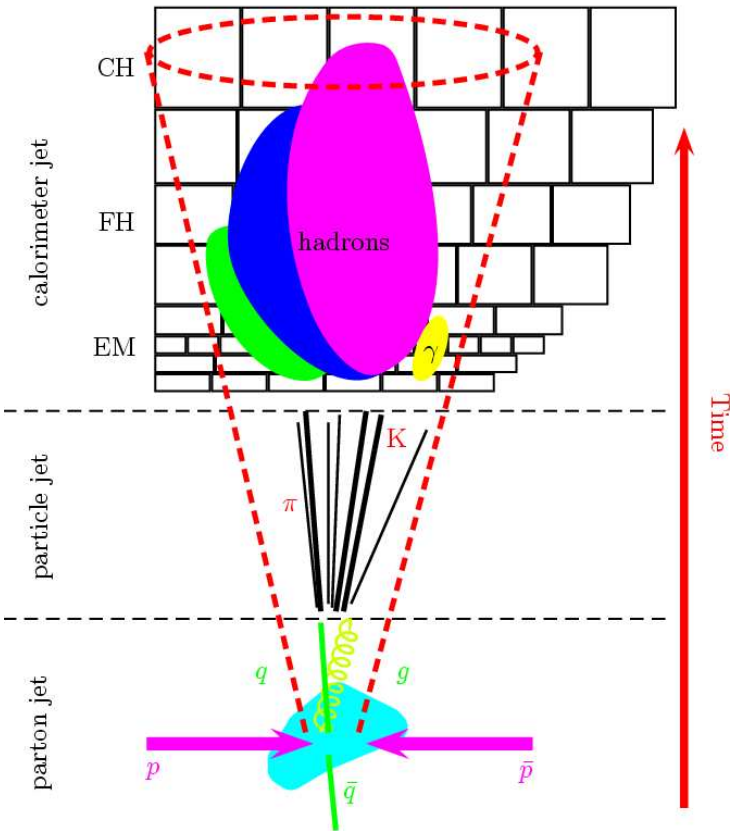

Figure 6.6.: Sketch of the evolution of a hard-scattered parton to a jet in the calorimeter.

6.5. Missing Transverse Energy

The missing transverse energy ($\not\!\!E_T$) measures the imbalance in the transverse plane of the deposited energy in the calorimeter. The imbalance comes from particles like neutrinos which do not deposit their energy in the detector. The missing transverse energy corresponds to the negative sum of the calibrated energy depositions in the detector. It is calculated from the raw missing transverse energy and additional corrections for the calorimeter response of physics objects [72]. The finite energy resolution of the calorimeter leads to a certain resolution of $\not\!\!E_T$. This is also worsened by additional detector effects like noise in the readout electronics. The amount of missing transverse energy in the event is an important signature for new physics. The precise knowledge of $\not\!\!E_T$ is vital for the analyses presented here.

The raw missing transverse energy (METB) is calculated using all calorimeter cells within the electromangetic and fine hadronic layers of the calorimeter that have non-zero energy. Cells from the coarse hadronic layer are excluded, except for coarse hadronic cells that belong to a good jet. This avoids mismeasured missing transverse energy from noise in the coarse hadronic layer. The projections of METB on the x and y axis are given by:

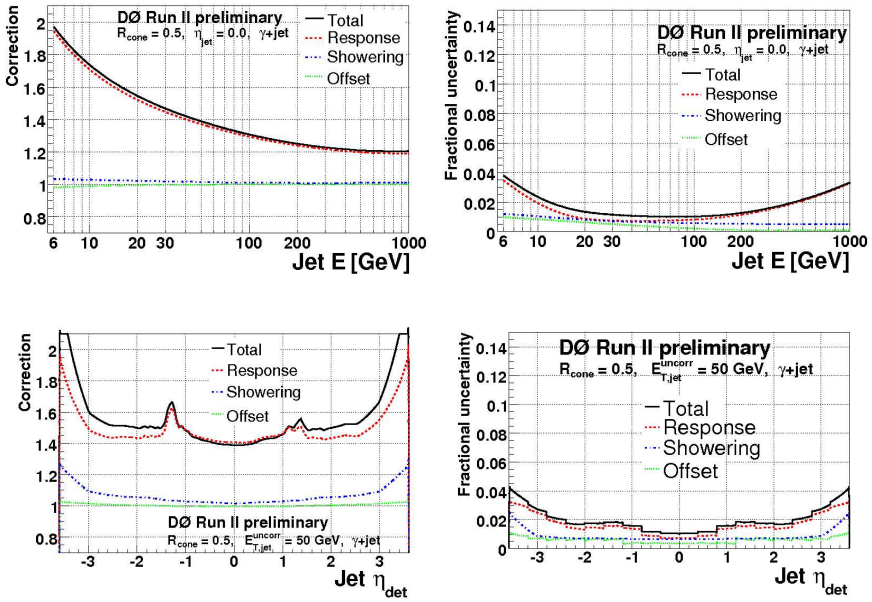

Figure 6.7.: The corrections to the jet energy with the corresponding errors for data as a function of the uncalibrated jet energy for $\eta_{det} = 0$ (top) and as a function of η_{det} for $E_{jet}^{uncorrected} = 50$ GeV (bottom) [71].

$$METB_{x,y} = -\left(\sum_{i \in \{E^{cell},\ \not{CH} > 0\}} E^i_{x,y} + \sum_{i \in \{good\ jets\ and\ E^{CH} > 0\}} E^i_{x,y} \right), \tag{6.8}$$

$$METB = \sqrt{METB_x^2 + METB_y^2}. \tag{6.9}$$

The raw missing transverse energy is corrected for the calorimeter response of the physics objects. For electron candidates, the difference of the fully calibrated energy of the electron and the sum of the corresponding calorimeter cells is propaged into $\not\!\!E_T$. For jet candidates, the jet energy scale calibration is propagated into the calculation of the missing transverse energy. Muons are minimum ionizing particles that deposit only a small amount of energy in the calorimeter. Their presence can thus also fake missing transverse energy in the detector. Their energy deposition is corrected by the difference to the full muon transverse momentum as measured in the muon system and in the tracker. It is crucial with a good calibration of the energy measurement of the physics objects in order to ensure a good MET resolution. Figure 6.9 shows the missing transverse energy resolution along the x-axis in Run IIa and Run IIb data.

6.6. Primary Vertex

The vertex of the hard scattering process is usually denoted primary vertex (PV). The measurement of the PV is crucial for an accurate determination of the transverse momentum of the

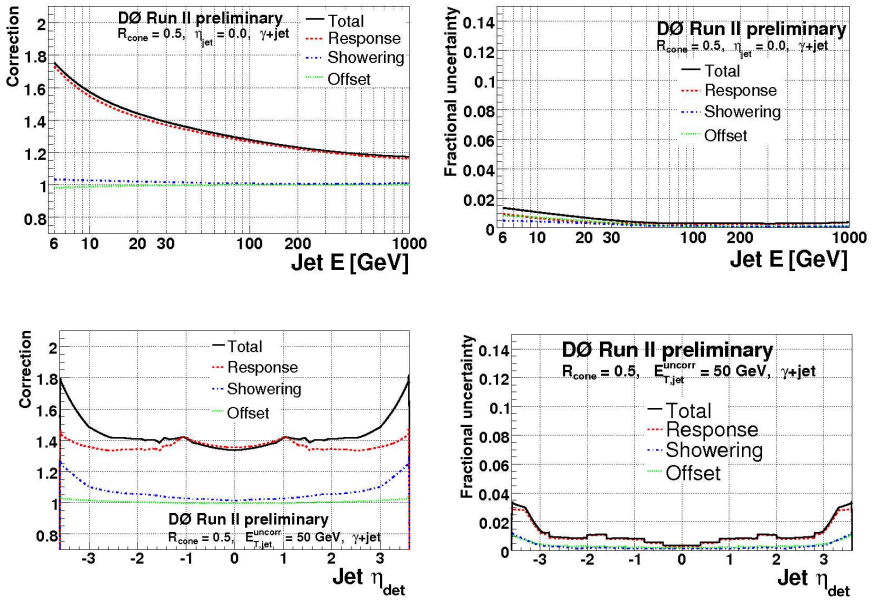

Figure 6.8.: The corrections to the jet energy with the corresponding errors for Monte Carlo simulation as a function of the uncalibrated jet energy for $\eta_{det} = 0$ (top) and as a function of η_{det} for $E_{jet}^{uncorrected} = 50$ GeV (bottom) [71].

physics objects, especially for the missing transverse energy. Due to additional softer minimum-bias interactions it is possible to have more than one PV in an event.

PV candidates are determined using reconstructed tracks [76]. At least three tracks with SMT hits have to point to the same vertex. The exact vertex position is determined by a fit that uses the associated tracks. The z position has to be within the SMT acceptance region ($|z_0| < 60$ cm). The primary vertex of a hard collision is picked among the vertex candidates based on track multiplicity and the transverse momentum of the associated tracks, since minimum bias interactions will result in tracks with smaller transverse momentum.

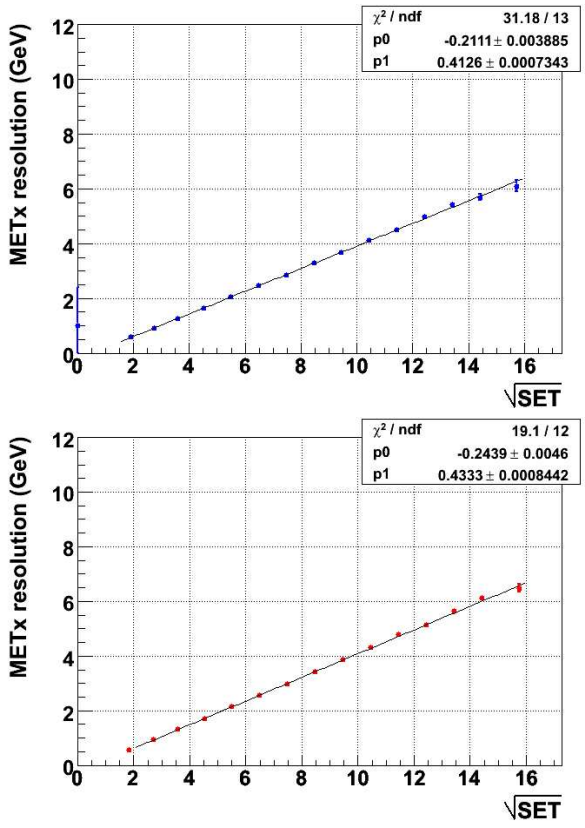

Figure 6.9.: Missing transverse energy resolution along the x direction in Run IIa minimum bias data above and Run IIb minimum bias data below. Minimum bias data corresponds to data recorded with a minimum bias trigger. Both plots show the resolution as a function of the square root of the scalar sum of the transverse energy in the calorimeter system [73].

7. Data and Monte Carlo Samples

The data sample for the analyses presented in this document was collected between April 2002 and August 2007 with the DØ detector. The first part of this chapter gives an overview over the data sample, the trigger requirements and the quality criteria for the data samples. The second part of the chapter describes the Standard Model and signal Monte Carlo samples that are used.

7.1. Data Sample

The data used in these analyses can be divided into two time periods. The first period is Run IIa and the data was collected between August 2002 and February 2006. Between February 2006 and June 2006 the DØ detector was upgraded and Run IIb started in June 2006. The data used here correspond to all the Run IIa and Run IIb data collected before August 2007.

7.1.1. Data Skims

In order to reduce the processing effort for the individual analyses, the DØ experiment produces subsets of the data. A skim is a preselection of data events containing specific physics objects [77]. In the $ee\ell$ analysis described in this thesis, the EMInclusive skim is used and in the $\mu\mu\ell$ analysis, the MUInclusive is used. A skim is a logical OR of several requirements. The MUInclusive skim contains several smaller subskims, and the requirement for an event to be contained in the MUInclusive skim is that it either contains at least two loose muons with $p_T > 1$ GeV or at least one loose muon with $p_T >8$ GeV or at least one loose muon with $p_T > 10$ GeV and 2 jets with $p_T > 8$ GeV. For an event to be part of the EMInclusive skim, it needs either two loose electrons with $p_T > 7$ GeV, or at least one electron with $p_T > 18$ GeV and loose HMatrix cut or $p_T > 20$ GeV and no HMatrix cut. The EMInclusive skim contains approximately 280 million events for RunIIa and 200 million events for RunIIb. For the MUInclusive skim the numbers are 260 million and 350 million events.

7.1.2. Data Quality Criteria

The signal selection relies on the identification of leptons, tracks, jets and the reconstruction of the missing transverse energy. Various quality requirements are imposed on the data in order to make sure that all detector components needed for the reconstruction of the objects mentioned above have been working well. The quality requirements are either evaluated for a run (usually up to four hours of data taking), a luminosity block (the fundamental unit of time for the

luminosity measurement which corresponds approximately to one minute of data taking) or a single event [78]. Some of the quality criteria that are used are listed in the following:

- Luminosity blocks with large average $\not\!\!E_T$, with external noise, peaks in the ϕ-distribution of jets or large positive and large negative energies in the same events are discarded.
- Runs with identified hot cells or other known hardware problems are removed.
- Events with electronic noise in for example calorimeter cells are removed. Figure 7.1 (left) shows an example of noise in the electromagnetic calorimeter, the "ring of fire". Due to limited space in the intercryostat region, the high voltage distribution layout for the electromagnetic layers is built as a ring electrode. The external noise can therefore be picked up by this electrode and affects all cells in the ϕ direction at a fixed value of η. This results in rings where more than 90% of the cells measure a signal [79].

The impact of bad runs, noise events and cells with readout problems on the missing transverse energy is shown in the right-hand plot in 7.1 [80]. Approximately 14% of the data are rejected in the EMInclusive skim when combining Run IIa and Run IIb. In the MUInclusive skim, 13% of the combined Run IIa and Run IIb dataset is excluded due to data quality.

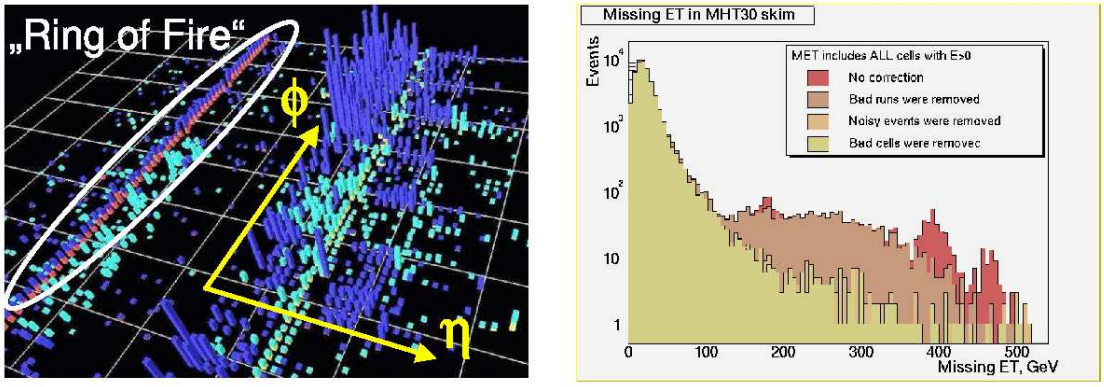

Figure 7.1.: Energy depositions in the calorimeter cells as a function of η and ϕ. This event shows the typical ring of fire characteristics (left). Bad runs, calorimeter cells and noisy events contribute to fake missing transverse energy.

7.1.3. Trigger Selection

Since the rate of $p\bar{p}$ collisions at the Tevatron is significantly higher than the rate at which events can be read out and stored for offline analysis, a dedicated trigger system (see Chapter 4.3.6) is used to select only interesting physics events and filter them out from the large background of inelastic proton-antiproton reactions. The events that are not triggered, are not stored for later analysis. Therefore, it is crucial to ensure high efficiency for the trigger system. The so called trigger lists describe the various triggers and the conditions that have to be met for them to fire. The triggers are continuously optimized for high efficiency and to adopt to changes of

the instantaneous luminosity. The data sample for this thesis has been collected using several trigger lists. The first trigger epoch (August 2002-June 2003) is covered by triger list v5-v11 and contains run numbers 151817-178721. The second trigger epoch (July 2003- August 2004) is covered by trigger list v12 and contains run numbers 178722-194566. Trigger list v13 contains run numbers 194567-208500 and list v14 contains 207217-215670. The last part of the dataset used in this thesis was collected with triggerlist v15 which was implemented among other things to meet the challenges with higher instantaneous luminosity in Run IIb. Triggerlist v15 contains runs 221993-240743. To maximize the efficiency, all single lepton, di-lepton and lepton+track triggers are used in the analyses presented in this thesis [81, 82, 83].

7.1.4. Integrated Luminosity

The total integrated luminosity after quality selection is estimated by normalizing the total number of $Z \rightarrow \ell\ell$ in Monte Carlo events to the same number of events observed in data. This approach is used instead of estimating the total integrated luminosity with the luminosity monitor that was described in Section 4.3.5. By performing this normalizing procedure, various systematic uncertainties cancel at leading order (for example lepton systematics). Another advantage is that events that would have been removed from the analyses due to failures in the luminosity monitor can be kept. This luminosity estimate is an effective luminosity with trigger efficiency folded in. Because the trigger efficiency is different for muons and electrons, the effective luminosity is also different. The $Z \rightarrow \ell\ell$ NNLO cross section (241.6 pb, see Table 7.3) is used to calculate the integrated luminosity. The effective luminosity is determined separately for Run IIa and Run IIb for both the $ee\ell$ and the $\mu\mu\ell$ analyses. In the both analyses, a mass window of 70 GeV $< M_{\ell\ell} <$ 110 GeV is defined, and for both data and Monte Carlo distributions, a fit with a double Gaussian is performed. The functional form of the double Gaussian is given in Equation 7.1:

$$f(x) = \text{A1} \cdot \text{Gauss(M1,S1)} + \text{A2} \cdot \text{Gauss(M2,S2)} \tag{7.1}$$

where A1(2), M1(2), S1(2) are fit parameters and are presented in Table 7.1 for the $\mu\mu\ell$ analysis and in Table 7.2 for the $ee\ell$ analysis. Figure 7.2 shows the di-muon invariant mass with a fit in the mass range between 70 GeV and 110 GeV and Figure 7.3 shows the di-electron mass with a fit of the double Gaussian in the same mass range. The normalization is performed at the preselection stage (see Chapter 9) and Monte Carlo correction factors (see Chapter 8) are applied to the Monte Carlo before normalization to the Z peak. Because of the different energy scale and resolution in data and Monte Carlo, the $Z \rightarrow ee$ Monte Carlo is smeared and scaled as described in Section 8.3.

Duplicated events and events that are rejected due to data quality are removed from Data and Monte Carlo before normalization. Monte Carlo events with zero instantaneous luminosity from the zero bias overlay are removed before normalizing. By performing this normalization procedure, the Run IIa luminosity was calculated to 1033 pb^{-1} in the $ee\ell$ analysis and 995 pb^{-1} in the $\mu\mu\ell$ analysis. The Run IIb luminosity was estimated to 1180 pb^{-1} in the $ee\ell$ analysis and 1087 pb^{-1} in the $\mu\mu\ell$ analysis. The total systematic error on the normalization factor is the sum of the PDF uncertainty, uncertainty on the NNLO $Z \rightarrow \ell\ell$ cross section and the statistical error on the data/MC normalization factor. Adding these contributions gives a systematic error of 6%, resulting in a luminosity estimate of (2210 $\pm$140) pb^{-1} in the $ee\ell$ analysis and (2080 $\pm$140) pb^{-1} in the $\mu\mu\ell$ analysis.

Table 7.1.: Fit parameters for the double Gaussians used to fit data and Monte Carlo in the normalization procedure for Run IIa and Run IIb data in the $\mu\mu\ell$ analysis.

	RunIIa DATA	RunIIa MC	RunIIb DATA	RunIIb MC
Amplitude 1 (A1)	5.12e+03	1.12e+05	5.70e+03	3.230e+04
Mean 1 (M1)	89.4	89.4	89.9	89.8
Sigma 1 (S1)	5.8	6.1	5.6	5.8
Amplitude 2 (A2)	3.43e+03	6.74e+04	2.72e+03	2.01e+04
Mean 2 (M2)	90.7	91.2	90.6	91.2
Sigma 2 (S2)	12.3	12.6	12.2	11.6

Table 7.2.: Fit parameters for the double Gaussians used to fit data and Monte Carlo in the normalization procedure for Run IIa and Run IIb data in the $ee\ell$ analysis.

	RunIIa DATA	RunIIa MC	RunIIb DATA	RunIIb MC
Amplitude 1 (A1)	1.45e+04	6.80e+04	1.28e+04	6.70e+04
Mean 1 (M1)	91.0	90.7	91.4	91.1
Sigma 1 (S1)	3.6	4.0	3.5	3.6
Amplitude 1 (A2)	2.99e+03	1.03e+04	3.02e+03	1.28e+04
Mean 2 (M2)	87.1	87.2	86.4	87.0
Sigma 2 (S2)	10.1	10.9	10.0	10.4

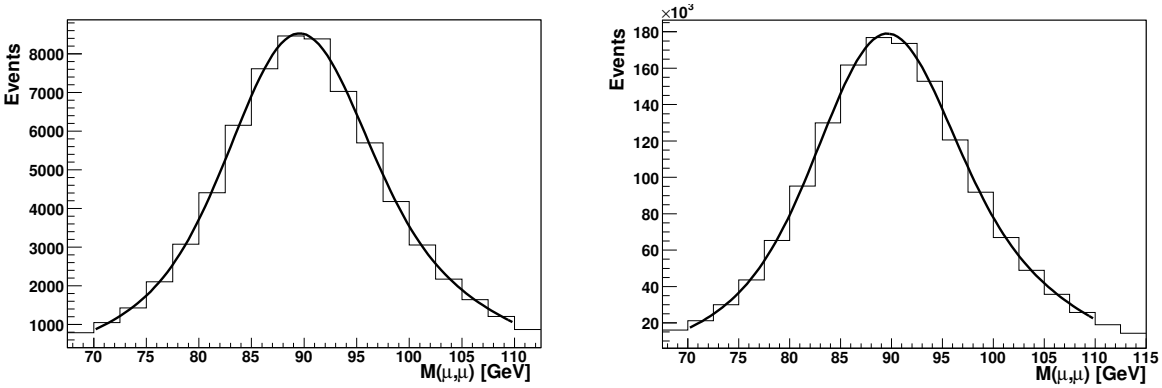

Figure 7.2.: Run IIa di-muon invariant mass zoomed in at the mass range between 70 GeV and 110 GeV at preselection level for data (left) and Monte Carlo (right). The distributions have been fitted with a double Gaussian between 70 GeV and 110 GeV.

The effective luminosity was compared to the luminosity calculated using the rate of inelastic collisions measured with the luminosity monitor. For Run IIa, the total integrated luminosity was determined to 1050 pb^{-1} for the EMInclusive skim [84] and 1070 pb^{-1} for the MUInclusive

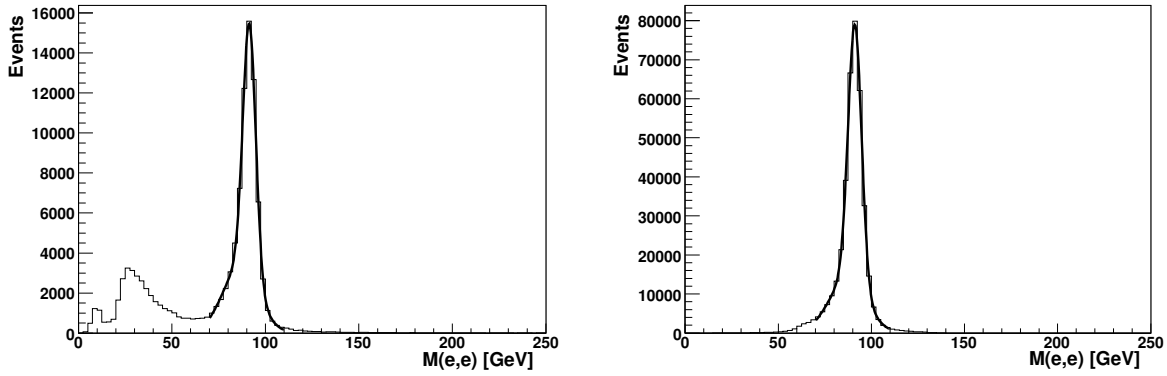

Figure 7.3.: Run IIb di-electron invariant mass at preselection level for data (left) and Monte Carlo (right). The distributions have been fitted with a double Gaussian between 70 GeV and 110 GeV.

skim [85]. For Run IIb, the luminosities measured with the luminosity monitor is 1200 pb^{-1} for both the EMInclusive and MUInclusive skims [86, 87]. Within the errors, the luminosities agree for the dielectron final state in both methods, which is expected since the trigger efficiency around the Z peak is 100% [81]. For the dimuon final state, the trigger efficiency is lower [82] and the inefficiecny is folded into the luminosity when normalizing to the Z resonance. For example, the scaling factor for Run IIb is found to be 0.88±0.02 which is in good agreement with the factor 0.87 found in [87].

7.2. Monte Carlo Samples

As described in Section 5.2 background processes which produce a similar detector signature as the SUSY tri-lepton signal, are simulated with Monte Carlo. In the following, the background and signal Monte Carlo samples are described.

7.2.1. Standard Model Background Monte Carlo Samples

The different background processes with their cross section and the number of generated Monte Carlo events are listed in Table 7.3. The Standard Model background processes have been generated with Pythia 6.319 [49] using the CTEQ6L1 [48] parton distribution functions except for $W(+jets) \to \ell\nu$. For the $W \to \ell\nu$ process, the Alpgen [50] event generator with the MLM [88] matching procedure is used. The $Z/\gamma^* \to \ell\ell$ cross section is calculated with CTEQ6.1M PDFs as $\sigma(Z/\gamma^* \to \ell\ell) = \sigma_{LO} \times K_{QCD}(Q^2)$, with the LO cross section calculated by Pythia and K_{QCD} at NNLO with NLO PDF, calculated according to [89, 90].

The $t\bar{t}$ NNLO cross section is taken from [91] and the WW, ZZ and WZ cross sections are calculated in [93] with MCFM [94] using CTEQ6.1M PDFs. The $W \to \ell\nu$ cross section is calculated at LO with Alpgen. In addition, K–factors have been applied to match the $W \to \ell\nu$

inclusive NNLO cross section calculated with CTEQ6.1M PDFs as listed in [89, 90]. The $W+jets$ samples consist of subsamples sorted by jet flavor: Wjj, $Wc\bar{c}$ and $Wb\bar{b}$, where Wjj includes the Wcj subprocess. The Wjj samples are produced in bins of light parton (lp) multiplicities, ranging from 0 lp up to 5 lp. For the samples 0-4 lp, the samples are exclusive, while for 5 lp, the sample is inclusive. Overlap between the Wjj samples and the $Wc\bar{c}$ and $Wb\bar{b}$ samples have been removed [95]. The K–factors and the $W \to \ell\nu$ background will be described in more detail in Section 8.10.

The errors due to the PDF uncertainty as calculated in [90] using the CTEQ6.1M PDF parametrization and the errors from varying the factorization and normalization scale [89, 90] are also listed in Table 7.3, if available. $\Upsilon \to \ell\ell$ Monte Carlo was scaled to data in the low invariant mass distribution.

7.2.2. Signal Monte Carlo Generation

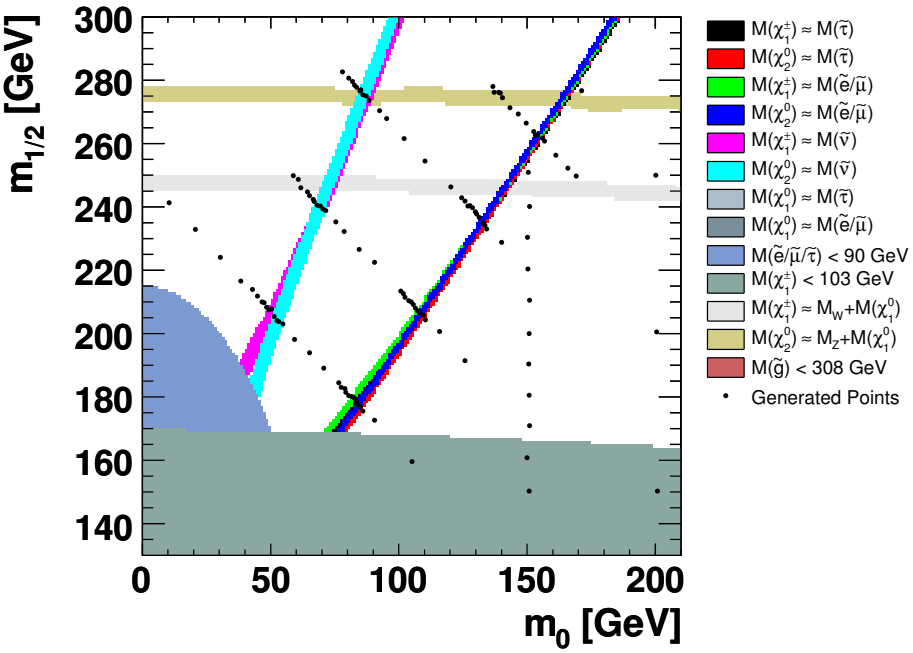

Figure 7.4.: The $(m_0, m_{1/2})$ plane. The black points represent signal Monte Carlo samples generated for this study. Regions excluded by LEP are indicated at the bottom and at the left part of the plot. The darker region at the bottom corresponds to $m_{\tilde{\chi}_1^\pm}$<103 GeV and the oval shaped region corresponds to $m_{\tilde{\ell}}$ <90 GeV. The lines $m_{\tilde{\chi}_1^\pm} \approx m_W + m_{\tilde{\chi}_1^0}$ and $m_{\tilde{\chi}_2^0} \approx m_Z + m_{\tilde{\chi}_1^0}$ are also indicated.

A large number of Monte Carlo samples for different parameter points (tanβ=3, $A_0 = 0$, $\mu > 0$ and varying m_0 and $m_{1/2}$) is generated to perform a search in the $(m_0, m_{1/2})$ plane. Points are generated in a way to cover the whole plane in the region where sensitivity might be achieved. The generated points are shown in the $(m_0, m_{1/2})$ plane in Figure 7.4. In this plot, regions excluded by LEP and the lines $m_{\tilde{\chi}_1^\pm} \approx m_W + m_{\tilde{\chi}_1^0}$ and $m_{\tilde{\chi}_2^0} \approx m_Z + m_{\tilde{\chi}_1^0}$ are also indicated. The

Table 7.3.: Cross section times branching ratio ($\sigma \times BR$) and number of generated events for the different background Monte Carlo samples. The error on the cross section is given by the PDF uncertainty [92]. The leading-order cross section is scaled with a K–factor. For the Z/γ^* and W inclusive samples K_{NNLO} from [89] is used. Cross sections for the di-boson samples are calculated in [93], while the cross sections for the $t\bar{t}$ samples are taken from [91].

Process	Mass Range [GeV]	$\sigma \times$ BR [pb]	# Events
$Z/\gamma^* \to \mu\mu$	5<M<15	from data	4.4M
$Z/\gamma^* \to \mu\mu$	15<M<60	409 ± 15.1	4.1M
$Z/\gamma^* \to \mu\mu$	60<M<130	241.6 ± 8.7	6.8M
$Z/\gamma^* \to \mu\mu$	130<M<250	1.96 ± 0.6	850k
$Z/\gamma^* \to \mu\mu$	250<M<500	0.1378	290k
$Z/\gamma^* \to \mu\mu$	M<500	0.004584	240k
$Z/\gamma^* \to ee$	5<M<15	from data	2.2M
$Z/\gamma^* \to ee$	15<M<60	409 ± 15.1	4.6M
$Z/\gamma^* \to ee$	60<M<130	241.6 ± 8.7	2.4M
$Z/\gamma^* \to ee$	130<M<250	1.96 ± 0.6	285k
$Z/\gamma^* \to ee$	250<M<500	0.1378	240k
$Z/\gamma^* \to ee$	M<500	0.004584	120k
$Z/\gamma^* \to \tau\tau$	5<M<15	from data	1.4M
$Z/\gamma^* \to \tau\tau$	15<M<60	409 ± 15.1	2.0M
$Z/\gamma^* \to \tau\tau$	60<M<130	241.6 ± 8.7	13.2M
$Z/\gamma^* \to \tau\tau$	130<M<250	1.96 ± 0.6	288k
$Z/\gamma^* \to \tau\tau$	250<M<500	0.1378	100k
$Z/\gamma^* \to \tau\tau$	M<500	0.004584	100k
$W + 0$ lp $\to \ell\nu + 0$ lp exclusive		5071 ± 2.1	30M
$W + 1$ lp $\to \ell\nu + 1$ lp exclusive		1412 ± 0.68	12M
$W + 2$ lp $\to \ell\nu + 2$ lp exclusive		410 ± 0.34	7.2M
$W + 3$ lp $\to \ell\nu + 3$ lp exclusive		97.2 ± 0.16	3.4M
$W + 4$ lp $\to \ell\nu + 4$ lp exclusive		22.14 ± 0.07	2.7M
$W + 5$ lp $\to \ell\nu + 5$ lp inclusive		7.374 ± 0.13	0.7M
$W + 2$ lp $\to \ell\nu +$ 2b 0lp exclusive		19.18 ± 0.01	2.5 M
$W + 2$ lp $\to \ell\nu +$ 2b 1lp exclusive		7.94 ± 0.005	0.7 M
$W + 2$ lp $\to \ell\nu +$ 2b 2lp exclusive		2.67 ± 0.003	810 K
$W + 2$ lp $\to \ell\nu +$ 2b 3lp exclusive		1.09 ± 0.003	670 K
$W + 2$ lp $\to \ell\nu +$ 2c 0lp exclusive		71.1 ± 0.04	2.1 M
$W + 2$ lp $\to \ell\nu +$ 2c 1lp exclusive		29.8 ± 0.04	1.5 M
$W + 2$ lp $\to \ell\nu +$ 2c 2lp exclusive		10.2 ± 0.02	820 K
$W + 2$ lp $\to \ell\nu +$ 2c 3lp exclusive		11.3 ± 0.02	800 K
WW incl.		12.3 ± 0.6	850k
WZ incl.		3.68 ± 0.007	640k
ZZ incl.		1.42 ± 0.06	640k
$Zb\bar{b}$ incl.		0.616	200k
$t\bar{t}$ incl		0.70 ± 0.04	640k
$\Upsilon(1S) \to \ell\ell$		from data	550k
$\Upsilon(2S) \to \ell\ell$		from data	500k

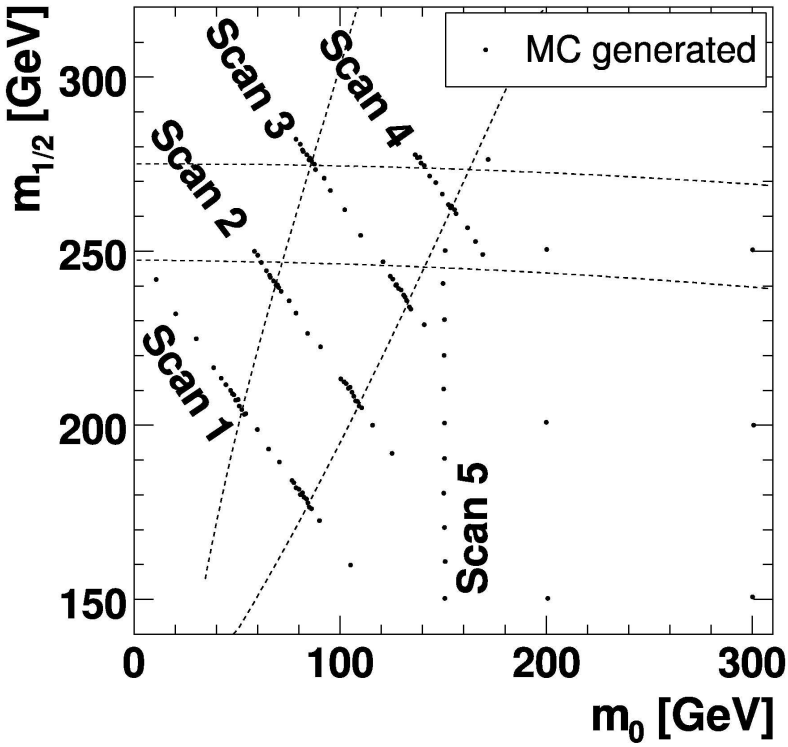

Figure 7.5.: The $(m_0, m_{1/2})$ plane. The black points represent signal Monte Carlo samples generated for this study, and the diagonals are labelled. The lines $m_{\tilde{\chi}_1^\pm} \approx m_W + m_{\tilde{\chi}_1^0}$ and $m_{\tilde{\chi}_2^0} \approx m_Z + m_{\tilde{\chi}_1^0}$ are also indicated.

SUSY points are grouped in five lines. Scan 1 to 4 are called diagonals. The diagonals are numbered such that diagonal 1 is the bottom left diagonal in Figure 7.4, diagonal 2 is above scan 1 etc. The vertical line is scan 5. This is clearly shown in Figure 7.5.

The points are produced in order to scan the two parameters $m_{\tilde{\chi}_1^\pm}$ and $\Delta m_{\tilde{\ell}} = m_{\tilde{\ell}} - m_{\tilde{\chi}_2^0}$ because the kinematics in the event are mainly a function of these quantities. The diagonals 1-4 are orthogonal to the transition line from 2 body decays to 3 body decays, where $\Delta m_{\tilde{\ell}} = 0$, and allow a parameterization of the efficiencies as a function of $\Delta m_{\tilde{\ell}}$. In regions of parameter space where the efficiencies of the analyses are expected to change rapidly with small variations of m_0 and $m_{1/2}$, a finer grid is generated. These difficult regions are around the line of equal $\tilde{\chi}_2^0$ and slepton mass as well as when decays via on–shell sneutrinos are possible. Table 9.1 in Section 9.1 gives an overview of the SUSY parameters for three benchmark points. Appendix A lists SUSY parameters for all the generated Monte Carlo samples. The cross sections are calculated using Prospino 2 [96], with SUSY spectra determined by Softsusy 2.0.14 [97]. The branching ratios are calculated by Pythia 6.323 [49], except in the 3-body decay region, where the decay of lightest chargino and second lightest neutralino is mediated by sleptons. For this region SDecay 1.3 [98] is used since Pythia only approximates stau mixing effects in the case of slepton mediated 3-body decays. For the generation of the signal samples, Pythia is used in combination with CTEQ6L1 parton distribution functions [48].

In order to study the signal efficiency and set limits on the production cross section times branching fraction into three leptons as a function of tan β (see Section 10.2.2), signal Monte Carlo for various values of tan β was also generated.

In order to cover the range from minimal to maximal stau mixing, they are chosen from the 3-body decay region with a large branching ratio into leptons where $m_{\tilde{e}_R,\tilde{\mu}_R} > m_{\tilde{\tau}} > m_{\tilde{\chi}_2^0}$ as shown in Figure 7.6 (left) [21]. Table 7.4 lists parameters and masses of the SUSY points used in the tan β scan. To ensure that the branching ratio into the three different lepton flavors is the only property that varies, the mass of the lightest chargino is fixed for these reference points. The value of $m_{\tilde{\chi}_1^\pm}$ =130 GeV is chosen since sensitivity is expected in this region. The branching ratios of the lightest chargino and next to lightest into different lepton flavours are shown in Figure 7.6 (right).

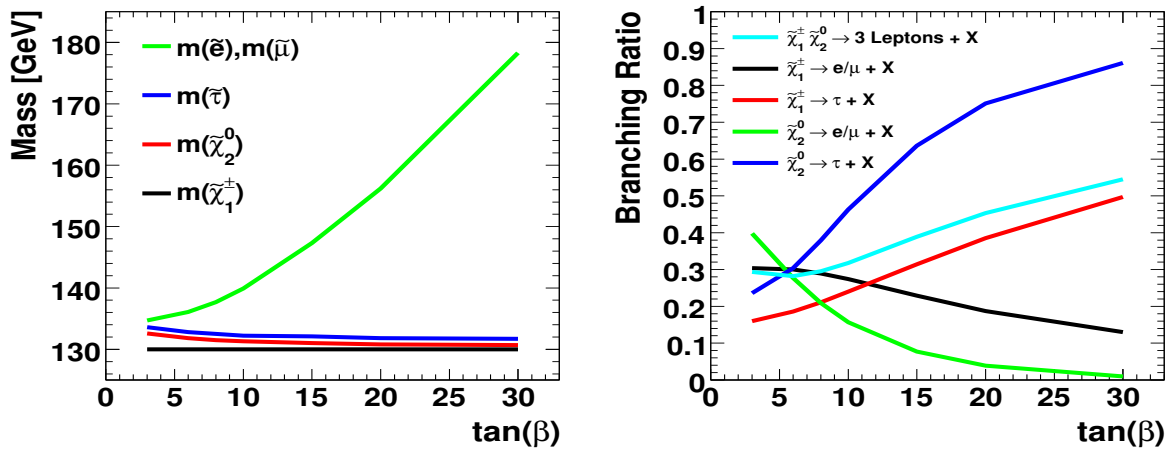

Figure 7.6.: Masses of SUSY particles (left) and branching ratio of lightest chargino and next to lightest neutralino into leptons (right), as a function of tan β for the SUSY points listed in Table 7.4 [21].

Table 7.4.: Parameters and masses of the SUSY points used in the tan β scan. All have $A_0 = 0$, positive μ and $\Delta m = m_{\tilde{\tau}_1} - m_{\tilde{\chi}_2^0} = 1$ GeV. All masses are given in units of GeV while the trilepton cross section, $\sigma\times$ BR(3ℓ) is given in units of pb.

$\tan\beta$	m_0	$m_{1/2}$	$m_{\tilde{\chi}_1^\pm}$	$m_{\tilde{\chi}_2^0}$	$m_{\tilde{\chi}_1^0}$	$m_{\tilde{\mu}_R}$	$m_{\tilde{\tau}_1}$	$\sigma\times$ BR(3ℓ)
3	104	198	130.0	132.6	71.8	134.7	133.6	0.108
6	105	195	130.0	131.8	72.0	136.1	132.8	0.103
8	107	193	130.0	131.5	71.9	137.7	132.5	0.108
10	120	192	130.0	131.3	71.9	139.9	132.2	0.117
15	120	190	130.0	131.0	71.8	147.3	132.1	0.143
20	131	189	130.0	130.8	71.6	156.2	131.8	0.168
30	157	188	130.0	130.7	71.5	178.3	131.7	0.205

7.3. Background from QCD Jet Production

In both the $ee\ell$ and the $\mu\mu\ell$ selections the expected contribution from multijet events (QCD) is estimated from data. To estimate the QCD contribution in the search sample, a region in phase space is used where the multijet background is expected to be dominant. The subsample of the data containing like-sign leptons (from now on called like-sign sample), is dominated by multi-jet events, because most of the standard model backgrounds have leptons of opposite charge in the final state. Therefore they only contribute to the like-sign sample if one of the lepton charges is mismeasured. Other contributions to the like-sign sample are expected from $W + jet/\gamma$ events, because the charge of the mismeasured jet or converted electron is arbitrary. This is also the case for the multi–jet background. Approximately 50% of this background are expected in the like-sign sample. The like-sign sample is used to normalize the QCD background, but can not be used to model the contribution at advanced stages of the selection, because the signal is partly likesign. It is therefore necessary to define QCD samples, where the signal contribution is negligable. In both the $ee\ell$ and $\mu\mu\ell$ analyses, this is done by reversing the lepton identification criteria. This will be discussed in the following for the different analyses.

QCD Background in the $ee\ell$ Analyis

For the $ee\ell$ analysis, the contribution of QCD multi-jet processes is determined from data using a sample of electron fakes obtained by requiring two EM objects with HMatrix7 > 35 and no likelihood requirement for the electron candidates. This fake sample will in the following be called the HMatrix sample. In order to keep the HMatrix sample and the search sample disjoint, at least one electron in the search sample is required to have HMatrix7 < 35. It corresponds to dijet events with a large EM-fraction and with jets that are broader than the jets which actually are preselected in the analysis. In this state, the HMatrix sample cannot be used to estimate the QCD contribution in the analysis, because the low p_T electron triggers are designed to have a lower efficiency for broader EM-jets than for electron-like jets. This leads to a different p_T turn-on for the HMatrix sample, and the like-sign sample is used to derive p_T-dependent scaling factors that are applied to the HMatrix sample.

The p_T spectrum of the leading electron in the like-sign sample is divided by the p_T spectrum of the leading electron in the HMatrix sample, and the p_T-dependent scaling factor is derived. The same is done for the next-to-leading electron. The Standard Model Monte Carlo is subtracted from the like sign distributions before they are divided by the distributions from the HMatrix sample. The probability for reconstructing the wrong electron charge is underestimated in Monte Carlo. To correct for this effect, a charge misidentification factor of 2.4 is derived in a data Monte Carlo comparison of the same sign di-electron invariant mass distribution at preselection stage. The correction factor is applied to the like-sign $Z \to ee$ events before they are subtracted from the QCD sample. The reweighting procedure is done iteratively for the leading and the next-to-leading electron. Figure 7.7 shows the p_T distribution of the leading electron in the like-sign selection before the HMatrix sample is reweighted with the p_T dependent factor. Figure 7.8 shows the p_T dependent weight factor for the leading (left) and next to leading electron (right). An exponential fit has been performed:

$$f(x) = 2.05 \cdot e^{-0.17 \cdot pt1} \tag{7.2}$$
$$f(x) = 1.49 \cdot e^{-0.12 \cdot pt2} \tag{7.3}$$

Equation 7.2 is used to reweight the p_T of the leading electron in the HMatrix sample and Equation 7.3 is used to reweight the next to leading electron in the HMatrix sample, after the reweighting of the first electron is performed.

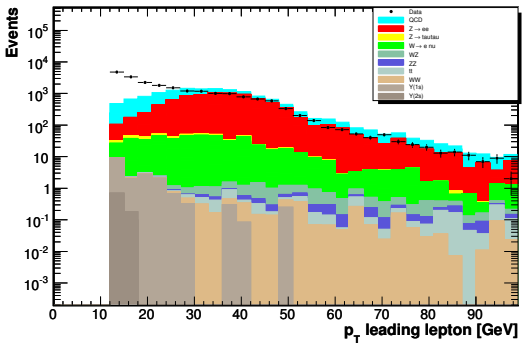

Figure 7.7.: p_T distribution of the leading electron in the like-sign selection before reweighting. The HMatrix sample has been scaled by a factor 0.1.

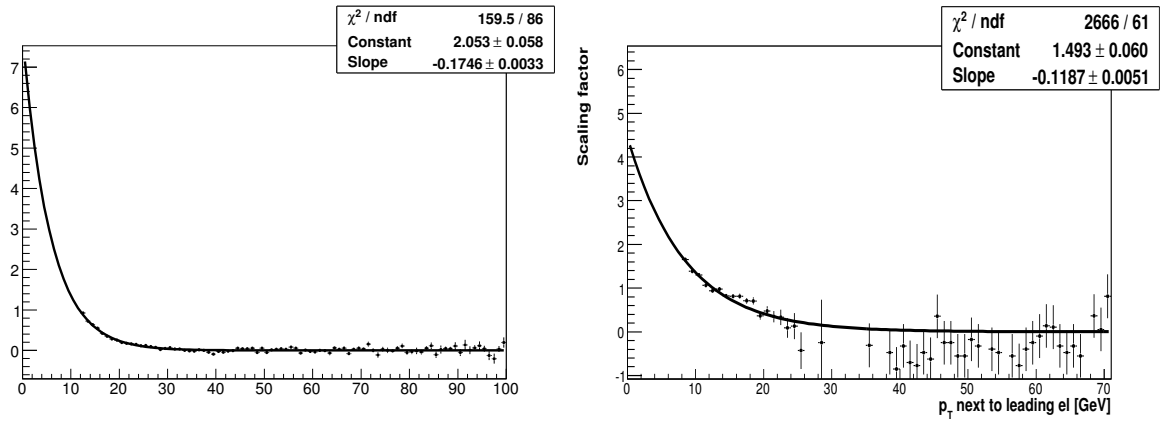

Figure 7.8.: Scaling factor as a funtion of electron p_T. In the left plot, the scaling factor as a function of the leading electron is shown. In the right plot, the scaling factor as a funtion of next to leading electron p_T after applying the leading electron scaling, is shown.

All standard selection cuts are applied to the HMatrix sample except cuts that strongly correlate to the HMatrix7. In particular this applies to cuts involving the electron likelihood. The rejection for cuts performed after the preselection level and which are strongly correlated with HMatrix7 is calculated with the like-sign sample and applied to the HMatrix sample.

QCD Background in the $\mu\mu\ell$ Analysis

The expected QCD background in the $\mu\mu\ell$ analysis is dominated by $b\bar{b}$ decays. The QCD background is determined from data by inverting the isolation criteria in the calorimeter and the tracker because muons arising from QCD events are predominantly non-isolated. The same isolation variables as in the normal analysis selection are used and data events with two anti-isolated muons are selected as QCD background. This sample will in the following be called the non-isolated sample. In order to increase statistics, two different criteria are chosen for an event to be selected as a QCD event:

- A QCD event is selected if for the leading muon candidate, the p_T sum of other tracks in a hollow cone around the muon is at least 4.0 GeV in the tracker and the transverse energy in the calorimeter is at least 4.0 GeV. For the next-to-leading muon, these cuts are 2.5 GeV.
- A QCD event is also selected if the transverse energy around the muon candidate is more than 4 GeV in either the tracker or the calorimeter for both muons. In addition, the total energy deposited in tracker and calorimeter around the muon candidates must be at least 8 GeV in this case.

In order to select QCD events that are kinematically similar to the selected signal candidates, the energy deposited around the muon candidates must not be larger than 11 GeV in tracker or calorimeter. This applies to both muons.

Because the muon triggers require isolation for low-p_T muons, a p_T dependent scale factor is derived. The scale factor is derived by fitting the p_T distribution of the leading muon in non-isolated like-sign events. Also the p_T distribution of the leading muon in like-sign events in the isolated sample is fitted. The ratio between the two fits defines the p_T dependent scale factor. This scale factor is then applied to the non-isolated sample. The same procedure is applied to the p_T distributions of the next-to-leading muon and the resulting scaling factor is applied to the non-isolated sample. Figure 7.9 shows the p_T of the leading muon before reweighting, and the reweighting factor as a function of p_T of the leading muon.

Absolute Normalization

After the p_T dependent reweighting has been performed, the QCD sample (HMatrix sample in the $ee\ell$ selection and the anti-isolated sample in the $\mu\mu\ell$ selection) needs to be correctly normalized. The absolute normalization of the multi jet background is described in the following. The number $N_{Sig}^{\pm\pm}$ of like-sign events in the search sample is determined, from which the expected contribution $N_{MC}^{\pm\pm}$ from all standard model backgrounds except the multi–jet background is subtracted. The excess

$$N_{QCD}^{\pm\pm} = N_{Sig}^{\pm\pm} - N_{MC}^{\pm\pm} \tag{7.4}$$

of events corresponds to the multi jet contribution in like-sign events in the search sample. Thus a normalization factor

$$f_{Norm}^{QCD} = \frac{N_{Sig}^{\pm\pm} - N_{MC}^{\pm\pm}}{N_{Bg}^{\pm\pm}} = \frac{N_{QCD}^{\pm\pm}}{N_{Bg}^{\pm\pm}} \tag{7.5}$$

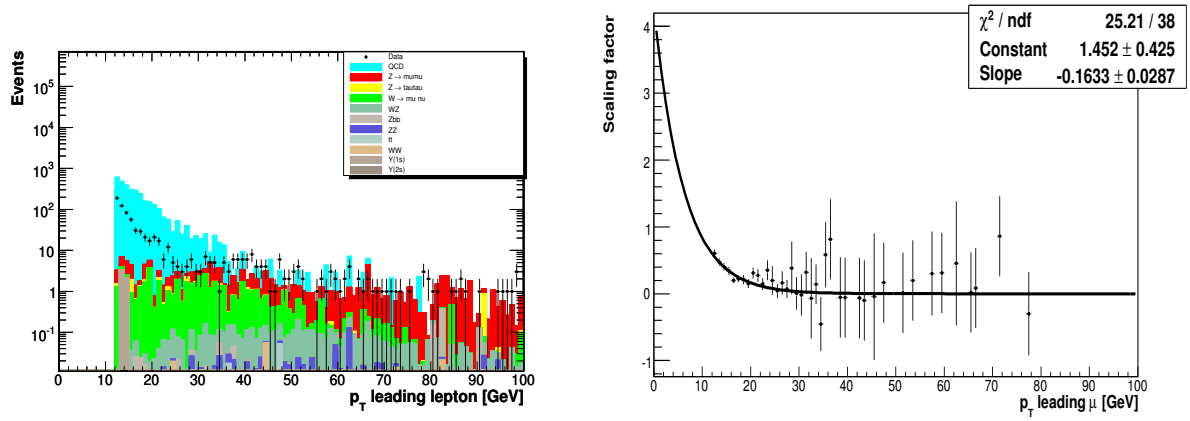

Figure 7.9.: Transverse momentum of the leading muon in the like-sign sample, before reweighting of the non-isolated sample (left). Scaling factor with an exponential fit, as a function of p_T of the leading muon (right).

is obtained, where $N_{Bg}^{\pm\pm}$ is the number of like-sign events in the QCD sample. The number of multi jet events N_{QCD} in the search sample (without any charge requirements) can be computed from the number N_{Bg} of events in the fake sample (without any charge requirements) using the equation

$$N_{QCD} = f_{Norm}^{QCD} \cdot N_{Bg} \ . \tag{7.6}$$

To get an estimate for the multi jet background after each selection criterion the normalization factor f_{Norm}^{QCD} is determined once after the preselection and is then kept constant. The rejection factors η_{QCD}^{i} of the selection criteria, where i corresponds to the i^{th} selection criterion, are determined using the fake sample. The rejection factors η_{QCD}^{i} can be obtained via the expression

$$\eta_{QCD}^{i} = \frac{\text{Number of multijet events after selection criterion } i}{\text{Number of multijet events after preselection}} = \frac{N_{Bg}^{i}}{N_{Bg}} \ . \tag{7.7}$$

Accordingly, the number of multi jet events N_{QCD}^{i} in the search sample after the selection criterion i is applied is given by

$$N_{QCD}^{i} = f_{Norm}^{QCD} \cdot \eta_{QCD}^{i} \cdot N_{Bg} \ . \tag{7.8}$$

The absolute normalization and p_T corrections are done once at preselection level and kept through the whole selection.

Figure 7.10 shows the the invariant mass distribution of like sign events and the p_T of the leading electron after reweighting. A global normalization factor for the HMatrix sample is derived by scaling the QCD sample to data in the low mass region, 20 GeV $< M_{ee} <$ 60 GeV.

The non-isolated like-sign events are normalized to the like-sign isolated sample in a mass window of 20 GeV $< M_{\mu\mu} <$ 60 GeV after all other background has been subtracted. The resulting scale factor is 0.83 ± 0.056. Figure 7.11 shows the p_T of the leading muon (left) and the next to leading muon (right) in the like-sign sample after p_T reweighting and the global normalization has been performed.

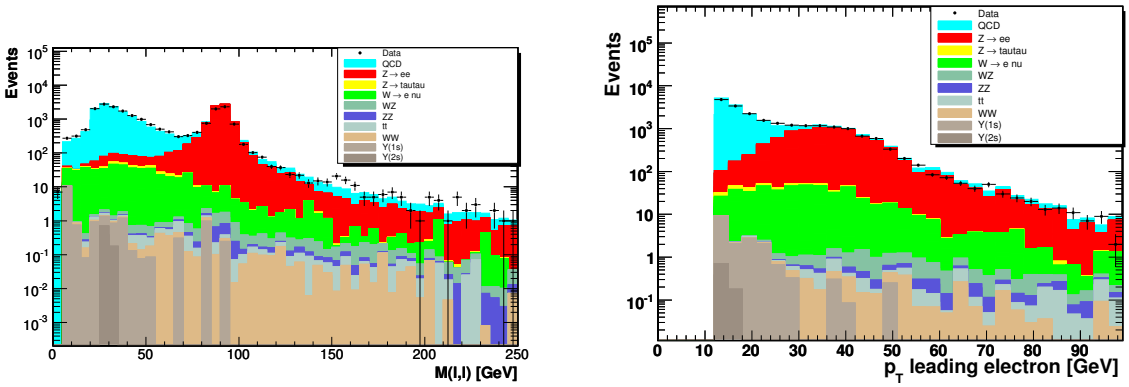

Figure 7.10.: The invariant mass distribution of like sign electrons (left) and the leading electron in the like sign sample (right). The sample used to model the QCD background is the HMatrix sample (see text) and both plots are shown after the HMatrix sample has been reweighted as a function of leading and next to leading electron p_T.

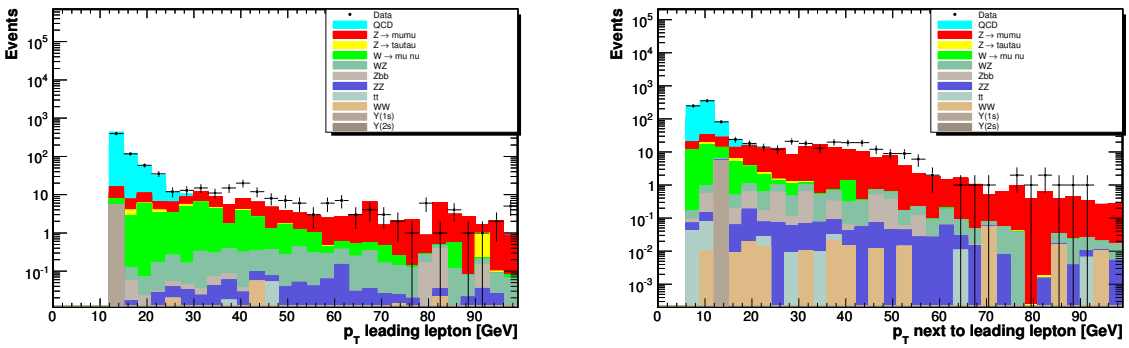

Figure 7.11.: p_T of leading muon (left) and next to leading muon (right) in the like-sign sample. For QCD, the non-isolated sample is used and the p_T dependent reweighting has been applied.

8. Monte Carlo Corrections and Data Monte Carlo Comparisons

The Monte Carlo does not always reproduce the data correctly and various corrections need to be applied to bring the Monte Carlo simulation in better agreement with data. This chapter will describe these corrections and how they are derived. The chapter also describes cross checks made to ensure that the Monte Carlo simulation correctly reproduces the data after application of the corrections.

8.1. Lepton Reconstruction and Identification Efficiency Corrections

The reconstruction efficiency of electrons and muons is not the same in data and simulation, and the Monte Carlo simulation needs to be corrected to take the differences into account. The efficiency is measured in $Z \to ee$ and $Z \to \mu\mu$ events in data and Monte Carlo and the ratio of the efficiency is applied to all Monte Carlo samples [63, 65]. The reconstruction and identification efficiencies are measured with the software tools em–cert [99] for electrons and muo–cert [100] for muons. To measure the efficiencies a *tag and probe* method is used, selecting a tag lepton that needs to fulfill tight selection criteria, and a probe lepton that must only fulfill requirements that do not bias the selection criteria under study [101]. The efficiency of the selection criteria, is then the fraction of probe leptons that pass the particular criteria. The efficiencies described below, correspond to the efficiencies for loose electrons as described in 6.2 and loose muons as described in 6.3.

8.1.1. Muon Efficiency Corrections

The correction factor applied to each Monte Carlo event in the $\mu\mu\ell$ analysis to take the differences in muon identification efficiencies into account, is divided into three parts: the muon type and quality, the track match and the isolation (see Section 6.3). The correction factors have been derived from $Z \to \mu^+\mu^-$ events in data and Monte Carlo. The overall correction factor is the product of the efficiencies of the three contributions:

$$correction\ factor = \frac{\epsilon^{data}_{type}}{\epsilon^{MC}_{type}} \times \frac{\epsilon^{data}_{trackmatch}}{\epsilon^{MC}_{trackmatch}} \times \frac{\epsilon^{data}_{isolation}}{\epsilon^{MC}_{isolation}} \tag{8.1}$$

where ϵ^{data}_{cut} is the efficiency in data for the given cut (type, track match, isolation) and ϵ^{MC}_{cut} is

the efficiency in Monte Carlo.

Muon Type Efficiency Corrections

The loose muon reconstruction efficiency in data and Monte Carlo, was measured as a function of η and ϕ and applied as a weight to the simulated events. Figure 8.1 shows the ratio of the reconstruction efficiency in data and Monte Carlo as a function of η_{phys}. The average efficiency correction for loose muons is 0.995±0.004 [65].

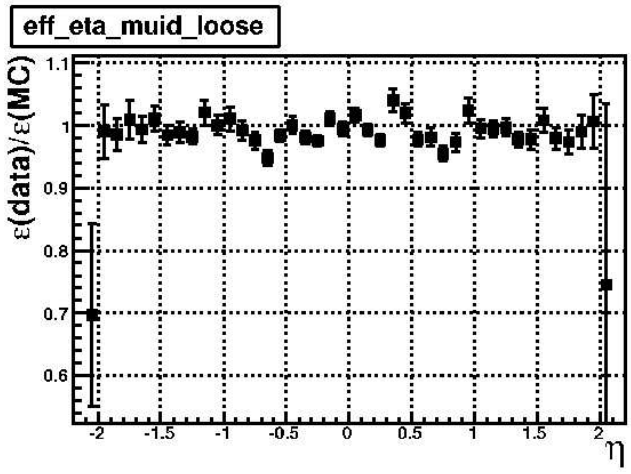

Figure 8.1.: Muon reconstruction efficiency correction as function of η^{μ}_{phys} for loose muons [65].

Tracking Efficiency Corrections

The tracking efficiency includes the efficiency for hits in the CFT and the matching efficiency between local muons and central tracks. The tracking efficiency is studied as a function of η and z position of the muon. Figure 8.2 shows the efficiency in data as a funtion of η_{phys} and the efficiency correction also as a function of η_{phys}. The average tracking efficiency for loose tracks is 94.2% in data and the average correction factor is 0.96 ± 0.021. The efficiency corrections derived for muon tracks are also applied to the selection of the third track in both the $ee\ell$ and the $\mu\mu\ell$ analyses.

Muon Isolation Efficiency Corrections

The isolation efficiency is applied as a function of the muon transverse momentum and number of jets in the event. Figure 8.3 presents the isolation efficiency as a function of muon p_T. The upper plot shows the efficiency in data and the lower plot shows the Monte Carlo efficiency correction. The efficiency is computed for isolation cuts corresponding to 2.5 GeV in tracker and calorimeter (*NPTight*) and 4.0 GeV in tracker and no requirement on isolation in the calorimeter (*NPLoose*).

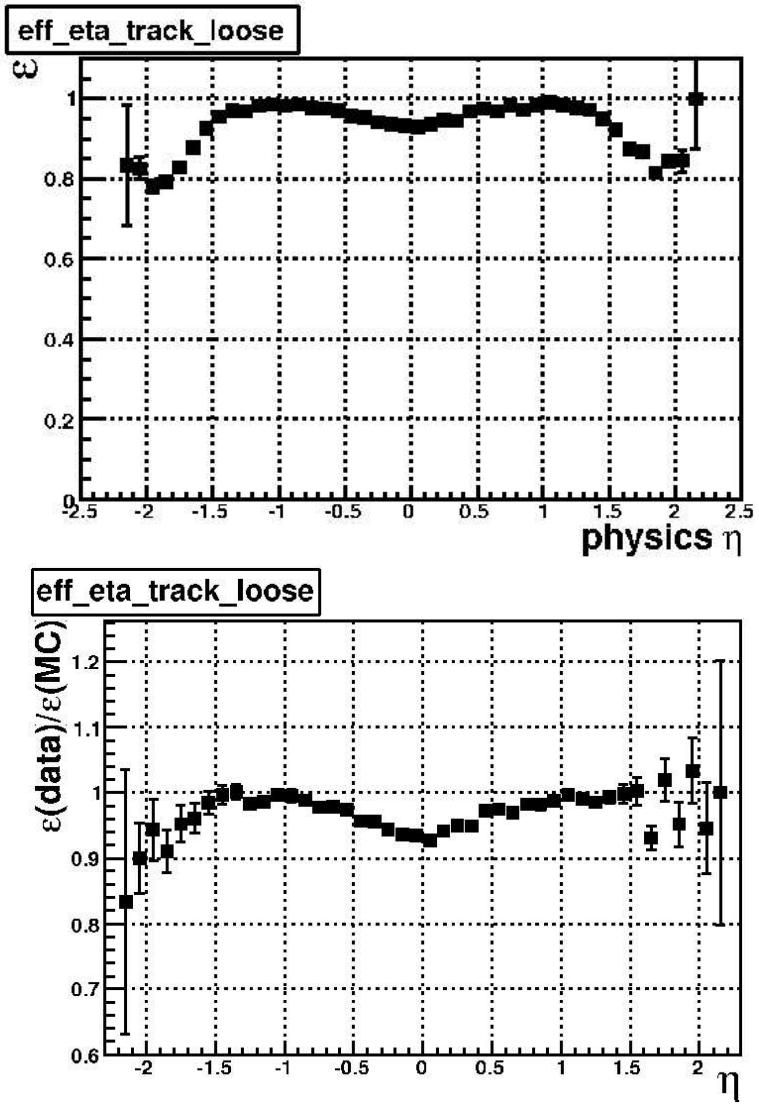

Figure 8.2.: Muon tracking efficiency in data as a function of η^{μ}_{phys} (above) and the efficiency correction as a function of η_{phys} (below) [65].

8.1.2. Electron Efficiency Corrections

For electrons, the corrections factor is divided into two parts: preselection and post-preselection. Preselection refers to the basic electron identifictation variables: ID, electromagnetic fraction and isolation (see Section 6.2). The post-preselection criterium used in the $ee\ell$ analysis, is the likelihood cut. The post-preselection efficiencies are calculated relative to the preselection efficiencies. The overall correction factor becomes

$$correction\ factor = \frac{\epsilon^{data}_{presel}}{\epsilon^{MC}_{presel}} \times \frac{\epsilon^{data}_{postpresel}}{\epsilon^{MC}_{postpresel}} \tag{8.2}$$

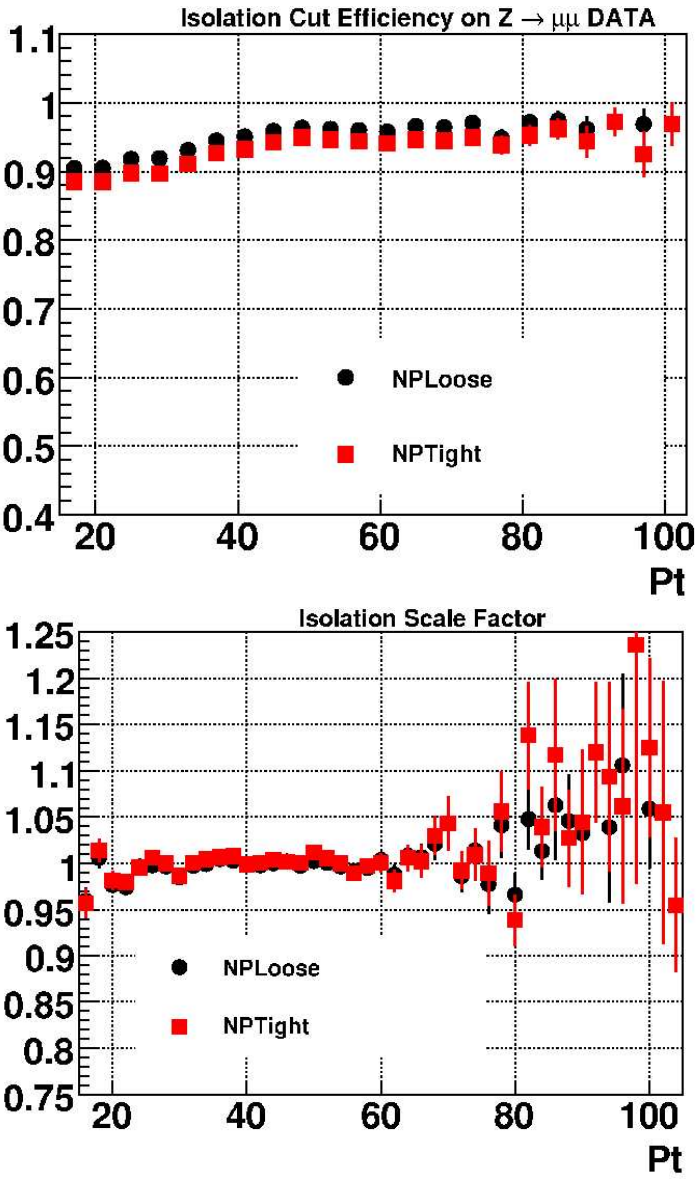

Figure 8.3.: Isolation efficiency for muon as a function of muon p_T in data (above) and the efficiency correction as a function of muon p_T (below) [65].

where $\epsilon^{data}_{(post)presel}$ is the efficiency for an electron in data to pass the (post)preselection and $\epsilon^{MC}_{(post)presel}$ is the efficiency for an electron in Monte Carlo to pass the (post)preselection.

Electron Preselection Efficiency Corrections

The preselection scale factor is parametrized as a function of η_{det} and is shown in Figure 8.4.Since the efficiencies for Monte Carlo and data agree within the errors, no correction factor is applied to correct the Monte Carlo for differences in the preselection efficiency.

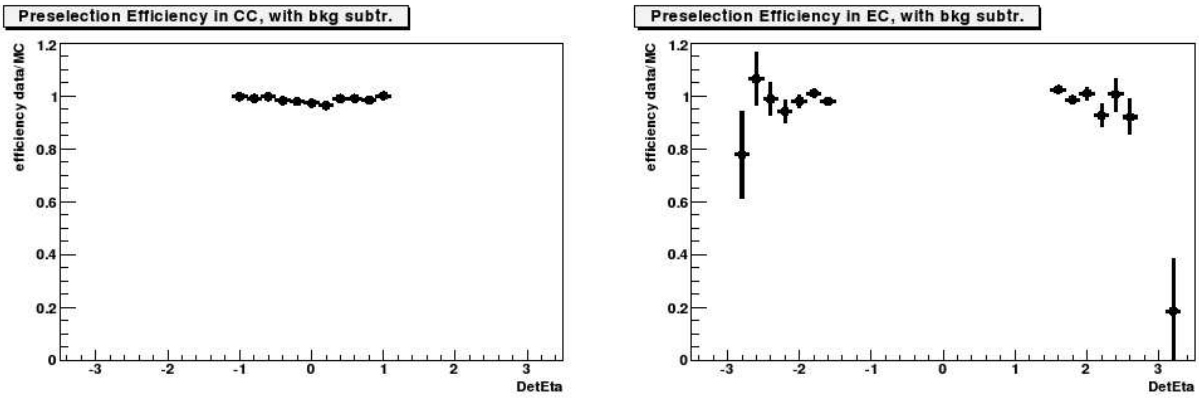

Figure 8.4.: The preselection efficiency correction as a function of η_{det} measured in $Z \rightarrow ee$ events in data and Monte Carlo.

Electron Post-Preselection Efficiency Corrections

The post-preselection requirement used in the $ee\ell$ analysis, is the likelihood requirement. The efficiency measurements are done in different bins of η_{det} for fiducial CC electrons, non-fiducial CC electrons and EC electrons. The resulting ratio of data and Monte Carlo is applied to all Monte Carlo samples in the $ee\ell$ analysis when the likelihood cut is performed. Figure 8.5 (upper) shows the efficiency in data and Monte Carlo as a function of η_{det} (left) and p_T (right), and the resulting Monte Carlo efficiency (bottom) as a function of η_{det} (left) and p_T (right).

8.2. Effective Trigger Efficiency

The efficiency corrections described in the previous chapter, were derived using $Z \rightarrow \ell\ell$ decays, which means that the transverse momenta of the leptons are higher than ∼15 GeV. To take into account possible inefficiencies not modeled by the Monte Carlo towards lower values of lepton-p_T, an effective trigger weight has been derived.

Triggers are also not simulated in the Monte Carlo, and trigger efficiencies have to be measured in data and then applied as a weight to the Monte Carlo. The efficiencies for all the triggers used in the analyses presented here, can be measured and combined to a logical OR. However, since both the analyses presented in this thesis rely on a large number of triggers, it is not practical to calculate the trigger efficiency of each trigger separately and then combining them. Instead, an effective trigger turn-on is calculated by comparing the p_T distribution in data and Monte Carlo. The trigger selection for the analyses presented in this thesis was described in Section 7.1.3. In the following, *turn-on* will mean trigger efficiency as a function of p_T. In both the $ee\ell$ and the $\mu\mu\ell$, the turn-on is derived at the preselection stage of the analysis.

The effective trigger weight is derived by subtracting the QCD contribution from data in the lepton p_T distribution and divide the resulting distribution with the lepton p_T of the sum of the MC processes. In the $ee\ell$ analysis, the p_T distribution of the leading electron in data and

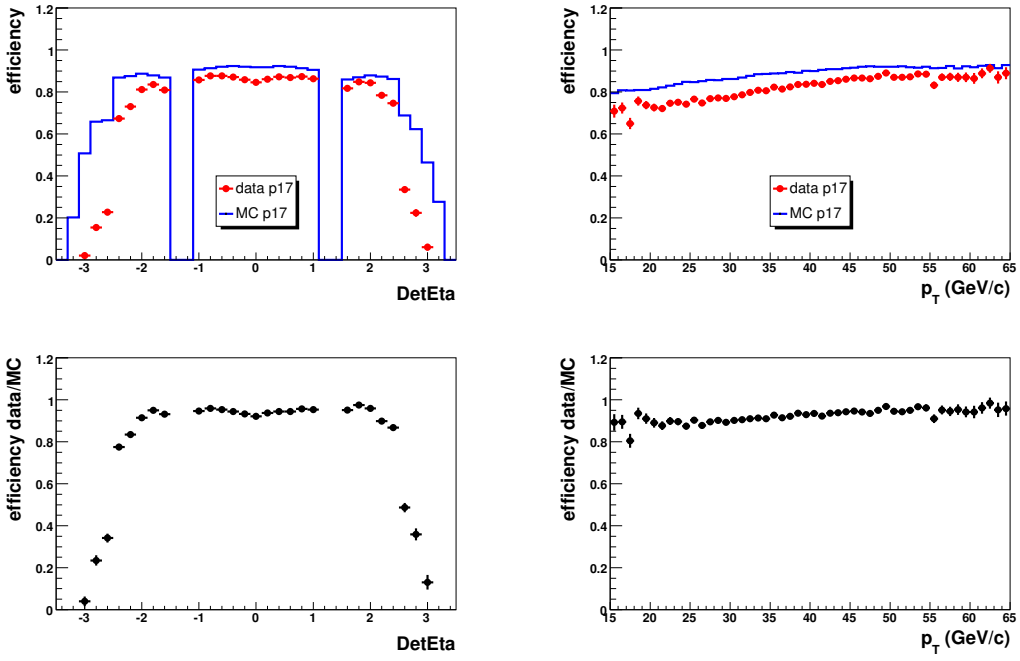

Figure 8.5.: Efficiency for likelihood>0.2 as a function of η_{det} (left) and p_T (right). Upper plot is efficiency for data (red dots) and Monte Carlo (blue histogram). The lower plot is the resulting Monte Carlo efficiency correction as a function of η_{det} and p_T respectively.

Monte Carlo are compared, and in the $\mu\mu\ell$ analysis, the p_T distribution of the next to leading muon is compared. The resulting weight is applied as a function of lepton p_T to all Monte Carlo processes.

In Figure 8.6, the p_T spectra of the leading and next to leading electron without reweighting are shown at preselection level. Figure 8.7 shows the same p_T distributions after reweighting is applied. Figure 8.8 shows the p_T spectra at preselection level in the muon analysis and in the low-p_T region of the next to leading muon, a small discrepancy is observed. The result of the reweighting procedure is shown in Figure 8.9. Figure 8.10 (left) shows the reweighting that is applied to the leading electron to account for trigger inefficiencies in the $ee\ell$ analysis, while the plot on the right shows the distribution used for the correction of the trigger effect in the $\mu\mu\ell$ analysis.

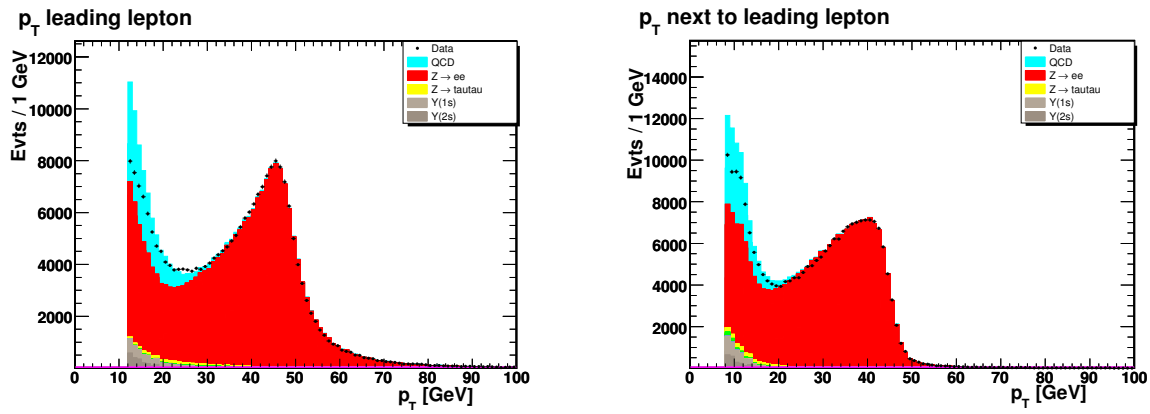

Figure 8.6.: The p_T distributions of the two electrons in the $ee\ell$ analysis without p_T dependent reweighting applied. All other corrections are applied to the Monte Carlo.

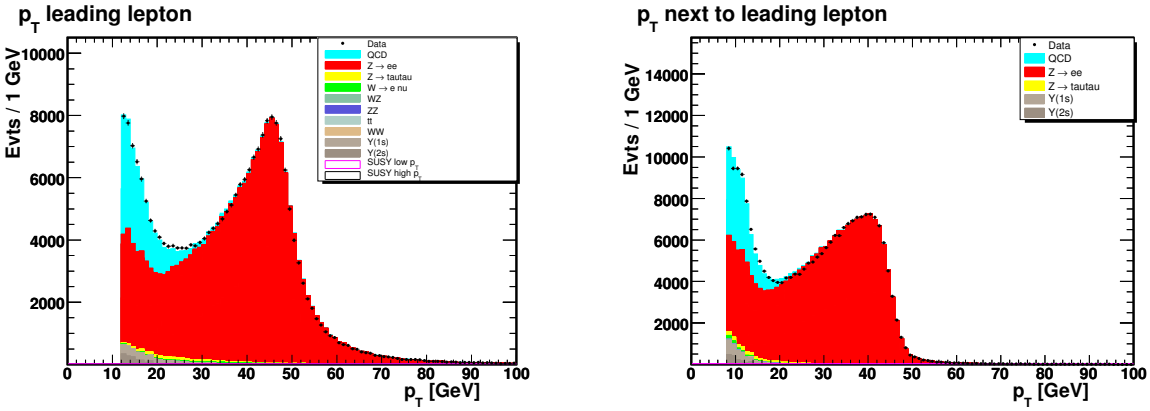

Figure 8.7.: The p_T distributions of the two electrons in the $ee\ell$ analysis when p_T dependent reweighting is applied. All other corrections are also applied to the Monte Carlo.

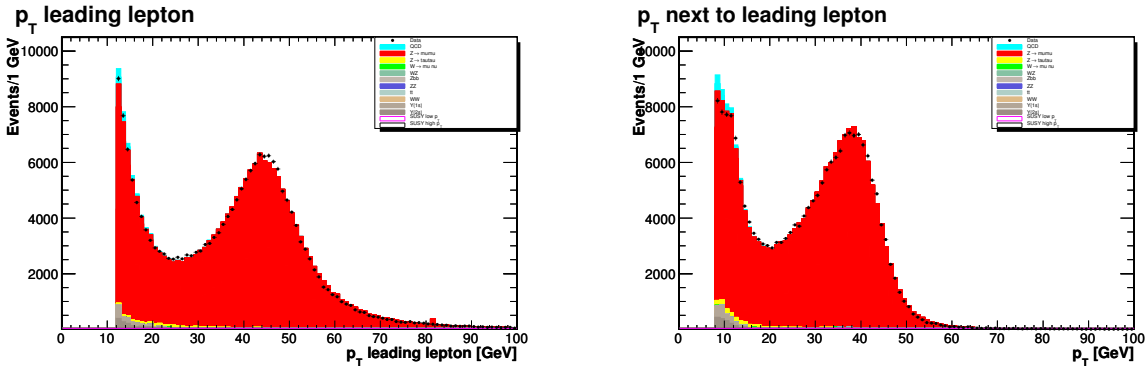

Figure 8.8.: The p_T distributions of the two muons in the $\mu\mu\ell$ analysis at preselection level. No p_T dependent trigger-weights applied.

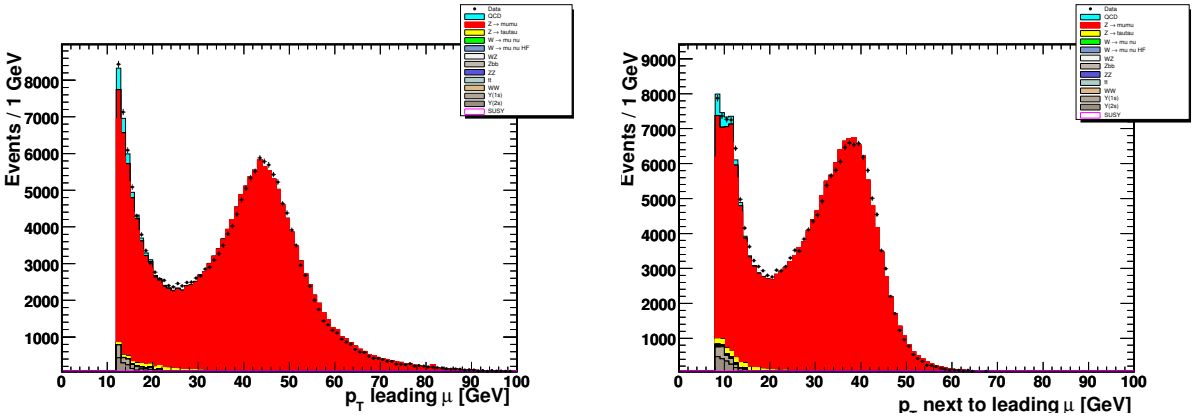

Figure 8.9.: The p_T distributions of the two muons in the $\mu\mu\ell$ analysis at preselection level. p_T dependent trigger-weights are applied.

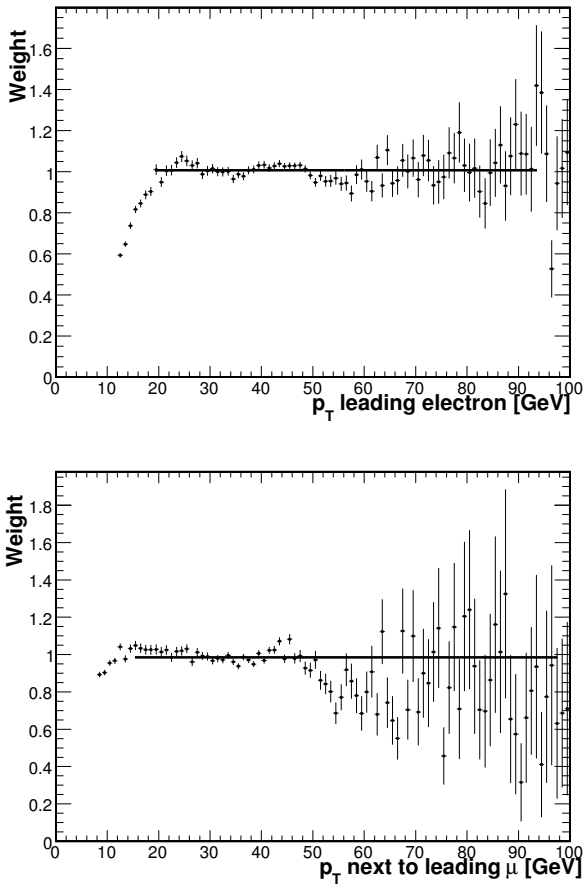

Figure 8.10.: Distribution used for trigger reweighting of the leading electron (left) and next-to-leading muon (right) in the dielectron and dimuon analysis, respectively.

8.3. Electron Energy Resolution and Scale Corrections

The modeling of calorimeter energy scale and resolution for electrons is not perfect. This is mainly due to insufficient modeling of the electronic noise and an incomplete description of the material in front of the calorimeter. To bring the Monte Carlo simulation in better agreement with data, the reconstructed electron energy in the simulation, has to be smeared and scaled.

To study the different energy scale and resolution in data and Monte Carlo, the dielectron invariant mass around the Z resonance is studied for different detector regions. The $ee\ell$ analysis presented in this thesis, uses electrons up to $|\eta_{det}|$ <3.0 without constraints on the azimuthal angle ϕ. This includes less sensitive detector regions (non-fiducial regions) which consist of the ϕ-cracks at the borders of a calorimeter tower in CC ($|\eta_{det}| < 1.1$) and the intercryostat region which corresponds to 1.1< $|\eta_{det}|$ <1.5 (see Section 4.3.3). These regions are characterized by worse electron p_T resolution hence the electron energy is scaled and smeared differently for fiducial and non-fiducial detector regions. The different detector regions studied are the following:

- central fiducial ($|\eta_{det}| < 1.1$)
- central non-fiducial (ϕ-cracks)
- intercryostat region (η-non-fiducial, $1.1 < |\eta_{det}| < 1.5$)
- end cap region ($1.5 < |\eta_{det}| < 3.0$)

The study is done separately for different data taking periods (Run IIa and Run IIb) because the resolution in data can change and the Monte Carlo simulation of the two data taking epochs are treated differently.

The energy is smeared with a Gaussian according to $E_{corr} = \epsilon E$ where $\epsilon = (scale + C + S)$. In this expression, C is a random number drawn from a Gaussian, Gauss$(0, scale \times c)$, where c depends on the detector region and data taking period. Similarly, S is a random number taken from a Gaussian, Gauss$(0, \frac{s}{(\sqrt{scale \times E})})$, where E is the un-smeared energy and s a parameter that depends on detector region and data taking period. S takes into account that the energy resolution for electrons, $\frac{\Delta E}{E}$, scales with $\frac{1}{\sqrt{E}}$.

In the central region ($|\eta_{det}| < 1.1$), the energy is smeared according to an asymmetric Gaussian. It is found that smearing with a symmetric Gauss provides good agreement on one side of the Z-peak, while oversmearing the other. Smearing with an asymmetric Gaussian provides the possibility to smear less on one side of the Z-peak.

In Appendix A.2, the mass distribution for various detector regions and for different data taking periods are presented. The impact of the smearing and scaling procedure is shown in Figure 8.11 for Run IIa and in Figure 8.12 for Run IIb where the improvement of the description of the di-electron invariant mass distribution is visible. In Table 8.1 the smearing and scaling parameters applied to Run IIa and Run IIb Monte Carlo electrons, are listed.

The Monte Carlo overestimates the probability of reconstructing the ϕ of an electron in the ϕ-non fiducial region, defined as $|\phi - \phi_0| < 0.02$ where ϕ_0 is the center of the ϕ-crack. A Monte

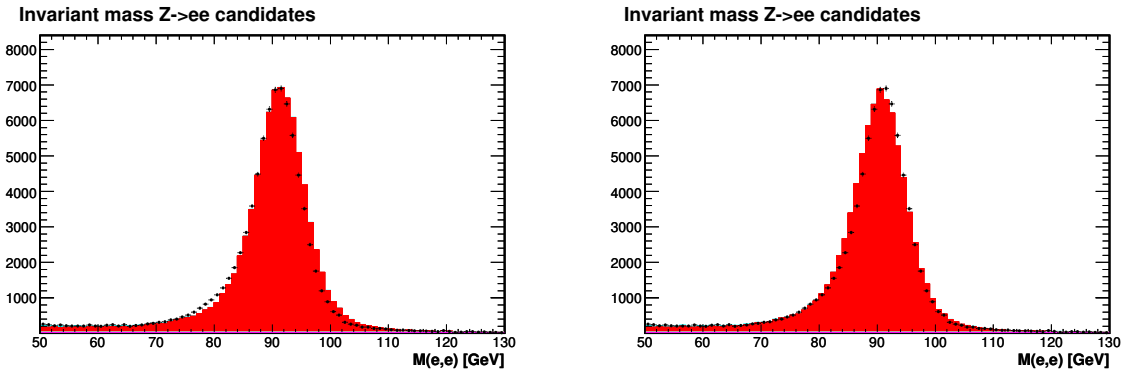

Figure 8.11.: Invariant di-electron mass in the Run IIa dataset. In the left plot no additional smearing or scaling is applied. In the right plot the smearing and scaling derived for this study are applied. In both plots, the Monte Carlo is corrected for the over estimation of electrons in ϕ-cracks.

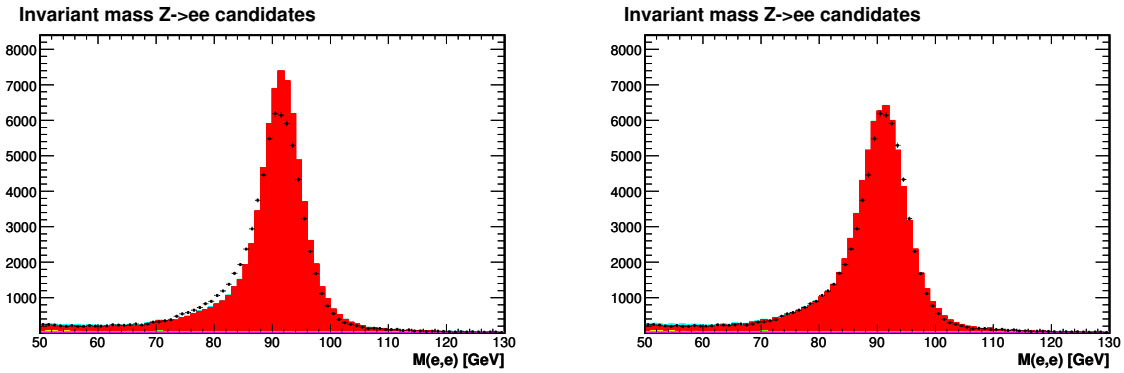

Figure 8.12.: Invariant di electron mass in the Run IIb dataset. In the left plot no additional smearing or scaling is applied, while in the right plot the smearing and scaling derived for this study are applied. In both plots, all other corrections are applied.

Carlo efficiency correction of 0.51 ± 0.01 is derived for electrons in ϕ-cracks. The weights are derived by comparing the invariant mass distribution in data and Monte Carlo where one electron is fiducial and one electron is ϕ-non-fiducial.

After the scaling and smearing are applied, there is still a disagreement between data and Monte Carlo that can be observed from Figures 8.11 and 8.12. However, the agreement has improved on the lower sholder of the Z peak, which is the most important for the analysis presented here, since the search region is restricted to lower values of the di-electron invariant mass (see Section 9.3.2).

Table 8.1.: Smearing and scaling parameters applied to electron energy for Run IIa and Run IIb Monte Carlo events.

	Run IIa		Run IIb	
Region	Smearing	Scale	Smearing	Scale
CC fiducial	0.014	0.998	0.032	1.0025
ϕ non fiducial	0.033	0.957	0.075	0.952
η non fiducial	0.0021	1.0	0.004	0.965
EC	0.0	0.991	0.014	0.993

8.4. Muon Smearing

The momentum resolution of muons in the Monte Carlo does not accurately reproduce the resolution in data. To reproduce the experimental resolution, an extra smearing is derived and applied to the transverse momentum of muons in the Monte Carlo simulation. Because the experimental resolution changes with time, different smearing is applied to Monte Carlo that describes different data taking periods. This is done in a way that the correct fraction of Monte Carlo is smeared according to different data taking epochs.

Figure 8.13 shows the M(μ, μ) invariant mass distribution at the analysis preselection level for the whole data taking period. In the upper plot, no additional muon momentum smearing has been applied, while in the bottom plot, the smearing has been applied. The impact of the smearing is clearly visible in the high mass tail.

The muon transverse momentum in Run IIa Monte Carlo (see 7.1) is smeared according to equation 8.3 [102] while Run IIb Monte Carlo is smeared according to equation 8.4 [103].

$$\frac{1}{p_T} \rightarrow \frac{1}{p_T} + (\mathrm{A} + \frac{\mathrm{B}}{p_T}) * \mathrm{G}_1(0,1) \tag{8.3}$$

$$\frac{1}{p_T} \rightarrow \frac{1}{p_T} + \mathrm{A}\ \mathrm{G}_1 + \frac{\mathrm{B}\sqrt{cosh\ \eta}}{p_T}\mathrm{G}_2 \tag{8.4}$$

where A and B are parameters that depend on number of hits in the tracking detector and run number. G_1 and G_2 are two independent random numbers distributed according to a Gaussian function with a mean value of 0 and width of 1. The smearing parameters for Run IIa Monte Carlo are listed in Table 8.2 and in Table 8.3 for Run IIb Monte Carlo.

8.5. Muon Track χ^2 Reweighting

The track fit χ^2 per degree of freedom distribution (χ^2/ndof) is not well described in Monte Carlo. The reason for this problem could be different hit resolution in data and Monte Carlo.

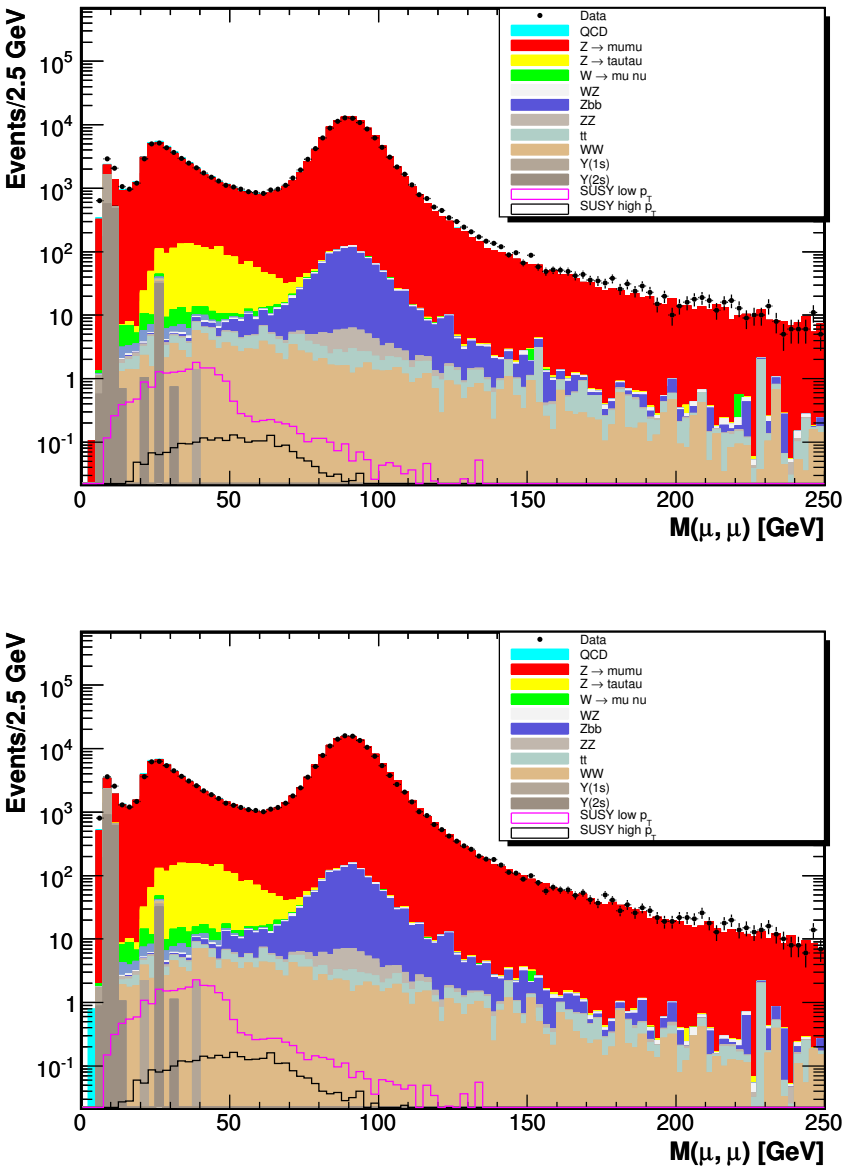

Figure 8.13.: Di-Muon invariant mass at preselection level. In the upper plot, no additional momentum smearing is applied. The muon transverse momentum has been smeared according to 8.3 and 8.4 in the lower plot. The impact of the smearing is clearly visible at high invariant mass.

Table 8.2.: Smearing parameters for the Run IIa data taking period [102].

	Run<200000		Run>200000	
Muon type	A	B	A	B
SMT hits η <1.6	0.00313	-0.0563	0.0308	-0.0370
SMT hits η >1.6	0.00273	-0.0491	0.00458	-0.0550
no SMT hits	0.00509	-0.0916	0.00424	-0.0509

Table 8.3.: Smearing parameters for the Run IIb data taking period [103].

Muon type	A	B
SMT hits η <1.6	0.0023	0.025
SMT hits η >1.6	0.0039	0.037
no SMT hits	0.0037	0.033

Another explanation could be that there are more hits from other tracks in data than in Monte Carlo, which will cause a worse χ^2/ndof in data.

To address this issue, a track χ^2/ndof dependent reweighting is derived at the preselection level in the $\mu\mu\ell$ analyis. At this stage, the sample is dominated by real muons from $Z \to \mu\mu$ decays. Figure 8.14 shows the χ^2/dof distribution for the leading and next to leading muon before reweighting and Figure 8.15 after reweighting. A large discrepancy can be observed for large χ^2/ndof values.

The reweighting is derived for both muons separately and the weights are applied to the event as a function of the track χ^2/ndof of the two muons. Since the correction is derived for real muons, it is not applied to fakes. For example, in $W(+jets) \to \mu\nu$ samples, this procedure is only applied to the leading muon.

The reweighting improves the agreement between data and Monte Carlo especially in the tail of the invariant mass distribution. Figure 8.16 shows the invariant mass distribution at preselection level in the $\mu\mu\ell$ analysis before (left) and after (right) the reweighing is applied. The weights as a function of track χ^2 for the leading and next to leading muon are shown in Fig. 8.17.

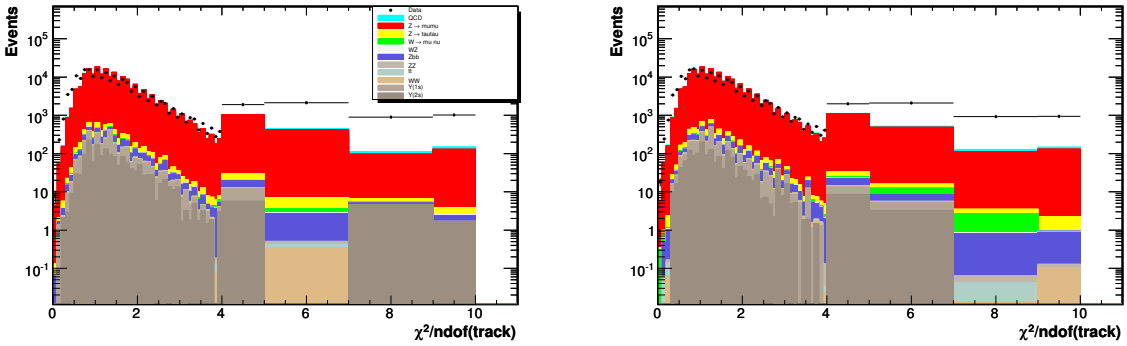

Figure 8.14.: χ^2/dof for leading muon (left) and next to leading muon (right) before χ^2 reweighting has been applied to both muons. All other corrections are applied.

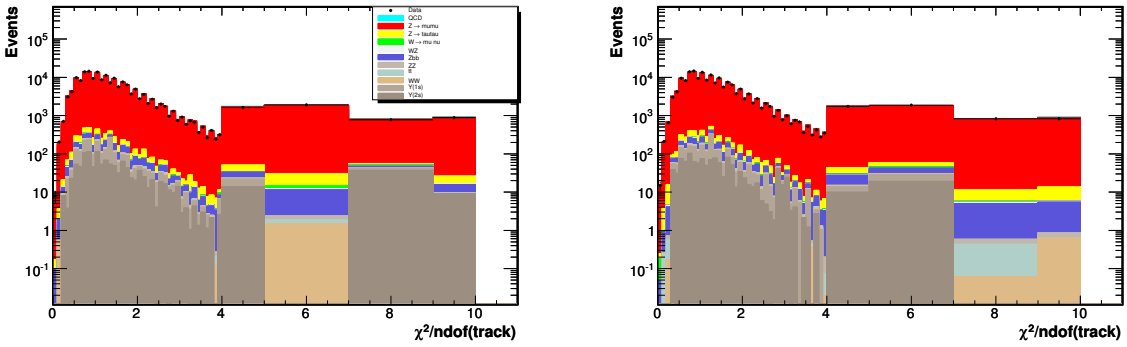

Figure 8.15.: χ^2/dof for leading muon (left) and next to leading muon (right) after χ^2 reweighting has been applied to both muons. All other corrections are also applied.

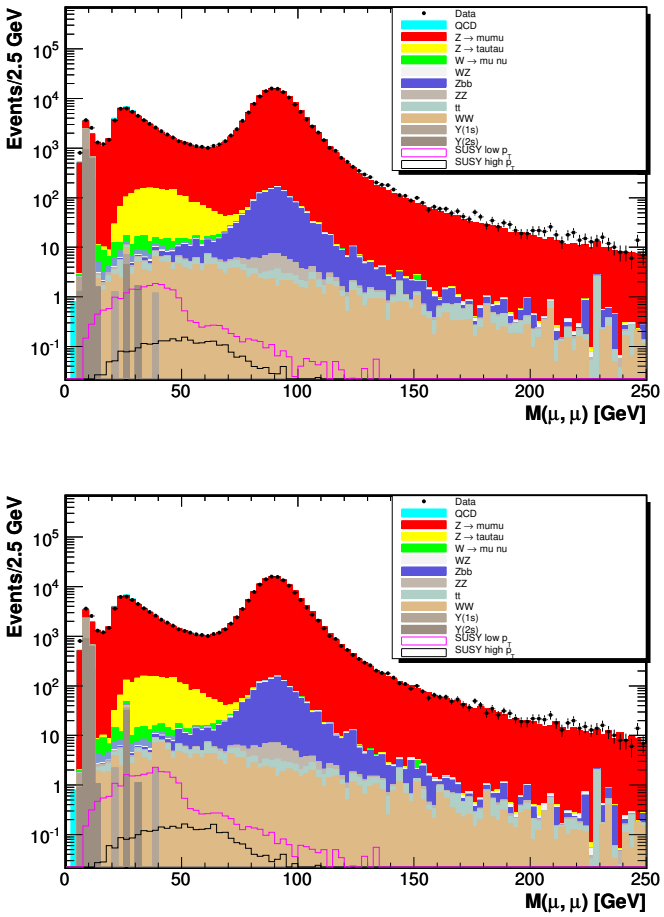

Figure 8.16.: Invariant mass distribution in the $\mu\mu\ell$ analysis at preselection level before (upper) and after (lower) χ^2/ndof reweighting. The impact of the reweighting is observed in the tail of the distribution. All other corrections are applied.

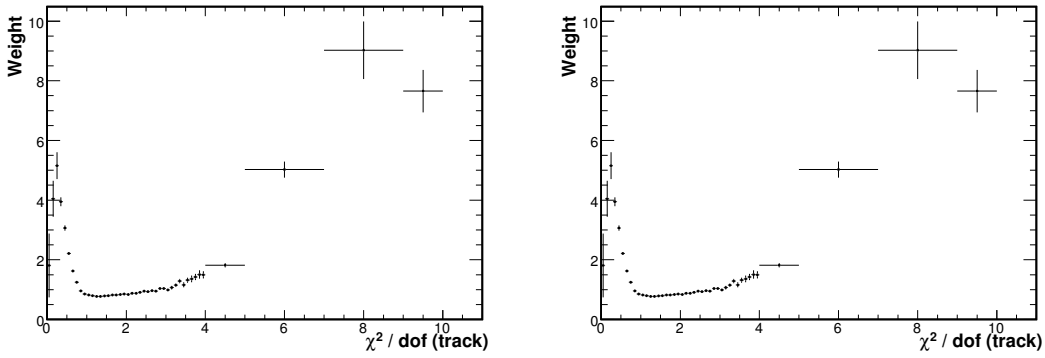

Figure 8.17.: The χ^2 weight as a function of χ^2 of leading muon (left) and next to leading muon (right).

8.6. Z-p_T Reweighting

The distribution of the transverse momentum of the Z boson, $p_T(Z)$ is not properly described by PYTHIA. The reason is that PYTHIA underestimates the transverse momenta of the Z boson, especially in events with jets from higher order corrections, due to the fact that PYTHIA is a leading order generator and does not use the whole matrix element. Therefore, a correction based on the differential Z boson production cross section $\frac{d\sigma}{dp_T}$ as measured in $Z/\gamma^* \to \mu\mu$ events in RunI and RunII data [104], is derived. Figure 8.18 shows the ratio of the number of events in the tuned and default Monte Carlo simulation in four different mass windows. These ratios have been fitted using a modified Fermi function and the correction factors, are used to reweight the $Z/\gamma^* \to \ell\ell$ Monte Carlo. For the mass bin 5 GeV $< M(Z/\gamma^*) <$ 15 GeV, the same function as in the 15-30 GeV mass window has been used and for the $M(Z/\gamma^*) >$ 250 GeV mass window, the same function as for 130 GeV $< M(Z/\gamma^*) <$ 250 GeV is applied. Additional correction factors are applied to keep the overall normalization constant. The same procedure is applied to the W boson and the WW system. W Monte Carlo is reweighted as a function of the transverse momentum of the W boson. The same function as for the Z boson in the mass range 60 GeV to 130 GeV is used. The transverse momentum of the WW system is calculated on generator level and the weighting factors applied as a function of the p_T of the WW system.

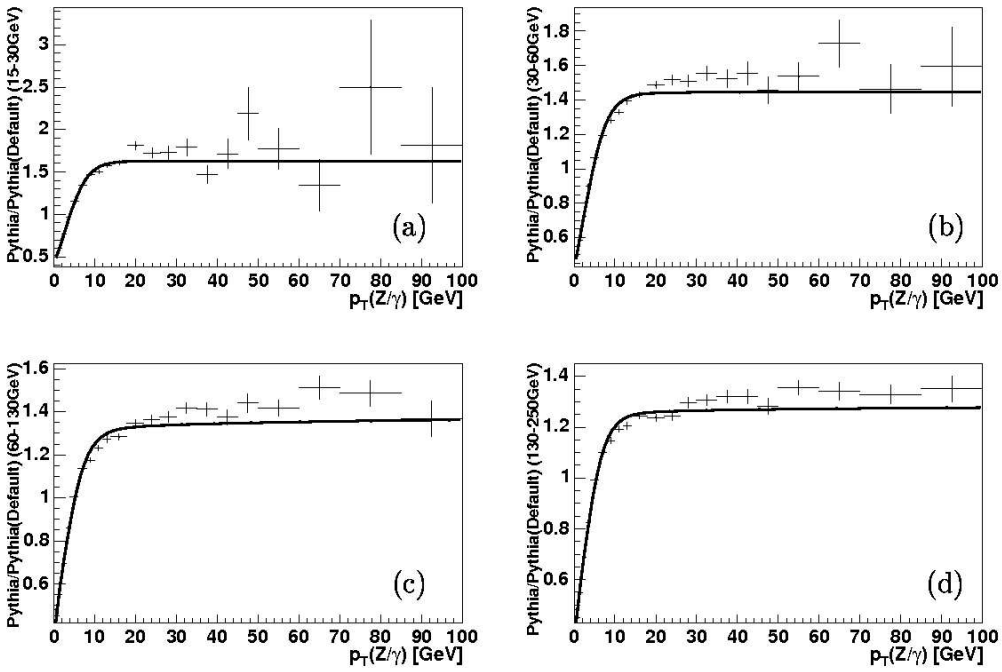

Figure 8.18.: Ratio between tuned and default PYTHIA 6.202 Monte Carlo as a function of the transverse momentum of the Z boson, $p_T(Z)$. The following four mass ranges were considered: (a) 15 GeV $< M(Z/\gamma^*) <$ 30 GeV (b) 30 GeV $< M(Z/\gamma^*) <$ 60 GeV (c) 60 GeV $< M(Z/\gamma^*) <$ 130 GeV (d) 130 GeV $< M(Z/\gamma^*) <$ 250 GeV [104].

8.7. Reweighting of the Instantaneous Luminosity Profile

As described in Section 5.2.4, the Monte Carlo events are overlaid with Zero Bias events from data to simulate noise and additional interactions in the same bunch crossing. The number of additional interactions depends strongly on the instantaneous luminosity. To bring the luminosity profile in Monte Carlo better in agreement with the data profile, Monte Carlo is reweighted as a function of instantaneous luminosity. This needs to be done because there are several efficiencies that depend on the instantaneous luminosity, for example the efficiency for reconstructing an isolated track, of importance to the analyses presented here. The instantaneous luminosity profile is measured in an unbiased data set both for the EMInclusive skim and the MUInclusive skim. For Monte Carlo simulation, the instantaneous luminosity is taken from the Zero Bias overlay and the profiles for simulation are measured in the different samples before any cuts are applied. The profiles in simulation were reweighted to match the profile measured in data. The impact of this procedure to the overall normalization is derived and all Monte Carlo samples are adjusted for this effect. Figure 8.19 shows the luminosity profile after reweighting in the $ee\ell$ analysis (left) and in the $\mu\mu\ell$ analysis (right). Both plots are from the analysis preselection. To avoid large weights from this reweighting procedure, the maximum value of weights is set to 3.0.

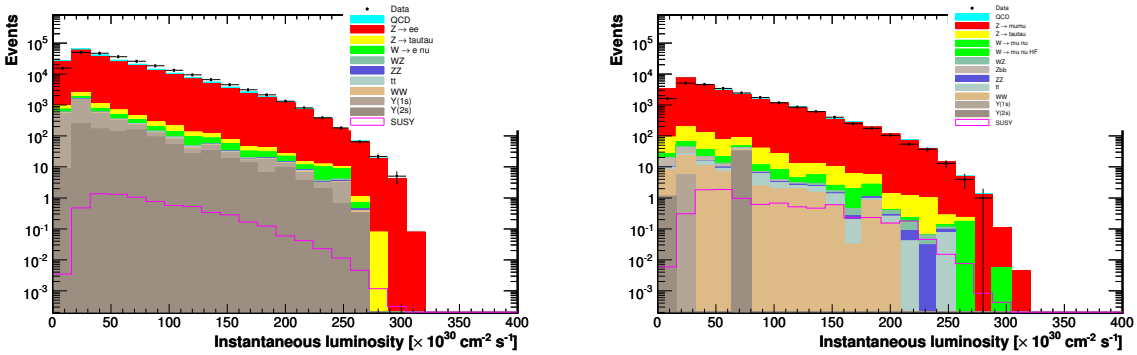

Figure 8.19.: Profile of the instantaneous luminosity at preselection level in the $ee\ell$ analysis (left) and in the $\mu\mu\ell$ analysis after cuts to reject resonant $Z \to \mu\mu$ production (right). The weight from the luminosity reweighting is required to be below 3.0.

8.8. Track Smearing, Reconstruction Efficiency and χ^2/ndof Reweighting.

As described in Section 8.4, the $1/p_T$ resolution of the tracker is not modeled correctly in the detector simulation. The transverse momentum of all tracks that pass the reconstruction treshold is consequently smeared according to equations 8.3 and 8.4 with the same parameters as listed in Tables 8.2 and 8.3.

Due to different efficiencies for reconstructing tracks in data and Monte Carlo, efficiency corrections need to be applied to the Monte Carlo. This is described in 8.1.1.

In section 8.5, the χ^2/ndof distribution was studied for muons. The disagreement in the χ^2/ndof is not restricted to muon tracks. Since the track χ^2/ndof distribution is not properly described by Monte Carlo, the distribution is reweighted to improve the agreement.

8.9. Description of the Track Isolation Variable

Both the $ee\ell$ and the $\mu\mu\ell$ analyses rely on the requirement of an isolated track in addition to the tracks of the two leptons.

Figure 8.20 shows the isolation in the tracker (See 4.3.1) for the additional track in the $ee\ell$ analysis at preselection. Left is shown the distribution of track isolation for tracks with transverse momentum larger than 2 GeV and right is shown the distribution for tracks with transvserse momentum larger than 4 GeV. The plots show good agreement between data and Monte Carlo. At this stage, the selection is dominated by $Z \to ee$ events. Figure 8.21 shows the same distribution at a stage of the selection where $W \to \ell\nu$ events dominate: before an additional track with $p_T > 4$ GeV is required in the event. Monte Carlo underestimates the number of events with low track isolation for tracks with $p_T > 4$ GeV, which can be seen as a discrepany in the Figure 8.21 (right). The agreement is better for tracks with $p_T > 2$ GeV which is seen in Figure 8.21 (left).

The track isolation variable is reweighted in both the $ee\ell$ and the $\mu\mu\ell$ analysis for $W \to \ell\nu$ Monte Carlo in events where the transverse momentum of the third track is greater than 4 GeV. Figure 8.22 shows the track isolation variable in the $ee\ell$ analysis for tracks with $p_T > 4$ GeV after the reweighting has been performed, and shows a good agreement between data and Monte Carlo.

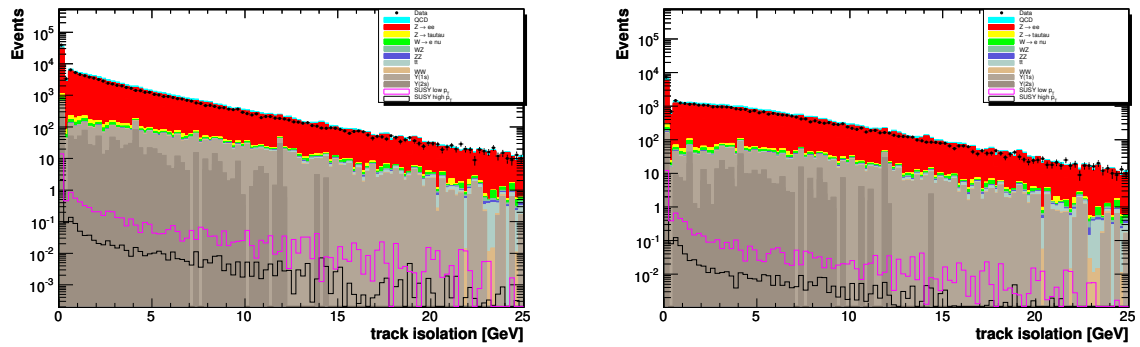

Figure 8.20.: Track isolation at preselection level for tracks with $p_T > 2$ GeV (left) and for tracks with $p_T > 4$ GeV.

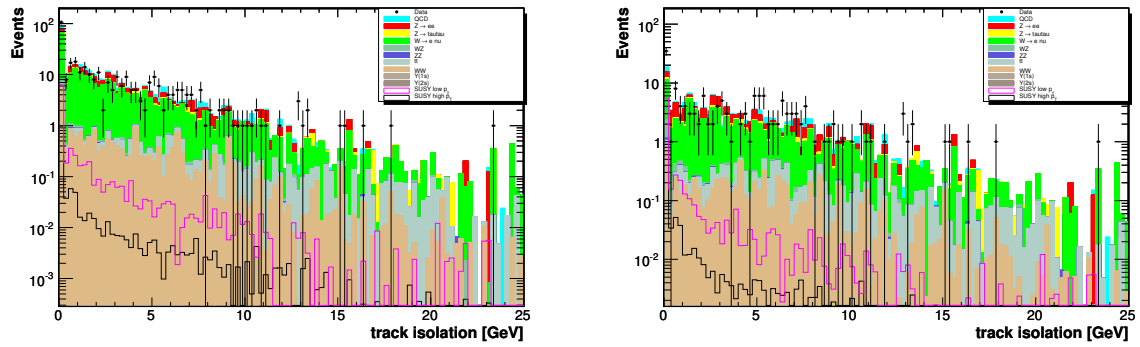

Figure 8.21.: Track isolation before reweighting the $W \to \ell\nu$ Monte Carlo, before requiring an additional track with p_T >4 GeV in the event. In the left plot, the third track must fulfill $p_T > 2$ GeV, while the p_T cut in the right plot is 4 GeV.

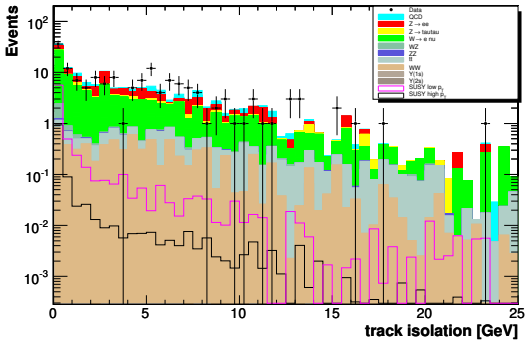

Figure 8.22.: Track isolation after requiring a track with $p_T > 4$ GeV in the event. The W Monte Carlo has been reweighted as a function of track isolation for tracks with $p_T > 4$ GeV. The description improves with applying the reweighting.

8.10. Reference Signals

Since the selection of the tri-lepton signal relies on an accurate efficiency estimation from the simulation of the reconstruction and identification of electrons and muons, reference signals are defined. This section presents these reference sa

8.10.1. $Z \to \ell\ell$

The di-electron invariant mass is shown in Figure 8.11 and Figure 8.12. The di-muon invariant mass is shown in Figure 8.16 (lower). After the various corrections described above have been applied, a good agreement between data and Monte Carlo is observed.

8.10.2. $W + (jets) \to \ell\nu$ Control Sample

The $W \to \ell\nu$ production constitutes an important background for the trilepton signal. Even though only one lepton is produced in leptonic W boson decays, jets and photons can produce detector signatures that can be misidentified as isolated leptons. The neutrino is the source of $\not\!\!E_T$. To study this background, a W-enriched data sample is defined in both analyses. In the $ee\ell$ analysis, the sample is defined as follows:

- $p_T^1 > 20$ GeV, $p_T^2 > 8$ GeV, lhood1>0.8, lhood2>0.2, dz(ℓ,PV)<1.5 cm.
  For QCD, the likelihood cuts are reversed.
- $\not\!\!E_T$ >40 GeV, $M_T^{1,2} > 20$GeV, Sig($\not\!\!E_T$) > 8 (see Section 9.2.3)
- Transverse mass of leading electron, M_T^1 >40 GeV
- 10 GeV $< M(\ell,\ell) <$ 70 GeV

In the $\mu\mu\ell$ analyses, the last three steps above are the same. In the first step, the likelihood requirement on the leptons is replaced with isolation cuts.

- $p_T^1 > 20$ GeV, $p_T^2 > 8$ GeV, track- and calo-isolation 4.0 GeV for both muons, dz(ℓ,PV)<1.5 cm

To define the QCD contribution in the $W \to \mu\nu$ sample, a sample with inverted isolation cuts is used as described in section 7.3.

Making this selection produces a clean W enriched sample, as shown in Figure 8.23 (left) which presents the transverse mass of the leading electron and $\not\!\!E_T$, and Figure 8.24 which shows the transverse mass between the leading muon and the $\not\!\!E_T$. The fact that the selections require a second lepton, also shows that the fakerate is properly modeled.

As described in Section 7.2.1, the ALPGEN [50] event generator was used to simulate the $W + jets \to \ell\nu$ background. ALPGEN calculates the full matrix element instead of using the parton shower method for ISR/FSR (see sec. 5.1). Therefore, the jet p_T spectra are better described with ALPGEN compared to PYTHIA. Since jets are faking the second and third lepton in the $W + (jets)$ events that pass the selection criteria in the analyses, it is important that the description of these quantities are as accurate as possible.

As mentioned in Section 7.2.1, K–factors are applied to the LO cross section. The factors are applied as a function of light parton multiplicity. A K–factor of 1.4 is applied to 2-5 W-light parton samples [105]. In order to match the total cross section of 7750 pb, the 0lp and 1lp samples a K–factor of 1.15 is applied. For the $Wb\bar{b}$ and $Wc\bar{c}$ samples, an additional K–factor of 2 is used [106].

The transverse mass of the leading electron and the missing transverse energy in the $W(+jets) \to e\nu$ selection after applying the K–factors is shown in Figure 8.23 (left). In Figure 8.23 (right), the

number of jets distribution is shown. Figure 8.24 shows the transverse mass distribution (left) and the jet multiplicity distribution (right) in the $W(+jets) \rightarrow \mu\nu$ sample. A reasonable agreement between data and Monte Carlo is observed. A 20% systematic uncertainty is assigned to the normalization of the $W(+jets)$ background (see Section 9.4).

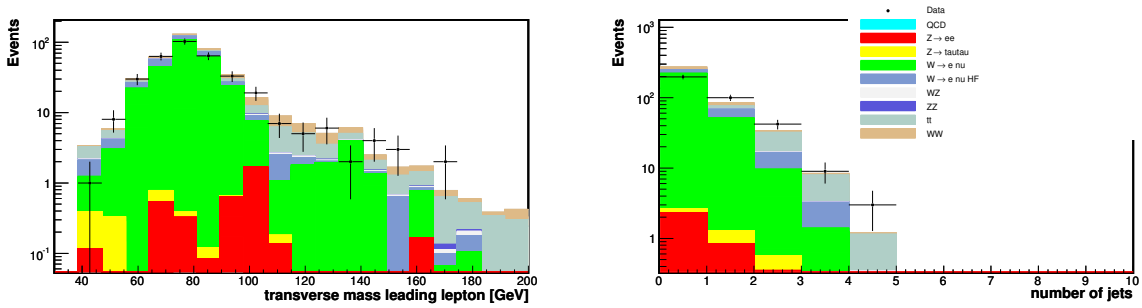

Figure 8.23.: Transverse mass of the leading electron and missing transverse energy (left) and number of jets (right) in the $W \rightarrow e\ell$ enriched sample. A K–factor of 1.15 has been applied to the W cross section for light parton multiplicities 0 and 1 and a K–factor of 1.4 has been applied to the other light parton multiplicities. The heavy flavor samples have been scaled up by a factor 2.8

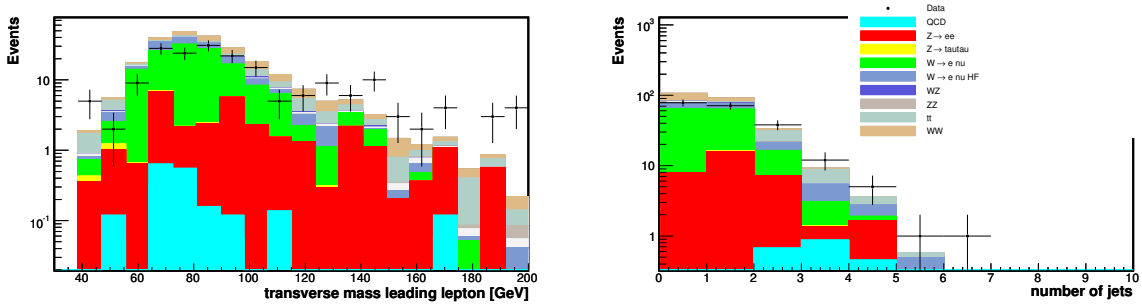

Figure 8.24.: Transverse mass of leading muon and $\not\!\!E_T$ and number of jets in the $W \rightarrow \mu\nu$ sample. A K–factor of 1.15 has been applied to the W cross section for light parton multiplicities 0 and 1 and a K–factor of 1.4 has been applied to the other light parton multiplicities. The heavy flavor samples have been scaled up by a factor 2.8

8.10.3. WZ, WW and $t\bar{t}$ Control Samples

$WZ \rightarrow 3\ell$ Signal

Figure 8.25 shows a data Monte Carlo comparison of the di-electron invariant mass in a WZ sample. The WZ sample is essentially the high-p_T $ee\ell$ selection, which will be described in Section 9.3. Important requirements to define this sample are the following:

- $p_T^{e1} > 18$ GeV, $p_T^{e2} > 16$ GeV

- $\not\!\!E_T >$ 20 GeV
- transverse momentum of additional track in event larger than 12 GeV (see Section 9.3.5)
- no cut on di-electron invariant mass

Figure 8.25 shows that the analysis selects a WZ signal in data that in both shape and rate is consistent with the Monte Carlo expectation.

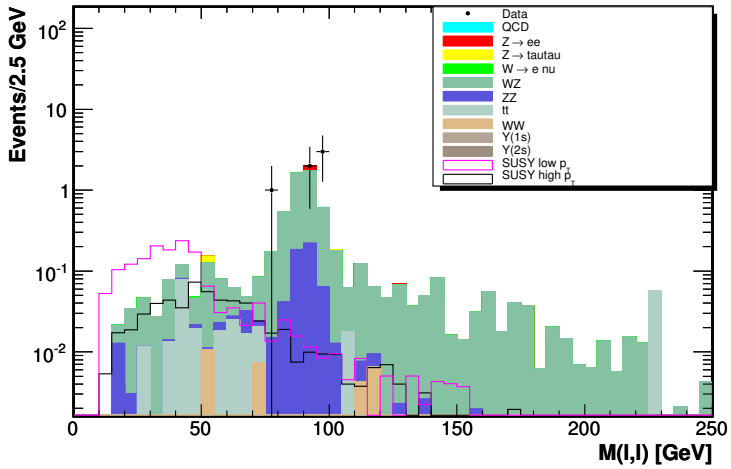

Figure 8.25.: The invariant di-electron mass after the cuts described in the text are applied. A clean WZ signal is observed in both data and Monte Carlo.

$WW \to \ell\ell$ Signal

To cross check the contribution from WW production, a region of phase space where WW production is dominating, was defined. Figure 8.26 (left) shows the transverse momentum of the next to leading electron in a sample defined as:

- $p_T^{e1} > 12$ GeV, $p_T^{e2} > 12$ GeV
- transverse momentum of additional track in event larger than 4 GeV
- $\not\!\!E_T >$ 24 GeV
- 30 GeV $< M(e,e) <$ 80 GeV or $M(e,e) >$ 110 GeV

A good agreement betweend data and Monte Carlo is observed in the tail of the distribution.

$t\bar{t}$ Signal

Figure 8.26 (right) shows the distribution of the scalar sum of all the identified jets in the event. This quantity is called H_T. Since two hard b-jets are present in a $t\bar{t}$ decay, the $t\bar{t}$ is expected to dominate the H_T distribution at higher values of H_T. Figure 8.26 shows a good agreement between data and Monte Carlo at high H_T values. The sample was defined as follows:

- $p_T^{e1} > 12$ GeV, $p_T^{e2} > 10$ GeV
- transverse momentum of additional track in event larger than 4 GeV
- $\not{E}_T >$ 25 GeV

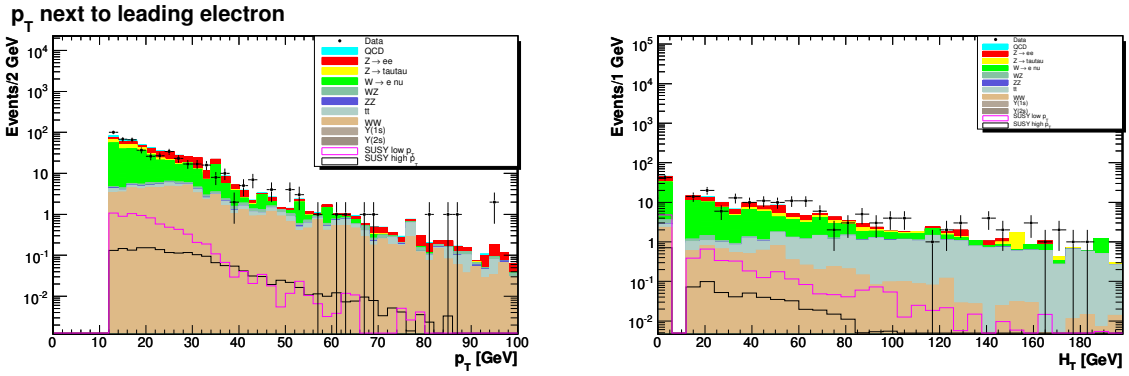

Figure 8.26.: The transverse momentum of the next to leading electron (left) in a WW enriched sample. The contribution from WW is dominating in the tail of the distribution, and a good agreement between data and Monte Carlo is observed.
The scalar sum of jet transverse momenta (right). At higher values $t\bar{t}$ events dominate due to the presence of hard b-jets in the event.

9. The $ee\ell$ and $\mu\mu\ell$ Analyses

This chapter describes in detail the $\mu\mu\ell$ and the $ee\ell$ analyses. The selection criteria developed to separate the trilepton signal from the Standard Model background processes are motivated and described.

For both the $\mu\mu\ell$ and the $ee\ell$ selections, a *high-p_T* selection and a *low-p_T* selection are defined. In both analyses, both the low- and high-p_T selections are optimized for best expected limit. The chapter starts with motivating and describing the optimization procedure, before the low- and high-p_T selections in the $\mu\mu\ell$ analysis are discussed. Then follows the description of the $ee\ell$ low- and high-p_T selections, which is briefer since in many aspects it is close to the $\mu\mu\ell$ selection.

9.1. Optimization Procedure

The selection efficiency depends mainly on the masses of the particles that participate in the decay of the chargino and neutralino. The $(m_0, m_{1/2})$ plane is divided into two regions of interest: a *3-body region* where the slepton masses are larger than the mass of the second neutralino, ($\Delta m_{\tilde{\ell}} = m_{\tilde{\ell}} - m_{\tilde{\chi}_2^0} > 0$), and a *2-body region* where the sleptons are lighter than the second neutralino. Section 10.1 addresses the signal efficiencies within the different regions.

Signal Monte Carlo samples are used for the optimization of the selection and the determination of the signal efficiency. Samples of signal Monte Carlo have been generated for a large set of combinations of SUSY parameters (see Sections 7.2.2 and A.1). In the following, a SUSY-point will mean a certain choice of $(m_0, m_{1/2})$ parameters.

To optimize the selection, three benchmark points were selected. In the three body region, the efficiency mainly depends on the mass of the lightest chargino $\tilde{\chi}_1^{\pm}$, but also the mass difference $\Delta m_{\tilde{\ell}} = m_{\tilde{\ell}} - m_{\tilde{\chi}_2^0}$ plays a role (see Figure 10.3). In a region with large masses, high signal efficiency is expected due to leptons with large transverse momentum in the final state. A typical reference point for this scenario, on the edge of the sensitivity region, has $m_0 = 150$ GeV and $m_{1/2} = 250$ GeV. If $\tilde{\chi}_1^{\pm}$ and $\tilde{\chi}_2^0$ masses are small, the lepton momenta decrease and also the efficiency goes down. The point $m_0 = 150$ GeV and $m_{1/2} = 170$ GeV, close to the LEP limits, is chosen to reflect this scenario.

For the two body region, the reference point corresponds to the parameters $m_0 = 76$ GeV and $m_{1/2} = 184$ GeV. In Table 9.1 the mass of the lightest chargino, the next to lightest neutralino and the right handed selectron are listed for the three benchmark points. For convenience, also the mass difference between the right handed selectron and the next to lightest neutralino is given.

Table 9.1.: Parameters for SUSY point used in the optimization. All units are GeV. The point with $m_0 = 150$ GeV and $m_{1/2} = 250$ GeV has been used in the high-p_T optimization. The other two are used in the low-p_T optimization. $A_0 = 0$, tanβ=3, $\mu > 0$ for all points.

Name	m_0	$m_{1/2}$	$m_{\tilde{\chi}_1^\pm}$	$m_{\tilde{\chi}_2^0}$	$m_{\tilde{\ell}_\mathrm{R}}$	$\Delta m_{\tilde{\ell}} = m_{\tilde{\ell}_\mathrm{R}} - m_{\tilde{\chi}_2^0}$
3-body high-p_T	150	250	176.6	176.4	181.2	4.8
3-body low-p_T	150	170	106.6	109.4	167.5	58.1
2-body	76	184	117.2	119.6	110.1	-9.5

The optimization using the point with $m_0 = 150$ GeV and $m_{1/2} = 250$ GeV, is referred to as the high-p_T selection, while the optimization using the other two points is called low-p_T selection. For the low-p_T selection, the two signal points were chosen to have reference scenaria in both the three and two body region. The two low p_T points show similar behaviour, and they are combined in one selection neglecting small differences. In A.1, the masses of the lightest chargino, the next to lightest and lightest neutralino, in addition to the slepton masses are listed for all generated signal samples. The production cross section times branching fraction into three leptons is also given for each specific sample.

In the following, the optimization of both the $\mu\mu\ell$ and the $ee\ell$ low- and high-p_T selections are described. The optimization is done for best expected limit and the limit is calculated with TLimit [107]. A more detailed description of the limit setting procedure is given in Section 10.2.1. A large set of the selection criteria used in the analyses are scanned and the cut value is chosen such that it gives the the best expected 95% CL limit on the signal cross section in the absence of SUSY. To ensure that the chosen value is not just an artifact of a fluctuation of background due to limited Monte Carlo statistics, the marginal distributions for every scan are taken into consideration. The marginal distribution shows a specific quantity with all other cuts but the quantity in question applied. In all the marginal distributions in this chapter, the SUSY signal is scaled up by an arbitrary factor for visibility.

9.2. The $\mu\mu\ell$ Selection

At the beginning of this section, the preselection of the $\mu\mu\ell$ will be defined before the optimization of the two selections are described. The optimization of the low-p_T and the high-p_T selection are described in parallel. Figures of all quantities at preselection stage are presented and also before the cut on the particular quantity is made. To illustrate the optimization procedure, marginal distributions and expected limit as a function of cut value are also presented for various quantities. Tables 9.2 and 9.3 list all the selection criteria and the cut values in the low- and high-p_T $\mu\mu\ell$ analyses.

9.2.1. $\mu\mu\ell$ Preselection Cuts

The $\mu\mu\ell$ selection starts with selecting muon candidates with an isolation in the tracker of less than 4 GeV. Both muons have to come from within 1.5 cm of the primary vertex. Muon candidates in Monte Carlo events are removed from further consideration according to the difference in ID efficiency between Monte Carlo and data. The removal of muons is important for the $\not\!\!E_T$ calculation in the event. Only the remaining muons are taken into account when recalculating the $\not\!\!E_T$. Further isolation criteria are required of the muon candidates. The leading muon must be isolated with $E_{\text{iso}} < 4$ GeV in the tracker and the calorimeter. The next to leading muon must fulfill $E_{\text{iso}} < 1.5$ GeV. This tight requirement helps rejecting background processes where the second reconstructed muon lies within a jet, for example $W \to \mu\nu$ background.

The p_T distributions of the leading and next to leading muon at preselection stage are shown in Figure 9.1. In the low-p_T selection, the transverse momentum of the leading muon is required to exceed 12 GeV whereas the next to leading muon is required to have a transverse momentum in excess of 8 GeV. In the high-p_T selection, the p_T of the leading and next to leading muon are raised to 20 and 10 GeV respectively. See Figure 9.2 and Figure 9.3 for the marginal distribution and the limit as a function of cut value for next to leading muon and leading muon respectively in the high-p_T selection.

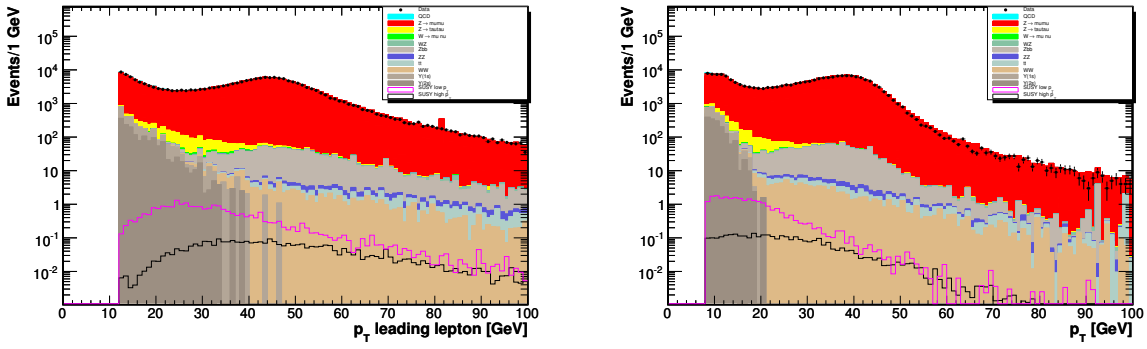

Figure 9.1.: p_T of leading muon (left) and next to leading muon (right). Both plots are shown at preselection level.

Muons from additional $p\bar{p}$ interactions (see 5.2.4) can mistakenly be considered as muons from the hard interaction. The characteristics of these muons are that they have no hits in the SMT detector, they tend to originate from further away from the primary vertex than real muons and the global chi-square χ^2_{global} (see 6.3) of these muons is worse. To reduce the background where events pass the selection due to muons from additional interactions, a chi-square χ^2_{zb}, is constructed. It is built from the χ^2_{global} and the dz(μ, PV):

$$\chi^2_{zb} = \frac{\chi^2_{global} - 1}{\sigma_{\chi^2_{global}}} + \frac{|dz(\mu, PV)|}{\sigma_{dz}} \tag{9.1}$$

The resolution of the two quantities entering χ^2_{zb}, $\sigma_{\chi^2_{global}}$ and σ_{dz}, are measured in data by calculating the RMS of χ^2_{global} and dz(μ,PV) at preselection stage in $Z \to \mu\mu$ data events.

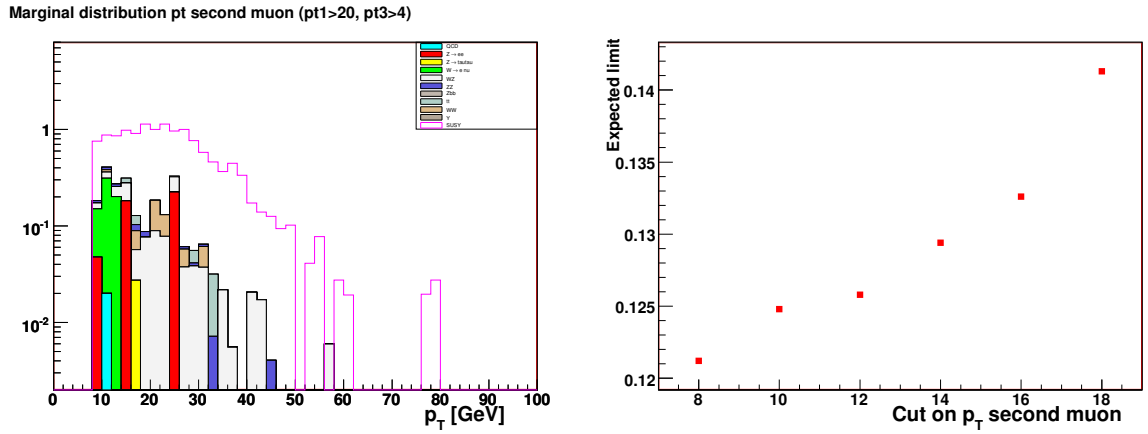

Figure 9.2.: Marginal distribution of p_T of next to leading muon and expected limit as a function of cut on p_T for the next to leading muon in the high-p_T selection. The susypoint has parameters $(m_0, m_{1/2})$=(150,250).

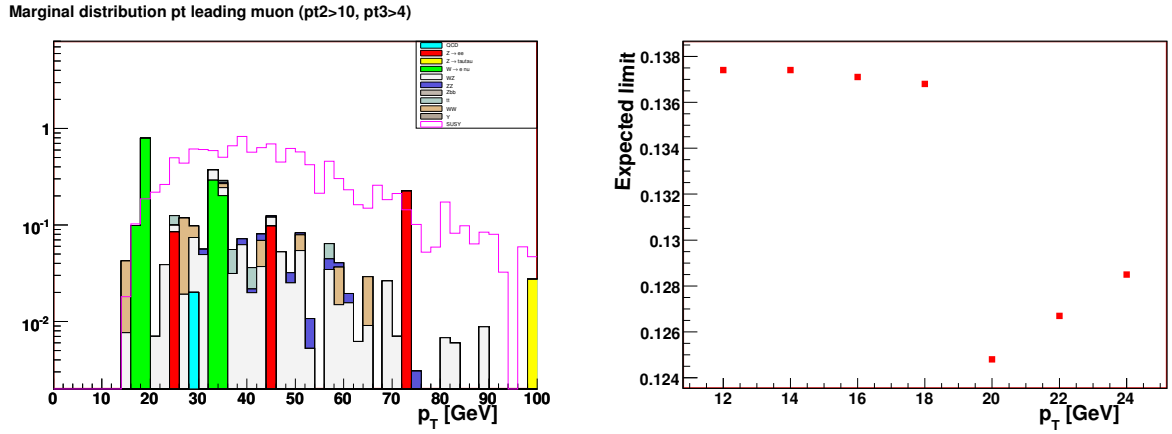

Figure 9.3.: Marginal distribution of p_T of leading muon and expected limit as a function of cut on p_T on leading muon in the high-p_T selection. The susypoint has parameters $(m_0, m_{1/2})$=(150,250).

These distributions are shown in Figure 9.4.

The χ^2_{zb} is required to be less than 50 for both muons and the cut is only applied for muons without SMT hits. A Monte Carlo efficiency correction is derived by applying the cut χ^2_{zb} <50 to $Z \to \mu\mu$ events in data and Monte Carlo and taking the ratio of the efficiencies. The efficiency correction is 1.001 for both muons. Figure 9.5 shows the distribution of χ^2_{zb} at preselection level for leading muon without SMT hits (left) and next to leading muon without SMT hits (right). A discrepancy can be observed, but above the cut value at 50.

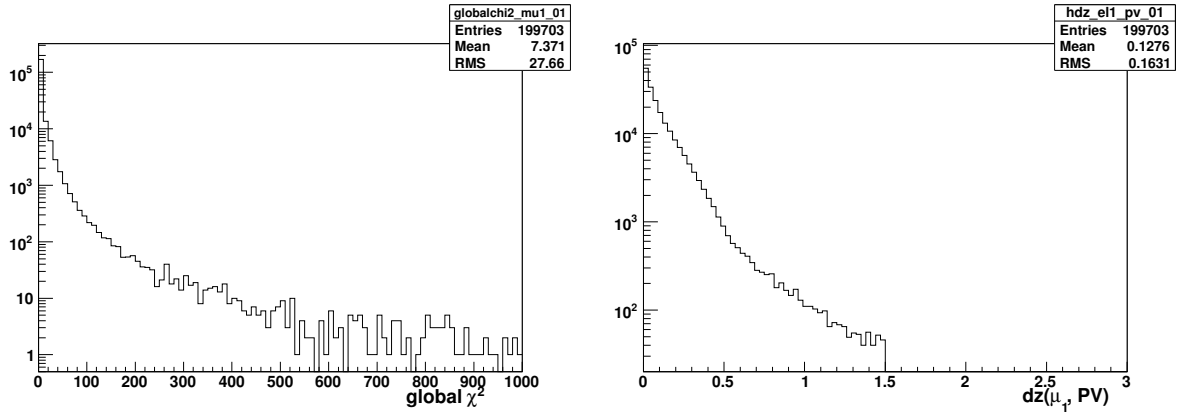

Figure 9.4.: χ^2_{global} and dz(μ_1) in data at preselection level.

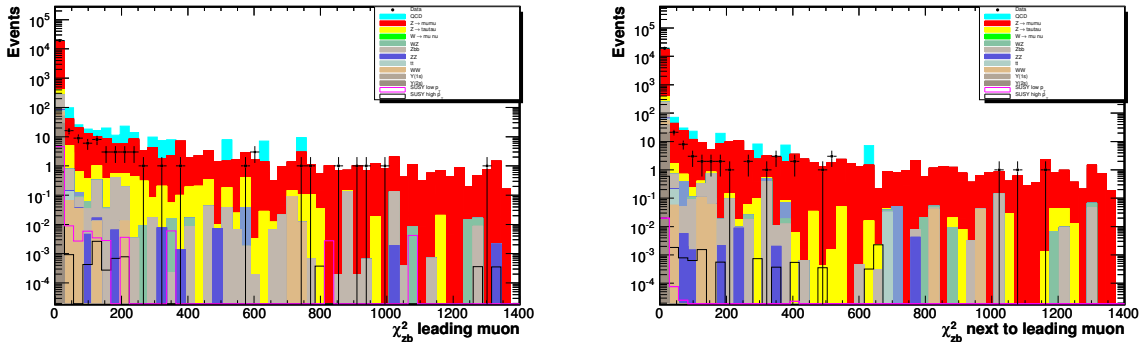

Figure 9.5.: χ^2_{zb} for leading muon left and next to leading muon right. Both plots are made for muons without SMT hits. The χ^2_{zb} is required to be less than 50 for both muons.

9.2.2. Anti Z Cuts

At preselection level, the search sample is dominated by $Z \rightarrow \mu\mu$ events. To remove events from the Z resonance, an upper cut on the invariant mass is made and to reject events from the Upsilon resonance, a lower mass cut can be made. In the high-p_T selection, the lepton p_T cuts in addition to the $\not\!\!E_T$ and third track requirement, are sufficient to remove Upsilon events and no lower cut on the di-muon invariant mass is necessary. Figure 9.6 shows the invariant mass at preselection stage in the low-p_T analysis (left) and in the high-p_T preselection stage (right). The invariant mass of the lepton pair must be 20 GeV $< M_{\mu\mu} <$ 60 GeV in the low-p_T selection. The cuts are relaxed to $0 < M_{\mu\mu} <$ 75 GeV in the high-p_T selection.

Leptons from $Z/\gamma^* \rightarrow \ell\ell$ and QCD events are mainly back-to-back in the transverse plane whereas the leptons from chargino and neutralino decay have no preferred azimuthal opening angle $\Delta\phi_{\ell,\ell}$. The azimuthal angle is also efficient for rejecting background from cosmic rays which leave a straight line in the detector. Figure 9.7 shows the azimuthal angle at preselection in the low-p_T selection (left) and before the cut is applied (right). The azimuthal angle is

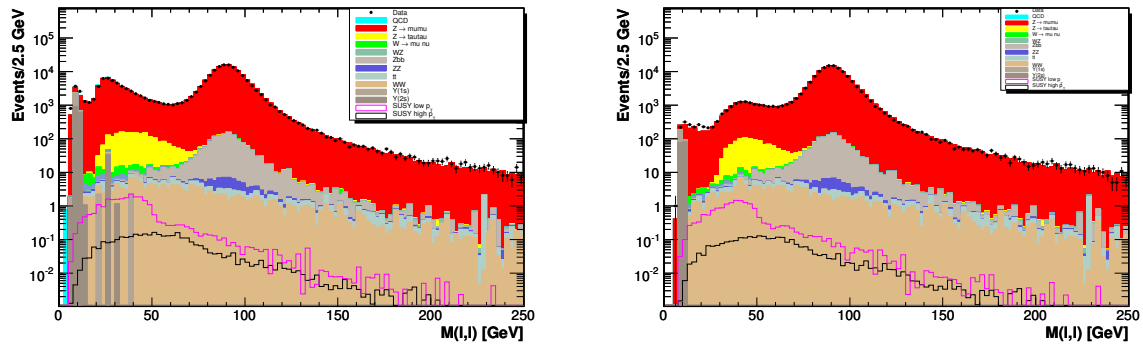

Figure 9.6.: Invariant mass, $M_{\mu\mu}$, distribution at preselection level in the low-p_T analysis (left) and in the high-p_T analysis (right). Two susy points are shown. The black line corresponds to 150.250 and the magenta to 150.170.

required to be less than 2.9 radians in both selections.

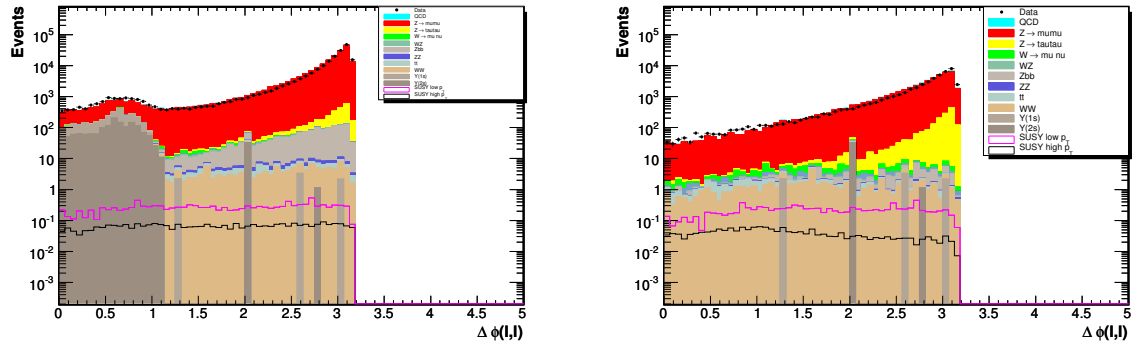

Figure 9.7.: The azimuthal angle, $\Delta\phi_{\ell,\ell}$ at preselection level (left) and before the requirement $\Delta\phi_{\ell,\ell} < 2.9$ is made (right).

9.2.3. $\not\!\!E_T$ Related Cuts

$Z/\gamma^* \to \ell\ell$ and QCD events are in general characterized by small values of $\not\!\!E_T$ while the signal has a significant amount of $\not\!\!E_T$ due to the neutrino and neutralinos in the final state. Section 6.5 provides a detailed definition of the $\not\!\!E_T$ variable. Figure 9.8 shows the $\not\!\!E_T$ distribution at the $\mu\mu\ell$ preselection stage in the low-p_T selection (left) and in the high-p_T selection (right). Figure 9.9 shows the $\not\!\!E_T$ distributions before the cut on $\not\!\!E_T$ is applied in the low- and high-p_T analyses.

The cut was scanned and the optimal value is 20 GeV in both selections. Figure 9.10 and Figure 9.11 shows the marginal distribution and the expected cross section limit as a function of the cut on $\not\!\!E_T$ for the low-p_T and high-p_T selections.

Large values of the missing transverse energy in $Z/\gamma^* \to \ell\ell$ and QCD events are mostly due

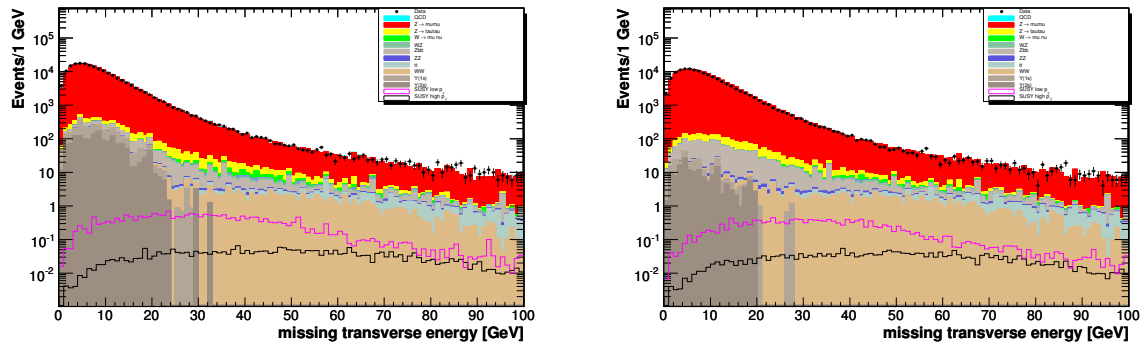

Figure 9.8.: Distribution of $\not\!\!E_T$ at the $\mu\mu\ell$ low-p_T preselection stage (left) and preselection stage in the high-p_T selection (right).

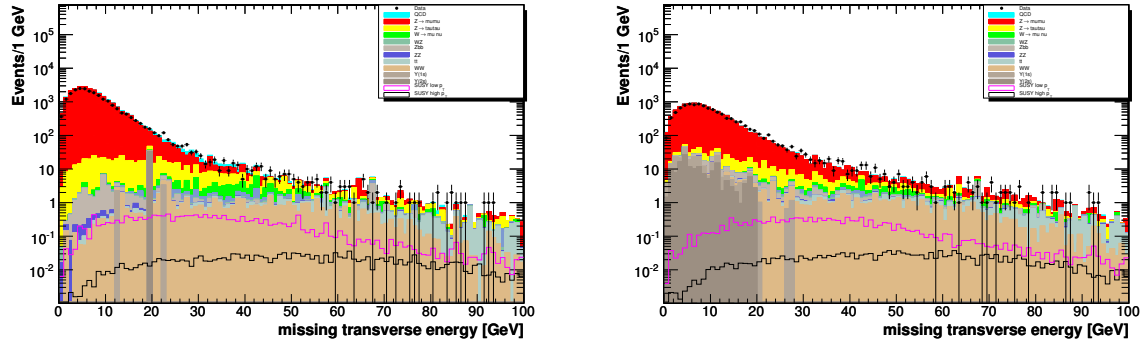

Figure 9.9.: Distribution of $\not\!\!E_T$ in the $\mu\mu\ell$ low-p_T selection before the cut is applied (left) and in the high-p_T selection before the cut is applied (right).

to fluctuation of the reconstructed jet energies. These events are characterized by small values of the missing transverse energy significance, Sig($\not\!\!E_T$). The resolution in the measurement of the jet energy in the transverse plane, can be approximated by $\Delta E^{\text{jet}} \cdot \sin\theta^{\text{jet}}$ where ΔE^{jet} is proportional to $\sqrt{E^{\text{jet}}}$. The opening angle $\Delta\phi\,(\text{jet}, \not\!\!E_T)$ between the projected energy fluctuation and the missing transverse energy, provides a measure of the contribution of the jet to the missing transverse energy. The missing transverse energy significance is defined as

$$\text{Sig}(\not\!\!E_T) = \frac{\not\!\!E_T}{\sqrt{\sum_{\text{jets}} \sigma^2_{E_T^j \| \not\!\!E_T}}}. \tag{9.2}$$

Figure 9.12 shows the Sig($\not\!\!E_T$) distribution at preselection stage (left) and before the cut is applied (right) in the low-p_T selection. The cut is only applied if there is at least one jet in the event. The event is rejected if Sig($\not\!\!E_T$)<8.

Large reconstructed $\not\!\!E_T$ in events without true $\not\!\!E_T$ can also be due to poorly measured lepton

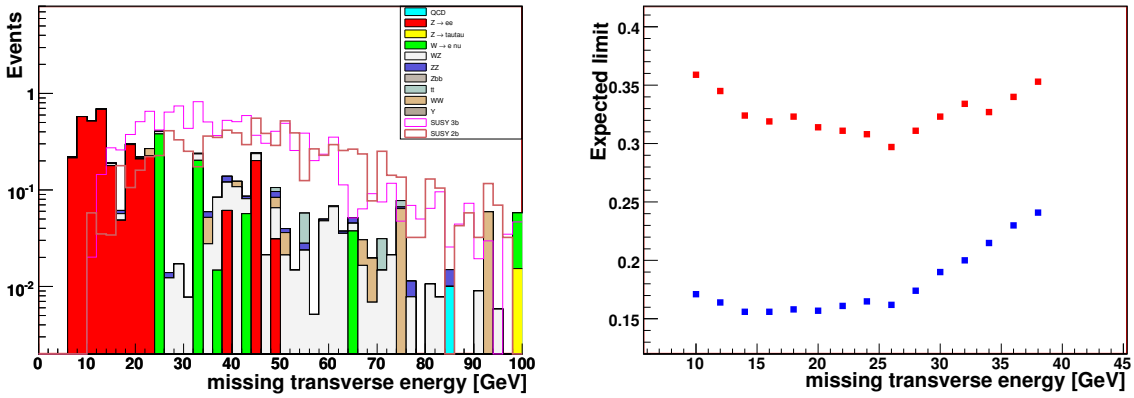

Figure 9.10.: Marginal distribution (left) for $\not\!\!E_T$ in the low-p_T selection. The two susypoints $(m_0, m_{1/2})$=(150 GeV,170 GeV) (labelled 3b) and $(m_0, m_{1/2})$=(76 GeV,184 GeV) (labelled 2b) are drawn. Limit as a function of cut on $\not\!\!E_T$(right) for the low-p_T selection (right). The limit is shown for the same two susypoints. $(m_0, m_{1/2})$=(150 GeV,170 GeV) is the lower line, while $(m_0, m_{1/2})$=(76 GeV,184 GeV) is the upper line.

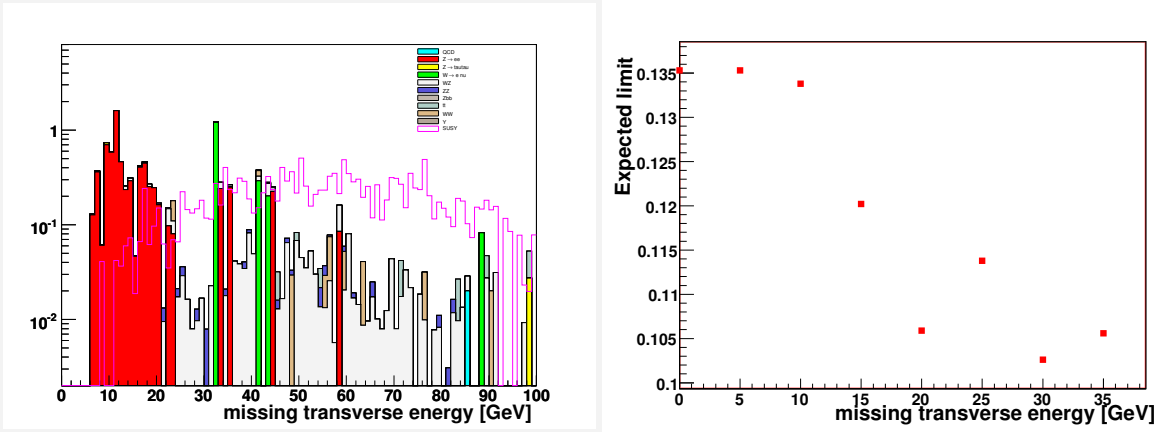

Figure 9.11.: Marginal distribution (left) and limit as a function of cut on $\not\!\!E_T$(right) for the high-p_T selection.

energies. In these cases, the $\not\!\!E_T$ and the lepton are pointing in the same direction, leading to small values of the azimuthal angle between the $\not\!\!E_T$ and the lepton. This in turn leads to small values of the transverse mass defined as

$$M_T = \sqrt{2\times \not\!\!E_T \times p_T(\ell) \times (1 - \cos(\Delta\phi(\not\!\!E_T, \ell)))}. \tag{9.3}$$

$Z \to \mu\mu$ and $Z \to \tau\tau$ background have in general low values of the transverse mass. $Z \to \tau\tau$ has real $\not\!\!E_T$ in the event, but since the angle between the $\not\!\!E_T$ and the leptons is small, $Z \to \tau\tau$ does not acquire large values of transverse mass. For signal there is no preferred direction between

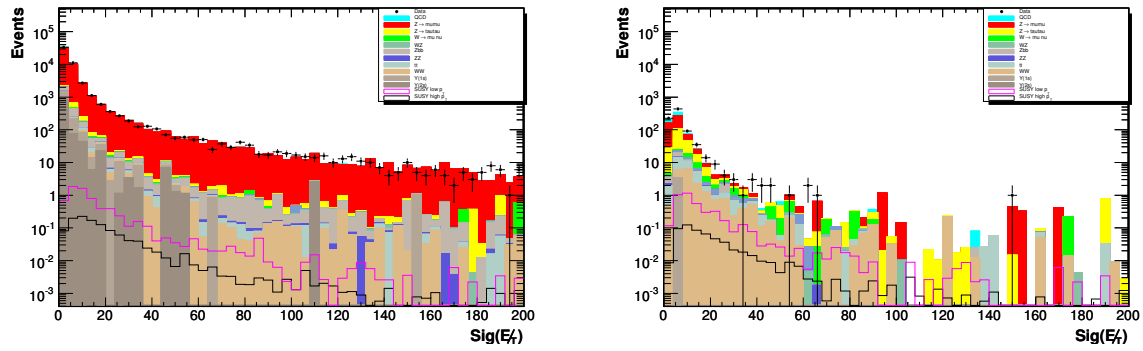

Figure 9.12.: Distribution of Sig($\not\!\!E_T$) in events with at least one jet at the $\mu\mu\ell$ preselection stage (left) and before the cut is applied (right). Both plots are from the low-p_T selection.

$\not\!\!E_T$ and the leptons, and the M_T extends to larger values. Figure 9.13 shows the distribution at preselection stage in the low-p_T selection (left) and before the cuts is applied in this selection (right).

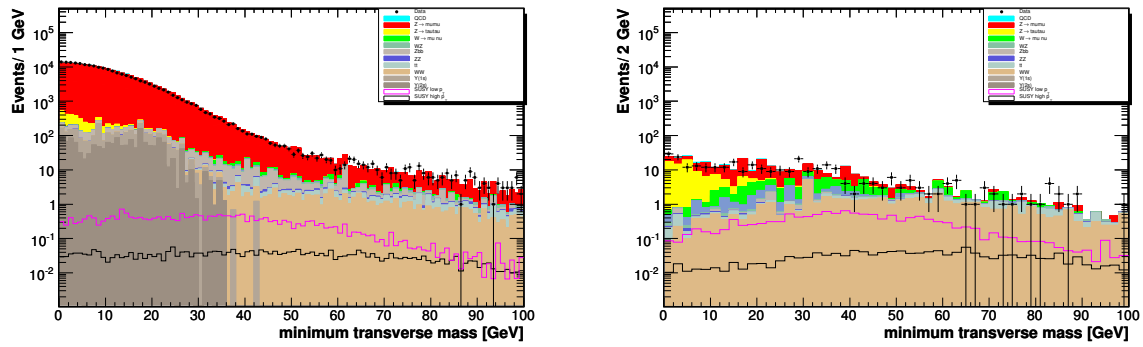

Figure 9.13.: Distribution of minimum transverse mass at the low-p_T $\mu\mu\ell$ preselection stage (left) and before the cut is applied (right) in the low-p_T analysis.

The cut was scanned in both the low- and high-p_T selections, and the optimal cut value was found. The transverse mass for both muons is required to be greater than 20 GeV in both the low- and high-p_T selections. Figure 9.14 and Figure 9.15 show the marginal distribution and the expected limit as a function of the cut on minimum transverse mass in the low- and high-p_T analysis, respectively.

9.2.4. Selection of a Third Track

Most of the background processes described in Chapter 3 do not have a third lepton in the final state, while a third isolated lepton is expected in the SUSY signal. With decreasing lepton identification efficiency for low values of lepton p_T, demanding a third lepton in the event reduces the sensitivity of the analyses, becuase the third lepton from the SUSY signal is expected to

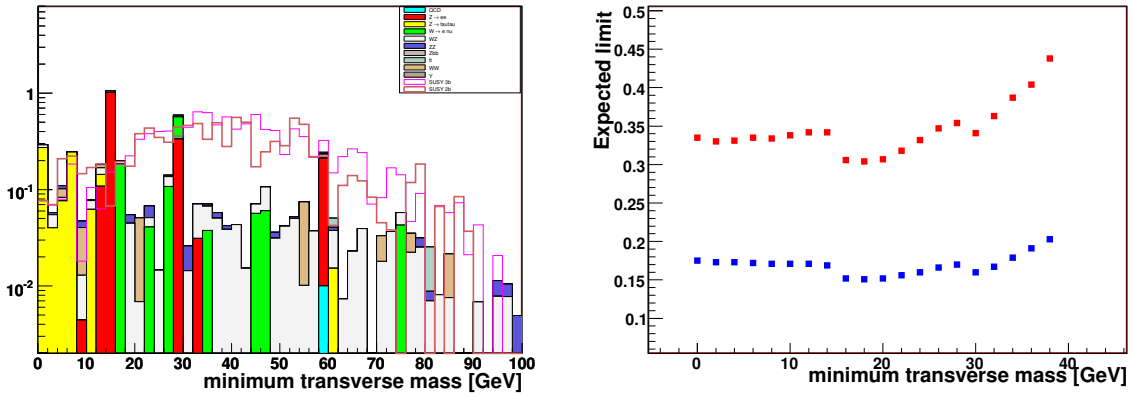

Figure 9.14.: Marginal distribution for minimum transverse mass in the low-p_T selection (left) with the two susypoints $(m_0, m_{1/2})$=(150 GeV,170 GeV) (labelled 3b) and $(m_0, m_{1/2})$=(76 GeV,184 GeV) (labelled 2b). Expected limit as a function of the cut on minimum transverse mass (right) where the lower line corresponds to $(m_0, m_{1/2})$=(150 GeV,170 GeV) and the upper line corresponds to $(m_0, m_{1/2})$=(76 GeV,184 GeV).

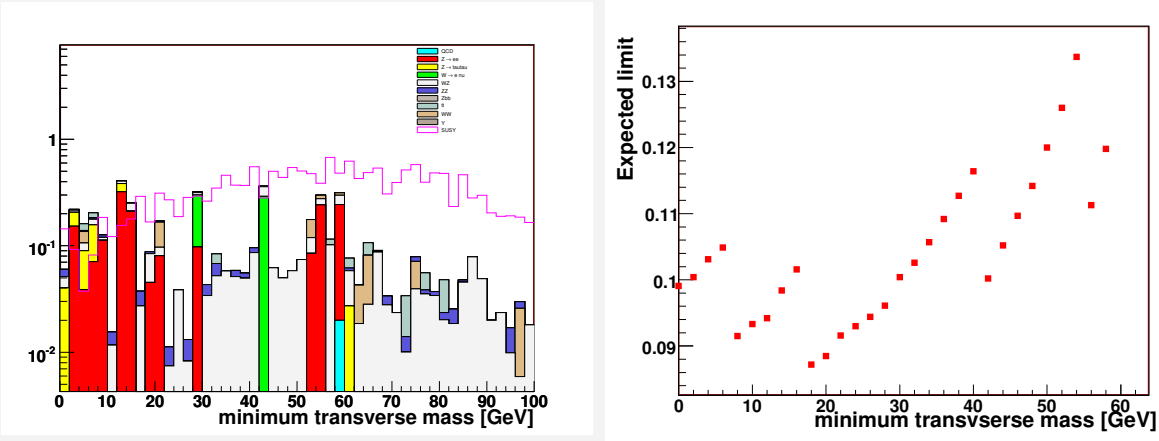

Figure 9.15.: Marginal distribution for minimum transverse mass in the high-p_T selection (left). Expected limit as a function of the cut on minimum transverse mass (right). The expected limit fluctuates due to limited Monte Carlo statistics. The marginal distribution was smoothened 'by eye' and the optimal cut value chosen.

be soft in large parts of the phase space. To exploit the presence of the third lepton in signal, the analyses require instead an isolated track, in addition to the tracks from the two lepton candidates. This additional track is referred to as *the third track*. The third track is required to originate from the same vertex as the two leptons ($\Delta\ z < 1$ cm) and to be well separated from them ($\Delta R = \sqrt{\Delta\eta^2 + \Delta\phi^2} > 0.4$). To ensure a good p_T measurement, the χ^2 per degree of freedom of the track fit is required to be less than 4 ($\chi^2/\text{ndof} < 4$) and at least 17 hits or at least 14 CFT hits are required. Tracks without CFT hits are rejected. Monte Carlo efficiency corrections, smearing and reweighting, which are derived using muons (compare Section 8.8),

are applied to the third track. In the low-p_T selection the p_T of the third track is required to be in excess of 5 GeV, while the cut is relaxed to 4 GeV in the high-p_T selection due to the tightened lepton p_T cuts. Figure 9.16 shows the marginal distribution and the expected limit as a function of the cut on track-p_T in the high-p_T selection. Figure 9.18 shows the p_T distribution at preselection level in the low-p_T analysis (left). The tracks are required to pass the quality criteria and have $p_T > 2$ GeV. The number of hits in the SMT tracker (see Section 4.3.1) is also presented (right) at preselection stage.

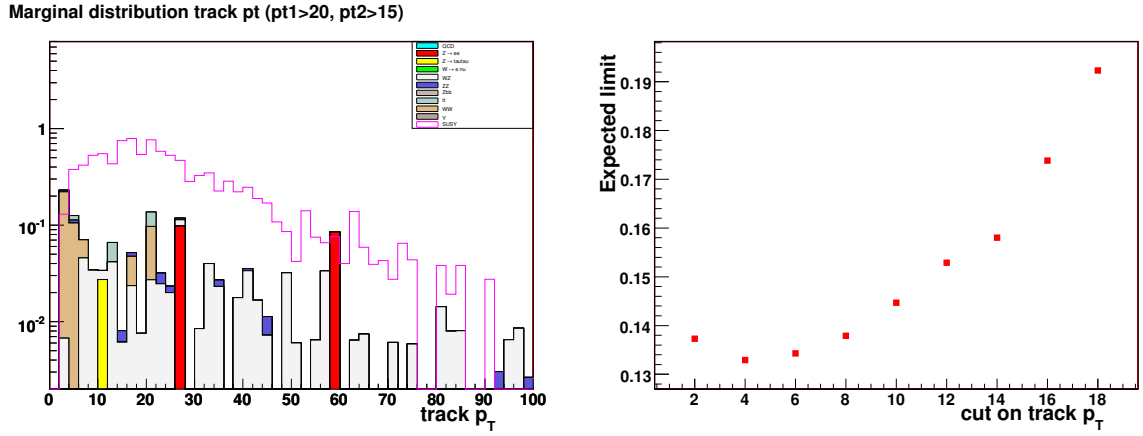

Figure 9.16.: Marginal distribution of track p_T and expected limit as a function of cut on track p_T in the high-p_T $\mu\mu\ell$ selection.

Isolation in the Tracker

For most of the events with a third track at preselection stage, the track does not come from a third lepton, but from a jet. These tracks are generally not isolated and background from $Z \to \ell\ell$, WW, $W + (jets)$ and QCD production can be reduced by requiring the energy around the third track to be small.

More specifically, the scalar sum of the track momenta of other reconstructed tracks in a hollow cone $0.1 < \Delta R < 0.4$ around the third track is required to be less than 1 GeV. Since the cone is required to be hollow, the sum does not take into account the transverse momentum of the third track. Only tracks originating from the same vertex are taken into account when calculating the tracker isolation. The isolation criterion is designed to be efficient for tracks from muons, electrons and taus. The hollow cone requirement is used to also be efficient for tau decays with three charged pions in the final state, since these produce additional tracks that are close in ΔR to the selected track. Figure 9.19 shows the distribution of scalar sum of the p_T of all tracks in the isolation cone around reconstructed tracks at preselection level. Monte Carlo efficiency corrections and smearing of the track momentum as described in Section 8.8, are also applied to the tracks that enter the track isolation calculation.

To further exploit the isolation, only events with exactly one or three tracks in the inner cone ($\Delta R < 0.1$) are accepted. The cut is made including the third track. The cut exploits the fact that most backgrounds have a third track from a jet and such are expected to have more tracks

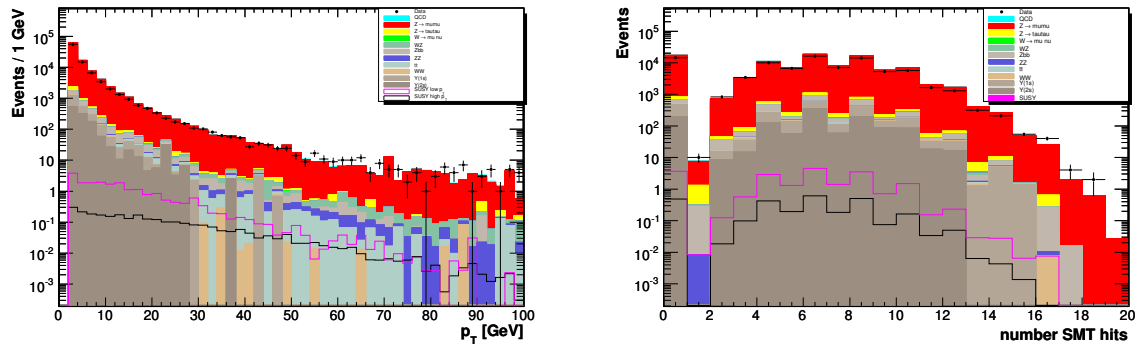

Figure 9.17.: p_T of the third track at preselection stage in the low-p_T analysis (left) and number of hits in the SMT tracker for the third track at preselection stage (right).

closer to the third track compared to signal, where the track is from an isolated lepton. Figure 9.18 shows the track multiplisity distribution at preselection level and before the requirement is made in the low-p_T $\mu\mu\ell$ analysis. The cut is applied in the low-p_T analysis.

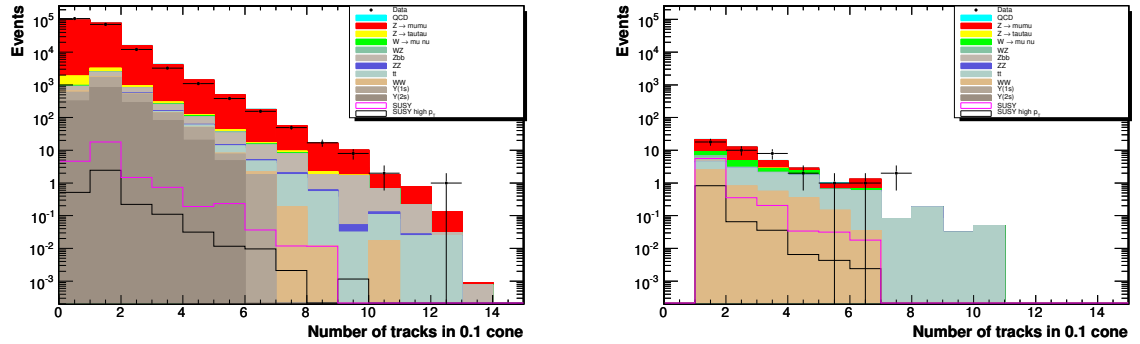

Figure 9.18.: Number of tracks in the 0.1 cone, including the third track, at preselection level (left) and after requiring a third track in the event (right) in the low-p_T selection.

Isolation in the Calorimeter

To further reduce the number of events where the track is faked by a jet, isolation in the calorimeter is also required. For the signal, the energy deposition in the calorimeter is contained in a small cone around the track, whereas the jets are characterized by calorimeter energy depostion in a larger cone. A cut on calorimeter isolation of the third track, helps to further suppress Drell-Yan background, ZZ and $W + (jets) \rightarrow \mu\nu$ background.

The calorimeter isolation uses the scalar sum of the transverse energy deposition in the cells of the electromagnetic and the fine-hadronic layers of the calorimeter in a hollow isolation cone of $0.2 < \Delta R < 0.4$ around the extrapolation of the third track into the calorimeter. The

calorimeter isolation variable at preselection stage is shown in Figure 9.19 (right). The isolation is calculated for all events with an additional track that passes the quality criteria and that has $p_T > 2$ GeV. In both the low-p_T analysis and high-p_T analysis, the calorimeter isolation of the third track is required to be less than 1.5 GeV.

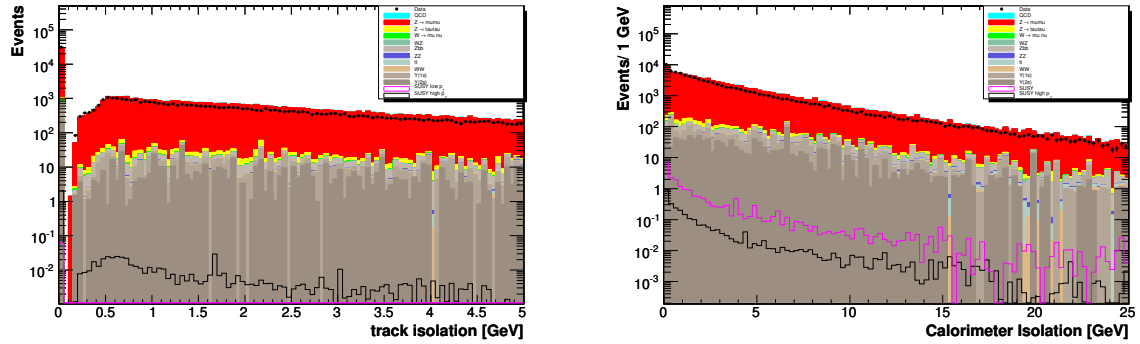

Figure 9.19.: Track isolation (left) and calorimeter isolation (right) at preselection level in the low-p_T selection.

9.2.5. Reduction of Fake $\not\!\!E_T$ Related to the Third Track

For the third track, a transverse mass $M_T(\text{track}, \not\!\!E_T) > 10$ GeV is required. This selection criterium removes a large fraction of the remaining $Z \to \mu\mu$ background. The cut was scanned in both the low- and high-p_T selection and the optimal value was 10 GeV in both analyses. Figure 9.20 shows the $M_T(\text{track}, \not\!\!E_T)$ distribution at preselection (left) and before the cut is applied (right) in the low-p_T analysis.

A fraction of the remaining background can be removed by requiring that the invariant mass of the leading muon and the third track is below or above the Z pole mass: $M_{\mu_1\ell_3} < 80$ GeV or $M_{\mu_1\ell_3} > 110$ GeV. The cut is only applied to events where the track goes into the bottom hole with limited coverage due to the support structures of the muon system. The bottom hole is defined as $4.25 < \phi < 5.15$ if $|\eta_{det}| < 1.25$. The cut is applied to reject events where one muon is lost in the muon chambers due to the limited coverage in this region, but still can be reconstructed as a track in the inner detector. The cut is only applied in the low-p_T selection. The distribution of transverse mass of the third track and the invariant mass of the track and the leading muon are shown in Figure 9.21.

9.2.6. p_T-Balance

For signal events, the vectorial sum of the lepton transverse momenta and $\not\!\!E_T$ should be equal to the p_T of the third track. For all backgrounds but WZ production, this is in general not true. The p_T balance is defined as

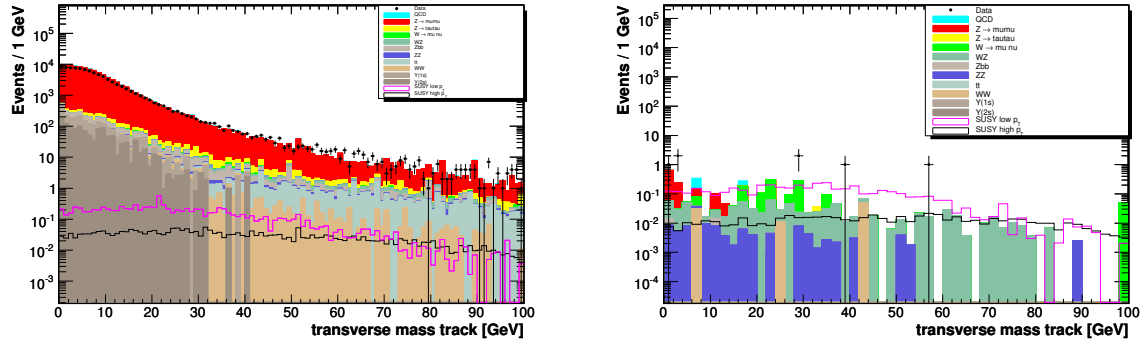

Figure 9.20.: Transverse mass of track and $\not\!\!E_T$ (left) and before the cut is applied (right) in the $\mu\mu\ell$ low-p_T selection.

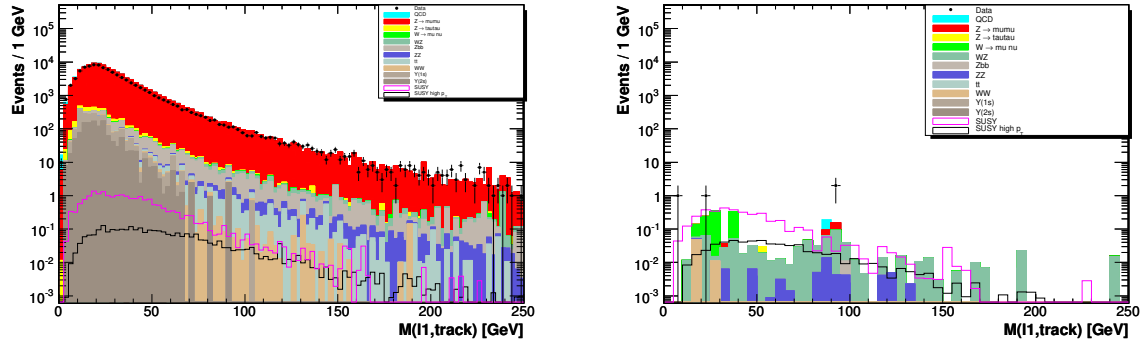

Figure 9.21.: Invariant mass of leading muon and third track at preselection stage (left) and before the cut is applied (right).

$$\frac{|\vec{p}_T^{\,\mu_1} + \vec{p}_T^{\,\mu_2} + \not\!\!E_T|}{p_T(track)} \,. \tag{9.4}$$

Figure 9.22 left shows the ratio of the vector sum of the momenta of muons and $\not\!\!E_T$ and the p_T of the third track. QCD and background from Z and W decays have a large fraction of events with high values of the p_T balance. In both the low- and high-p_T selection, a selection of events with p_T balance less than 4 is made.

9.2.7. Combined Cut on $\not\!\!E_T$ and p_T(track)

A combined cut on $\not\!\!E_T$ and p_T of the third track exploits the two most important features of the SUSY signal: large amount of $\not\!\!E_T$ and a third track. Figure 9.23 shows the marginal distribution and the expected limit as a function of the cut on the product of $\not\!\!E_T$ and p_T(track). Figure 9.24 shows the product of the $\not\!\!E_T$ and the p_T of the third track in the low-p_T selection at preselection

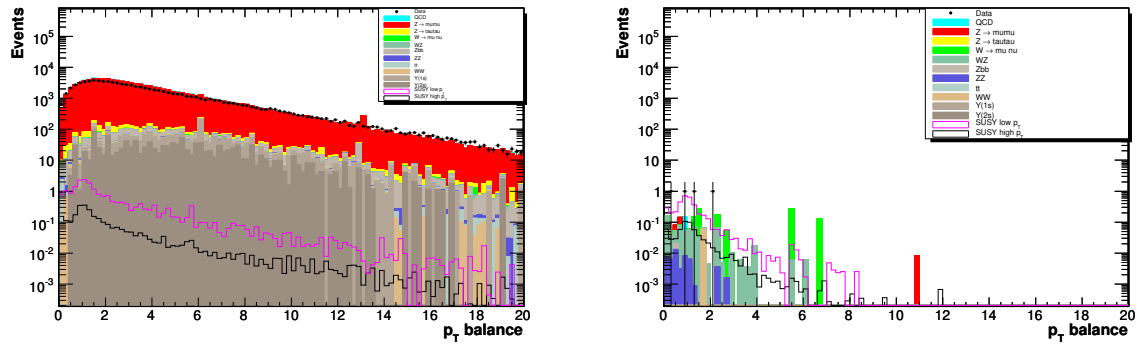

Figure 9.22.: p_T balance at preselection stage (left) and before the cut is applied (right) in the low-p_T analysis.

stage (left) and before the cut is applied in the low-p_T selection. Since Drell Yan events are characterized by fake $\not\!\!E_T$ and a fake track, the values of both quantities are expected to be small and the product $\not\!\!E_T \times p_T$ should be small. Background from $W \to \mu\nu$ background have mainly low values of $\not\!\!E_T \times p_T$ because the p_T of the third track in $W \to \mu\nu$ events tends to be low. The requirement $\not\!\!E_T \times p_T(track) > 200$ GeV^2 is used to reduce this background. In the low-p_T analysis, the combined cut on $\not\!\!E_T$ and p_T(track) reduces the remaining background with 25% with a 7% inefficiency for signal. 68% of the remaining $W \to \mu\nu$ background is removed. The cut is tightened to 300 GeV^2 in the high-p_T selection. In this selection, the cut reduces the remaining background with 23% with a signal inefficiency of 4%. 80% of the remaining $W \to \mu\nu$ background and 16% of the $Z \to \mu\mu$ background is rejected.

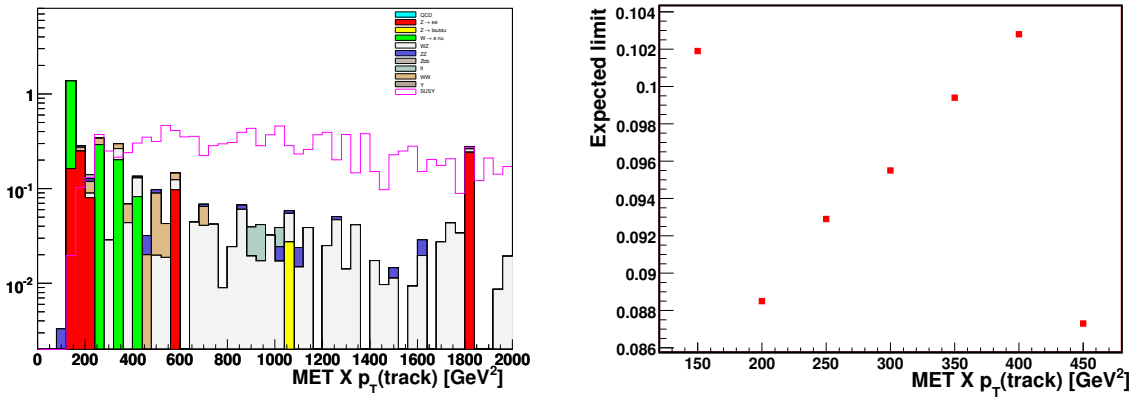

Figure 9.23.: Marginal distribution (left) of $\not\!\!E_T \times p_T(track)$ in the high-p_T muon selection and the expected limit as a function of cut on the $\not\!\!E_T \times p_T(track)$ variable (right).

Since the available Monte Carlo statistics is low for $Z \to \mu\mu$ background, rejection factors have been used to estimate the contribution of $Z \to \mu\mu$ background after the cut on calorimeter isolation for the third track. The rejection factors were calculated in a loose $Z \to \mu\mu$ sample, where the tracker and calorimeter isolation cuts for the next to leading muon were relaxed to 4 GeV, the upper invariant mass cut was relaxed to 160 GeV and the $\Delta\phi$ and Sig($\not\!\!E_T$) cuts were

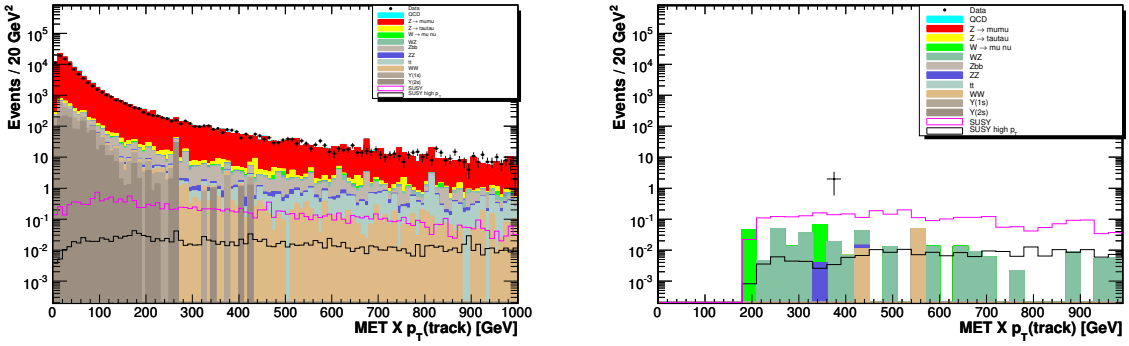

Figure 9.24.: $\not\!\!E_T \times p_T(track)$ at low-p_T muon preselection (left) and before the cut is made. Two data events are outside the range of the histogram.

removed.

9.2.8. Results of the $\mu\mu\ell$ Selection

The number of candidate events for the background Monte Carlo and the data is given in Table 9.4 for the low-p_T selection and in Table 9.5 for the high-p_T selection. In the low-p_T selection 4 events are observed in data, while 1.17±0.19 (stat)±0.12 (syst) (see Section 9.4) events are expected from Standard Model processes. The signal efficiency for the point with m_0=150 GeV and $m_{1/2}$=170 GeV is 2.82%±0.10%. The dominant backgrounds after all cuts, are WZ which constitutes 60% of the total expected background and $W \to \ell\nu$ that contributes 15%. Other sources of background are WW/ZZ (10%) and $Z/\gamma^* \to \mu\mu$ (10%).

Also in the high-p_T selection, 4 events are observed in data, with 2.02± 0.33 (stat)± 0.17 (syst) expected from Standard Model background. In the high-p_T selection, again WZ is the biggest background source, while $Z/\gamma^* \to \mu\mu$ is the next largest (25%). Other di-boson production WW/ZZ, contributes 30%. $W \to \ell\nu$ is less important in the high-p_T selection due to the tighter lepton p_T cuts. The signal efficiency for the signal point with $m_0 = 150$ GeV, $m_{1/2} = 250$ GeV is 5.03%±0.14%.

Since the low-p_T selection and high-p_T selection can select the same events in data, signal and background, the overlap between the selections need to be taken into account. The overap is subtracted from the high-p_T selection, because the low-p_T selection has a better signal to background ratio. The overlap in background, signal and data is subtraced. After the background subtraction, 1 event is selected in data in the high-p_T selection and 1.93± 0.24 (stat)± 0.17 (syst) are expected from Standard Model background processes.

Table 9.6 to Table 9.9 list the run number, event number and kinematic properties of the selected events in the low-p_T selection, and Table 9.10 lists the run number, event number and kinematic properties of the data event observed in the high-p_T selection after subtraction of events selected by both the low- and high-p_T selections. In Section A.3.1, event displays of one of the candidate events selected in the low-p_T analysis are presented. In Section A.3.2 event

displays of the event selected in the high-p_T analysis are shown.

Table 9.2.: List of cuts used for the low-p_T selection in the $\mu\mu\ell$ analysis.

	Selection criteria	Value
Cut 1	Preselection	Trigger, $p_T^{\mu 1} > 12$ GeV and $p_T^{\mu 2} > 8$ GeV calorimeter isolation < 4 (1.5) GeV and tracker isolation < 4 (1.5) GeV for the leading (next to leading) muon dz(μ,PV) < 1.5 cm, $\chi^2_{zb} < 50$ if no SMT hits for both muons
Cut 2	Invariant Mass:	20 GeV $< M(\mu_1, \mu_2) <$ 60 GeV
Cut 3	Transverse opening angle leptons:	$\Delta\phi(\mu_1, \mu_2) < 2.9$
Cut 4	Missing Transverse Energy	$\not\!\!E_T > 20$ GeV
Cut 5	$\not\!\!E_T$ significance:	Sig($\not\!\!E_T$) > 8 or no jets
Cut 6	Transverse Mass $\mu_{1,2}$	$M_T(\mu, \not\!\!E_T) > 20$ GeV for both muons
Cut 7	p_{T} of third track	$p_T(track) > 5.0$ GeV
Cut 8	track isolation	$\Sigma p_T <$ 1GeV number of tracks in 0.1 cone 1 or 3
Cut 9	calorimeter isolation	$E_T < 1.5$ GeV
Cut 10	Transverse Mass ℓ_3	$M_T(\ell_3, \not\!\!E_T) > 10$ GeV
Cut 11	Mass $\mu_1\ell_3$	$M(\mu_1, \ell_3) <$ 80 GeV or $M(\mu_1, \ell_3) >$110 GeV
Cut 12	p_{T} balance	$\frac{\lvert\vec{p}_T^{\,\mu 1} + \vec{p}_T^{\,\mu 2} + \not\!\!E_T\rvert}{p_T(track)} < 4$
Cut 13	p_{T} product	$\not\!\!E_T$ * $p_T(\ell_3) > 200$ GeV^2

Table 9.3.: List of cuts used for the high-p_T selection in the $\mu\mu\ell$ analysis.

	Selection criteria	Value
Cut 1	Preselection	Trigger, $p_T^{\mu 1} > 20$ GeV and $p_T^{\mu 2} > 10$ GeV calorimeter isolation < 4 (1.5) GeV and tracker isolation < 4 (1.5) GeV for the leading (next to leading) muon dz(μ,PV) < 1.5 cm, χ^2_{zb} <50 if no SMT hits for both muons
Cut 2	Invariant Mass:	0 GeV $< M(\mu_1, \mu_2) <$ 75 GeV
Cut 3	transverse opening angle:	$\Delta\phi(\mu_1, \mu_2) < 2.9$
Cut 4	Missing Transverse Energy:	$\not\!\!E_T > 20$ GeV
Cut 5	$\not\!\!E_T$ significance:	Sig($\not\!\!E_T$) > 8 or 0 jets
Cut 6	Transverse Mass $\mu_{1,2}$	$M_T(\mu, \not\!\!E_T) > 20$ GeV for both muons
Cut 7	p_{T} of third track	$p_T(track) > 4.0$ GeV
Cut 8	track isolation:	$\Sigma p_T <$ 1GeV
Cut 9	calorimeter isolation:	$E_T < 1.5$ GeV
Cut 10	Transverse Mass ℓ_3	$M_T(\ell_3, \not\!\!E_T) > 10$ GeV
Cut 11	p_{T} balance	$\frac{\lvert\vec{p}_T^{\,\mu_1} + \vec{p}_T^{\,\mu_2} + \not\!\!E_T\rvert}{p_T(track)} < 4$
Cut 12	p_{T} product	$\not\!\!E_T$ * $pT(\ell_3) > 300$ GeV^2

Table 9.4.: Number of candidate events observed and number of background events expected from Standard Model processes, at different stages of the low p_T muon selection. The number of expected signal events and the signal efficiency for the point m_0 =150 GeV, $m_{1/2}$ = 170 GeV are also given. The different cutstages are defined in Table 9.2 Errors are statistical.

Cut	Upsilon	WW	$t\bar{t}$	ZZ	$Zb\bar{b}$
1	2987 ± 80	141 ± 2.4	62.2 ± 1.6	44.6 ± 0.46	1265.6 ± 10.9
2	40.7 ± 32.2	59.5 ± 1.6	22.3 ± 1.0	3.91 ± 0.11	39.8 ± 2.5
3	38.6 ± 32.1	55.8 ± 1.5	21.4 ± 1.0	3.60 ± 0.11	33.3 ± 2.4
4	3.35 ± 3.35	47.9 ± 1.4	20.5 ± 0.96	1.43 ± 0.07	8.40 ± 1.44
5	0.00 ± 0.00	44.9 ± 1.3	10.6 ± 0.62	0.87 ± 0.05	2.34 ± 0.74
6	0.00 ± 0.00	41.6 ± 1.3	9.49 ± 0.59	0.59 ± 0.04	2.00 ± 0.73
7	0.00 ± 0.00	4.42 ± 0.44	8.12 ± 0.53	0.18 ± 0.02	1.21 ± 0.78
8	0.00 ± 0.00	0.25 ± 0.09	0.22 ± 0.07	0.12 ± 0.02	0.27 ± 0.18
9	0.00 ± 0.00	0.09 ± 0.06	0.00 ± 0.00	0.10 ± 0.02	0.01 ± 0.01
10	0.00 ± 0.00	0.06 ± 0.05	0.00 ± 0.00	0.06 ± 0.01	0.01 ± 0.01
11	0.00 ± 0.00	0.06 ± 0.05	0.00 ± 0.00	0.05 ± 0.01	0.01 ± 0.01
12	0.00 ± 0.00	0.06 ± 0.05	0.00 ± 0.00	0.05 ± 0.01	0.01 ± 0.01
13	0.00 ± 0.00	0.06 ± 0.05	0.00 ± 0.00	0.05 ± 0.01	0.01 ± 0.01

Cut	WZ	$W \to \ell\nu$	$Z \to \tau\tau$	$Z \to \mu\mu$	fakes
1	79.6 ± 0.83	123.3 ± 5.67	1755 ± 11.6	187295 ± 155	1803.49± 13.43
2	6.61 ± 0.24	85.3 ± 4.59	1564 ± 11.1	44796 ± 100	1601.72± 12.68
3	5.99 ± 0.23	78.0 ± 4.44	464 ± 6.7	24582 ± 81	784.26 ± 8.87
4	4.27 ± 0.19	67.1 ± 4.24	179 ± 4.5	440 ± 11	138.14 ± 3.39
5	3.26 ± 0.16	61.7 ± 4.19	74.8 ± 1.62	145 ± 7	9.99 ± 0.84
6	2.64 ± 0.15	48.0 ± 3.70	1.62 ± 0.33	72.5 ± 4.9	2.56 ± 0.39
7	1.33 ± 0.10	5.35 ± 0.75	0.23 ± 0.06	22.5 ± 2.5	0.73 ± 0.18
8	1.02 ± 0.09	1.24 ± 0.39	0.01 ± 0.01	2.20 ± 0.70	0.19 ± 0.15
9	0.79 ± 0.08	0.90 ± 0.36	0.01 ± 0.01	0.94 ± 0.56	0.05 ± 0.03
10	0.67 ± 0.07	0.86 ± 0.36	0.01 ± 0.01	0.48 ± 0.26	0.03 ± 0.03
11	0.62 ± 0.07	0.86 ± 0.36	0.01 ± 0.01	0.38 ± 0.24	0.03 ± 0.03
12	0.61 ± 0.07	0.47 ± 0.25	0.01 ± 0.01	0.33 ± 0.20	0.03 ± 0.03
13	0.61 ± 0.07	0.15 ± 0.09	0.01 ± 0.01	0.25 ± 0.13	0.03 ± 0.03

Cut	SUM BACKGROUND	DATA	SUSY	SIGNAL EFF
1	195556.78 ± 176.94	194006	38.70 ± 0.40	0.1979± 0.0025
2	48220.13 ± 106.27	47140	30.79 ± 0.36	0.1575± 0.0023
3	26066.56 ± 88.43	22766	28.57 ± 0.35	0.1462± 0.0022
4	910.32 ± 13.87	996	21.85 ± 0.30	0.1117± 0.0020
5	353.10 ± 8.89	332	20.08 ± 0.29	0.1027± 0.0019
6	181.01 ± 6.41	178	17.12 ± 0.27	0.0875± 0.0018
7	44.05 ± 2.88	42	9.52 ± 0.19	0.0487± 0.0014
8	5.53 ± 0.87	10	8.17 ± 0.18	0.0418± 0.0013
9	2.88 ± 0.69	7	6.71 ± 0.16	0.0343± 0.0012
10	2.18 ± 0.46	4	5.76 ± 0.15	0.0295± 0.0011
11	2.02 ± 0.40	4	5.76 ± 0.15	0.0295± 0.0011
12	1.57 ± 0.33	4	5.63 ± 0.15	0.0288± 0.0011
13	1.17 ± 0.19	4	5.51 ± 0.15	0.0282± 0.0010

Table 9.5.: Number of candidate events observed and background events expected at different stages of the high p_T muon selection. The number of expected signal events and the signal efficiency for the point with $m_0 = 150$ GeV, $m_{1/2} = 250$ GeV are also given. The different cutstages are defined in Table 9.3. Errors are statistical.

Cut	Upsilon	WW	$t\bar{t}$	ZZ	$Zb\bar{b}$
1	265.88 ± 20.58	122.72± 2.16	53.66 ± 1.41	40.05± 0.35	1172.16 ± 10.21
2	265.88 ± 20.58	73.56 ± 1.71	28.04 ± 1.02	5.79 ± 0.14	102.96 ± 3.61
3	265.88 ± 20.58	68.30 ± 1.65	26.10 ± 0.98	5.26 ± 0.13	80.51 ± 3.34
4	2.82 ± 1.63	60.07 ± 1.54	24.49 ± 0.95	2.59 ± 0.10	17.49 ± 1.65
5	1.01 ± 1.01	56.70 ± 1.50	14.40 ± 0.73	1.37 ± 0.07	3.14 ± 0.59
6	1.01 ± 1.01	52.70 ± 1.44	13.10 ± 0.70	1.09 ± 0.06	1.59 ± 0.43
7	0.00 ± 0.00	7.27 ± 0.56	11.62 ± 0.63	0.34 ± 0.03	0.86 ± 0.30
8	0.00 ± 0.00	1.01 ± 0.21	0.81 ± 0.14	0.22 ± 0.02	0.29 ± 0.17
9	0.00 ± 0.00	0.54 ± 0.18	0.07 ± 0.04	0.16 ± 0.02	0.03 ± 0.02
10	0.00 ± 0.00	0.40 ± 0.15	0.07 ± 0.04	0.10 ± 0.02	0.03 ± 0.02
11	0.00 ± 0.00	0.38 ± 0.15	0.06 ± 0.04	0.09 ± 0.01	0.03 ± 0.02
12	0.00 ± 0.00	0.21 ± 0.12	0.03 ± 0.02	0.08 ± 0.01	0.03 ± 0.02

Cut	WZ	$W \to \ell\nu$	$Z \to \tau\tau$	$Z \to \mu\mu$	fakes
1	72.84 ± 0.78	48.71 ± 3.35	951.59 ± 2.97	138939.56 ± 1.78	114.23 ± 2.60
2	11.75 ± 0.35	43.94 ± 3.24	920.02 ± 2.94	20158.96 ± 0.92	106.48 ± 2.51
3	10.56 ± 0.33	40.54 ± 3.18	272.32 ± 2.38	9821.57 ± 0.71	53.50 ± 1.78
4	5.90 ± 0.22	36.45 ± 3.06	102.61 ± 1.86	568.43 ± 0.53	18.01 ± 1.03
5	4.21 ± 0.18	33.60 ± 3.02	46.11 ± 1.65	170.41 ± 0.19	1.75 ± 0.32
6	3.59 ± 0.17	27.62 ± 2.73	1.01 ± 0.51	73.92 ± 0.14	0.82 ± 0.22
7	1.99 ± 0.12	6.31 ± 1.17	0.25 ± 0.29	36.21 ± 0.11	0.46 ± 0.16
8	1.56 ± 0.11	0.84 ± 0.25	0.03 ± 0.15	5.66 ± 0.10	0.06 ± 0.06
9	1.19 ± 0.09	0.56 ± 0.21	0.01 ± 0.10	1.16 ± 0.09	0.06 ± 0.06
10	1.05 ± 0.09	0.39 ± 0.19	0.01 ± 0.10	0.83 ± 0.09	0.06 ± 0.06
11	1.02 ± 0.09	0.27 ± 0.19	0.01 ± 0.10	0.68 ± 0.68	0.06 ± 0.06
12	0.98 ± 0.09	0.06 ± 0.06	0.01 ± 0.10	0.56 ± 0.56	0.06 ± 0.06

Cut	SUM BG	DATA	SUSY	SIGNAL EFFICIENCY
1	141781.41 ± 120.01	140417	4.24 ± 0.04	0.1964± 0.0025
2	21717.39 ± 63.36	21931	3.30 ± 0.04	0.1526± 0.0023
3	10644.55 ± 51.32	10349	3.11 ± 0.04	0.1440± 0.0022
4	838.86 ± 11.94	948	2.85 ± 0.04	0.1319± 0.0021
5	332.71 ± 7.82	326	2.68 ± 0.03	0.1239± 0.0021
6	176.45 ± 5.73	173	2.46 ± 0.03	0.1138± 0.0020
7	65.34 ± 3.64	62	1.82 ± 0.03	0.0845± 0.0018
8	10.48 ± 1.23	10	1.54 ± 0.03	0.0714± 0.0016
9	3.79 ± 0.50	7	1.28 ± 0.02	0.0592± 0.0015
10	2.94 ± 0.44	4	1.18 ± 0.02	0.0545± 0.0014
11	2.59 ± 0.40	4	1.13 ± 0.02	0.0524± 0.0014
12	2.02 ± 0.33	4	1.09 ± 0.02	0.0503± 0.0014

Table 9.6.: Kinematic properties of the objects reconstructed in one of the events selected in data in the $\mu\mu\ell$ selection.

Run number: 207 947			Event number: 52 507 016			
object	p_T	η	ϕ	χ^2/ndof	trackiso	caliso
μ_1	16.4 GeV	-1.5	4.7	1.4	2.3 GeV	0.5 GeV
μ_2	13.4 GeV	-0.4	3.9	0.3	0 GeV	1.2 GeV
track	10.6 GeV	-0.6	2.9	2.2	0 GeV	0 GeV
$M(\mu,\mu)$	20.6 GeV					
$\not{E}_T$	35.3 GeV					

Table 9.7.: Kinematic properties of the objects reconstructed in one of the events selected in data in the $\mu\mu\ell$ selection.

Run number: 229 154			Event number: 71 622 290			
object	p_T	η	ϕ	χ^2/ndof	trackiso	caliso
μ_1	20.5 GeV	-0.84	1.3	6.5	1.1 GeV	0.4 GeV
μ_2	14.1 GeV	0.19	5.9	3.4	0 GeV	0.2 GeV
track	10.8 GeV	-0.4	1.0	1.9	0 GeV	0.5 GeV
$M(\mu,\mu)$	30.7 GeV					
$\not{E}_T$	34.8 GeV					

Table 9.8.: Kinematic properties of the objects reconstructed in one of the events selected in data in the $\mu\mu\ell$ selection.

Run number: 231 184			Event number: 34 078 340			
object	p_T	η	ϕ	χ^2/ndof	trackiso	caliso
μ_1	25.3 GeV	1.1	4.16	0.6	2.0 GeV	0.8 GeV
μ_2	24.7 GeV	0.6	1.65	1.1	0 GeV	0.6 GeV
track	19.5 GeV	-1.6	1.30	2.5	0 GeV	0.8 GeV
$M(\mu,\mu)$	48.9 GeV					
$\not{E}_T$	52.8 GeV					

Table 9.9.: Kinematic properties of the objects reconstructed in one of the events selected in data in the $\mu\mu\ell$ selection.

Run number: 233 379			Event number: 21 162 880			
object	p_T	η	ϕ	χ^2/ndof	trackiso	caliso
μ_1	42.3 GeV	-1.2	1.23	1.1	0 GeV	0 GeV
μ_2	25.4 GeV	-0.2	2.16	1.1	0 GeV	0.4 GeV
track	23.1 GeV	0.8	4.06	0.7	0 GeV	1.2 GeV
$M(\mu,\mu)$	44.8 GeV					
$\not\!\!E_T$	61.9 GeV					

Table 9.10.: Kinematic properties of the objects reconstructed in the event observed in the high-p_T selection after overlap subtraction.

Run number: 232 675			Event number: 28 439 048			
object	p_T	η	ϕ	χ^2/ndof	trackiso	caliso
μ_1	30.9 GeV	0.0	0.4	1.0	0.6 GeV	0.4 GeV
μ_2	27.1 GeV	-1.6	2.7	1.0	0 GeV	1.3 GeV
track	20.8 GeV	-0.5	2.2	1.7	0 GeV	1.0 GeV
$M(\mu,\mu)$	73.7 GeV					
$\not\!\!E_T$	41.5 GeV					

9.3. The $ee\ell$ Selection

The following section describes the low- and high-p_T $ee\ell$ selections. Table 9.13 lists the cuts applied in both selections. The discussion of the various cuts will be briefer than in the $\mu\mu\ell$ section. Selection criteria that are the same in both the $\mu\mu\ell$ and $ee\ell$ selections are described in detail in the previous chapter. Selection cuts that are unique to the $ee\ell$ analysis will be described in detail here.

9.3.1. $ee\ell$ Preselection Cuts

The $ee\ell$ preselection requires two electrons from the same primary vertex (Δz (lepton, primary vertex) < 1.5 cm). The pseudorapidity, $|\eta_{det}|$, is restricted to be less than 3.0 for both electrons and at least one electron is required to be central, $|\eta_{det}| < 1.1$. The η_{phys} distributions at preselection for the two electrons are shown in Figure 9.25. The likelihood (see Section 6.2.2) is required to be greater than 0.2 for both electrons.

The process $W \rightarrow e\nu + \gamma$ is an important background in the $ee\ell$ analysis. The photon can radiate from the W or the electron, or come from a π^0 or a ρ^0 decay, and it can convert into an e^+e^- pair. The electron from the W decay is mostly reconstructed as the leading electron, while the conversion electron is reconstructed as the next to leading electron. Since the electrons are required to be matched to a track, the conversion must take place in the tracker. In order to reduce the contribution from $W \rightarrow e\nu$ with electrons from conversions, at least one SMT hit is required for the next to leading electron if it is within the acceptance of the SMT, $|z_0| < 35$ cm. If the electron is outside the acceptance of the SMT, the likelihood cut is tightened to 0.8.

As in the muon analysis, cuts on the transverse momenta of the electrons were scanned and optimized both in the low- and in the high-p_T selection. Figure 9.26 shows the marginal distribution and the expected limit as a function of the p_T-cut of the second electron in the high-p_T analysis. Figure 9.27 shows the same for the leading electron. The p_T distribution at preselection stage was shown in Figure 8.7.

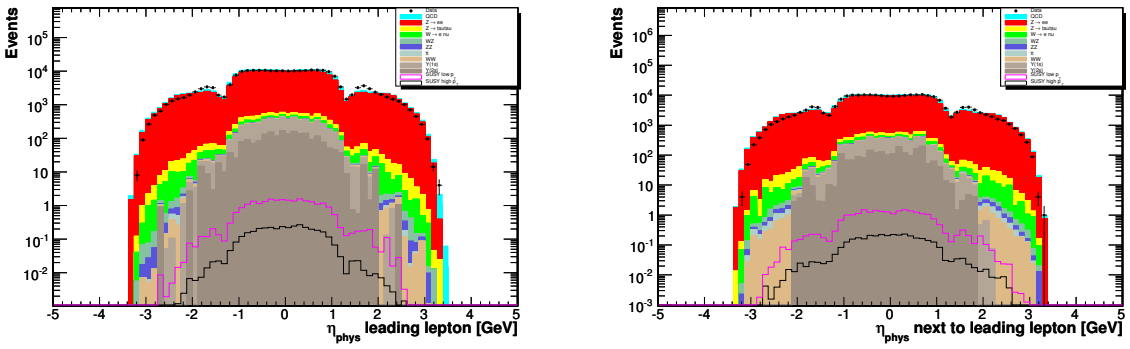

Figure 9.25.: η_{phys} distribution at preselection level for the leading electron (left) and the next to leading electron (right).

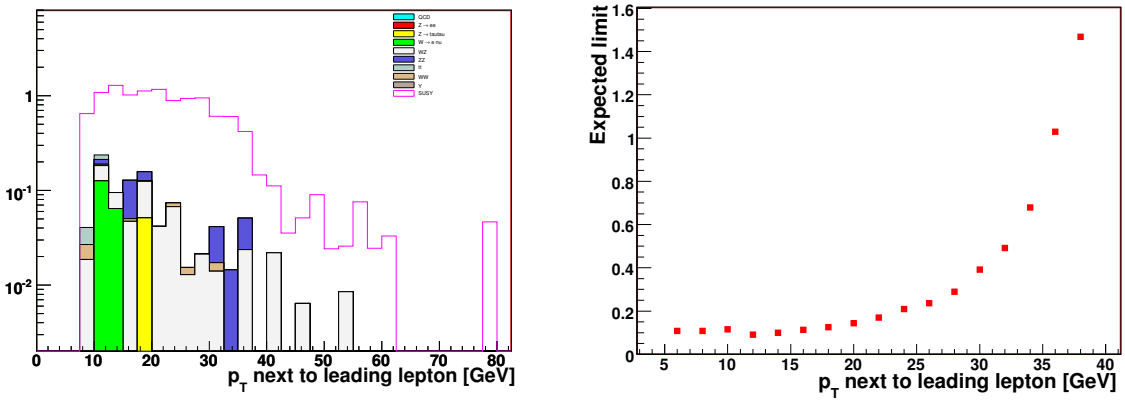

Figure 9.26.: Marginal distribution of the p_T of the next to leading electron (left) expected limit (right) in the high-p_T selection. The signal point corresponds to m_0 =150 GeV and $m_{1/2}$ =250 GeV.

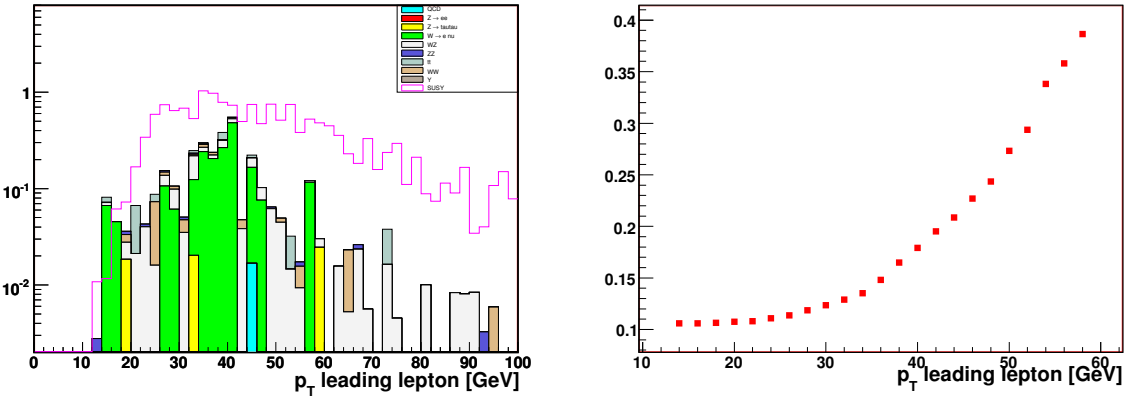

Figure 9.27.: Marginal distribution of the p_T of the leading electron (left) expected limit (right) in the high-p_T selection. The signal point corresponds to m_0 =150 GeV and $m_{1/2}$ =250 GeV.

9.3.2. Anti Z Cut

In the $ee\ell$ analysis, the invariant mass in the low-p_T selection is required to be between 18 GeV and 60 GeV. The cuts are relaxed to 0 GeV and 75 GeV in the high-p_T selection. Figure 9.28 shows the marginal distribution and the expected limit as a function of cut on invariant mass in the high-p_T selection. The invariant mass is shown in Figure 9.29 at preselection in the low-p_T (left) and high-p_T selection (right).

As in the muon analysis, a cut on the azimuthal angle between the two electrons is made to reject $Z \to ee$, $Z \to \tau\tau$ and QCD events. The azimuthal angle is required to be less than 2.9 radians. Figure 9.30 shows the distribution at preselection stage (left) and before the cut is applied (right) in the low-p_T selection.

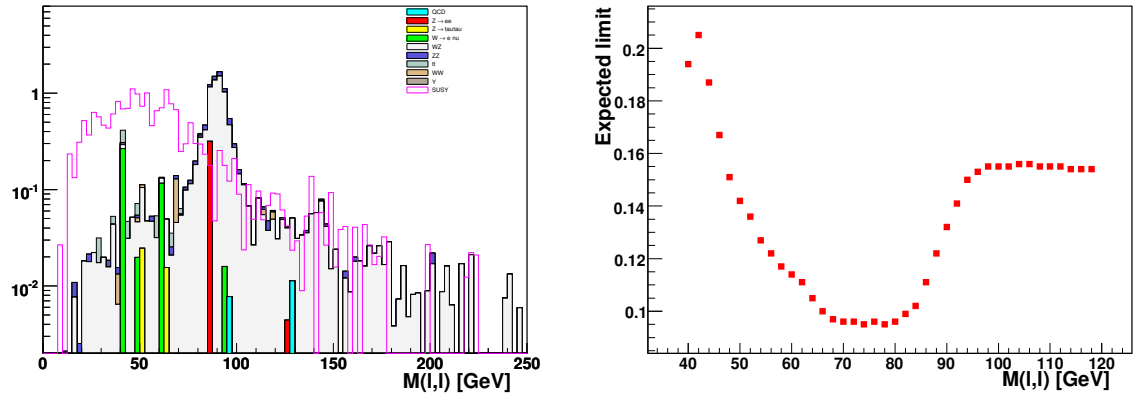

Figure 9.28.: Marginal distribution of invariant mass and expected limit as a function of upper cut on mass in the high-p_T selection.

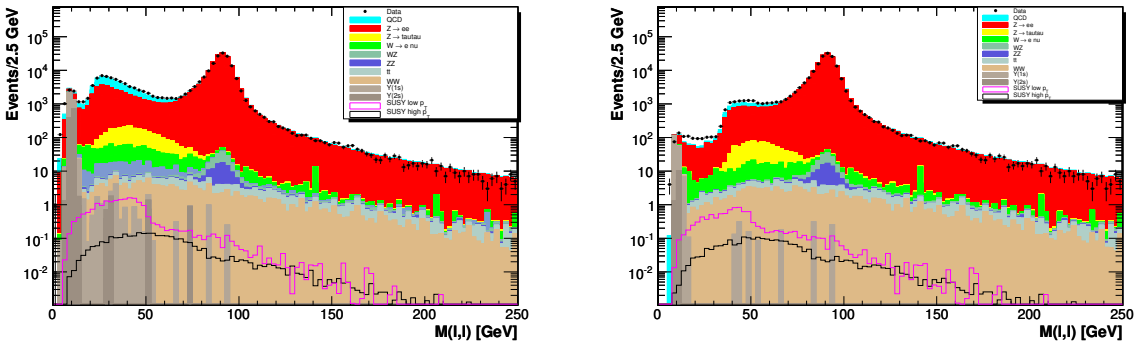

Figure 9.29.: Invariant mass in the low-p_T selection (left) and in the high-p_T selection (right) at preselection stage.

9.3.3. Sum of Jet Transverse Momenta, H_T

Top pair production constitutes an important background because there is true missing transverse energy in top quark decays. The missing transverse energy comes from the leptonically decaying W. In contrast to the signal, however, $t\bar{t}$ events have at least two hard jets from the decay of the top quarks. Therefore only events with $H_T < 80$ GeV are accepted, where H_T is defined as the scalar sum of the jet transverse momenta in the event. Since high-p_T jets are much more rare in signal events, this cut rejects a large fraction of $t\bar{t}$ background while it results only in a small inefficiency for signal. Figure 9.31 shows the H_T distribution at preselection stage (left) and before the cut is applied (right) in the high-p_T $ee\ell$ analysis.

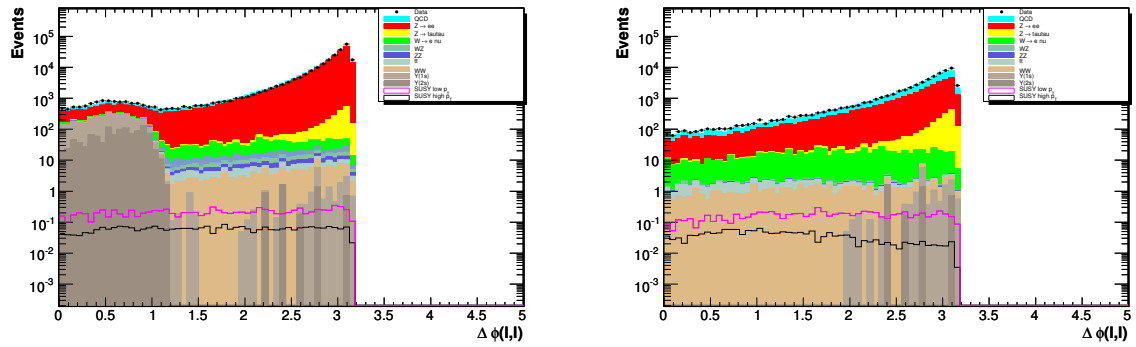

Figure 9.30.: Azimuthal angle $\Delta\phi$ between the two electrons in the low-p_T selection at preselection stage (left) and before the cut is applied (right).

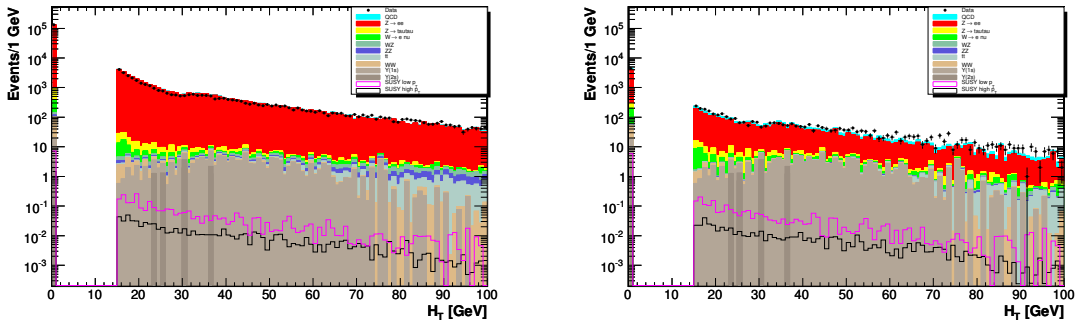

Figure 9.31.: H_T at preselection stage in the high-p_T analysis (left) and before the cut is applied (right).

9.3.4. $\not\!\!E_T$ Related Cuts

The $\not\!\!E_T$, the Sig($\not\!\!E_T$) and minimum transverse mass cuts were scanned in both the low- and in the high-p_T selection. Events with $\not\!\!E_T$ below 22 GeV are discarded in the low-p_T selection. In the high-p_T selection, the cut is relaxed to 20 GeV. For the cut on Sig($\not\!\!E_T$) the cut value is 8 in both selections, while only events with minimum transverse mass above 20 GeV (14 GeV) are accepted in the low(high)-p_T selection. Figure 9.32 shows the distributions of $\not\!\!E_T$ (left), Sig($\not\!\!E_T$) (middle) and minimum transverse mass of the two electrons (right) at preselection in the high-p_T analysis. Figure 9.33 shows the $\not\!\!E_T$-distribution (left) Sig($\not\!\!E_T$) (middle) and minimum transverse mass of the two electrons (right), before the respective cuts are applied in the low-p_T selection.

9.3.5. Third Track

The same quality criteria for the third track (number of hits and χ^2/ndof of the track fit), are imposed in the $ee\ell$ analysis as in the $\mu\mu\ell$ analysis. In the low-p_T analysis, the third track is

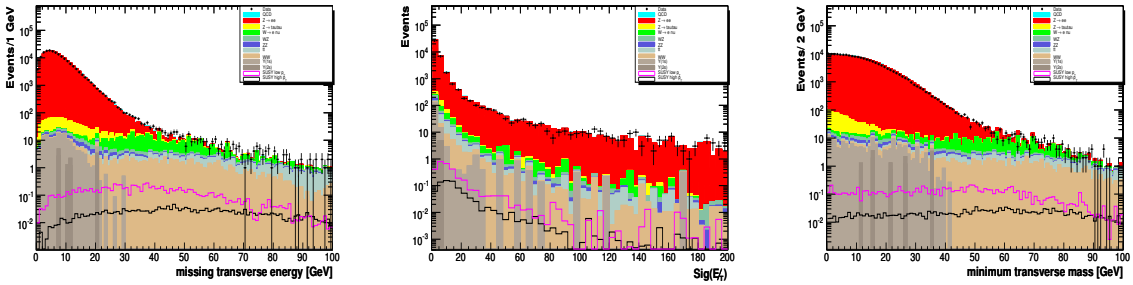

Figure 9.32.: $\not\!\!E_T$, Sig($\not\!\!E_T$) and minimum transverse mass. All distribution are from preselection stage in the high-p_T selection.

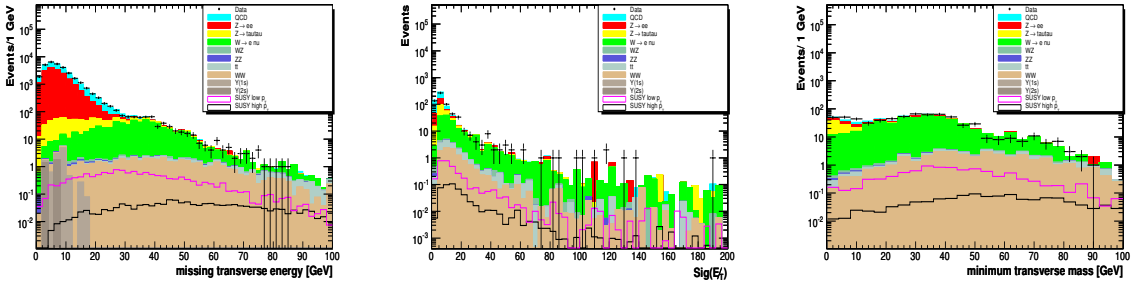

Figure 9.33.: Missing tranvserse energy (left), significance of $\not\!\!E_T$(middle) and minimum transverse mass (right) in the low-p_t selection. All distributions are shown before the cut on the particular quantity is applied.

required to have a transverse momentum that exceeds 4 GeV, while this cut is thightened to 12 GeV in the high-p_T selection. Both cuts were scanned and optimized for the best expected limit. The reason for the very different track momenta cuts in the $ee\ell$ analysis and the $\mu\mu\ell$ analysis is caused by the fact that $W + (jets)$ background contributes to the total background to a much larger extent in the $ee\ell$ analysis, since the rate for a jet faking the second lepton is higher in the $ee\ell$ analysis. As described in Section 3.2, a third track present in $W + (jets)$ events must come from a jet and consequently have an exponentially falling p_T spectrum and a tight cut on the track momentum will greatly reduce this background. The requirement $p_T(\text{track}) > 12$ GeV reduces the remaining $W + (jets)$ background by a factor of four while only 7.3% of the signal is lost.

As in the $\mu\mu\ell$ analyses, the third track is required to be isolated and the same isolation criteria are imposed on the track. The isolation in the tracker is required to be less than 1 GeV and events with isolation in the calorimeter larger than 1.5 GeV are rejected. Also, only events with exactly one or three tracks in the isolation cone in the tracker are kept.

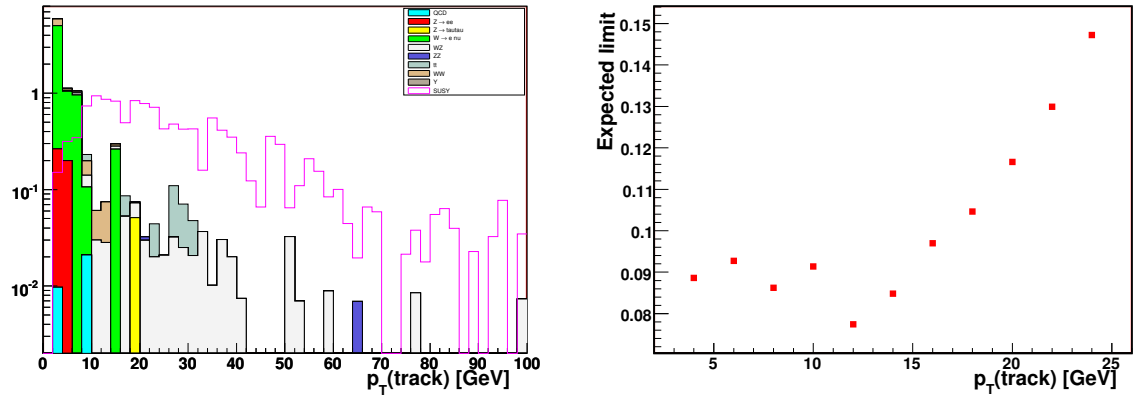

Figure 9.34.: Marginal distribution of track p_T (left) and expected limit as a function of cut on track p_T (right) in the high-p_T selection.

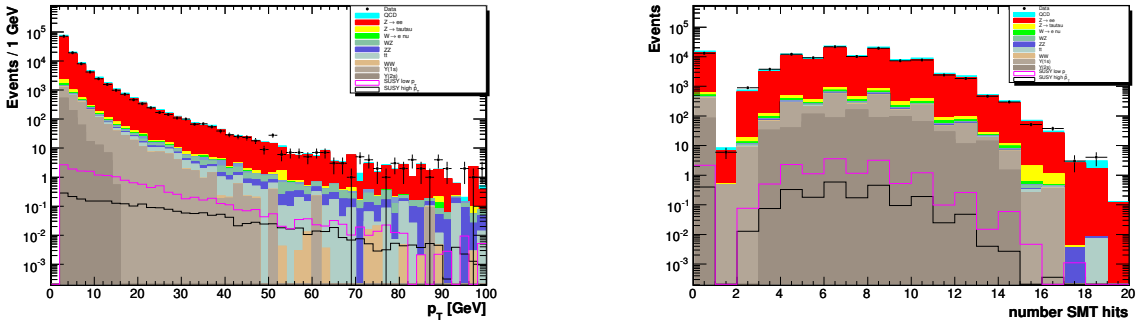

Figure 9.35.: p_T of third track at preselection stage (left) and number of SMT hits of this track at preselection stage (right).

9.3.6. Anti-W Cut

In $W + (jets)$ events, the second electron is expected to have worse electron ID because it is faked by a jet. The third track is also expected to have low transverse momentum. In order to reduce the remaining $W + (jets)$ background, the likelihood requirement is tightened to 0.8 for the second electron in events where the transverse momentum of the third track is below 15 GeV. The cut is not applied in the high-p_T selection, because of the tight cut on the track momentum. This requirement removes 60% of the remaining $W \to e\nu$ events at this stage in the low-p_T selection.

9.3.7. Cut on Transverse Mass of Track and $\not\!\!E_T$

A cut on the transverse mass of the track and $\not\!\!E_T$, $M_T(\text{track}, \not\!\!E_T)$ is applied. In both low-p_T and high-p_T selection, the transverse mass is required to be greater than 10 GeV. Figure 9.37

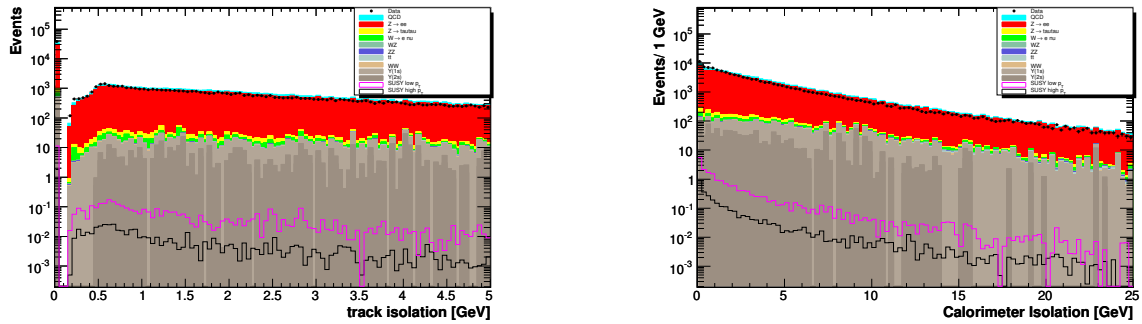

Figure 9.36.: Track isolation (left) and calorimeter isolation at preselection stage (right) in the low-p_T analysis.

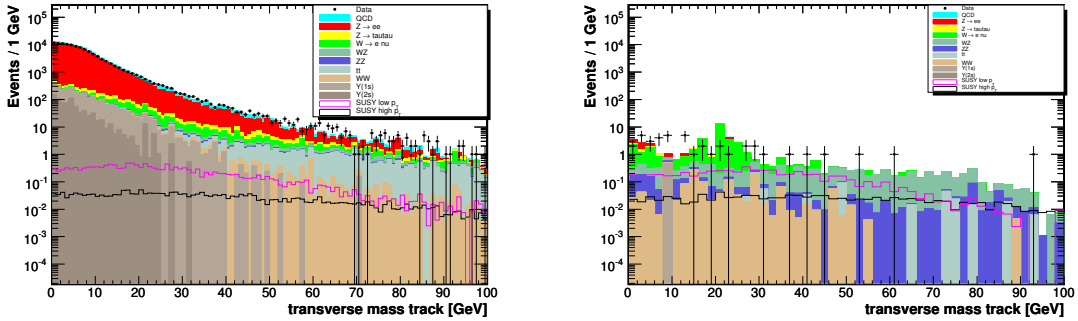

Figure 9.37.: Transverse mass of third track at preselection stage (left) and before the cut is applied (right) for the low-p_T analysis.

shows the $M_T(\text{track}, \not\!\!E_T)$ distribution at preselection level and before the cut is applied in the low-p_T selection and Figure 9.38 shows the marginal distribution and the expected limit as a function of the $M_T(\text{track}, \not\!\!E_T)$-cut in the high-$p_T$ analysis.

9.3.8. Combined Cut on $\not\!\!E_T$ and p_T(track) and Cut on p_T Balance

The combined cut on $\not\!\!E_T$ and track p_T is used also in the $ee\ell$ analysis. In the low-p_T selection, all events are required to have $\not\!\!E_T \times p_T(\text{track})$ greater than 220 GeV^2. This requirement is automatically met in the high-p_T selection. Figure 9.39 shows the distribution at preselection level in the low-p_T analysis and before the cut is applied (right). Figure 9.40 shows the marginal distribution (left) and the expected limit as a function of the cut value (rigth) for this quantity.

The p_T-balance is required to be lower than four in both selections. Figure 9.41 shows the p_T-balance distribution at preselection and before the cut is applied in the low-p_T selection.

Since the available Monte Carlo statistics for certain background samples is limited, loose samples are used to calculate the rejection factor. This is done for the $Z \to ee$ background in the

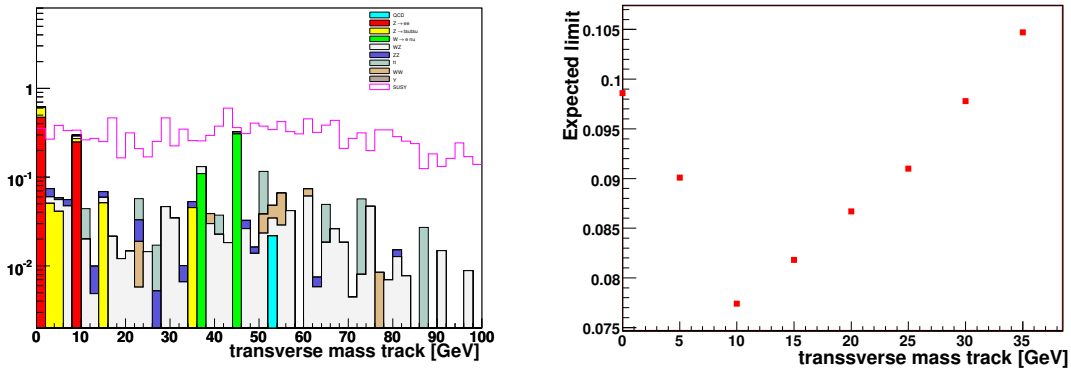

Figure 9.38.: Marginal distribution (left) and expected limit (right) as a function of the cut on the track transverse mass.

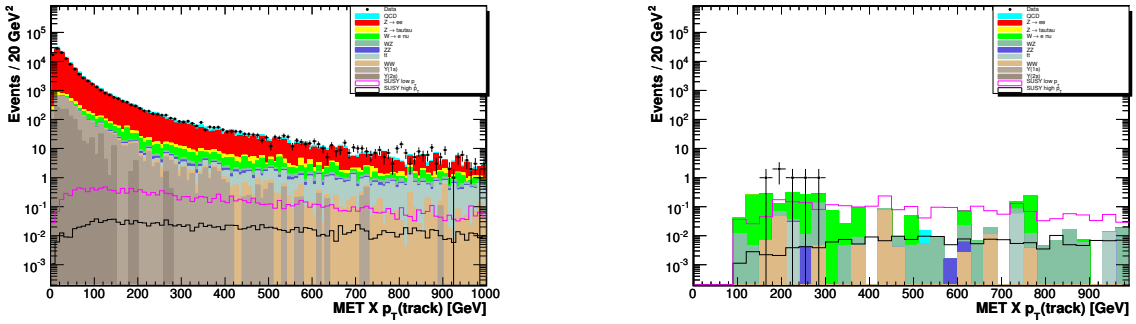

Figure 9.39.: $\not\!\!E_T \times p_T$(track) distribution at preselection (left) and before the cut is applied (right). Both plots are from the low-p_T analysis.

low-p_T analysis after the cut on calorimeter isolation for the third track. The loose sample was defined by loosening the invariant mass cut to 120 GeV and lowering the p_T cut of the leading electron to 8 GeV. Furthermore, the $\Delta\phi$ cut was removed along with the H_T cut. The cut on Sig($\not\!\!E_T$) was also removed and the third track was selected without the χ^2/ndof requirement and isolation requirments.

9.3.9. Results of the $ee\ell$ Selection

Table 9.14 presents the number of events selected in data and the Standard Model background expectation for the low-p_T electron selection, while Table 9.15 gives a summary of the high-p_T selection. In Table 9.14, the signal efficiency for the signal point $m_0 = 150$ GeV, $m_{1/2} = 170$ GeV is given and in Table 9.15 for point $m_0 = 150$ GeV, $m_{1/2} = 250$ GeV.

In the low-p_T selection 2 events are observed in data, while 1.80±0.22 (stat)±0.22 (syst) events are expected from Standard Model processes. The signal efficiency for the point with m_0=150 GeV and $m_{1/2}$ =170 GeV is 2.13%±0.09%. The dominant backgrounds after all cuts, are $W \to \ell\nu$

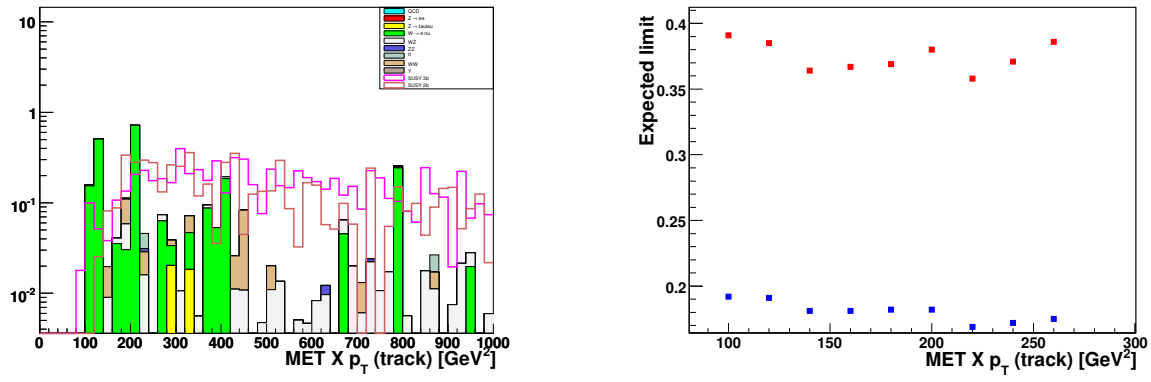

Figure 9.40.: Marginal distribution (left) with the two susypoints $(m_0, m_{1/2})$=(150 GeV,170 GeV) (labelled 3b) and $(m_0, m_{1/2})$=(76 GeV,185 GeV) (labelled 2b) and expected limit as a function of cut on the $\not{E}_T \times p_T$(track) variable (right) with $(m_0, m_{1/2})$=(150 GeV,170 GeV) as the lower line and $(m_0, m_{1/2})$=(76 GeV,185 GeV) as the upper.

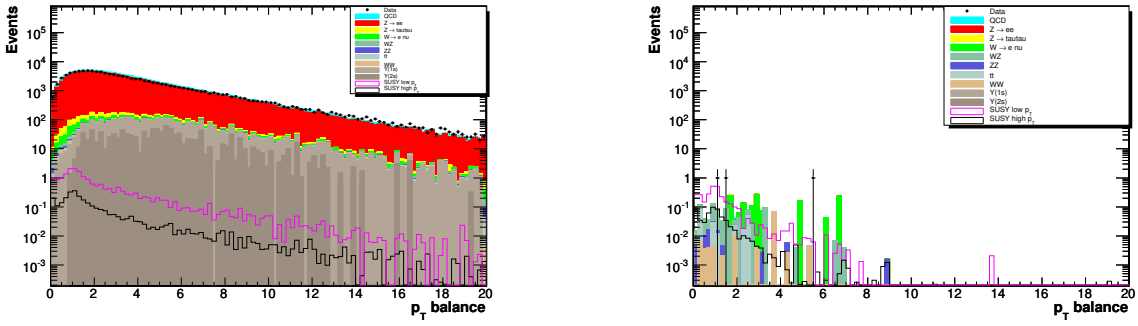

Figure 9.41.: The p_T balance at preselection (left) and before the cut is applied (right) in the low-p_T selection.

that constitutes 40% of the total expected background and WZ that contributes 32%.

In the high-p_T selection, zero events are observed in data, with 0.80± 0.23(stat)± 0.03(syst) expected from Standard Model processes. In the high-p_T selection, WZ is the biggest background component with 60%, while $t\bar{t}$ contributes with 20%. $W \to \ell\nu$ is less important in the high-p_T selection due to the tighter p_T cuts. The signal efficiency for the high-p_T point with m_0 = 150 GeV, $m_{1/2}$ = 250 GeV is 3.06%±0.11%. After subtraction of overlapping events between the low- and high-p_T $ee\ell$ selections, the expected number of background events is 0.34±0.13 (stat)±0.03 (syst) in the high-p_T analysis.

Table 9.11 and Table 9.12 list the run number, event number and kinematic properties of the objects reconstructed in the two data events observed in the low-p_T $ee\ell$ selection.

The number of observed events in data and the background expectations from Standard Model

Table 9.11.: Kinematic properties of the objects reconstructed in one of the events selected in data in the $ee\ell$ low-p_T selection.

Run number: 202 326			Event number: 3 858 114	
object	p_T	η	ϕ	
e_1	28.5 GeV	0.03	4.1	likelihood=0.99
e_2	9.5 GeV	−0.52	5.8	likelihood=0.99
track	10.4 GeV	−0.31	3.07	trackiso=0 GeV, caliso=0.24 GeV
$M(e,e)$	26.8 GeV			
$\not{E}_T$	27.6 GeV			

Table 9.12.: Kinematic properties of the objects reconstructed in one of the events selected in data in the $ee\ell$low-p_T selection.

Run number: 213 428			Event number: 57 824 208	
object	p_T	η	ϕ	
e_1	37.4 GeV	0.4	2.2	likelihood=0.40
e_2	20.1 GeV	1.7	0.9	likelihood=0.98
track	4.7 GeV	−1.0	2.1	trackiso=0.98 GeV, caliso=0 GeV
$M(e,e)$	46.0 GeV			
$\not{E}_T$	54.9 GeV			

processes after applying all selection criteria are summarized in Table 9.17 for all selections. In this table, overlap between the different selections is taken into account, because the low-p_T and high-p_T selections can select the same events. The overlap in data between the low- and high-p_T muon selections is 3 events. The overlap in signal and backgroun is subtracted from the high-p_T selections. The overlap between the low- and high-p_T muon selection ranges between 30% and 70% depending on SUSY parameters, and the overlap in the electron analyses ranges between 50% and 90%.

The number of expected events from Standard Model background processes in the four selections is 5.07±0.42 (stat)±0.30 (syst) while 7 events are observed in data. Systematic uncertainties will be discussed in the next section. In Table 9.17 is also listed number of expected signal events in the high-p_T and low-p_T selections. The number of expected signal events varies between 0.71 and 5.51, depending on selection.

Table 9.13.: A complete list of the cuts used in the $ee\ell$ analysis. The cuts used in the high-p_T selection are in parentheses. If a cut is removed in the high-p_T selection, it is noted (-), if the cut is unchanged, no indication is given.

	Selection criterion	Value
Cut 1	DiEM Preselection	Trigger, ID, $p_T^{e_1} > 12(18)$ GeV and $p_T^{e_2} > 8(16)$ GeV electron likelihood > 0.2, electrons from primary vertex, no ECEC. for $\lvert z_0\rvert < 35$ cm: at least 1 SMT hit, for $\lvert z_0\rvert >$ 35 cm, 2nd electron likelihood > 0.8
Cut 2	Invariant Mass	$18(0)$ GeV $< M(e,e) < 60(75)$ GeV
Cut 3	transverse openeing angle:	$\Delta\phi(e,e) < 2.9$
Cut 4	jet transverse momenta	$H_T < 80$ GeV (-)
Cut 5	Missing Transverse Energy:	$\not\!\!E_T > 22$ GeV (20 GeV)
Cut 6	$\not\!\!E_T$ signficance	Sig($\not\!\!E_T$) > 8.0 or no jets
Cut 7	Transverse Mass $M_T(e_{1,2})$	$M_T(e, \not\!\!E_T) > 20$ (14) GeV for both electrons
Cut 8	p_{T} of third track	$p_T(track) > 4.0$ (12.0) GeV
Cut 9	track isolation	$\Sigma p_T < 1$ GeV number of tracks in 0.1 cone 1 or 3 (-)
Cut 10	calorimeter Isolation	$E_{iso} < 1.5$ GeV
Cut 11	Transverse Mass ℓ_3	$M_T(\ell_3, \not\!\!E_T) > 10$ GeV
Cut 12	Anti-W cut:	electron likelihood 2nd electron > 0.8 for $p_T(track) < 15$ GeV (-)
Cut 13	$\not\!\!E_T$ and track p_T	$\not\!\!E_T \cdot p_T(track) > 220$ GeV^2 (-)
Cut 14	p_T balance	$\frac{\lvert \vec{p}_T^{\,\mu_1} + \vec{p}_T^{\,\mu_2} + \vec{\not\!\!E}_T\rvert}{p_T(track)} < 4$

Table 9.14.: Number of candidate events observed and background events expected at different stages of the low p_T electron selection. The expected number of events for the signal point $m_0 = 150$ GeV,$m_{1/2} = 170$ GeV is also given. Table 9.13 lists all the cuts that are applied. Errors are statistical.

Cut	Upsilon	WW	$t\bar{t}$	ZZ
1	3526.93±41.53	135.51±2.05	93.33± 0.44	74.49±0.81
2	15.99 ± 2.43	52.46 ± 1.29	32.40± 0.10	3.87±0.21
3	10.76 ± 2.14	48.82 ± 1.26	31.38± 0.10	3.52±0.21
4	10.76 ± 2.14	46.81 ± 1.22	9.59± 0.08	2.54±0.20
5	0.00 ± 0.00	38.89 ± 1.09	9.03± 0.05	0.91±0.15
6	0.00 ± 0.00	36.99 ± 1.06	7.14± 0.05	0.76±0.13
7	0.00 ± 0.00	34.63 ± 1.04	6.55± 0.04	0.54±0.12
8	0.00 ± 0.00	6.64 ± 0.52	5.93± 0.02	0.14±0.10
9	0.00 ± 0.00	0.71 ± 0.14	0.33± 0.01	0.08±0.08
10	0.00 ± 0.00	0.19 ± 0.08	0.21± 0.01	0.05±0.07
11	0.00 ± 0.00	0.17 ± 0.08	0.21± 0.01	0.04±0.07
12	0.00 ± 0.00	0.16 ± 0.08	0.19± 0.01	0.04±0.07
13	0.00 ± 0.00	0.11 ± 0.07	0.19± 0.01	0.04±0.07
14	0.00 ± 0.00	0.10 ± 0.07	0.19± 0.01	0.03±0.07
Cut	WZ	$W \to \ell\nu$	$Z \to \tau\tau$	fakes
1	106.84 ± 0.21	1205.17 ± 21.40	1851.27± 11.68	28275.30±50.73
2	7.33 ± 0.16	695.91 ± 14.80	1595.19± 10.88	16979.20±55.99
3	6.87 ± 0.16	631.65 ± 14.15	503.44± 6.94	8610.50± 41.12
4	5.89 ± 0.13	617.03 ± 14.11	484.91± 6.85	8193.20± 41.42
5	3.71 ± 0.11	488.70 ± 12.34	121.92± 3.37	309.30± 4.92
6	2.92 ± 0.09	454.48 ± 12.00	49.52± 2.05	51.40± 1.73
7	2.40 ± 0.08	356.73 ± 10.56	1.81± 0.33	21.40± 0.76
8	1.43 ± 0.06	65.79 ± 3.41	0.90± 0.22	7.40± 0.37
9	1.03 ± 0.03	20.24 ± 2.85	0.61± 0.17	1.60± 0.09
10	0.70 ± 0.03	7.02 ± 1.98	0.35± 0.09	0.50± 0.04
11	0.65 ± 0.03	4.32 ± 1.66	0.03± 0.03	0.40± 0.02
12	0.64 ± 0.03	1.78 ± 0.40	0.03± 0.03	0.20± 0.01
13	0.60 ± 0.03	1.19 ± 0.34	0.03± 0.03	0.10± 0.01
14	0.58 ± 0.03	0.77 ± 0.19	0.03± 0.03	0.10± 0.01
Cut	$Z \to ee$	SUM BG	DATA	SUSY
1	197467.85 ±185.02	232736.70 ± 201.84	235474	31.17 ±0.0419
2	30940.41 ± 64.83	50322.76 ± 79.75	60957	24.31 ±0.0318
3	17337.22 ± 53.42	27184.16 ± 63.86	31356	22.21 ±0.0311
4	17228.36 ± 53.21	26599.09 ± 63.33	30827	21.50 ±0.0306
5	138.04 ± 4.98	1110.50 ± 15.36	1085	16.14 ±0.0293
6	51.05 ± 3.22	654.27 ± 13.42	680	14.70 ±0.0285
7	25.33 ± 2.23	449.38 ± 11.48	465	13.77 ±0.0280
8	13.98 ± 1.68	102.22 ± 4.12	105	8.68 ±0.0239
9	0.89 ± 0.39	25.49 ± 3.04	30	7.27 ±0.0216
10	0.23 ± 0.20	9.25 ± 1.99	16	5.90 ±0.0190
11	0.07 ± 0.07	5.89 ± 1.67	9	4.99 ±0.0180
12	0.07 ± 0.07	3.11 ± 0.42	6	4.93 ±0.0178
13	0.02 ± 0.02	2.28 ± 0.36	3	4.43 ±0.0177
14	0.02 ± 0.02	1.80 ± 0.22	2	4.26 ±0.0174

Table 9.15.: Number of candidate events observed and background events expected at different stages of the high p_T electron selection. The signal efficiency for the signal point m_0 = 150 GeV,$m_{1/2}$ = 250 GeV is also given. Table 9.13 lists all the cuts that are applied. Errors are statistical.

Cut	Upsilon	WW	$t\bar{t}$	ZZ
1	171.41 ±7.75	108.8 ±1.87	73.76 ±0.44	66.69±0.42
2	170.85 ±7.74	50.85 ± 1.29	31.88 ±0.10	3.97±0.10
3	170.41 ±7.73	47.21 ± 1.25	30.54 ±0.10	3.56±0.10
4	7.00 ±2.59	41.99 ± 1.18	27.78 ±0.08	1.58±0.07
5	4.42 ±2.41	39.44 ± 1.14	16.75 ±0.05	0.99±0.05
6	4.42 ±2.41	38.50 ± 1.14	15.57 ±0.05	0.76±0.04
7	0.00 ±0.00	0.77 ± 0.12	8.07 ±0.04	0.12±0.02
8	0.00 ±0.00	0.12 ± 0.08	0.47 ±0.02	0.11±0.02
9	0.00 ±0.00	0.02 ± 0.01	0.21 ±0.01	0.07±0.01
10	0.00 ±0.00	0.02 ± 0.01	0.20 ±0.01	0.05±0.01
11	0.00 ±0.00	0.02 ± 0.01	0.20 ±0.01	0.05±0.01
Cut	WZ	$W \to \ell\nu$	$Z \to \tau\tau$	fakes
1	95.11±0.76	334.10 ± 13.98	656.41 ± 7.04	3652.52± 9.05
2	8.37±0.23	217.57 ± 9.91	615.00 ± 6.88	2888.72± 8.96
3	7.57±0.22	202.25 ± 9.62	174.74 ± 4.10	1191.54± 5.81
4	4.68±0.17	183.64 ± 9.41	51.23 ± 2.27	92.40 ± 1.45
5	3.37±0.14	165.94 ± 9.09	14.58 ± 1.15	10.36 ± 0.46
6	3.02±0.14	159.54 ± 9.04	1.77 ± 0.60	2.80 ± 0.24
7	1.08±0.08	2.06 ± 0.39	1.31 ± 0.68	0.25 ± 0.07
8	0.93±0.08	0.47 ± 0.26	0.32 ± 0.12	0.10 ± 0.06
9	0.58±0.06	0.23 ± 0.23	0.15 ± 0.05	0.00 ± 0.00
10	0.52±0.06	0.23 ± 0.23	0.03 ± 0.03	0.00 ± 0.00
11	0.51±0.06	0.002 ± 0.002	0.03 ± 0.03	0.00 ± 0.00
Cut	$Z \to ee$	SUM BG	DATA	SUSY
1	165038.14 ±173.21	170197.01 ± 174.64	171001	3.47± 0.036
2	14406.86 ±47.40	18394.07 ± 51.18	20932	2.55± 0.031
3	6109.92 ±34.59	7937.74 ± 38.55	8273	2.41± 0.030
4	234.86 ± 6.60	645.16 ± 12.49	657	2.24± 0.029
5	93.75 ± 4.33	349.60 ± 10.76	329	2.11± 0.029
6	38.03 ± 2.94	264.41 ± 10.18	244	2.01± 0.028
7	3.81 ± 1.26	17.47 ± 1.55	15	1.09± 0.021
8	0.88 ± 0.53	3.39 ± 0.62	0	1.00± 0.020
9	0.23 ± 0.15	1.50 ± 0.29	0	0.80± 0.018
10	0.08 ± 0.08	1.11 ± 0.25	0	0.73± 0.017
11	0.08 ± 0.08	0.80 ± 0.09	0	0.71± 0.016

Table 9.16.: Signal efficiency with statistical uncertainty for low-p_T and high-p_T. In the low-p_T column, the efficiencies for the signal point $m_0 = 150$ GeV, $m_{1/2} = 170$ GeV are given and in the high-p_T column, the efficiencies for the signal point $m_0 = 150$ GeV, $m_{1/2} = 250$ GeV are quoted. Table 9.13 lists all the cuts that are applied. Errors are statistical.

low-p_T		high-p_T	
Cut	Efficiency	Cut	Efficiency
1	0.1544 ± 0.0023	1	0.1489± 0.0023
2	0.1204 ± 0.0021	2	0.1091± 0.0020
3	0.1100 ± 0.0020	3	0.1033± 0.0019
4	0.1065 ± 0.0020	4	0.0959± 0.0019
5	0.0800 ± 0.0017	5	0.0905± 0.0018
6	0.0728 ± 0.0016	6	0.0862± 0.0018
7	0.0682 ± 0.0016	7	0.0467± 0.0013
8	0.0430 ± 0.0013	8	0.0428± 0.0013
9	0.0367 ± 0.0012	9	0.0343± 0.0012
10	0.0296 ± 0.0011	10	0.0312± 0.0011
11	0.0249 ± 0.0010	11	0.0306± 0.0011
12	0.0246 ± 0.0010		
13	0.0221 ± 0.0009		
14	0.0213 ± 0.0009		

Table 9.17.: Number of events observed, events expected from Standard Model processes and events expected for signal point after applying all selection criteria. Both the statistical and systematic uncertainty on the number of events are quoted. For the high-p_T selections, the number of signal events for the point $m_0 = 150$ GeV, $m_{1/2} = 250$ GeV are given, and for the low-p_T, the signal events for $m_0 = 150$ GeV, $m_{1/2} = 170$ GeV are given. Overlap between the selections is taken into account.

Selection	Data	Expected Background from Standard Model	Signal Expectation
$\mu\mu\ell$ low-p_T	4	1.17 ± 0.19 (stat) ± 0.11 (syst)	5.51 ± 0.15 (stat) ± 0.46 (syst)
$\mu\mu\ell$ high-p_T	1	1.93 ± 0.24 (stat) ± 0.17 (syst)	1.09 ± 0.02 (stat) ± 0.09 (syst)
$ee\ell$ low-p_T	2	1.80 ± 0.22 (stat) ± 0.22 (syst)	4.26 ± 0.12 (stat) ± 0.37 (syst)
$ee\ell$ high-p_T	0	0.34 ± 0.13 (stat) ± 0.03 (syst)	0.71 ± 0.02 (stat) ± 0.06 (syst)
Total	7	5.24 ± 0.40 (stat) ± 0.30 (syst)	

9.4. Systematic Uncertainties

The estimates for expected numbers of background and signal events depend on numerous measurements that each introduces a systematic uncertainty. The different sources can be grouped as in the following:

- detector modeling (efficiency, resolution, calibration)
- modeling of the physics process (PDFs, NLO processes)
- calculation of the expected QCD background

The systematic uncertainties are determined after applying all selection criteria. The total systematic error is calculated as the square root of the quadratic sum of the individual errors, assuming they are independent. The sources of systematic uncertainty are described below and summarized in Table 9.18.

Since the integrated luminosity is determined by normalizing the MC events to data using $Z \to \ell\ell$ decays, trigger efficiencies, lepton identification and reconstruction efficiencies are assumed to cancel. Conservatively, a 4% systematic uncertainty is assigned to take into account possible p_T or η dependences of these efficiencies. The systematic error on the normalization factor sums up from a combination of the PDF uncertainty (4%), uncertainty on the NNLO $Z->\ell\ell$ cross section (4%) and from the statistical error on the data/Monte Carlo normalization factor (2%). These contributions give a systematic error of 6%.

The jet energy scale was varied within $\pm 1\sigma$ as determined in [71]. The uncertainty in signal was found to be (1%) and for background events (1%). The contribution to the total systematic uncertainty is small since the selection does not a use an explicit jet requirement and the impact on the analyses is only via the cuts on $\not\!\!E_T$ and H_T.

The uncertainty due to the smearing of track transverse momenta was estimated to ($< 1\%$) by changing the smearing applied to the track momenta by 5%. The correction applied to the Monte Carlo simulation for the reconstruction efficiency of the isolated track is varied within $\pm 1\sigma$. The resulting uncertainty on signal and background is 1%.

The PDF-related errors on the Standard Model background cross sections are presented in Table 7.3, and are calculated according to [90]. The PDF uncertainty on the signal cross section increases with the chargino and neutralino masses. For a chargino mass of 130 GeV, the errors was calculated to 4.5% [112].

The uncertainty on the multijet normalization is estimated to 30%. The uncertainty was derived by varying the global scale factor by an amount that still kept the invariant mass distribution in acceptable agreement. The relevant distributions are shown in Figure 7.10 and Figure 7.11.

The uncertainty on the normalization of W background was determined to 20%. The uncertainty on modeling of $W \to \ell\nu$ background is based on the transverse mass distribution of leading lepton and $\not\!\!E_T$ in the $W \to \ell\nu$ control sample. The normalization was varied within

the error while still keeping an acceptable agreement. The relevant distributions are shown in Figure 8.23 and Figure 8.24.

The systematic uncertainty for the signal was estimated to 8.4% and between 8.7% and 12.1% for background, depending on selection. Table 9.18 summarizes the various sources of systematic uncertainties, along with the total for the different selections described in this thesis.

Table 9.18.: Systematic uncertainties on the number of events expected from Standard Model processes and from SUSY processes after the last selection cut. The quadratic sum are quoted individually for the different analyses and selections because the multijet background and contribution from $W + (jets)$ are different.

Source	Background	Signal
trigger, lepton identification , reconstruction efficiencies	4%	4%
Jet Energy Scale	1%	1%
Track Momentum	1%	1%
Track Reconstruction	1%	1%
PDF/scale errors on the cross section	4.5%	4.5%
Multi-jet normalization	30%	-
$W + (jets)$ normalization	20%	-
Luminosity	6%	6%
Quadratic sum total low-p_T $\mu\mu\ell$	9.6%	8.4%
Quadratic sum total high-p_T $\mu\mu\ell$	8.8%	8.4%
Quadratic sum total low-p_T $ee\ell$	12.1%	8.4%
Quadratic sum total high-p_T $ee\ell$	8.7%	8.4%

10. Interpretation of the Results

Due to the agreement of the expected Standard Model background with the number of observed events, no evidence for the associated production of charginos and neutralinos is found and upper limits on the production cross section times the leptonic branching ratio, $\sigma \times \mathrm{BR}(3\ell)$, are extracted from the results of the previous chapter. The upper limits are compared to predictions from different SUSY models to derive constraints on SUSY parameters. First the upper limit versus the mass of the lightest chargino will be discussed. Then follows a discussion of the limit versus tan β, and more generally in the $(m_0, m_{1/2})$ plane. The results derived in this thesis are combined with two other analyses that search for the associated production of charginos and neutralinos: one with one electron, one muon and a third track in the final state and one with one muon, one tau and a third track or tau in the final state.

10.1. Signal Efficiency in the $(m_0, m_{1/2})$ Plane

The signal efficiency depends strongly on the kinematics of the final state, which is determined by the mass of the particles that take part in the reaction. In mSUGRA, the following mass relation between the lightest chargino, the next to lightest neutralino and the lightest neutralino holds: $m_{\tilde{\chi}_2^0} \approx m_{\tilde{\chi}_1^\pm} \approx 2 \cdot m_{\tilde{\chi}_1^\pm}$. The kinematics are determined by the mass of the lightest chargino, $m_{\tilde{\chi}_1^\pm}$, the mass difference between slepton and next to lightest neutralino, $\Delta m_{\tilde{\ell}}$=$m_{\tilde{\ell}}$-$m_{\tilde{\chi}_2^0}$, and the mass difference between next to lightest neutralino and sneutrino, $\Delta m_{\tilde{\nu}} = m_{\tilde{\nu}}$-$m_{\tilde{\chi}_2^0}$. $\Delta m_{\tilde{\ell}}$ is calculated using the mass of the right handed selectron and $\Delta m_{\tilde{\nu}}$ is calculated using the mass of the left handed electron sneutrino.

It was described in Section 3.1.2 how the $(m_0, m_{1/2})$ plane can be divided into a 3-body region ($m_{\tilde{\ell}} > m_{\tilde{\chi}_2^0}$) and a 2-body region ($m_{\tilde{\ell}} < m_{\tilde{\chi}_2^0}$). In the 3-body region, the gauginos decay via virtual sfermions and gauge bosons, and the mass of the lightest chargino is the most important factor for the signal efficiency. In the 2-body region, the next to lightest neutralino decays into a real slepton and a charged lepton, $\tilde{\chi}_2^0 \to \tilde{\ell}\ell$, and the lightest chargino decays into a slepton and a neutrino, $\tilde{\chi}_1^\pm \to \tilde{\ell}\nu$. The signal efficiency as a function of $\Delta m_{\tilde{\ell}}$ is shown in Figure 10.1. For small negative $\Delta m_{\tilde{\ell}}$, the p_T of the third lepton is small since its phase space is reduced. This results in a large decrease in the signal efficiency. Towards larger negative $\Delta m_{\tilde{\ell}}$, the available phase space for the lepton increases. This results in an increase of the signal selection efficiency. When the $|\Delta m_{\tilde{\ell}}|$ continues to increase, the phase space for decay of the lightest chargino into real sneutrinos, $\tilde{\chi}_1^\pm \to \tilde{\nu}\ell$ and the decay of next to lightest neutralino into sneutrino and neutrino, $\tilde{\chi}_3^0 \to \tilde{\nu}\nu$, opens up. First, the available phase space for the lepton is small, but it increases again with increasing negative $\Delta m_{\tilde{\nu}}$, leading to the rise in efficiency that can be observed in Figure 10.1. The decay of the second lightest neutralino to sneutrinos is not taken into consideration since it does not contribute to the trilepton signature. For larger values

of $m_{1/2}$ ($m_{1/2} > 248$ GeV), the phase space for chargino decays via real W bosons opens up, ($\tilde{\chi}_1^{\pm} \rightarrow W\tilde{\chi}_1^0$), because the lightest chargino gets massive enough for this reaction to take place. This region is on the border of the sensitivity of the analyses, since the production cross section is relatively small due to the high mass of the chargino. A problem in Pythia was discovered in the transition between chargino decays to virtual and real W bosons. In order not to overestimate the sensitivity of the analysis in this region, the branching ratio into real W bosons was set to zero above ($m_{1/2} > 248$ GeV). The branching ratio into sleptons for $m_{1/2} > 248$ GeV is set equal to the branching fraction just below the line $m_{1/2} = 248$ GeV.

In order to parametrize the signal efficiency as a funtion of $(m_0, m_{1/2})$, the efficiencies need to be fitted to determine a function dependent on m_0 and $m_{1/2}$. In the 2-body region, instead of fitting the total signal efficiency, the fits were made for two separate chargino decays: chargino decaying via slepton and chargino decaying via sneutrino in order to study the efficiencies according to the possible decays of the chargino. The efficiencies are combined when calculating the limit, taking the correct branching fractions into account. Figure 10.2 (left) shows the fitted signal efficiency $\tilde{\chi}_1^{\pm} \rightarrow \tilde{\ell}\nu$ as a function of $\Delta m_{\tilde{\ell}}$. The efficiency is normalized to number of events where the chargino decays via a slepton and a neutrino for $\Delta m_{\tilde{\ell}} < 0$ and number of events with leptonic decays of the chargino and neutralino for $\Delta m_{\tilde{\ell}} < 0$. The signal efficiency as a function of $\Delta m_{\tilde{\nu}}$ is shown in Figure 10.2 (right). The efficiency rises when the mass difference between the sneutrino and the slepton gets bigger because the transverse momentum of the lepton increases. The efficiency is normalized to the number of events with $\tilde{\chi}_1^{\pm} \rightarrow \tilde{\nu}\ell$.

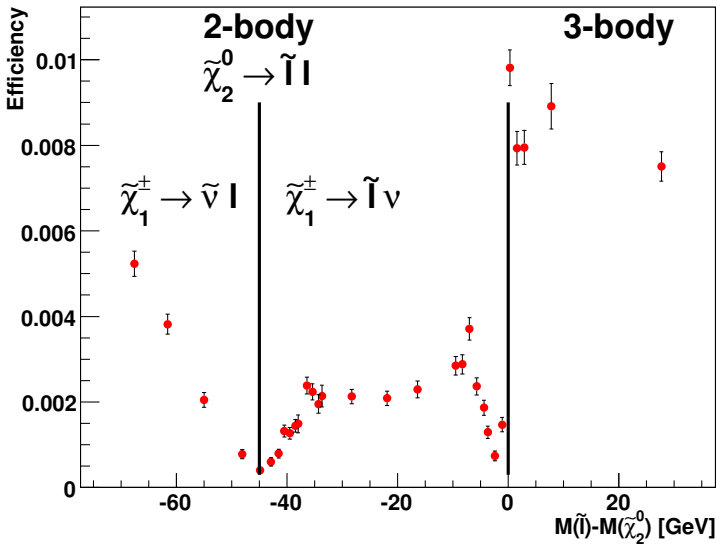

Figure 10.1.: Signal efficiency as a function of $\Delta m_{\tilde{\ell}} = m_{\tilde{\ell}} - m_{\tilde{\chi}_2^0}$, relative to number of events with chargino and neutralino decays into three charged leptons. The drop in signal efficiency around $\Delta m_{\tilde{\ell}} \approx 0$ is due to the softness of the third lepton in the transition from 3-body decay to 2-body decay of the next to lightest neutralino. The other minimum occurs when the phase space allows for decays of charginos into real sneutrinos. Arbitrary scaling.

The signal efficiency in the 3-body region as a function of $m_{\tilde{\chi}_1^{\pm}}$ is shown in Figure 10.3 (left). The increase of the selection efficiency with the chargino mass is a result of the increase of the

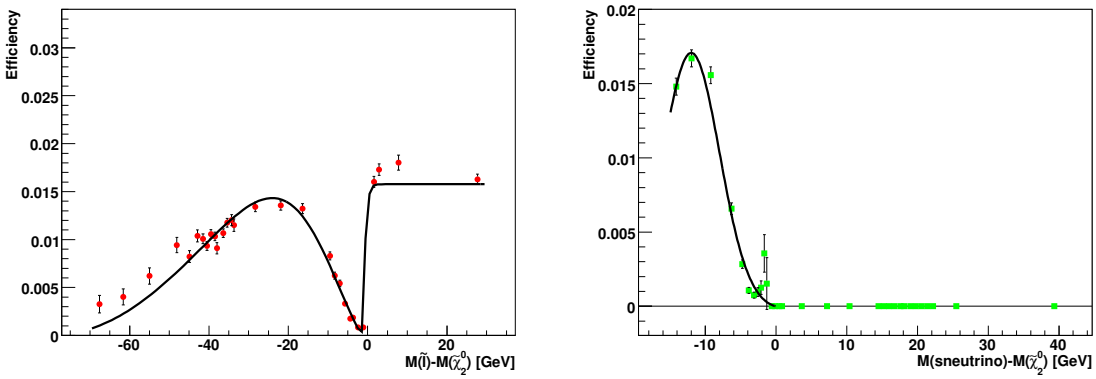

Figure 10.2.: Signal efficiency as a function of $\Delta m_{\tilde{\ell}}$ (left). The efficiency is normalized to the number of charginos that decay into sleptons for negative mass difference (2-body region) and total number of leptonic decays for positive mass difference (3-body region), and fitted with the function described in Section 10.1.1. Signal efficiency as a function of $\Delta m_{\tilde{\nu}} = m_{\tilde{\nu}}$-$m_{\tilde{\chi}_2^0}$(right). The efficiency is normalized to the number of charginos that decay into sneutrinos. The efficiency is fitted with the function described in Section 10.1.1. Both plots are from the $\mu\mu\ell$ low-p_T selection.

p_T of the final state leptons. When approaching the transition $\Delta m_\ell = 0$, a reduced efficiency is observed. This is visible in Figure 10.3 (left), where the green points correspond to points on the diagonals 1, 2 and 3 close to the transition region. To investigate the dependence of the signal efficiency on the mass difference between the slepton and next to lightest neutralino, the efficiency ratio as a function of this mass difference is shown in Figure 10.3 (right). The efficiency ratio is obtained by dividing out the parametrization as a function of $m_{\tilde{\chi}_1^\pm}$.

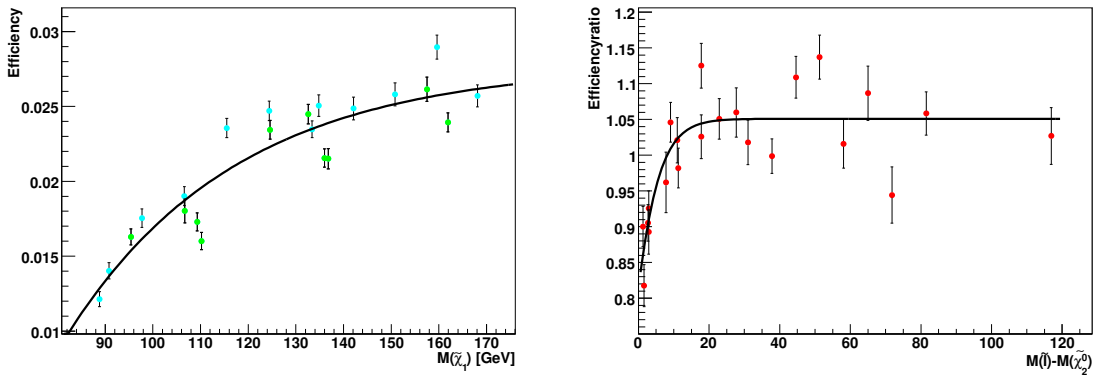

Figure 10.3.: Signal efficiency, relative to chargino and neutralino decays into three leptons, in the 3-body region as a function of $m_{\tilde{\chi}_1^\pm}$ for the low-p_T muon selection (left). Signal efficiency ratio as a function of $\Delta m_{\tilde{\ell}}$ (right), where the dependence of the chargino mass has been divided out. Both plots are from the $\mu\mu\ell$ low-p_T selection.

10.1.1. Fitting the Signal Efficiencies for the $\mu\mu\ell$ Selection

As described in the previous section, the signal efficiencies are fitted in order to parametrize the efficiencies in the part of $(m_0, m_{1/2})$ plane where the trilepton analyses are sensitive. Different functions are used to fit the efficiencies in different regions and for different decay modes. In the following, the functional forms of the fits are described. The discussion is done separately for the 2-body and 3-body regions, and also separated into different decay modes of the lightest chargino. The parameters of the fit are summarized in Section A.4.

2-body region, $\tilde{\chi}_1^\pm \to \tilde{\ell}\nu$, $\tilde{\chi}_2^0 \to \tilde{\ell}\ell$:
To fit the signal efficiency as a function of $\Delta m_{\tilde{\ell}}$=$m_{\tilde{\ell}}$-$m_{\tilde{\chi}_2^0}$ in the 2-body region, a combination of a parabola and a tanh function is used:

$$f(x) = \begin{cases} \text{par0} \cdot (x - \text{par1})^2 - \text{par2} \cdot (\tanh(x - \text{par3}) \cdot \text{par4} + 1) & \text{if } x < -2 \\ \text{par5} \cdot (\tanh(x - \text{par6}) \cdot \text{par7} + 0.5) & \text{if } x > -2 \end{cases} \tag{10.1}$$

where par0 to par7 are parameters and $x \equiv \Delta m_{\tilde{\ell}}$. From the equation above, it is seen that par0 and par1 denote the amplitude and position of the parabola. par0 is fitted and par1 is fixed for each diagonal. The fixed value for par1 corresponds to the $\Delta\tilde{\ell}$ at $m_0 \approx 0$. par2 gives the amplitude of the first tanh-function, par3 gives the position and par4 gives the width, while p5 to p7 denote the same for the second tanh. The amplitudes are fitted, while the position and width of the tanh are fixed on each diagonal. The shape of the fit takes into account the plateau in the 3-body region, the drop in signal efficiency with the transition from 3-body to 2-body decays and the increase and further decrease with larger transverse momenta of the decay products. The fit values for the $\mu\mu\ell$ low$-p_T$ fits for diagonal 1, 2 and 3 (see Figure 7.4) can be found in Table A.7.

2-body region, $\tilde{\chi}_1^\pm \to \tilde{\nu}\ell$:
To fit the signal efficiency as a function of $x \equiv \Delta m_{\tilde{\nu}} = m_{\tilde{\nu}}$-$m_{\tilde{\chi}_2^0}$ in the 2-body region, a function of the form

$$f(x) = \text{par0} \cdot \text{Gauss}(\text{par1}, \text{par2}) \cdot \left(\frac{1}{1 + \exp(x)} - 0.5\right) \tag{10.2}$$

where par0 to par2 are the fit parameters, is used. par0 gives the amplitude of the gaussian, par1 gives the position and p2 gives the width. par1 and par2 are kept fixed and par0 is fitted on each diagonal. The fit takes into account the bell shape form of the efficiency at larger negative $\Delta m_{\tilde{\nu}}$ and the fact that the efficiency goes to zero when the mass difference goes to zero. The fitvalues for the three diagonals are listed in Table A.8.

3-body region, $m_{\tilde{\chi}_1^\pm}$-dependence:
To fit the signal efficiency in the 3-body region as a function of the mass of the lightest chargino ($x \equiv m_{\tilde{\chi}_1^\pm}$), a function of the form

$$f(x) = -\exp(\text{par0} \cdot x - \text{par1}) + \text{par2}. \tag{10.3}$$

where par0 to par2 are again the fit parameters. The shape of this function takes into account the increasing efficiency as the p_T spectrum of the leptons become harder. The fit values can be found in Table A.9 for the low-p_T $\mu\mu\ell$ analysis.

3-body region, $\Delta m_{\tilde{\ell}}$ -dependence:
Figure 10.3 shows that the signal efficiency in the 3-body region also depends on the mass difference between the slepton and next to lightest neutralino. A function of the form

$$f(x) = \text{par0}/(1 + \text{par1} \cdot \exp(\text{par2} \cdot x)); \tag{10.4}$$

parametrizes the $x \equiv \Delta m_{\tilde{\ell}}$ dependence. The fit values can be found in Table A.9.

Interpolation of the Functions

To estimate the signal efficiency in an arbitrary $(m_0, m_{1/2})$ point in the region under consideration, the signal efficiency parametrizations from the three scans must be interpolated to the whole relevant $(m_0, m_{1/2})$ region. It is therefore necessary to find the $(m_0, m_{1/2})$ dependence of the coefficients from the fits. The only free parameter in the fits of the signal efficiency of $\tilde{\chi}_1^{\pm} \rightarrow \tilde{\nu}\ell$, is the amplitude. Figure 10.4 (top) shows the weighted mean of the efficiencies on diagonals 1, 2 and 3 for this kind of decay, normalized to the efficiency on diagonal 1 for the same $\Delta m_{\tilde{\ell}}$. The means are shown as functions of $\Delta m_{\tilde{\chi}_1^{\pm}}$ where the chargino mass is calculated with respect to the chargino mass on diagonal 1 for the same $\Delta m_{\tilde{\ell}}$. Two extra points are shown in Figure 10.4 (top). The points with $\Delta m_{\tilde{\chi}_1^{\pm}} \approx 5$ and 12 are extra Monte Carlo points that were generated between diagonal 1 and 2. The efficiency reaches a plateau on the second diagonal. Figure 10.4 (bottom) shows the evolution of the different coefficients that enter the parametrization of the fits of the efficiencies of $\tilde{\chi}_1^{\pm} \rightarrow \tilde{\ell}\nu$ decays. The evolution is shown as a function of the diagonal, which is converted to chargino mass. The mapping between a diagonal and $\Delta m_{\tilde{\chi}_1^{\pm}}$, is given by

$$\textit{diagonal} = (\Delta m_{\tilde{\chi}_1^{\pm}} + 30)/30. \tag{10.5}$$

10.1.2. Fitting the Signal Efficiencies for the low-p_T $ee\ell$ Selection

The signal efficiencies were also fitted in the $ee\ell$ analysis. The shapes of the efficiencies are the same as in the $\mu\mu\ell$ analysis. Figure 10.5 shows the selection efficiency for signal as a function of the mass difference between slepton and the next to lightest neutralino, $\Delta m_{\tilde{\ell}} = m_{\tilde{\ell}} - m_{\tilde{\chi}_2^0}$ (upper left), the signal efficiency as a function of mass difference between sneutrino and next to lightest neutralino (upper right), the signal efficiency in the 3-body region as a function of $m_{\tilde{\chi}_1^{\pm}}$ mass (lower left) and efficiency as a function of mass difference between slepton and $\tilde{\chi}_2^0$ normalized to the chargino efficiency (lower right). Figure 10.6 shows the evolution of the coefficients and the fit values are given in Table A.10 for the fits of $\tilde{\chi}_1^{\pm} \rightarrow \tilde{\ell}\nu$ decays, in Table A.11 for $\tilde{\chi}_1^{\pm} \rightarrow \tilde{\nu}\ell$ decays and in Table A.12 for 3-body decays.

10.1.3. Fitting the Signal Efficiencies for the high-p_T $\mu\mu\ell$ and $ee\ell$ Selections

The signal efficiencies were also fitted in the high-p_T selections. The shape of the efficiencies are the same as in the low-p_T selections. Figure 10.7 shows the selection efficiency for signal as

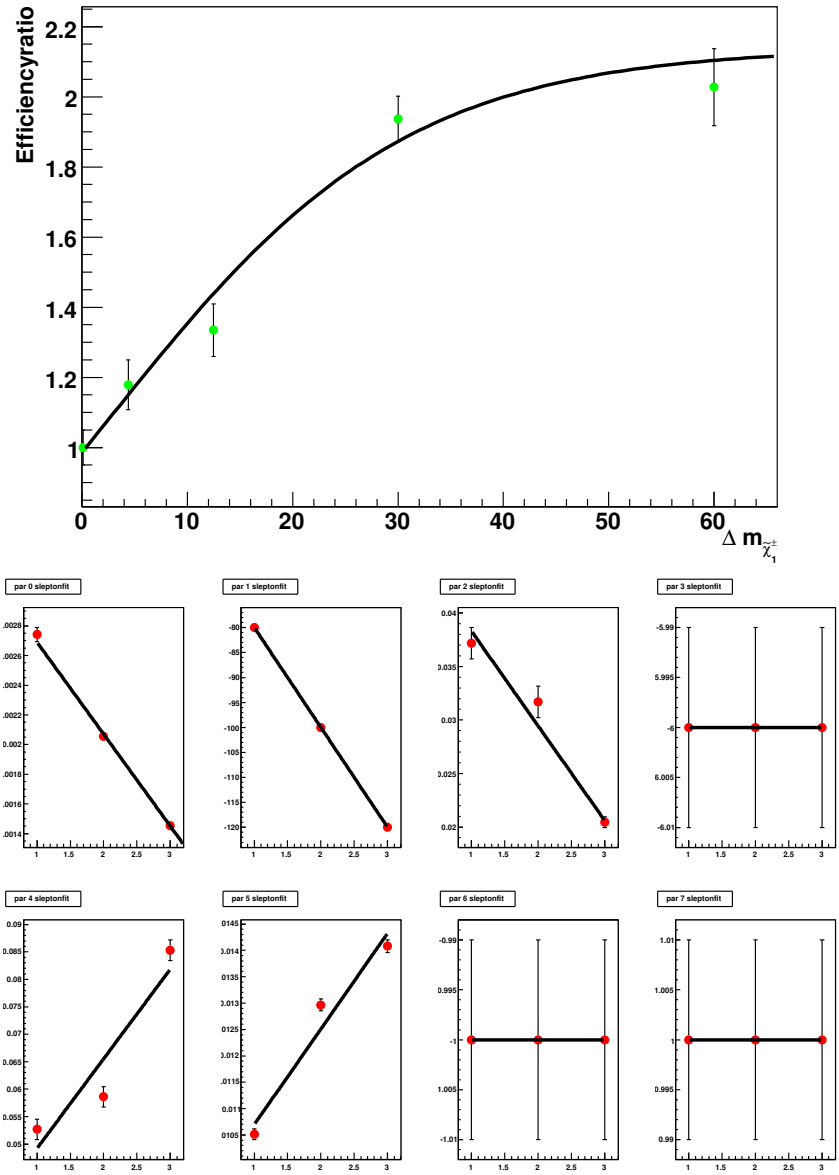

Figure 10.4.: Signal efficiency ratio (top) as a function of $\Delta m_{\tilde{\chi}_1^\pm}$ for diagonal 1, 2 and 3 in the low-p_T $\mu\mu\ell$ selection. In addition two signal points between diagonal 1 and 2 are shown. This function is used to scale the efficiency for $\tilde{\chi}_1^\pm \rightarrow \tilde{\nu}\ell$ decays, as shown in Figure 10.2 (right).
Fits to the slepton coefficients (bottom). The coefficients are defined in Equation 10.1. The plots labelled par0, par2 and par4 are fitted, while the others are fixed.

a function of the mass difference between slepton and the next to lightest neutralino, $\Delta m_{\tilde{\ell}} = m_{\tilde{\ell}} - m_{\tilde{\chi}_2^0}$ for diagonal 1 and 2 in the high-p_T $\mu\mu\ell$ selection and for diagonal 2 and 3 in the high-p_T $ee\ell$ selection below. Figure 10.8 shows the evolution of the coefficients in the case of chargino to slepton decays for both high-p_T selections. Table A.13 to Table A.18 show the parameters used in the fits of the efficiencies in the two high-p_T selections.

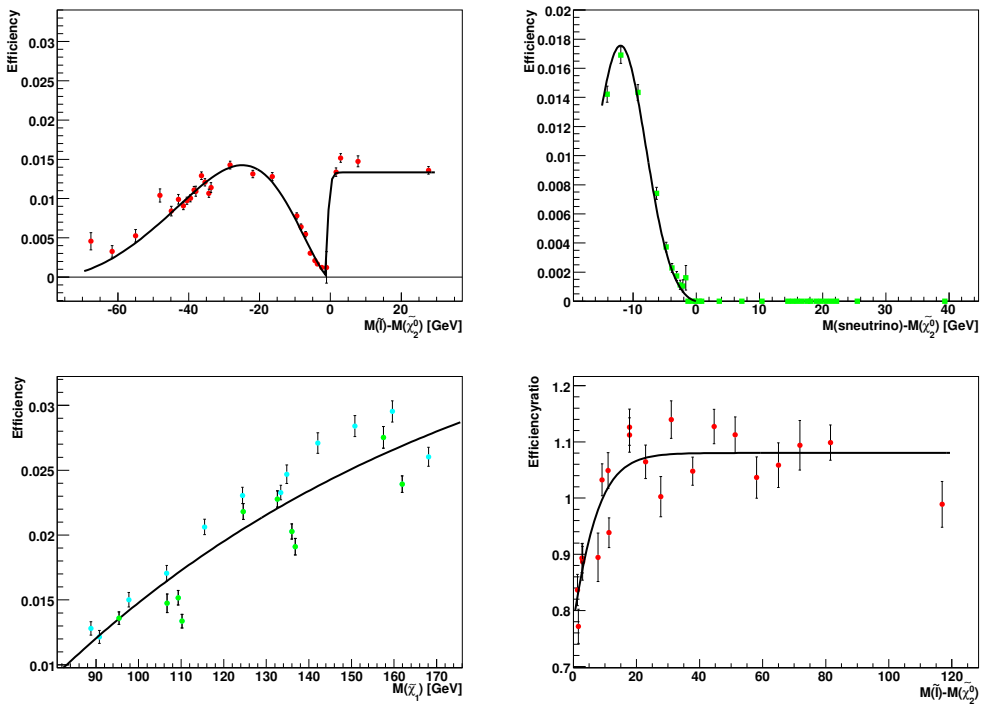

Figure 10.5.: Fits from the low-p_T $ee\ell$ analyses. Upper left is shown the signal efficiency for chargino decays via sleptons as a function of $\Delta m_{\tilde{\ell}}$ for diagonal 1 and normalized to number of charginos that decay into sleptons. Upper right is the signal efficiency for charginos that decay via sneutrinos for diagonal one. Lower left is the signal efficiency as a function of $m_{\tilde{\chi}_1^{\pm}}$in the 3-body region, and lower right is the signal efficiency as a function of $\Delta m_{\tilde{\ell}}$ in the 3-body region, where the chargino mass dependence has been divided out.

10.2. Interpretation of the Results

After all the selection cuts are applied in the low- and high-p_T selections in the $\mu\mu\ell$ and $ee\ell$ analyses, 7 candidate events are observed in data, in agreement with the expectation of 5.24±0.4 events from Standard Model processes. The results are combined with two other trilepton analyses and the combined result is translated into upper limits on the product of the cross section for associated production of charginos and neutralinos, $\sigma(\chi_1^{\pm}\chi_1^0)\times\mathrm{BR}(3\ell)$, from now on called the trilepton cross section.

10.2.1. Statistical Methods

To extract the limit on the trilepton cross section, a test statistic is defined [108, 109]. A test statistic is a function of the outcome of n experiments, resulting in n measured values $\mathbf{x}=(x_1, x_2, ..., x_n)$. The test statistic is used to investigate the agreement between observed data and a hypotesis, for example that there is a Supersymmetric signal. For n independent counting experiments, one approach to define a test statistic, is to use the number of events. Two statisti-

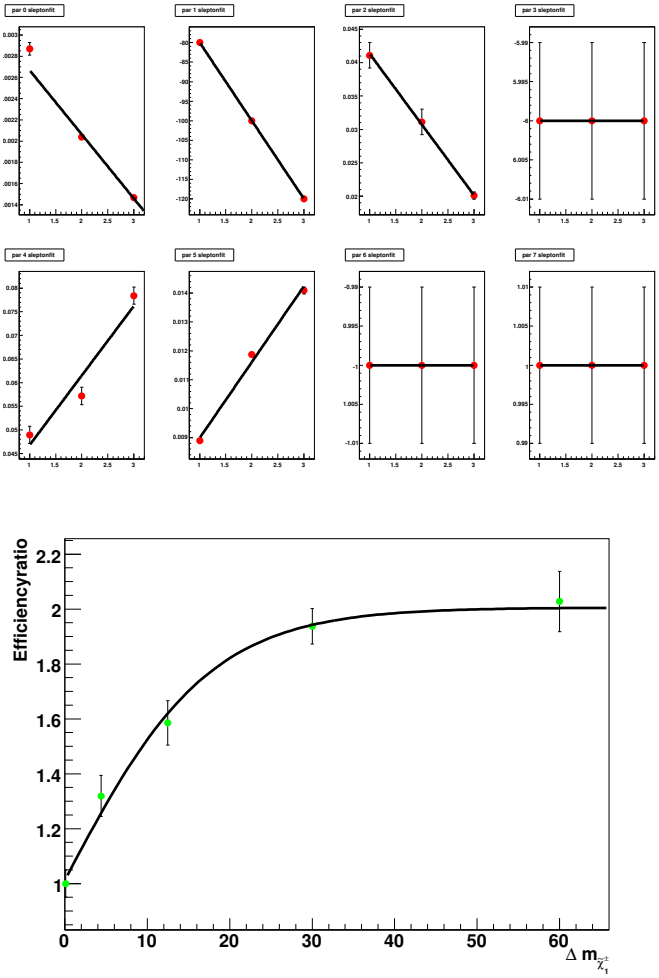

Figure 10.6.: Fits to the slepton coefficients (top) for the $ee\ell$ selection. Signal efficiency ratio (bottom) as a function of $\Delta m_{\tilde{\chi}_1^\pm}$. This function is used to scale the efficiency $\tilde{\chi}_1^\pm \rightarrow \tilde{\nu}\ell$.

cal hypotheses are then constructed: the *background only hypothesis* where only Standard Model background processes contribute to the accepted event rate, and the *signal+background hypothesis* where the SUSY signal is added. A signal of new physics is expected as an enhancement over the background. The likelihood ratio Q of the Poisson probabilities of the two hypothesis is defined as

$$\mathrm{Q} = \frac{\mathrm{P}_{\mathrm{Poisson}}(data|signal + background)}{\mathrm{P}_{\mathrm{Poisson}}(data|background)}. \tag{10.6}$$

The confidence level (CL) for excluding the possibility of simultaneous presence of a signal from new physics and background (signal+background hypothesis), is

$$CL_{s+b} = P_{s+b}(Q \leq Q_{obs}) = \beta. \tag{10.7}$$

This is the probability that the test statistic is smaller or equal to the observed value in data

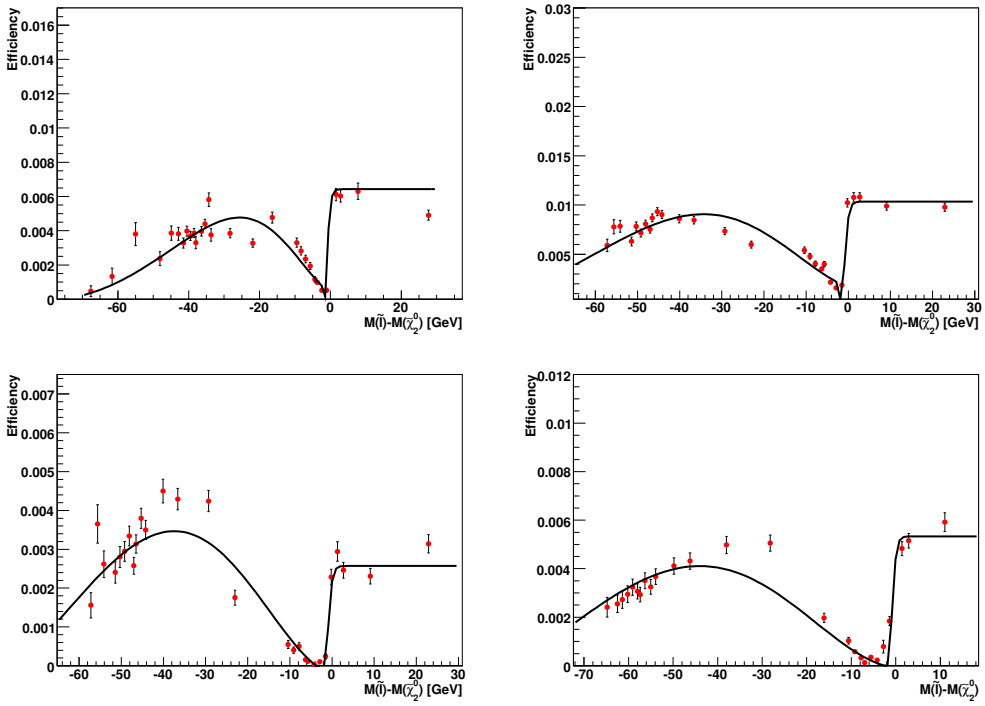

Figure 10.7.: Fits for high-p_T selections. The two upper plots are from the $\mu\mu\ell$ selection. The signal efficiency for $\tilde{\chi}_1^{\pm} \rightarrow \tilde{\ell}\nu$ is shown as a function of $\Delta m_{\tilde{\ell}}$ for diagonal 1 (left) and diagonal 2 (right). The signal efficiencies for the high-p_T $ee\ell$ for the same chargino decay are shown below for diagonal 2 and 3. The fit is conservatively describing the signal efficiency in regions where the shape is not perfectly described by the fit.

under the assumption that signal is present. The CL for the presence of background only is

$$CL_b = P_b(Q \leq Q_{obs}) = 1 - \alpha \tag{10.8}$$

which represents the probability that background processes give a smaller or an equal number of events than observed. Exclusion limits can be given in terms of the confidence level (1-CL_{s+b}). However, this has the undesired property that the signal or background may be excluded at a high confidence level if too few candidate events are observed to account for the estimated background. In order to be less sensitive to this effect, the confidence level in the *modififed frequentist approach* [110] is defined as the ratio of CL_{s+b} and CL_b

$$CL_s = \frac{CL_{s+b}}{CL_b}. \tag{10.9}$$

This implies a small reduction of sensitivity, but the resulting limit can not be more restrictive than the one obtained by using CL_{s+b}. A signal hypothesis is considered as excluded at 95% CL if $CL_s < 0.05$.

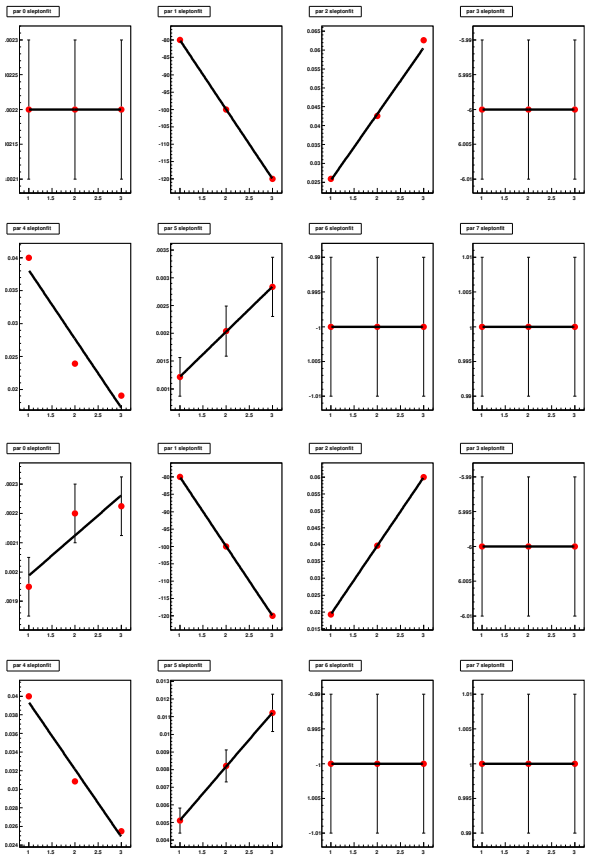

Figure 10.8.: Fits to the coefficients of the fits of chargino to slepton decays in the high-p_T selections. The upper six plots are taken from the high-p_T electron analysis, and the lower six plots are from the high-p_T $\mu\mu\ell$ selection.

10.2.2. Results

The results of the analyses discussed in this thesis are combined with the results from two other trilepton analyses, thereby improving the combined sensitivity. The other trilepton analyses that are taken into consideration are:

- final states with one electron, one muon and a third lepton, ($e\mu\ell$ low-p_T and high-p_T selection) [111],
- final states with one muon, one hadronically decaying tau and a third lepton, ($\mu\tau_h\ell$ selection) [21].

Table 10.1 lists the number of events selected in data and the expected number of events from the Standard Model background for the $e\mu\ell$ selections and the $\mu\tau\ell$ analysis. Combining the $ee\ell$ and $\mu\mu\ell$ selections with the $e\mu\ell$ and $\mu\tau\ell$ selections, a total background of 8.05$\pm$ 0.47 (stat) $\pm$ 0.35 (syst) events is expected after all cuts, while 10 are observed in data. No evidence for the associated production of charginos and neutralinos is observed and an upper limit on the total

Table 10.1.: Number of events observed, background events expected for the $e\mu\ell$ low- and high-p_T selections and the $\mu\tau_h\ell$ selection, after applying all the selection criteria. Overlap between the different selections is subtracted.

Selection	Data	Expected Background from Standard Model
$e\mu\ell$ low-p_T	2	0.78 ± 0.12 (stat) ± 0.12 (syst)
$e\mu\ell$ high-p_T	0	0.53 ± 0.05 (stat) ± 0.08 (syst)
$\mu\tau_h\ell$	1	1.5 ± 0.2 (stat) ± 0.1 (syst)

cross section is set using the likelihood ratio method. The statistical and systematic uncertainties of each analyis are taken into account including their correlations.

Signal events that are selected by more than one analysis are assigned to one channel and removed from the other channels to avoid double counting. The events are assigned to the analysis with the best signal to background ratio. The overlap between $ee\ell$ and $\mu\mu\ell$ is negligible, but significant between $ee\ell$ and $e\mu\ell$, and $\mu\mu\ell$ and $e\mu\ell$. The total overlap that is subtracted from the $e\mu\ell$ analysis due to the $ee\ell$ and $\mu\mu\ell$ selections, varies with m_0 and $m_{1/2}$ and amounts to between 20% and 60%. The overlap between the $e\mu\ell$ and $\mu\tau_h\ell$ is also large since the misidentification rate of electrons as hadronically decaying tau leptons is large due to similar signature in the detector. The overlap is assigned to the $e\mu\ell$, and varies in the range between 18% and 60%, depending on the parameters m_0 and $m_{1/2}$. Overlap between backgrounds is also subtracted. Systematic uncertainties are treated as fully correlated, except the modelling of the $W + (jet)$ bacground and modelling of the multi-jet bacground which are regarded as uncorrelated.

The number of events translates into upper limits on the trilepton cross section. The cross section limit ($\sigma(\chi_1^\pm\chi_1^0)\times$BR$(3\ell)$) is interpreted in the 3ℓ-max scenario which was introduced in 3.3.1. Figure 10.9 shows the combined expected and observed limit as a function of $m_{\tilde{\chi}_1^\pm}$ for tanβ=3,$\mu > 0$ and assuming degenerated slepton masses. Comparing the observed trilepton cross section to the theoretical cross section, shows that it is possible to exlude chargino masses up to 138 GeV in the 3ℓ-max scenario beyond the existing LEP upper limits of $m_{\tilde{\chi}_1^\pm}$=103.5 GeV. The expected limit on the trilepton cross section varies between 0.04 pb and 0.08 pb in the relevant chargino mass range.

The cross section limit is interpreted in the 3ℓ-max scenario as a function of tan β, which allows a scan from minimal to maximal branching ratio into tau leptons. The tan β scan was introduced in Section 7.2.2, and Figure 7.6 (right) shows the branching fraction of the lightest chargino and next to lightest neutralino into leptons. Figure 10.10 (upper left) shows the signal efficiency as a function of tan β in the low-p_T electron selection and in the low-p_T $\mu\mu\ell$ selection (upper right). The expected and observed limit as a function of tanβ for $m_{\tilde{\chi}_1^\pm}$= 130 GeV and mass difference between $\tilde{\tau}_1$ and next to lightest neutralino of 1 GeV is shown in Figure 10.10 (below). The combination of the analyses mentioned here, exclude for chargino mass of 130 GeV and $m_{\tilde{\tau}_1} - m_{\tilde{\chi}_2^0} = 1$ GeV, values of tan β below 9.6 which significantly extends the exclusion region from the LEP experiments [23].

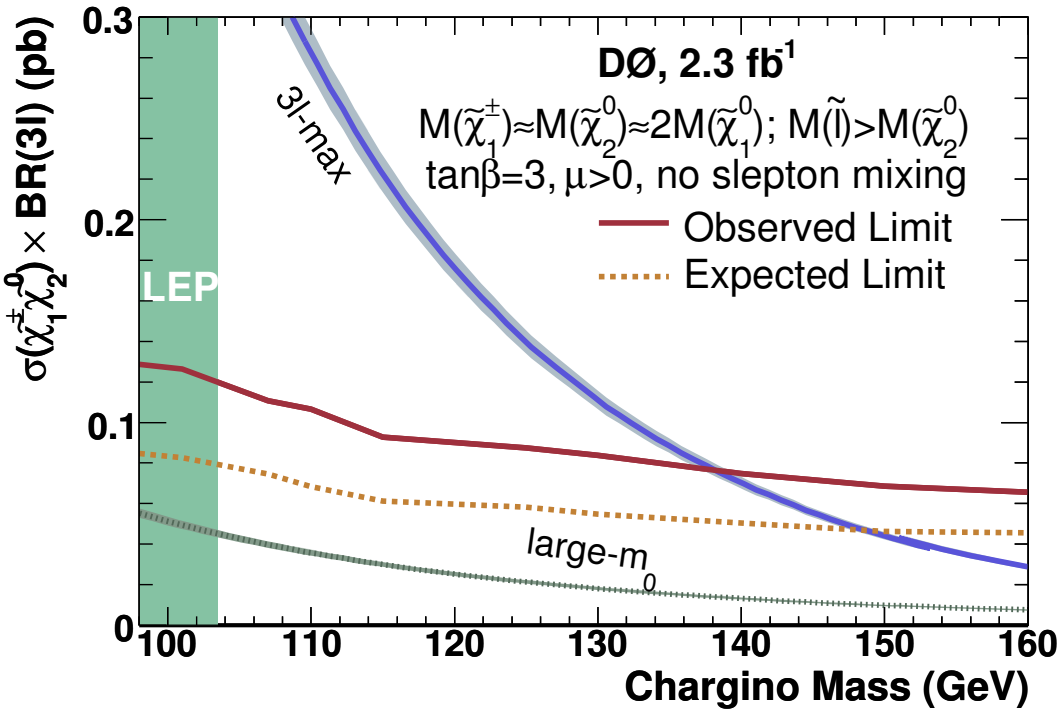

Figure 10.9.: The expected and observed limit on the trilepton cross section as a function of $m_{\tilde{\chi}_1^\pm}$. The limits from searches from LEP on the chargino mass $m_{\tilde{\chi}_1^\pm} > 103$ GeV is indicated in green. The benchmark model lines that are plotted as a reference, correspond to the 3ℓ-max scenario and the large m_0 scenario (see detailed explanations in the text). PDF-related errors on the cross section are shown as shaded bands. Chargino masses below 138 GeV are excluded.

The result is also interpreted more generally in the $(m_0, m_{1/2})$ plane. The expected and observed limits are calculated as a function of $(m_0, m_{1/2})$ and the limits compared to the predictions from mSUGRA. Figure 10.11 shows the region excluded at 95% CL, in the $(m_0, m_{1/2})$ plane. The result of the analyses allows to exclude a significant fraction of the mSUGRA parameter space beyond the existing excluded regions given by the lower limits from the LEP experiments of $m_{\tilde{\chi}_1^\pm}$>103.5 GeV and $m_{\tilde{e}}$> 99.9 GeV. The combined result of the all the analyses allows to exclude $m_{1/2}$ values below maximally 250 GeV (corresponding to a chargino mass of 176 GeV), highly depending on m_0, for tan β=3, $A_0 = 0$ and positive μ. The transition region between 2-body decays and 3-body decays is not excluded because of the low sensitivity of the analyses in this region. The region defined by the black line is excluded by the CDF result (see Section 10.5). The three lines $m_{\tilde{g}} \approx 400$ GeV, $m_{\tilde{\ell}} \approx m_{\tilde{\chi}_2^0}$ and $m_{\tilde{\nu}} \approx m_{\tilde{\chi}_1^0}$ are also indicated in Figure 10.11. This is the world's best limits on m_0 and $m_{1/2}$ for tan β=3, $A_0 = 0$ and $\mu > 0$.

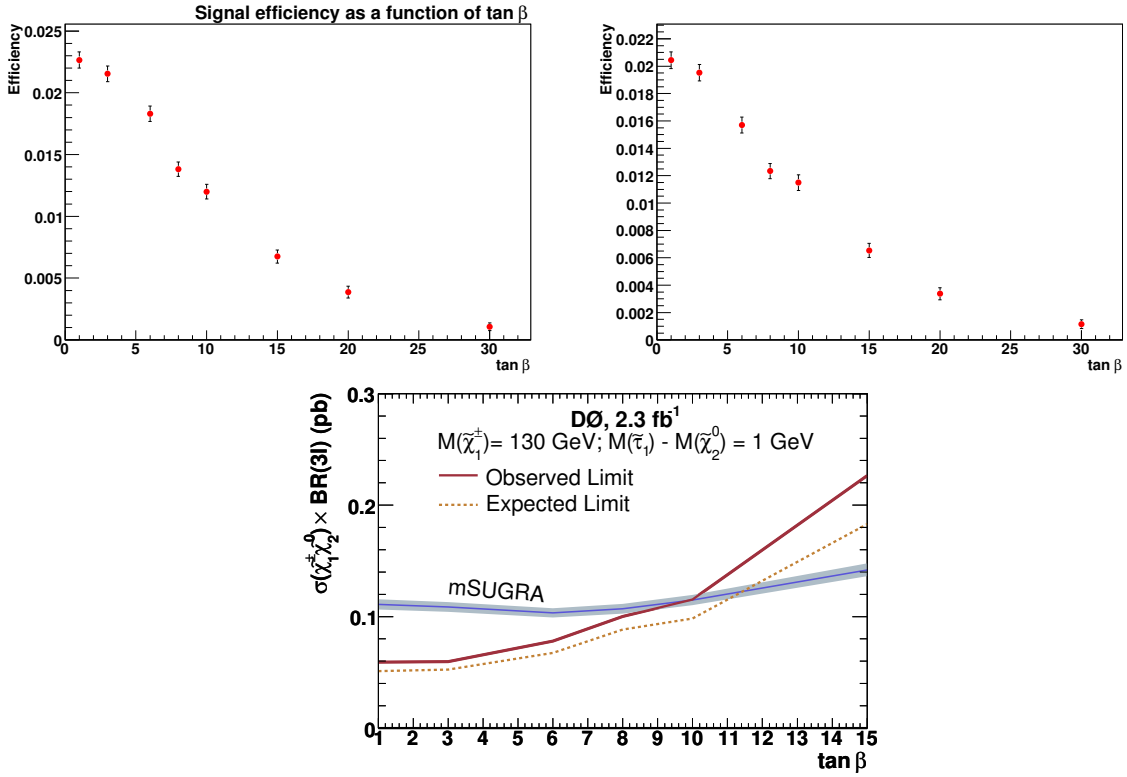

Figure 10.10.: Signal efficiency relative to number of leptonic chargino and neutralino decays, as a function of tan β in the low-p_T $ee\ell$ analysis (upper left) and in the low-p_T $\mu\mu\ell$ selection (upper right). Expected and observed limit (below) as a function of tanβ when all analyses are combined, for $m_{\tilde{\chi}_1^\pm}$=130 GeV, $m_{\tilde{\tau}_1} - m_{\tilde{\chi}_2^0} = 1$ GeV, $A_0 = 0$ and $\mu > 0$.

10.3. Projections for SUSY Searches in Trilepton Final States for RunII

The sensitivity of the DØ trilepton search is limited mainly by the amount of data available. It is therefore expected that the accessible regions will increase with the amount of recorded data during Run II of the Tevatron. A further increase of sensitivity can also be achieved by reducing the background expected from Standard Model processes. By the end of Run II, the total integrated luminosity expected to have been recorded at DØ and CDF is about 7 fb^{-1} which will make it possible to extend the reach towards larger m_0, $m_{1/2}$ and tanβ.

In order to investigate the upper limits of the trilepton cross section, $\sigma \times BR(3\ell)$, as a function of integrated luminosity in the absence of a SUSY signal, a study was done, assuming equal sensitivity of the two experiments and that the number of expected events from Standard Model processes scales with the luminosity. It is also assumed that the statistical and systematic errors are unchanged. Figure 10.12 shows the expected limit on the trilepton cross section as a function of $m_{\tilde{\chi}_1^\pm}$when the results of DØ and CDF are combined. Depending on the $m_{\tilde{\chi}_1^\pm}$, the trilepton cross section can be excluded at 95% CL in a range between 0.015 pb and 0.03 pb with the

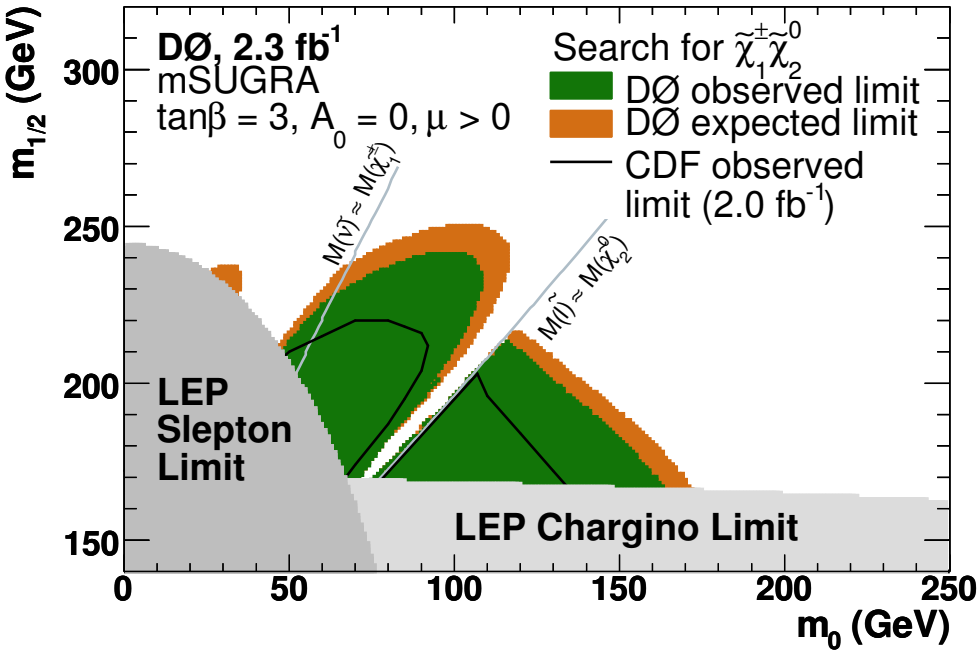

Figure 10.11.: Exclusion region in $(m_0, m_{1/2})$ plane for tanβ=3, $A_0 = 0$ and $\mu > 0$. Regions excluded by searches at LEP and CDF (Section 10.5) are indicated. Both the expected excluded region and the observed excluded region are indicated.

integrated luminosity exptected by the end of RunII. In the 3ℓ-max scenario, chargino masses below 178 GeV are expected to be excluded.

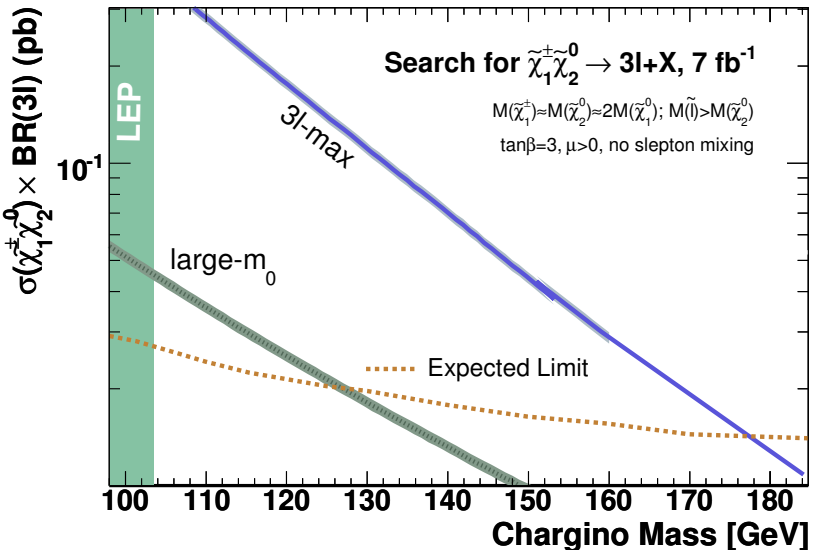

Figure 10.12.: Projection of the expected limit at the 95% CL on the trilepton cross section in a combination with results from CDF. The expected limit is shown as a function of the mass of the lightest chargino for $7fb^{-1}$, the integrated luminosity expected at the end of Run II.

10.4. Squark-gluino Analysis at DØ .

Another important channel in the search for supersymmetric particles is the production and decay of squarks and gluinos. At hadron colliders, squark and gluinos, if they are sufficiently light, will be the most copiously produced supersymmetric particles [113]. The final states consist of jets and missing transverse energy. Since the final states consist of jets, the large QCD background is a bigger problem than in the tri-lepton search. In this section, a brief overview of a search for supersymmetric particles in final states with jets and $\not\!\!E_T$ will be presented [17]. The analysis is using 2.1 fb^{-1} of data collected by the DØ detector.

Three analyses were optimized for different regions of m_0 and combined when computing the limits to improve the sensitivity. In all selections, the number of observed candidates is in good agreement with the Standard Model expectation In total, 31 events are selected in data, while 32.6±1.7(stat) are expected from the background. Since no evidence for supersymmetry is observed, limits on the total cross section times branching fraction can be set. Figure 10.13 shows the region of the $(m_0, m_{1/2})$ plane that is excluded by the squark gluino search. Figure 10.14 shows the excluded region in the squark-gluino mass plane. Gluino masses below 380 GeV are excluded for all squark masses, for tanβ=3, $A_0 = 0$ and negative μ. The region excluded in the $(m_0, m_{1/2})$ plane by the squark-gluino analysis, extends to higher values for m_0 compared to the results derived in this thesis, but the range in $m_{1/2}$ only extends up to ∼160 GeV.

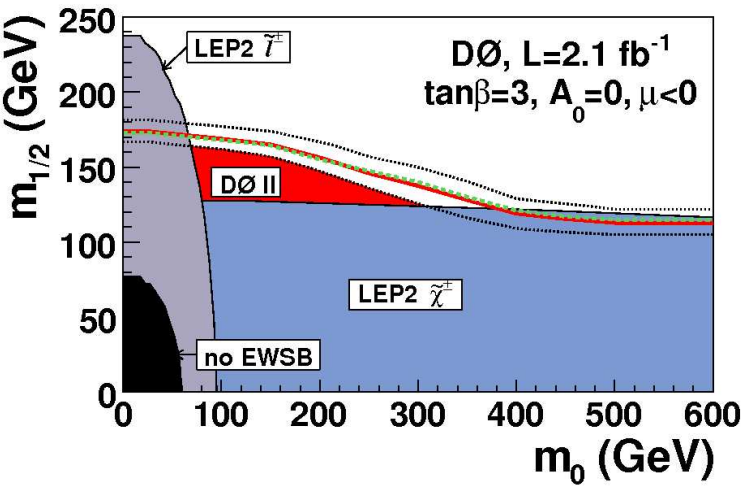

Figure 10.13.: Regions excluded at the 95% CL by the squark gluino analysis in the mSUGRA framework for tan β=3, $A_0 = 0$ and $\mu < 0$. The red line shows the excluded region for the central PDF and renormalization and factorization scale. The corresponding expected limit is the dashed line. [17].

10.5. Trilepton Analysis at CDF

A search for the trilepton signature is also performed at the CDF experiment [116]. CDF reports 7 candidate events in data, consistent with 6.4 events expected from the Standard Model

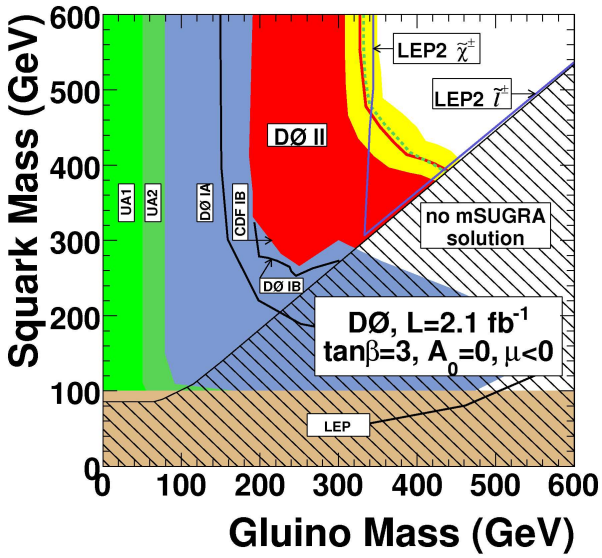

Figure 10.14.: Regions excluded by the squark-gluino analysis at 95% CL in the squark and gluino mass plane in the mSUGRA framework for tan β=3, $A_0 = 0$ and $\mu < 0$. The red line shows the excluded region for the central PDF and renormalization and factorization scale,$\mu_{rf} = Q$. The corresponding expected limit is the dashed green line. The yellow band shows the effect of PDF uncertainites and of varying μ_{rf} by a factor of two. There is no mSUGRA solution in the black hashed region [17].

background. Since no evidence for Supersymmetric particles is found, limits on the production cross section times branching fraction into three leptons are set to constrain the mSUGRA model. Figure 10.15 shows the exluded region in the $(m_0, m_{1/2})$ plane.

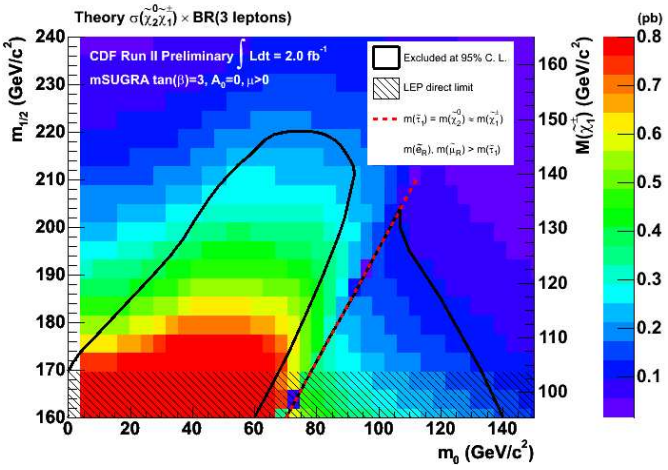

Figure 10.15.: The excluded region in the $(m_0, m_{1/2})$ plane from CDF [117].

10.6. SUSY Prospects at the LHC

Even with the full data set expected for RunII, the Tevatron experiments will not be sensitive in a large part of the SUSY parameter space. The two experiments ATLAS and CMS which will start data taking at the LHC in 2009 using pp collisions at $\sqrt{s}$ =14 TeV, will search for SUSY beyond the Tevatron range [114].

At the large center-of-mass energy of the LHC, the direct squark/gluino production is the dominant production channel for SUSY. A variety of signatures containing leptons, jets and missing transverse energy can arise from cascade decays of the squarks and gluinos. Figure 10.16 shows a typical cascade decay of a squark. The direct production of chargino pairs and the associated production of chargino-neutralino give rise to final states with two or three leptons, less jet activity and missing transverse energy.

The discovery reach for an integrated luminosity of 10 fb^{-1} for various SUSY signatures in the $(m_0, m_{1/2})$ plane for A_0=0 and moderate values of tanβ is shown in Figure 10.17. The covered domain corresponds to squark/gluino masses up to $\approx$ 2 TeV. Parts of the $(m_0, m_{1/2})$ plane will be covered already within a few weeks of data taking at low luminosity and a commissioned detector. The mass range 1.5-2 TeV will be accessible within one year of running at low luminosity. The final reach with the design luminosity of 300 fb^{-1} will allow for SUSY mass ranges up to 2.5 TeV to be excluded or discovered.

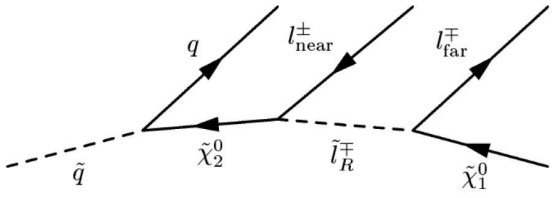

Figure 10.16.: Example of a cascade decay of a squark to quarks, leptons and $\not{E}_T$.

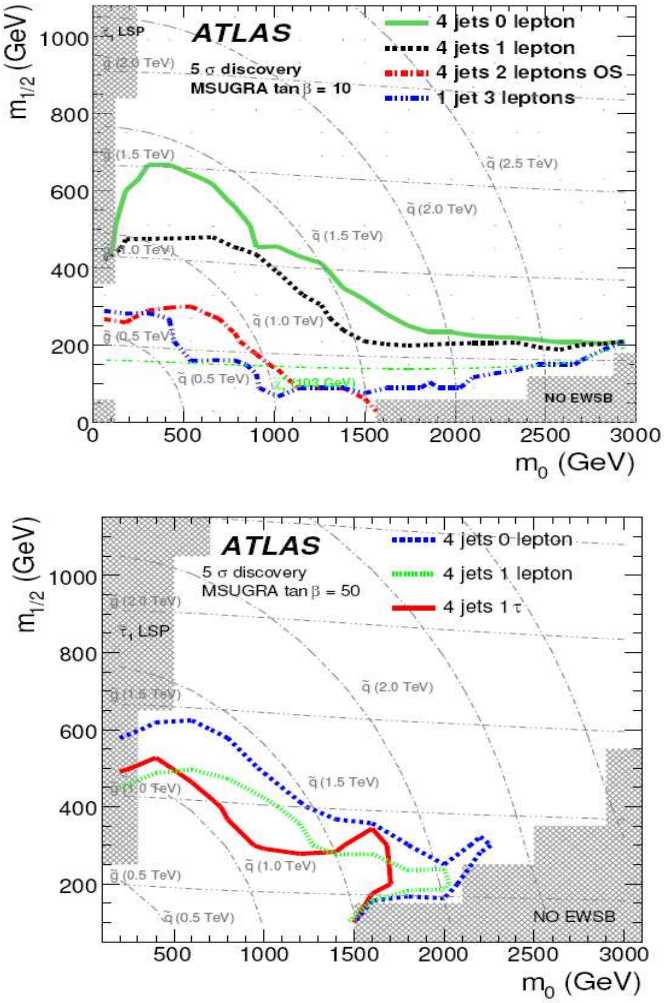

Figure 10.17.: 5σ discovery reach for the ATLAS experiment in analyses with 4 or 1 jet and different lepton requirements for an integrated luminosity of 1fb$-$1. $A_0 = 0$, $\mu > 0$ and tanβ=10 (*top*) and tanβ=50 (*bottom*). Shaded regions are not possible theoretically [115].

11. Conclusion and Outlook

A search for the associated production of the lightest chargino and the next to lightest neutralino with subsequent decay into three leptons and missing transverse energy has been performed using 2.3 fb^{-1} of data. The data sets were collected with the DØ detector and provided by the Tevatron with $p\bar{p}$ collisions at a center of mass energy of 1.96 TeV.

Two analyses have been presented: one with two electrons and an additional isolated track in the final state, and one with two muons and an additional isolated track. This tri lepton signature represents one of the most promising channels in the search for Supersymmetry at the Tevatron due to the small number of Standard Model background processes that contribute to the final states. For each analysis, a high-p_T selection and a low-p_T selection was defined and the selection cuts optimized.

After having applied all selection critera, 7 events were observed in data in agreement with 5.24±0.40 (stat)±0.30 (syst) expected by Standard Model processes. Since no evidence for a SUSY signal was found, upper limits on the trilepton cross section $\sigma \times \mathrm{BR}(3\ell)$ at 95% confidence level were derived as a function of the lightest chargino mass, $m_{\tilde{\chi}_1^\pm}$, and tan β, in a combination with two other tri-lepton analyses. In the 3ℓ-max scenario, chargino masses below 138 GeV are excluded.

The results were also interpreted in the mSUGRA model where they restrict the parameter space beyond existing imits from the LEP experiments. The interpretation was done in the $(m_0, m_{1/2})$ plane for tanβ=3, $A_0 = 0$ and $\mu > 0$. The excluded parameter space reaches up to values of $m_{1/2}$ of 250 GeV, depending on m_0, which is the world's best limits on m_0 and $m_{1/2}$ for tan β=3, $A_0 = 0$ and $\mu > 0$.

The sensitivity of the search is mainly limited by the amount of available data. At the end of Run II of the Tevatron, the DØ and CDF collaborations expect to record data corresponding to an integrated luminosity of approximately $7fb^{-1}$ per experiment. The sensitivity of combined DØand CDF trilepton searches is expected to increase up to chargino masses of about 200 GeV in the 3ℓ-max scenario. With the recent startup of the LHC, the search for supersymmetric particles will continue at ATLAS and CMS. It is expected that the two experiments will be able to probe supersymmetric particle masses up to 2.5 TeV and to either confirm or to rule out the existence of Supersymmetry.

A. Appendix

A.1. SUSY Parameters for Signal Monte Carlo Points

As described in Section 9.1, several SUSY signal samples are generated in order to interpret the results of the analyes. The SUSY points considered are selected to allow for a parameterization of the selection efficiencies of all trilepton analyses in the $(m_0, m_{1/2})$–plane. The SUSY points for which a Monte Carlo sample is generated are indicated in the $(m_0, m_{1/2})$–plane in Figure 3.5. For all SUSY points, $\tan\beta = 3$, $A_0 = 0$ and $\mu > 0$. The points are produced in order to scan the two parameters $m_{\tilde{\chi}_1^\pm}$ and $\Delta m = m_{\tilde{\ell}} - m_{\tilde{\chi}_2^0}$ because the kinematics in the event are mainly a function of these quantities. Points are produced in a region of the plane where sensitivity is expected. Scans 1-4 are orthogonal to the transition line from 2 body decays to 3 body decays, where $\Delta m = 0$, and allow a parameterization of the efficiencies as a function of Δm. fraction, the scan is performed in fine steps, i.e. for $m_{\tilde{\chi}_2^0} \approx m_{\tilde{\ell}}$ and $m_{\tilde{\chi}_2^0} \approx m_{\tilde{\nu}}$, while for regions with moderately changing branching fractions, the steps are wider. Scan 5 allows a parameterization as a function of $m_{\tilde{\chi}_1^\pm}$. Tables A.1– A.6 summarize the SUSY spectra of the generated SUSY Monte Carlo samples. The tables list m_0, $m_{1/2}$, $m_{\tilde{\chi}_1^\pm}$, $m_{\tilde{\chi}_2^0}$, $m_{\tilde{\chi}_1^0}$, $m_{\tilde{\ell}}$, $m_{\tilde{\tau}}$ and $\sigma \times$ BR.

Table A.1.: Parameters of the generated SUSY points for scan 1.

m_0 [GeV]	$m_{1/2}$ [GeV]	$m_{\tilde{\chi}_1^\pm}$ [GeV]	$m_{\tilde{\chi}_2^0}$ [GeV]	$m_{\tilde{\chi}_1^0}$ [GeV]	$m_{\tilde{e},\tilde{\mu}}$ [GeV]	$m_{\tilde{\tau}}$ [GeV]	$\sigma \times$ BR [pb]
10.0	241.0	167.6	167.2	90.2	99.6	98.2	0.0456
20.0	232.0	159.6	159.6	86.1	98.0	96.6	0.0688
30.0	224.0	152.6	152.9	82.5	97.9	96.5	0.1046
38.0	216.0	145.6	146.2	78.9	98.1	96.7	0.1615
42.0	213.0	143.0	143.7	77.6	98.8	97.4	0.1941
44.0	211.0	141.2	142.0	76.7	99.1	97.7	0.2152
46.0	210.0	140.4	141.2	76.2	99.7	98.3	0.2302
47.0	209.0	139.5	140.3	75.8	99.8	98.4	0.2415
48.0	208.0	138.6	139.5	75.3	100.0	98.6	0.2531
49.0	207.0	137.7	138.7	74.9	100.2	98.8	0.2667
50.0	207.0	137.7	138.7	74.9	100.7	99.3	0.2689
51.0	205.0	136.0	137.0	74.0	100.6	99.2	0.2880
52.0	204.0	135.0	136.2	73.5	100.8	99.4	0.2991
53.0	203.0	134.1	135.3	73.1	101.0	99.7	0.3074
54.0	203.0	134.1	135.3	73.1	101.6	100.2	0.3073
59.0	198.0	129.6	131.2	70.8	102.9	101.6	0.3558
65.0	193.0	125.1	127.0	68.5	105.1	103.8	0.4110
70.0	189.0	121.6	123.7	66.7	107.3	106.0	0.4580
76.0	184.0	117.2	119.6	64.4	110.1	108.8	0.4918
77.0	183.0	116.3	118.8	63.9	110.5	109.2	0.4891
78.0	182.0	115.4	118.0	63.5	111.0	109.7	0.4800
79.0	181.0	114.5	117.2	63.0	111.5	110.2	0.4590
80.0	180.0	113.7	116.3	62.6	111.9	110.7	0.4234
81.0	180.0	113.7	116.4	62.6	112.7	111.4	0.3917
82.0	179.0	112.8	115.5	62.1	113.1	111.9	0.1308
83.0	178.0	111.9	114.7	61.6	113.6	112.4	0.2931
84.0	177.0	111.0	113.9	61.2	114.2	112.9	0.1833
85.0	176.0	110.2	113.1	60.7	114.7	113.4	0.2723
86.0	175.0	109.3	112.3	60.3	115.2	113.9	0.2665
90.0	172.0	106.7	109.8	58.9	117.6	116.3	0.2557
105.0	159.0	95.4	99.3	52.7	127.0	125.8	0.2853

Table A.2.: Parameters of the generated SUSY points for scan 2.

m_0 [GeV]	$m_{1/2}$ [GeV]	$m_{\tilde{\chi}_1^\pm}$ [GeV]	$m_{\tilde{\chi}_2^0}$ [GeV]	$m_{\tilde{\chi}_1^0}$ [GeV]	$m_{\tilde{e},\tilde{\mu}}$ [GeV]	$m_{\tilde{\tau}}$ [GeV]	$\sigma \times$ BR [pb]
58.0	249.0	174.6	174.3	93.8	117.1	115.9	0.0654
60.0	248.0	173.8	173.4	93.4	117.8	116.6	0.0694
61.0	246.0	172.1	171.8	92.5	117.7	116.5	0.0769
64.0	244.0	170.4	170.1	91.6	118.7	117.5	0.0875
65.0	243.0	169.6	169.3	91.1	119.0	117.7	0.0919
66.0	242.0	168.7	168.4	90.7	119.2	118.0	0.0957
67.0	241.0	167.9	167.6	90.3	119.5	118.3	0.0992
68.0	240.0	167.0	166.8	89.8	119.8	118.6	0.1024
69.0	240.0	167.0	166.8	89.8	120.3	119.1	0.1023
70.0	239.0	166.2	165.9	89.4	120.6	119.4	0.1050
71.0	238.0	165.2	165.1	88.9	120.9	119.7	0.1082
75.0	235.0	162.6	162.6	87.6	122.5	121.3	0.1175
78.0	232.0	160.0	160.1	86.3	123.5	122.4	0.1273
84.0	226.0	154.8	155.1	83.6	125.8	124.7	0.1484
90.0	222.0	151.4	151.9	81.9	128.9	127.8	0.1618
100.0	213.0	143.7	144.4	77.9	134.0	132.9	0.1784
101.0	212.0	142.8	143.6	77.5	134.5	133.4	0.1758
102.0	211.0	141.9	142.8	77.0	135.0	133.9	0.1714
103.0	210.0	141.1	141.9	76.6	135.6	134.5	0.1637
104.0	210.0	141.1	142.0	76.6	136.3	135.2	0.1556
105.0	209.0	140.2	141.1	76.2	136.9	135.8	0.1441
106.0	208.0	139.4	140.3	75.7	137.4	136.3	0.1283
107.0	207.0	138.5	139.5	75.3	138.0	136.9	0.0985
108.0	206.0	137.7	138.7	74.8	138.5	137.5	0.0082
109.0	205.0	136.8	137.8	74.4	139.1	138.0	0.0853
110.0	204.0	136.0	137.0	73.9	139.7	138.6	0.0827
115.0	200.0	132.6	133.7	72.2	142.8	141.8	0.0778
125.0	191.0	124.6	126.4	68.2	149.3	148.3	0.0810

Table A.3.: Parameters of the generated SUSY points for scan 3.

m_0 [GeV]	$m_{1/2}$ [GeV]	$m_{\tilde{\chi}_1^\pm}$ [GeV]	$m_{\tilde{\chi}_2^0}$ [GeV]	$m_{\tilde{\chi}_1^0}$ [GeV]	$m_{\tilde{e},\tilde{\mu}}$ [GeV]	$m_{\tilde{\tau}}$ [GeV]	$\sigma \times$ BR [pb]
78.0	282.0	203.0	202.3	108.0	137.5	136.4	0.0218
80.0	280.0	201.3	200.6	107.1	138.1	137.0	0.0236
81.0	279.0	200.5	199.8	106.7	138.4	137.3	0.0243
82.0	278.0	199.6	198.9	106.3	138.7	137.6	0.0248
83.0	277.0	198.8	198.1	105.8	139.0	137.9	0.0251
84.0	276.0	198.0	197.3	105.4	139.3	138.2	0.0253
85.0	276.0	198.0	197.3	105.4	139.9	138.8	0.0249
86.0	275.0	197.1	196.5	105.0	140.2	139.1	0.0253
87.0	274.0	196.3	195.6	104.6	140.6	139.5	0.0257
88.0	273.0	195.4	194.8	104.1	140.9	139.8	0.0266
92.0	270.0	192.9	192.4	103.2	142.6	141.5	0.0292
95.0	267.0	190.4	189.9	101.9	143.7	142.7	0.0321
102.0	261.0	185.3	184.9	99.3	146.9	145.9	0.0394
110.0	254.0	179.5	179.1	96.2	150.9	149.8	0.0527
120.0	246.0	172.7	172.6	92.8	156.5	155.5	0.0593
124.0	242.0	169.4	169.3	91.1	158.7	157.7	0.0594
125.0	241.0	168.6	168.4	90.6	159.2	158.3	0.0583
126.0	240.0	167.7	167.6	90.2	159.8	158.8	0.0567
127.0	240.0	167.7	167.6	90.2	160.6	159.6	0.0542
128.0	239.0	166.9	166.8	89.8	161.2	160.2	0.0517
129.0	238.0	166.1	166.0	89.3	161.8	160.8	0.0482
130.0	237.0	165.3	165.1	88.9	162.3	161.4	0.0422
131.0	236.0	164.4	164.3	88.5	162.9	162.0	0.0277
132.0	235.0	163.6	163.5	88.0	163.5	162.6	0.0203
133.0	234.0	162.8	162.7	87.6	164.1	163.2	0.0276
134.0	233.0	161.9	161.8	87.2	164.7	163.8	0.0269
140.0	228.0	157.5	157.7	85.0	168.7	167.7	0.0255

Table A.4.: Parameters of the generated SUSY points for scan 4.

m_0 [GeV]	$m_{1/2}$ [GeV]	$m_{\tilde{\chi}_1^\pm}$ [GeV]	$m_{\tilde{\chi}_2^0}$ [GeV]	$m_{\tilde{\chi}_1^0}$ [GeV]	$m_{\tilde{e},\tilde{\mu}}$ [GeV]	$m_{\tilde{\tau}}$ [GeV]	$\sigma \times$ BR [pb]
136.0	277.0	199.4	198.9	106.5	175.6	174.7	0.0161
137.0	276.0	198.6	198.1	106.1	176.2	175.3	0.0164
138.0	276.0	198.6	198.1	106.1	177.0	176.1	0.0162
139.0	275.0	197.8	197.3	105.7	177.5	176.6	0.0166
140.0	274.0	196.9	196.4	105.2	178.1	177.2	0.0174
143.0	271.0	194.4	194.0	104.0	179.8	178.9	0.0174
146.0	269.0	192.8	192.3	103.1	181.8	180.9	0.0173
149.0	266.0	190.3	189.9	101.8	183.6	182.7	0.0169
152.0	263.0	187.8	187.4	100.5	185.4	184.5	0.0102
153.0	262.0	187.0	186.6	100.1	186.0	185.1	0.0045
154.0	262.0	187.0	186.6	100.1	186.8	185.9	0.0062
155.0	261.0	186.1	185.8	99.7	187.5	186.6	0.0080
156.0	260.0	185.3	184.9	99.2	188.1	187.2	0.0079
161.0	256.0	182.0	181.7	97.5	191.5	190.6	0.0076
165.0	252.0	178.7	178.4	95.8	194.1	193.2	0.0079
169.0	249.0	176.2	175.9	94.5	197.0	196.1	0.0080

Table A.5.: Parameters of the generated SUSY points for scan 5.

m_0 [GeV]	$m_{1/2}$ [GeV]	$m_{\tilde{\chi}_1^\pm}$ [GeV]	$m_{\tilde{\chi}_2^0}$ [GeV]	$m_{\tilde{\chi}_1^0}$ [GeV]	$m_{\tilde{e},\tilde{\mu}}$ [GeV]	$m_{\tilde{\tau}}$ [GeV]	$\sigma \times$ BR [pb]
150.0	150.0	88.8	93.0	48.9	164.8	163.8	0.1898
150.0	160.0	97.7	101.1	53.8	166.1	165.1	0.1357
150.0	170.0	106.6	109.4	58.7	167.5	166.5	0.0994
150.0	180.0	115.5	117.7	63.4	169.0	168.0	0.0746
150.0	190.0	124.4	126.0	68.0	170.6	169.6	0.0565
150.0	200.0	133.4	134.4	72.5	172.2	171.2	0.0432
150.0	210.0	142.1	142.8	77.1	173.8	172.9	0.0333
150.0	220.0	150.8	151.2	81.5	175.6	174.7	0.0260
150.0	230.0	159.6	159.6	86.0	177.4	176.5	0.0202
150.0	240.0	168.1	168.0	90.4	179.3	178.3	0.0157
150.0	250.0	176.7	176.4	94.8	181.2	180.3	0.0114

Table A.6.: Parameters of additionally generated SUSY points.

m_0 [GeV]	$m_{1/2}$ [GeV]	$m_{\tilde{\chi}_1^\pm}$ [GeV]	$m_{\tilde{\chi}_2^0}$ [GeV]	$m_{\tilde{\chi}_1^0}$ [GeV]	$m_{\tilde{e},\tilde{\mu}}$ [GeV]	$m_{\tilde{\tau}}$ [GeV]	$\sigma \times$ BR [pb]
200.0	150.0	90.8	94.3	49.7	211.2	210.3	0.0580
200.0	200.0	134.8	135.5	73.0	217.0	216.1	0.0185
200.0	250.0	177.8	177.4	95.2	224.2	223.4	0.0046
300.0	150.0	95.1	97.4	51.5	307.3	306.4	0.0017
300.0	200.0	138.0	138.1	73.8	311.3	310.5	0.0023
300.0	250.0	180.1	179.5	95.7	316.4	315.6	0.0001
171.0	276.0	199.1	198.6	106.0	203.7	202.8	0.0014

A.2. Mass Plots for Different Detector Regions

This section contains mass plots for the $ee\ell$-analysis to illustrate the difference in smearing for different detector regions and different Monte Carlo and data taking periods. See Section 8.3 for the definitions of different detector regions and details on the implementation.

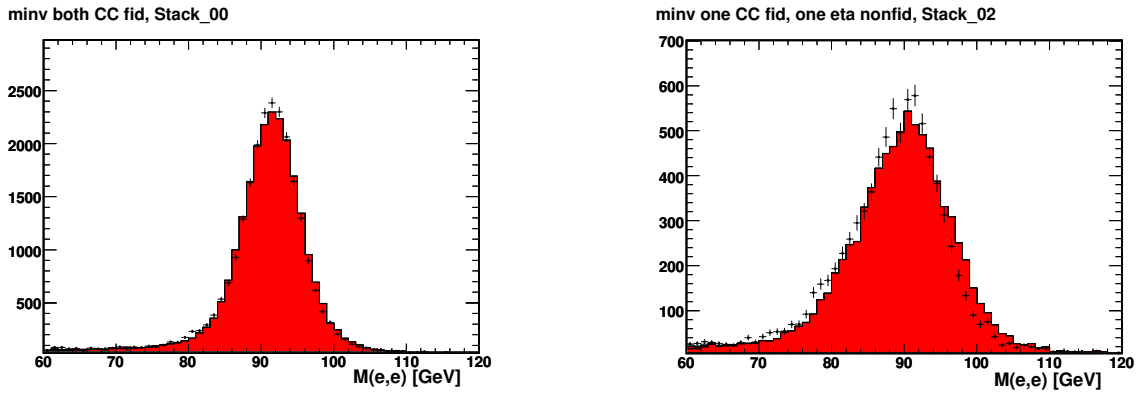

Figure A.1.: Invariant mass distribution of the RunIIa dataset when no additional smearing or scaling has been applied to the Monte Carlo. In the left plot are both electrons required to be central ($|\eta_{det}| < 1.1$) and fiducial. In the right plot, one electron is central and fiducial and the other electron is required to be non-eta fiducial. Both plots are made the analysis preselection. The Monte Carlo has been corrected for taking into account the overestimation of electrons in ϕ-cracks.

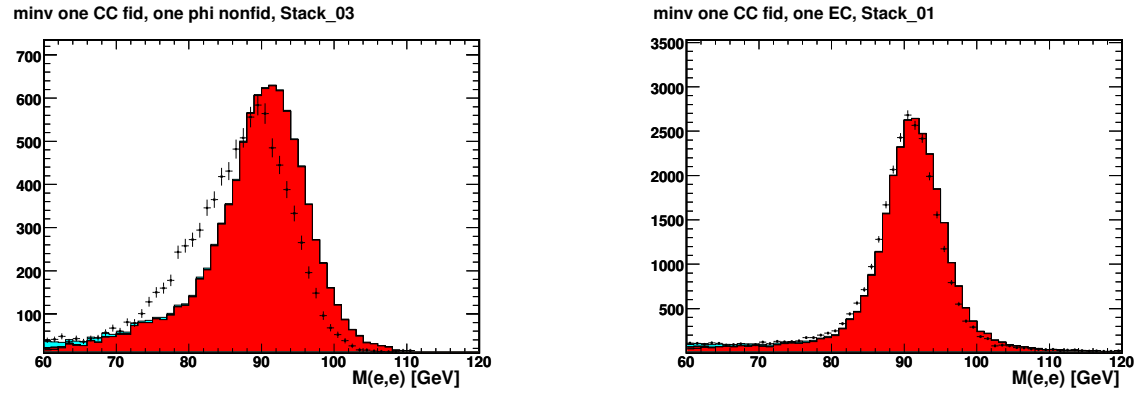

Figure A.2.: Invariant mass of at preselection stage of the RunIIa dataset when no additional smearing or scaling has been applied to the Monte Carlo. In the left plot is one electron central and fiducial, while the other is non-phi-fiducial. In the right plot is one electron central and fiducial and the other is required to be in the EC region, ($|\eta_{det}| > 1.5$). The Monte Carlo has been corrected for taking into account the overestimation of electrons in ϕ-cracks.

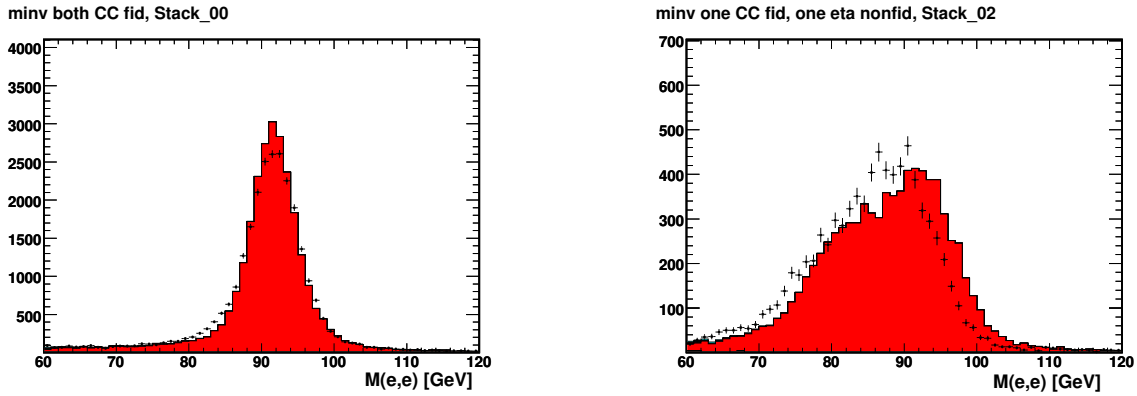

Figure A.3.: Invariant mass of RunIIb dataset when no additional smearing or scaling has been applied to the Monte Carlo. In the left plot are both electrons fiducial and CC, to the right one is fidcuial and CC while the other is required to be non eta fiducial. Both plots are made at the preselection stage. Monte Carlo has been corrected for electrons in ϕ-cracks.

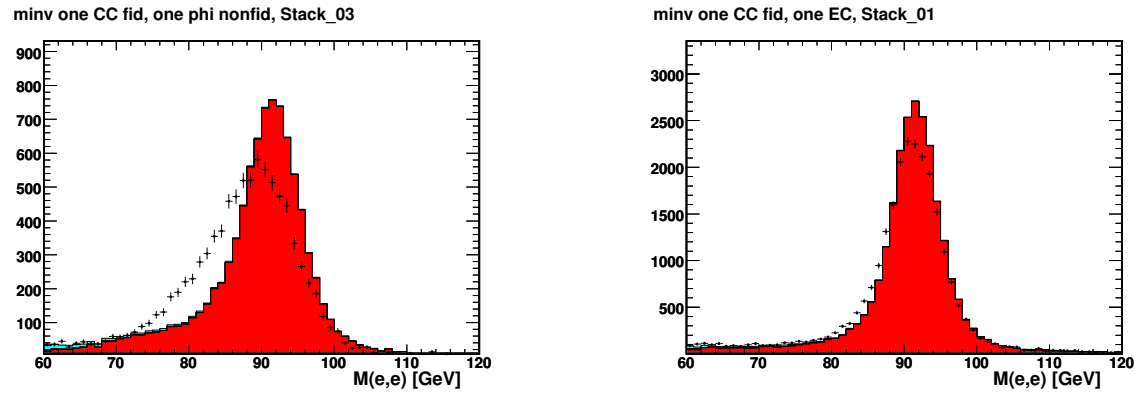

Figure A.4.: Invariant mass of RunIIb dataset when no additional smearing has been applied to the Monte Carlo. In the left plot is one electron CC and ficucial and the other is non-phi-fiducial. In the right plot is one electron CC fiducial while the other is EC. The plots are made at the preselection stage and Monte Carlo has been corrected for electrons in ϕ-cracks.

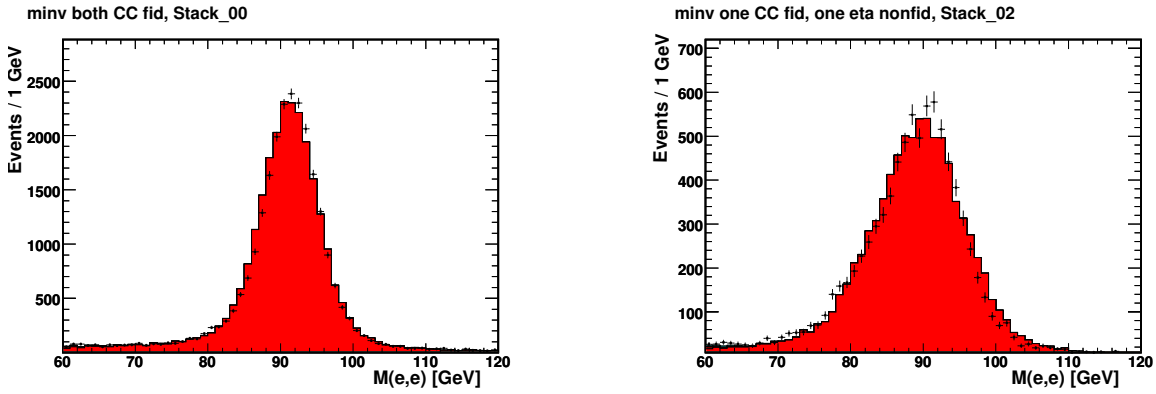

Figure A.5.: Invariant mass of RunIIa dataset when additional smearing and scaling derived in this analysis has been applied to the Monte Carlo. In the left plot are both electrons required to be central and fiducial. In the right plot is one electron non-eta fiducial. Both plots are made at the preselection stage.

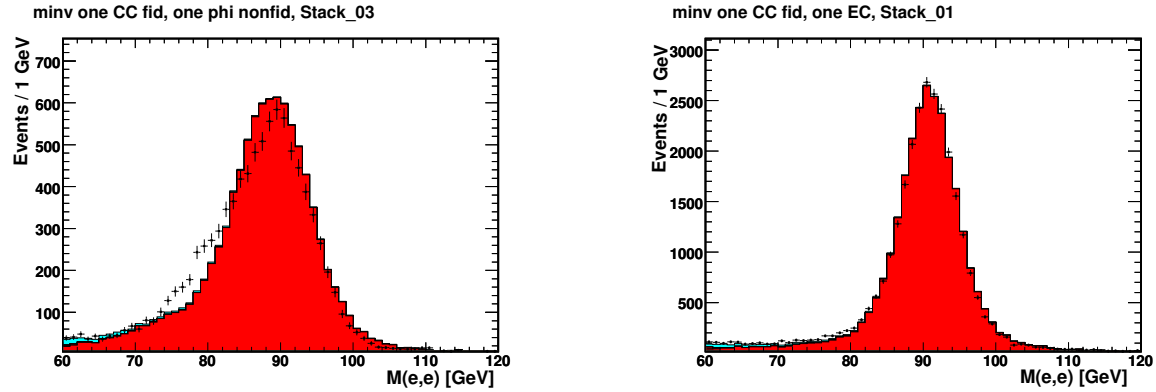

Figure A.6.: Invariant mass of RunIIa dataset when smearing and scaling derived here has been applied to the Monte Carlo. Correction factor for electrons in the non-fiducial regions has been applied. In the left plot is one electron CC fiducial and the other is non-phi-fiducial. In the right plot is one electron CC fiducial and the other EC. The plot are made at the preselection stage.

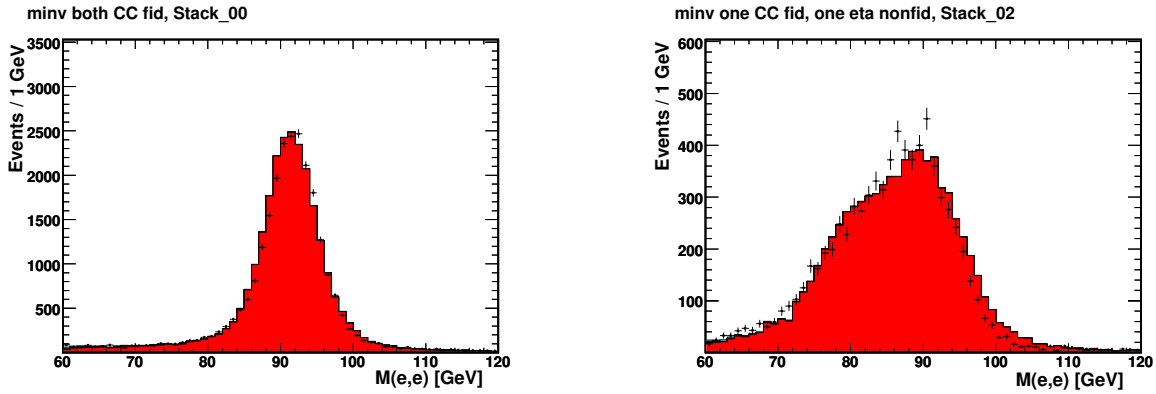

Figure A.7.: Invariant mass of RunIIb dataset when additional smearing and scaling derived in this analysis has been applied to the Monte Carlo. In the left plot are both electrons required to be central and fiducial. In the right plot is one electron non-eta fiducial. Both plots are made at the preselection stage.

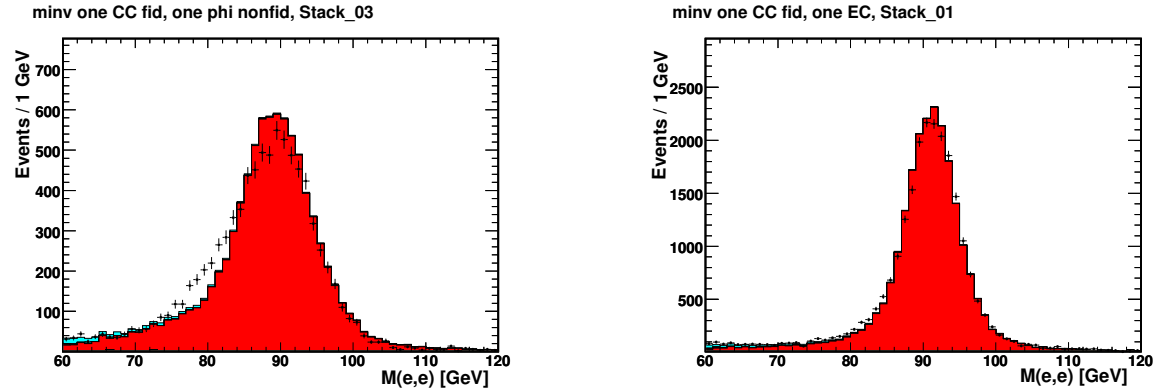

Figure A.8.: Invariant mass of RunIIb dataset with p20 MC when smearing and scaling derived here has been applied to the Monte Carlo. Correction factor for electrons in the non-fiducial regions has been applied. In the left plot is one electron CC fiducial and the other is non-phi-fiducial. In the right plot is one electron CC fiducial and the other EC. The plot are made at the preselection stage.

A.3. Eventdisplay

A.3.1. Muon Low-p_T Event

Event displays of one of the data events selected in the low-p_T $\mu\mu\ell$ analysis after event overlap subtraction are presented in this section. Figure A.9 shows a lego plot, Figure A.10 an $r-\phi$ view, and Figure A.11 shows an $r-z$ view.

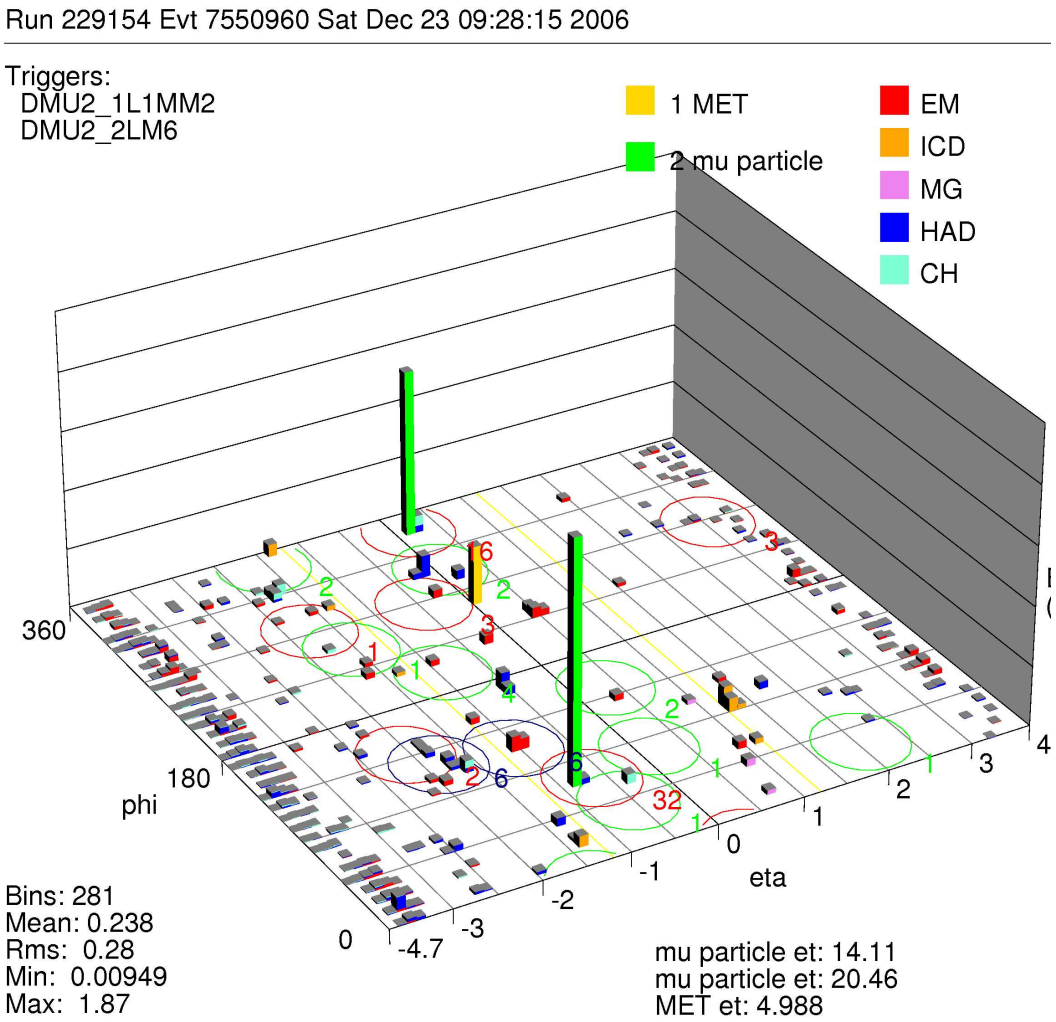

Figure A.9.: Eventdisplay of one of the remaining events in the muon analysis after applying all selection criteria. The energy deposition in the calorimeter in the $\eta-\phi$ plane is shown. The two muons are shown in green.

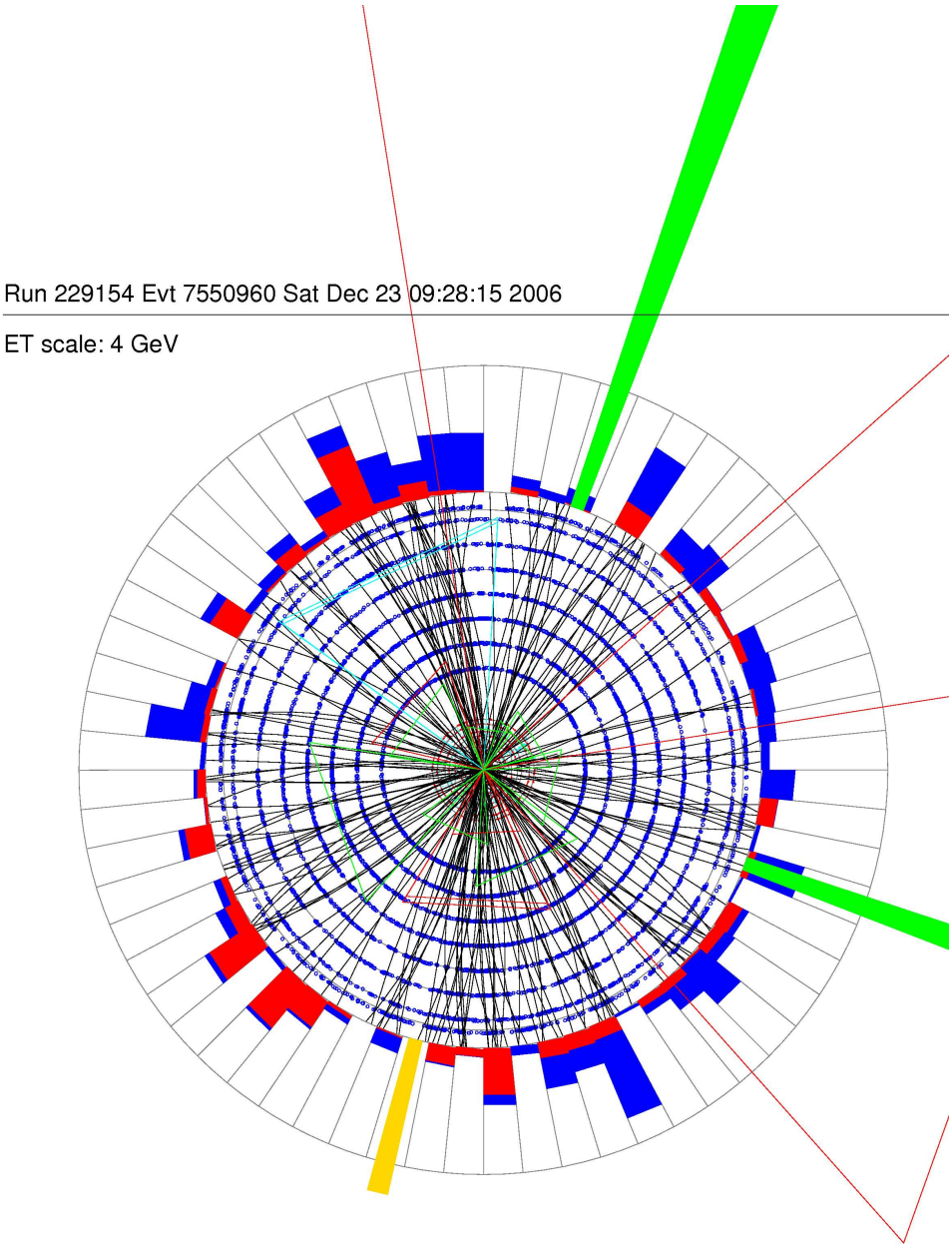

Figure A.10.: xy-view of one of the remaining events in the low-p_T muon analysis after applying all selection criteria. The two muons are shown in green.

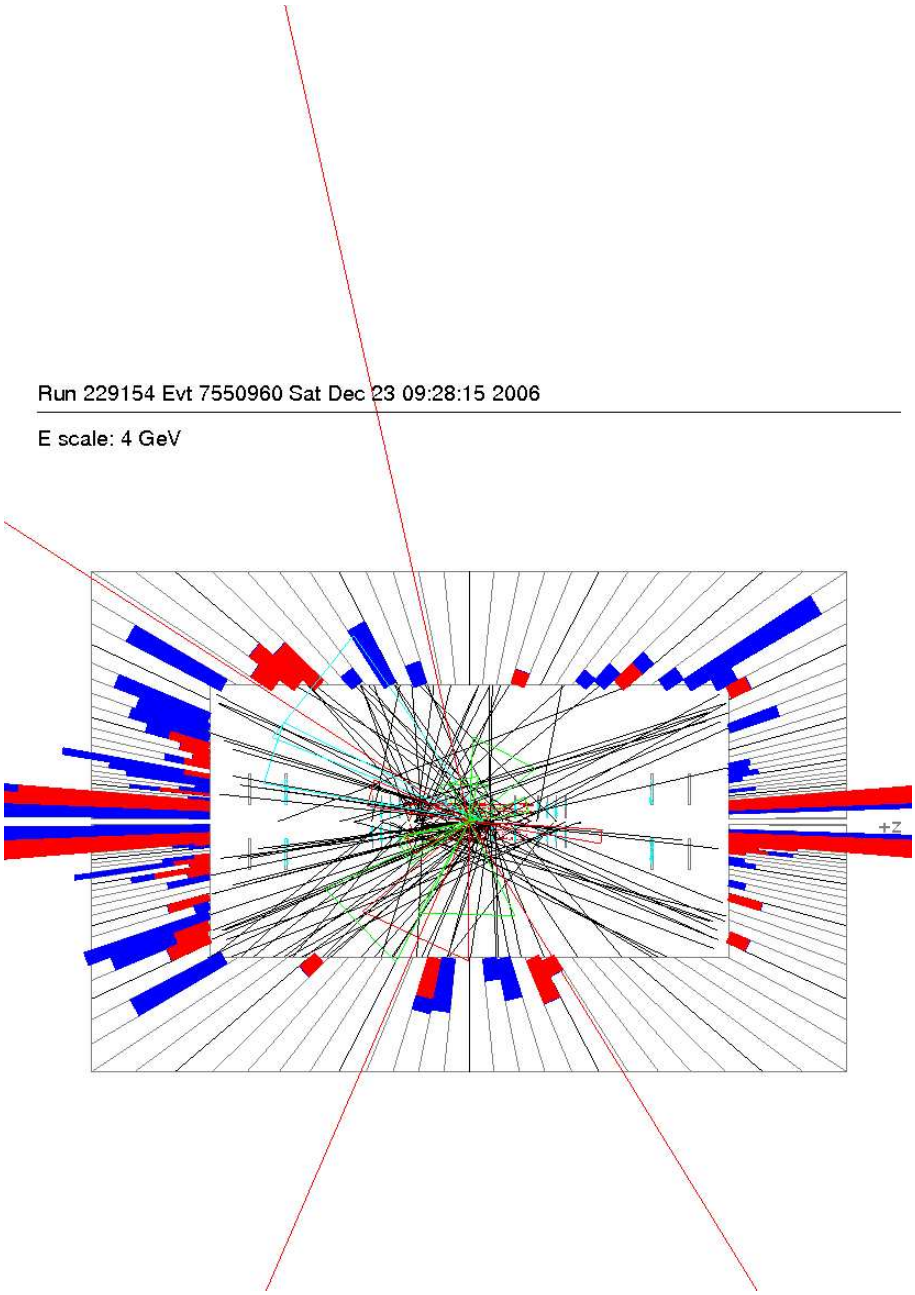

Figure A.11.: $r-z$-view of one of the remaining events in the muon low-p_T analysis after applying all selection criteria. The two muons are shown in green.

A.3.2. Muon High-p_T Event

Event displays of the data event selected in the high-p_T $\mu\mu\ell$ analysis after event overlap subtraction are presented in this section. Figure A.12 shows a lego plot, Figure A.13 an $r-\phi$ view, and Figure A.14 shows an $r-z$ view.

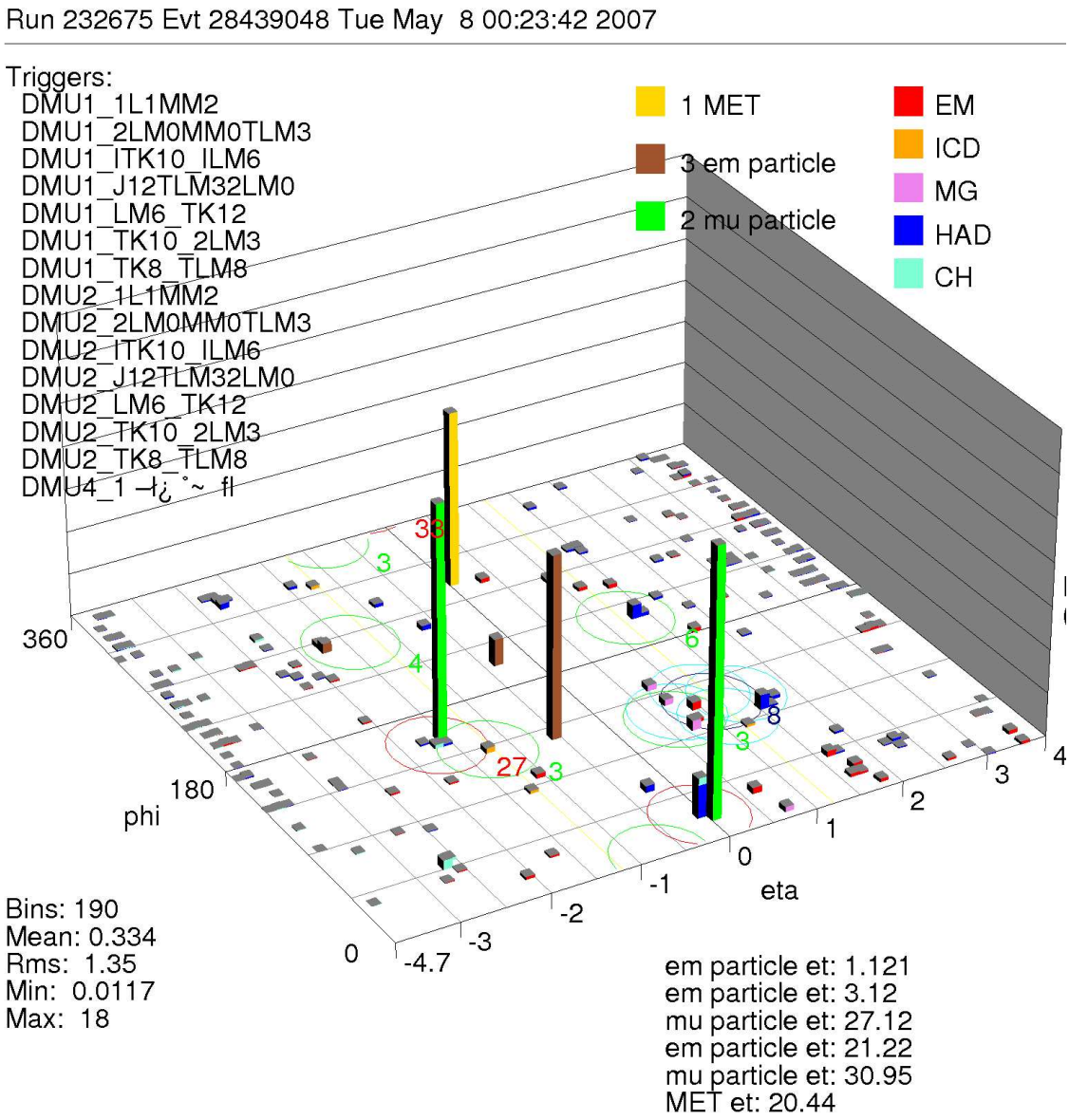

Figure A.12.: Legoplot of the event selected in the high-p_T $\mu\mu\ell$ analysis after applying all selection criteria.

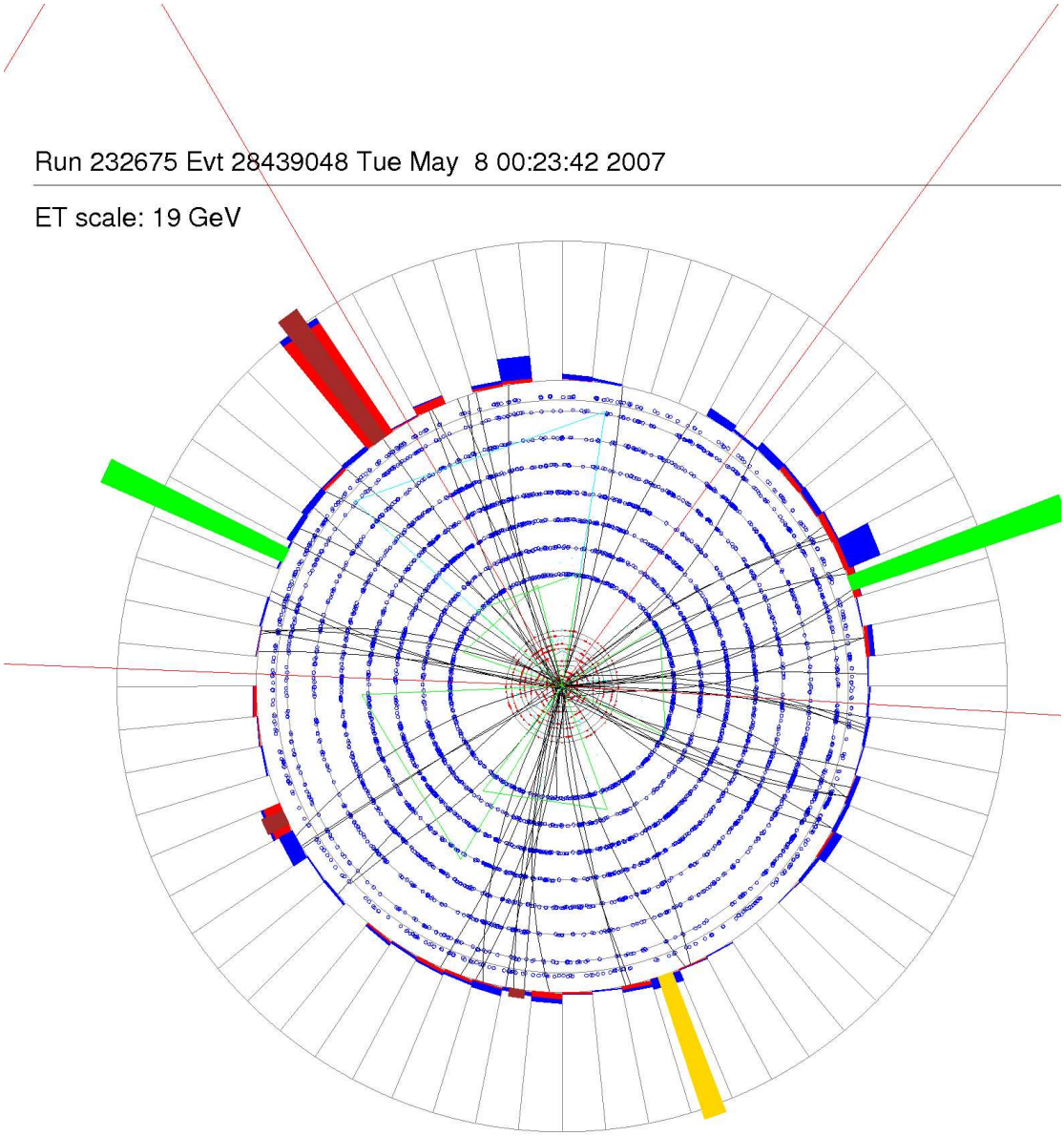

Figure A.13.: Eventdisplay of the event selected in the high-p_T $\mu\mu\ell$ analysis after applying all selection criteria.

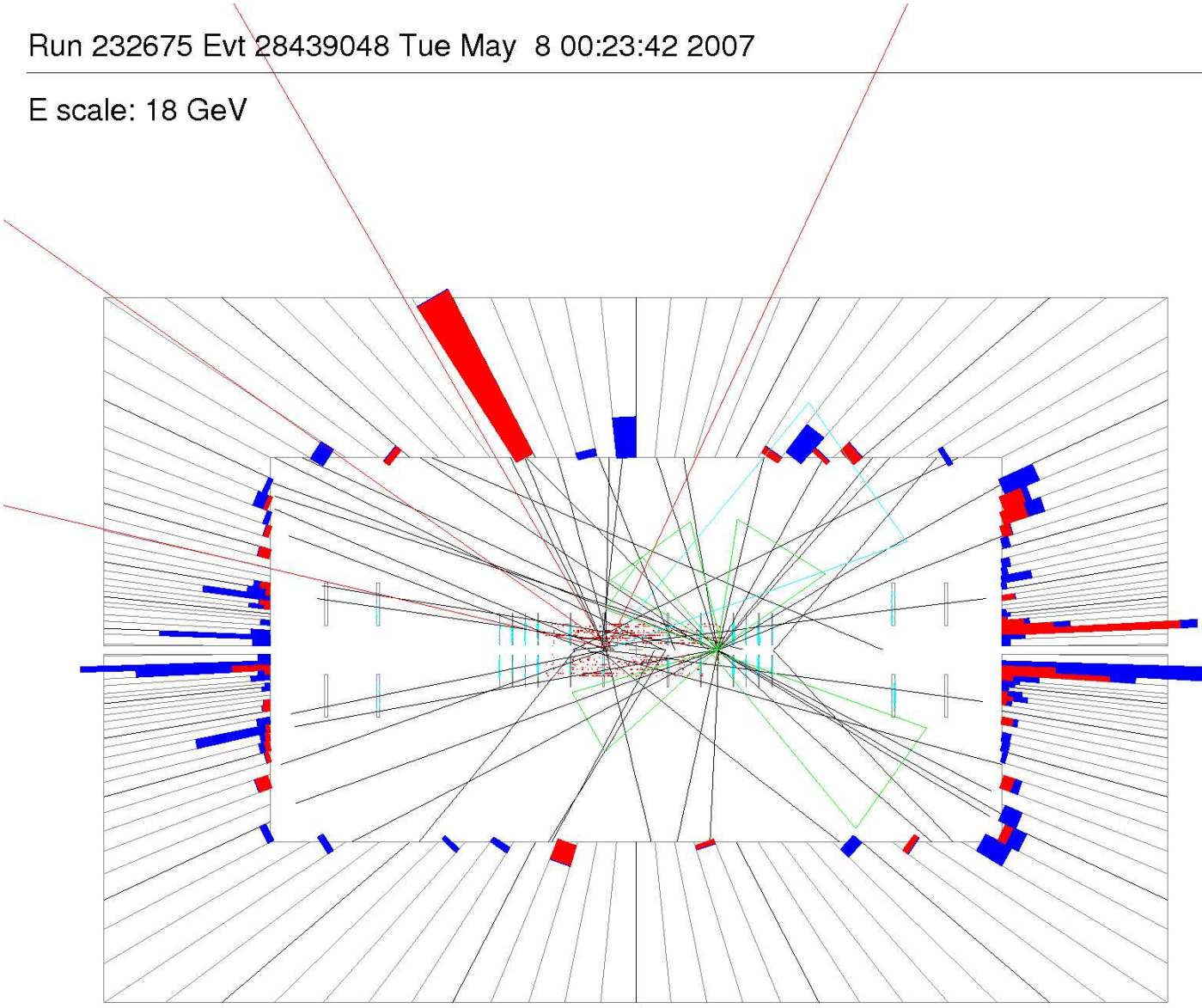

Figure A.14.: Eventdisplay of the event selected in the high-p_T $\mu\mu\ell$ analysis after applying all selection criteria.

A.3.3. Electron Events

One of the events observed in data in the low-p_T $ee\ell$ selection. Figure A.15 shows a lego view, Figure A.16 shows an xy-view and Figure A.17 presents an $r-z$ view.

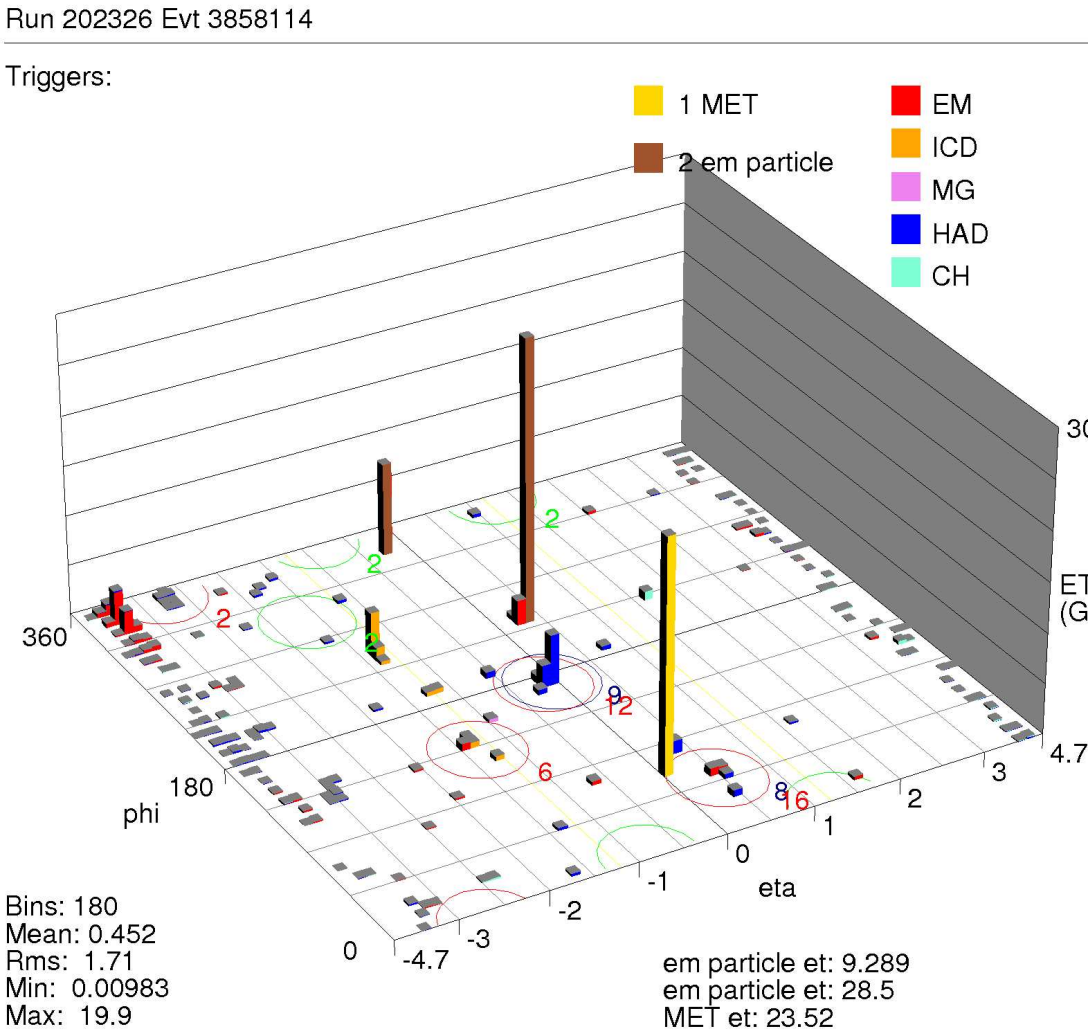

Figure A.15.: Eventdisplay of one of the remaining events in the electron analysis after applying all selection criteria. The electrons are marked in brown.

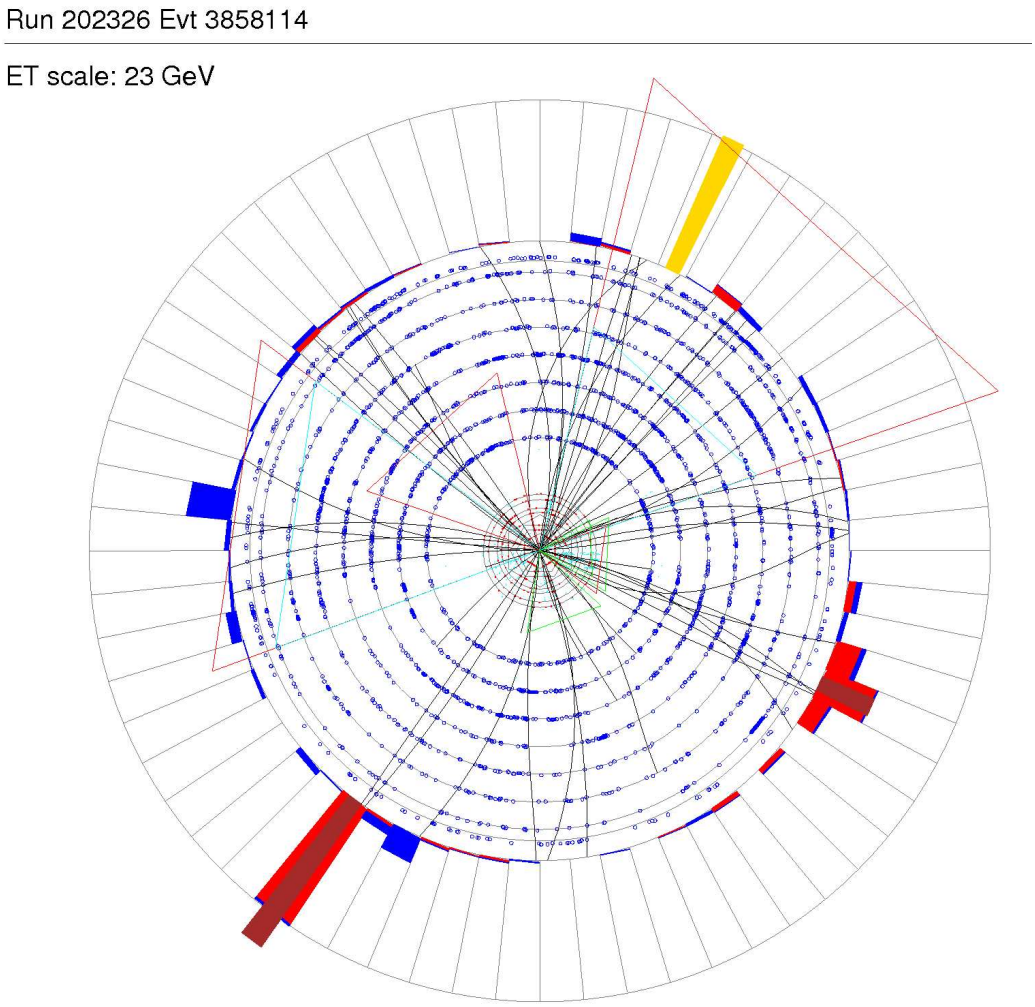

Figure A.16.: *xy* display of one of the remaining data events in the electron analysis after applying all selection criteria. The electrons are visible as brown. A jet fakes the third track.

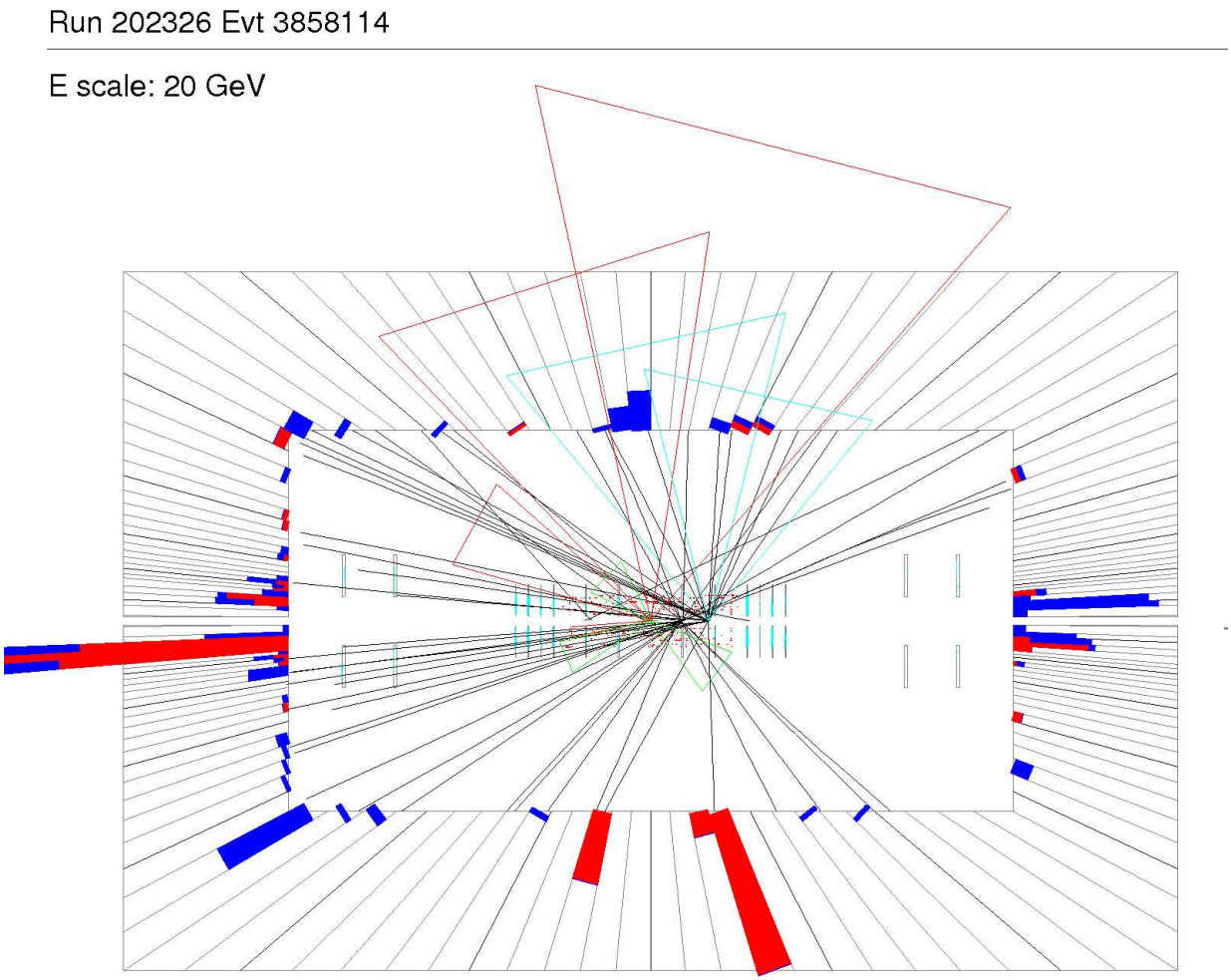

Figure A.17.: $r-z$ display of one of the remaining data events in the electron analysis after applying all selection criteria. The electrons are visible as brown. A jet fakes the third track.

A.4. Fit Parameters of Signal Efficiencies

This section contains the parameters used for the fit functions of the various selections.

A.4.1. Low-p_T $\mu\mu\ell$ Selection

Table A.7.: Fit parameters for the fits in the 2-body region (see Figure 10.4) in the low-p_T $\mu\mu\ell$ analysis as a function of $\Delta m_{\tilde{\ell}}$. The parameters are listed for diagonal 1, 2 and 3 shown in Figure 7.4.

Parameter	Diagonal 1	Diagonal 2	Diagonal 3
par0	2.65e-03	2.01e-03	1.44e-03
par1	-80	-100	-120
par2	3.45e-02	3.03e-02	2.07e-02
par3	-6	-6	-6
par4	5.78e-02	6.88e-02	1.08e-01
par5	1.05e-02	1.30e-02	1.64e-02
par6	-1	-1	-1
par7	1	1	1

Table A.8.: Parameters of the functions used to fit the signal efficiency $\tilde{\chi}_1^{\pm} \rightarrow \tilde{\nu}\ell$, as a function of mass difference between sneutrino and next to lightest neutralino in the 2 body region. The parameters are listed for diagonal 1-3 (see Figure 7.4) in the low-p_T $\mu\mu\ell$ analysis. par0 denotes the amplitude of the Gaussian used in the fit. The position and width of the Gaussian are kept constant.

Parameter	Diagonal 1	Diagonal 2	Diagonal 3
par0	1.71e-02	2.53e-02	1.73e-01
par1	-12	-12	-12
par2	4	4	4

Table A.9.: Fit parameters for the fits in the 3-body region in the low-p_T $\mu\mu\ell$ analysis.

Parameter	$m_{\tilde{\chi}_1^{\pm}}$ dependence	$\Delta m_{\tilde{\ell}}$ dependence
par0	-2.80e-02	1.075
par1	1.72	0.35
par2	2.78e-02	-0.14

A.4.2. Low-p_T $ee\ell$ Selection

Table A.10.: Parameters for the fits as a function of $\Delta m_{\tilde{\ell}}$ for $\tilde{\chi}^{\pm} \rightarrow \tilde{\ell}\nu$ decays in the low-p_T $ee\ell$ analysis The parameters are listed for diagonals 1, 2 and 3 shown in Figure 7.4.

Parameter	Diagonal 1	Diagonal 2	Diagonal 3
par0	2.76e-03	1.99e-03	3.16e-02
par1	-80	-100	-120
par2	3.77e-02	2.98e-02	2.01e-02
par3	-6	-6	-6
par4	5.35e-02	6.64e-02	1.67e-02
par5	8.88e-03	1.18e-02	1.41e-02
par6	-1	-1	-1
par7	1	1	1

Table A.11.: Fit parameters for 2-body region as a function of $\Delta m_{\tilde{\nu}}$. The fit parameters are listed for diagonal 1-3 (see Figure 7.4) in the low-p_T $ee\ell$ analysis

Parameter	Diagonal 1	Diagonal 2	Diagonal 3
par0	1.76e-02	7.97e-02	3.56e-02
par1	-12	-12	-12
par2	4	4	4

Table A.12.: Fit parameters for 3-body region for the low-p_T $ee\ell$ analysis.

Parameter	$m_{\tilde{\chi}_1^{\pm}}$ dependence	$\Delta m_{\tilde{\ell}}$ dependence
par0	1.08	1.075
par1	3.86e-01	0.35
par2	-1.69e-01	-0.14

A.4.3. Fit Parameters $\mu\mu\ell$ and $ee\ell$ High-p_T Selections

Table A.13.: Fit parameters for the fits in the 2-body region in the high-p_T $\mu\mu\ell$ analysis as a function of $\Delta m_{\tilde{\ell}}$. The parameters are listed for diagonal 1,2 and 3 shown in 7.4.

Parameter	Diagonal 1	Diagonal 2	Diagonal 3
par0	1.95e-03	2.20e-03	2.22e-03
par1	-80	-100	-120
par2	1.93e-02	3.97e-02	6.00e-02
par3	-6.0	-6.0	-6.0
par4	4.00e-02	3.09e-02	2.55e-02
par5	4.29e-03	6.90e-03	1.14e-02
par6	-1.0	-1.0	-1.0
par7	1.0	1.0	1.0

Table A.14.: Fit parameters for the fits in the 2-body region in the high-p_T $ee\ell$ analysis as a function of $\Delta m_{\tilde{\ell}}$. The parameters are listed for diagonal 1,2 and 3 shown on 7.4.

Parameter	Diagonal 1	Diagonal 2	Diagonal 3
par0	2.20e-03	2.20e-03	2.20e-03
par1	-80	-100	-120
par2	2.59e-02	4.26e-02	6.27e-02
par3	-6.00	-6.00	-6.00
par4	4.00e-02	2.39e-02	1.91e-02
par5	1.02e-03	1.71e-03	3.56e-03
par6	-1.0	-1.0	-1.0
par7	1.0	1.0	1.0

Table A.15.: Fit parameters for 2-body region as a function of $\Delta m_{\tilde{\nu}}$. The fit parameters are listed for diagonal 1-3 in the high-p_T $\mu\mu\ell$ analysis

Parameter	Diagonal 1	Diagonal 2	Diagonal 3
par0	0.0059	0.0371	0.0373
par1	-12	-12	-12
par2	4	4	4

Table A.16.: Fit parameters for 2-body region as a function of $\Delta m_{\tilde{\nu}}$. The fit parameters are listed for diagonal 1-3 in the high-p_T $ee\ell$ analysis

Parameter	Diagonal 1	Diagonal 2	Diagonal 3
par0	0.00054	0.0089	0.0091
par1	-12	-12	-12
par2	4	4	4

Table A.17.: Fit parameters for 3-body region for the high-p_T $\mu\mu\ell$ analysis.

Parameter	$m_{\tilde{\chi}_1^\pm}$ dependence	$\Delta m_{\tilde{\ell}}$ dependence
par0	-0.0001423	1.002
par1	-0.21	0.21
par2	1.219	-0.214

Table A.18.: Fit parameters for 3-body region for the high-p_T $ee\ell$ analysis.

Parameter	$m_{\tilde{\chi}_1^\pm}$ dependence	$\Delta m_{\tilde{\ell}}$ dependence
par0	-5.96e-05	1.077
par1	0.1458	0.46
par2	0.86	-0.32

Bibliography

[1] S. L. Glashow, Nucl. Phys **22** (1961) 579;
S. Weinberg, Phys. Rev. Lett. **19** (1967) 1264;
A. Salam, *Elementary Particle Theory*, ed. N. Svartholm (Almquist and Wiksell, Stockholm, 1968), 367;
P.W. Higgs, Phys. Rev. Lett. **13** (1964) 508-509.

[2] H. Baer, X. Tata, *Weak Scale Supersymmetry: From Superfield to Scattering Events*, Cambridge University Press (2006)

[3] Y. Fukuda *et al.,* Phys. Rev. Lett. **81** (1998) 1562-1567.

[4] S. Eidelmann *et al.,* [Particle Data Group] Phys. Lett. **B592**, 283-288 (2004).

[5] D. J. Gross and F. Wilczek, Phys. Rev. **D8** (1973) 3633;
H. D. Politzer, Phys. Rep. **14** (1974) 129.

[6] P. W. Higgs, *Broken summetries and the masses of gauge bosons.* Phys. Rev. Lett. 13 (1964) 508

[7] LEP Electroweak Working Group `ttp://lepewwg.web.cern.c`/LEPEWWG/.

[8] R.N. Mohapatra, *Unification and Supersymmetry*, Springer Verlag, New York, Berlin, Heidelberg (2003).

[9] M. Drees, *An Introduction to Supersymmetry*, APCTP-5 KEK-TH-501 (1996), hep-ph/9611409.

[10] E. Komatsu *et al., Five-Year Wilkinson Microwave Anisotropy Probe (WMAP) Observations: Cosmological Interpretation*, Submitted to the Astrophysical Journal Supplement Series, astro-ph/0803.0547, 2008

[11] S. P. Martin, *A Supersymmetry Primer*, hep-ph/9709356.

[12] M.B. Green, J.H. Schwarz and E. Witten, *Superstring Theory*,
Cambridge Univerity Press, Cambridge (1987).

[13] Y.A. Golfand and E.P. Likhtman, JETP Lett. **13** (1971) 452;
D. Volkov and V.P. Akulow, JETP Lett. **16** (1972) 438;
H.P. Nilles, Phys. Rep. **110** (1984) 1;
H.E. Haber and G.L. Kane, Phys. Rep. **117** (1985) 75.

[14] E.Cremmer *et al.,* Phys. Lett. **B116** (1982) 231;
A.H. Chamseddine, R. Arnowitt and P. Nath, Phys. Rev. Lett. **29** (1082) 970;
J. Bagger and E. Witten, Phys. Lett. **B118** (1982) 103.

[15] S. Abel *et al., Report of SUGRA Working Group for Run II of the Tevatron*, hep-ph/0003154.

[16] G.F. Giudice, R. Rattazzi, *Theories with Gauge-Mediated Supersymmetry Breaking*, hep-ph/9801271.

[17] DØCollaboration, *Search for Squarks and Gluinos in Events with Jets and Missing Transverse Energy using 2.1 fb^{-1} of $p\bar{p}$ Collision Data at $\sqrt{s}$ = 1.96 TeV*, Phys. Lett. **B660** (2008) 449.

[18] CDF Collaboration, *Search for Gluinos and Squarks in Multi-Jets plus Missing Transverse Energy Final States*, CDF Note 9229.

[19] W. Beenakker *et. al., The Production of Charginos/Neutralinos and Sleptons at Hadron Colliders*, Phys. Rev. Lett. **83** (1999), hep-ph/9906298.

[20] C. Noeding, *Suche nach Neuer Physik in Elektron-Tau Endzustaenden in Proton-Antiproton Kollisionen bei 1.96 TeV.*, Ph.D. thesis, University of Freiburg (2006).

[21] I. Torchiani, *Search for the Associated Production of Charginos and Neutralinos in the $\mu + \tau + \ell$ Final State*, DØ Note 4743. Ph.D. thesis, University of Freiburg (2008).

[22] LEPEWWG and ALEPH and DELPHI and L3 and OPAL experiments, `http://lepsusy.web.cern.ch/lepsusy/Welcome.html`.

[23] LEPSUSYWG and ALEPH and DELPHI and L3 and OPAL experiments, LEPSUSYWG/04-01.1, `http://lepsusy.web.cern.ch/lepsusy/Welcome.html`

[24] LEPSUSYWG and ALEPH and DELPHI and L3 and OPAL experiments, LEPSUSYWG/02-06.2, `http://lepsusy.web.cern.ch/lepsusy/Welcome.html`

[25] LEPSUSYWG and ALEPH and DELPHI and L3 and OPAL experiments, LEPSUSYWG/02-06.1, `http://lepsusy.web.cern.ch/lepsusy/Welcome.html`

[26] B. Abbott *et al., Search for Trilepton Signatures from Associated Gaugino Pair Production*, Phys. Rev. Lett. **80** (1998) 8.

[27] F. Abe *et al., Search for Chargino-Neutralino Associated Production at the Fermilab Tevatron Collider*, Phys. Rev. Lett. **80** (1998) 5275.

[28] V. Abazov *et al., Search for Supersymmetry via Associated Production of Charginos and Neutralinos in Final States with Three Leptons*, Phys. Rev. Lett. **95** (2005).

[29] S. Heinemeyer, X. Miao, S. Su, G. Weglein, *B-Physics Observables and Electroweak Precision Data in the CMSSM, mGMSB and mAMSB,* arXiv:hep-ph/0805.2359v2 (2008).

[30] NATIONAL AERONAUTICS AND SPACE ADMINISTRATION, Wilkinson Microwave Anisotropy Probe, `ttp://map.gsfc.nasa.gov/}.%\bibitem{wilkinson2}% J.~Dunkley{\itet.al.,}%Five-YearWilkinsonMicrowaveAnisotropyProbe(WMAP) Observations:%{\itLikeli`oods and Parameters from the WMAP data,

[31] O. Buchmueller *et.al., Predictions for Supersymmetric Particle Masses using Indirect Experimental and Cosmological Constraints* arXiv:hep-ph/0808.4128v1 (2008).

[32] `http://www-d0.fnal.gov`

[33] Fermilab Beams Division, `http://www-bd.fnal.gov/`

[34] `http://www.fnal.gov/`

[35] `http://lhc-new-homepage.web.cern.ch/lhc-new-homepage`

[36] `http://public.web.cern.ch/Public/Welcome.html`

[37] `http://www-cdf.fnal.gov`

[38] F. Abe *et.al.,* (CDF Collaboration), *Observation of the Top Quark in $p\bar{p}$ Collisions with the Collider Detector at Fermilab*, Phys. Rev. Lett. **74**, 2626 (1995), hep-ex/9503002.

[39] S. Abachi *et.al.,* (DØ Collaboration), *Observation of the Top Quark*, Phys. Rev. Lett. **74**, 2632 (1995), hep-ex/9503003.

[40] S. Abachi *et al.,* Nucl. Instr. and Meth. **A338** (1994) 185.

[41] V.M. Abazov *et al., The Upgraded DØ Detector*, hep-ph/0507191.

[42] DØRunIIb Upgrade Technical Design Report

[43] D. Chapin *et al., Measurement of $Z \rightarrow ee$ and $W \rightarrow e\nu$ Production Cross Sections Using One Tight Central Electron*, DØ Note 489 (2005).

[44] M. Voutilainen, C. Royon, *Jet p_T resolution using JetCorr v7.1*, DØ Note 5381 (2007).

[45] C. C. Mia (The DØCollaboration), *The DØRun II luminosity monitor*, Nucl. Phys. Proc. Suppl. **78**, 342 (1999).

[46] M. Abolins, *et al., The RunIIb Trigger Upgrade for the DØ Experiment*, IEEE Transactions on Nuclear Science, VOL. 51, NO. 3, June 2004

[47] T.Sjostrand, *2006 European School of High Energy Physics, Aronsborg Sweden, 18 Jun-1 Jul 2006: Proceedings*, CERN-200-005, 2007

[48] CTEQ group *New Generation of Parton Distributions with Uncertainties from Global QCD Analysis (CTEQ6)*, hep-ph/0201195.

[49] T. Sjostrand *et al.,* Comp. Phys. Commun. **135** (2001) 238.

[50] M.L. Mangano *et al.*, J. High Energy Phys. 07 (2003) 001.

[51] G. Altarelli, G. Parisi, Nucl. Phys. **B126** (1977) 298.

[52] T. Sjostrand *et al.,* Comp. Phys. Commun. **135** (2001) 238.

[53] B. Andersson *et al.,* Phys. Rep. **97** (1983);
B. Andersson, *The Lund Model*, Cambridge University Press (1998).

[54] Y. Fisyak, J. Womersley, *DØGSTAR, DØ GEANT simulation of the Total Apparatus Response*, DØ Note 3191.

[55] `http://www-d0.fnal.gov/computing/MonteCarlo/simulation/d0sim.html`

[56] Application Software Group, CERN Computing and Networks Division, *GEANT, Detector Description and Simulation Tool*, CERN Program Library Long Writeup W5013.

[57] `http://www-d0.fnal.gov/computing/mcprod/Certification/ZBcertPlots.html`.

[58] `http://www-d0.fnal.gov/D0Code/source/d0reco`.

[59] R. Brun, F. Rademakers, and S. Panacek, *ROOT, an object oriented data analysis framework*.

[60] Getting started with electron/photon ID. URL `http://www-d0.fnal.gov/phys_id/emid/d0_private/emid_intro.html`

[61] J. Koszminski. R. Kehoe, H. Weerts, S.-J. Park, A. Quadt, J. Gardner, S. Jabeen, *Electron Likelihood in p14*, DØ Note 4449.

[62] A. Abdesselam, *Comparison of H-Matrices for electron identification in DØ Run II*, DØ Note 3745.

[63] J. Hays, J. Mitrevski, C. Schwanenberger, T. Toole *Single Electron Efficiencies in p17 Data and Monte-Carlo Using p18.05.00 d0correct* DØ Note 5105.

[64] M. Strang, I. Iashvili *Measurement of* $p\bar{p} \to ZZ \to \ell^+\ell^-\ell'^+\ell'^-$ *production cross section using Run IIb Data.* DØ Note in preparation.

[65] DØMuon ID group, *Muon Identification for p17 Data*, DØNote 4350.

[66] E. Busato, B. Andrieu, *Jet Algorithms in the DØ Run II Software: Description and User's Guide*, DØ Note 4457.

[67] `http://www-d0.fnal.gov/computing/algorithms/calgo/jet_met/certification.html`

[68] `http://www-d0.fnal.gov/phys_id/jets/jetid.html`

[69] J-L. Agram *et al., Jet Energy Scale at DØ Run II*, DØ Note 4720.

[70] `http://www-d0.fnal.gov/phys_id/jes/d0_private/jes.html`.

[71] DØ Jet Energy Scale Group, Jet Energy Scale Determination at DØ Run II (Final p17 Version), DØ Note 5382.

[72] S. Trincaz-Duvoid, P. Verdier, *Missing ET reconstruction in p17* (2004). DØ Note 4474

[73] P. Verdier, *Status of missing ET in RunIIb data.* Presented at the Joint Algorithms/Physics Conveners Meeting, September 1, 2006.

[74] G. Borisov, `http://www-d0.fnal.gov/global_tracking/talks/20030228/talk-adm-030228.ps`

[75] A. Khanov, *HTF: Histogramming Method for Finding Tracks*, DØ Note 3778.

[76] A. Schwartzman, C. Tully *Primary vertex reconstruction by means of adaptive vertex fitting* (2005). DØ Note 4918.

[77] DØ Common Samples Group, `http://www-d0.fnal.gov/Run2Physics/cs/index.html`.

[78] DØ Data Quality Group, `http://www-d0.fnal.gov/computing/data_quality`.

[79] L. Duflot,V. Shaary,R. Zitoun,I. Torchiani, *cal_event_quality package*, DØ Note 4614.

[80] Talks from V. Shaary, G. Bernardi, P. Verdier given at the DØWinter Physics Workshop, February 22-24, 2004. `http://www-d0.hef.kun.nl/fullAgenda.php?ida=a04273`.

[81] J. Hays *et.al.*, *Electron Trigger Efficiencies using Calorimeter Information in p17 Data*, DØ Note 5138.

[82] DØ Trigger Studies Group, *ORing Single Muon Triggers in p17 Data*, DØ Note 5329.

[83] DØ Collaboration, *Triggermeister Web Page*, `http://www-d0online.fnal.gov/www/groups/tm/tm_main.html`.

[84] B. Penning, R. Bernhard, *Search for the Higgs boson in* $H \rightarrow WW^* \rightarrow ee$ *decays at DØ using Neural Networks with* $3fb^{-1}$ *of Data*, DØ Note 5712.

[85] T. Gadfort,A. Haas,D. Johnston,B. Penning, *Search for the Higgs boson in* $H \rightarrow WW^* \rightarrow \mu\mu$ *decays at DØ using Neural Networks with* $3fb^{-1}$ *of Data*, DØ Note in preparation.

[86] B. Penning, *Search for the Higgs boson in* $H \rightarrow WW^* \rightarrow ee$ *decays at DØ using Neural Networks and Matrix Elements*, DØ Note 5575.

[87] T. Gadfort,A. Haas, *Search for* $H \rightarrow W^+W^- \rightarrow \mu^+\nu_\mu\mu^-\bar{\nu}_\mu$ *Using Matrix Elements and a Neural Network in* $1.2fb^{-1}$ *of Run IIb Data*, DØ Note 5623.

[88] S. Hoeche *et. al., Matching Parton Showers and Matrix Elements*, arXiv:hep-ph/0602031 (2006).

[89] R. Hamberg, W. L. van Neerven and T. Matsuura, *A Complete calculation of the Order* α_s^2 *Correction to the Drell-Yan K-Factor*, Nucl. Phys. **B359** (1991) 343 [Erratum-ibid. B 644 (2002) 403].

[90] T. Nunnemann, *NNLO Cross-Sections for Drell-Yan, Z and W Production using Modern Parton Distribution Functions*, DØ Note 4476.

[91] N. Kidonaiks, R. Vogt, Int.J.Mod.Phys **20** (2005) 3171

[92] V. Buescher, J.-F. Grivaz, T. Nunnemann, M. Wobisch, *Conclusions of Mini-Workshop on PDF uncertainties and related topics*, DØ Note 4618.

[93] DØ New Phenomena MC webpage,
`http://www-clued0.fnal.gov/~nunne/cross-sections/mcfm_cross-sections.html`

[94] J. Campbell, K. Ellis, MCFM–A Monte Carlo for FeMtobarn processes at Hadron Colliders http://mcfm.fnal.gov/

[95] D. Gillberg, *Heavy Flavour Removal and Determination of Weighting Factors for ALPGEN W+jets Monte Carlo*, DØ Note 5129.

[96] W. Beenakker, R. Heopker,M. Spira, PROSPINO: A Program for the Production of Supersymmetric Particles in Next-to-leading Order QCD hep-ph/9611232

[97] B.C. Allanach, SOFTSUSY: A Program for Calculating Supersymmetric Spectra `http://www.citebase.org/abstract?id=oai:arXiv.org:hep-ph/0104145`,

[98] M. Muhlleitner, A. Djouadi, and Y. Mambrini, SDECAY: A Fortran Code for the decays of the supersymmetric particles in the MSSM. *Computer Physics Communications*, 168:46, 2005

[99] J. Hays, J. Mitrevski, C. Schwanenberger, *The Program Package em_cert: Version p18-br-20*, DØ Note 5070.

[100] DØ muo cert documentation,
`https://plone4.fnal.gov/P1/D0Wiki/object-id/mu_id/muo_cert/`

[101] DØ Collaboration, *Measurement of the Cross Section for W and Z Production to Electron Final States with the DØ Detector at* $\sqrt{s} = 1.96$ TeV, DØ Note 4403-CONF (2004);
D. Chapin *et al., Measurement of* $Z \to ee$ *and* $W \to e\nu$ *production cross sections with* $|\eta| < 1.05$,
`http://www-d0.fnal.gov/Run2Physics/d0_private/eb/Run2EB_003/Run2EB_003.html`

[102] M. Arthaud, F. Deliot, B. Tuchming, V. Sharyy, D. Vilanova, *Muon Momentum Oversmearing for p17 Data*, DØ Note 5444.

[103] M. Arthaud, F. Deliot, B. Tuchming, V. Sharyy, D. Vilanova, *Muon Momentum Oversmearing for p20 Data*, DØ Note 5449.

[104] B. Tiller, T. Nunnemann, *Measurement of the differential Z0-boson production cross-section as function of transverse momentum*, DØ Note 4660.

[105] E. Shabalina, *Summary of V+Jets Workshop*, Talk in All DØ meeting 04.04.2008.

[106] G. Bernardi *et.al., Search for WH associated production using a Neural Net and Matrix Element Approach with 2.7* fb^{-1} *of RunII data*, DØ Note 5714.

[107] *TLimit, C++ Class for Limit Computaion in ROOT*, Code adapted from MCLimit code from T. Junk.

[108] G. Cowan, *Statistical Data Analysis*, Oxford University Press, Oxford, New York, 1998.

[109] R.J. Barlow, *Statistics, a guide to the use of statistical methods in the physical sciences*, John Wiley and Sons, New York, 1997.

[110] V. Büscher *et. al.,* Recommendations of the Ad-Hoc Commitee on Limit-Setting Procedures to be Used by DØ in Run II, DØ Note 4629.

[111] V. Büscher, M. Hohlfeld, O. Mundal, I. Torchiani, *Search for the Associated Production of Chargino and Neutralino in* $\mu\mu\ell$, $ee\ell$ *and* $e\mu\ell$ *Final States and Combination with* $\mu\tau_h\ell$ *Analyses* DØ Note in preparation

[112] U. Blumenschein, *Suche nach assoziierter Chargino-Neutralino Produktion in Proton-Antiproton Kollisionen bei 1.96 TeV*, PhD thesis, University of Freiburg (2005).

[113] W. Beenakker, R. Hopker, M. Spira, P.M. Zerwas, *Squark and Gluino Production at Hadron Colliders*, Nucl. Phys. **B492** (1997), hep-ph/9610490.

[114] F. Gianotti, M. Mangano, *LHC phycics: the first one-two year(s)*, CERN-PH-TH/2005/072, [arXiv:hep-ph/0504221] (2005).

[115] Atlas Collaboration, CSC Note, Supersymmetry.

[116] CDF Collaboration, *Search for Supersymmetry in ppbar Collisions at sqrt(s)=1.96 TeV Using the Trilepton Signature of Chargino-Neutralino Production* arXiv:hep-ex/0808.2446, 2008.

[117] CDF Collaboration, `http://www-cdf.fnal.gov/physics/exotic/r2a/20080110.trilepton_dube/`

Acknowledgements

There are many people that were of invaluable support during my PhD studies and I would like to take the opportunity to thank all of them.

First of all I would like to thank Prof. Dr. Volker Büscher for all his help and support the last 3.5 years. His door was never closed and he was always ready to answer every possible questions I might have. Also thank to Dr. Marc Hohlfeld who was of invaluable support during the time in Bonn. I could always ask for help, not only physics questions, but also for things like putting up the curtains, painting the appartment and storing my stuff at his place.

I began the work on this thesis in Freiburg, and I would like to thank Prof. Dr. Karl Jakobs for giving me the opportunity to start in his group. Special thanks to Ulla Blumenschein and Carsten Nöding who helped me in the first months of working with DØ and I should also not forget the other people in the Freiburg DØ group: Harald Fox, Maxim Titov, Björn Penning, Jens Konrad and Ralf Bernhard. In addition: Thanks to Ingo Torchiani and to Henrik Nilsen. Ingo, it was always good to hear "breathe in-breathe out" from you, when the to-do list was growing longer than a role of toilet paper. And Henrik, I will never hold against you that you are from Bergen.

The Atlas part of the group in Freiburg also made this a memorable time: Michael Heldmann and Michael Dührssen, especially for computing assistance, Giacinto, Inga, Andrea and Uli Parzefall who helped a poor Norwegian the first confusing days in Germany March 2005.

Also thanks to all the people at Fermilab: Gernot, Alexander, Yvonne, Matthias, Christian (Schwani), Jörg, Philippe, Hendrik, Carsten, Thorsten and Maren. And a warm thank you to Marc-Andre and Heather!

I also wish to thank the New Phenomena group with current and past conveners: Jean-Francois Grivaz, Arnd Meyer, Yurii Gehrstein, Patrice Verdier, Todd Adams and Arnaud Duperrin. During my stay at Fermilab, I also had an interesting time in the Calorimeter group, lead by Norm Buchanan.

When I moved to Bonn January 2007, I was given a warm welcome by Prof. Dr. Norbert Wermes' group, and I would like to thank everybody for the last two years. Special thanks to Jan Schumacher for life-saving software help and to Robindra Prabhu, with whom I could talk Norwegian and share common frustrations.

Thanks to old friends in Oslo and all over the world; Øystein, Mustafa, Gustav, Marius, Cathrine, Bernt and Lars-Ole and everyone who I don't mention explicitly, but who I haven't forgotten.

Skype has been a good way of staying in touch, and not few (friendly) insults have been thrown.

I would like give my whole family a warm thank you, and especially my father and my aunt, my mother and Finn for their help and support, and my sisters, Line, Marianne, Anneli and Sunniva. When I was far away, I would always know that it would be good to come home.

And to Su-Jung: for being who you are and for always being there.